Electron Spin Resonance in Low-Dimensional Spin Chains and Metals

Von der Fakultät Mathematik und Physik der Universität Stuttgart zur Erlangung der Würde eines Doktors der Naturwissenschaften (Dr. rer. nat) genehmigte Abhandlung

Vorgelegt von

Shadi Shaikh Yasin

geboren in Kuwait, Jordanien

Hauptberichter	Prof. Dr. M. Dressel
Mitberichter	Prof. Dr. D. Schweitzer

Tag der mündlichen Prüfung: 24. November 2008

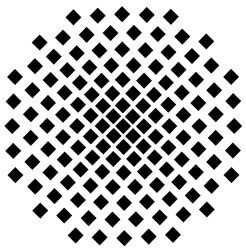

1. Physikalisches Institut der Universität Stuttgart

November 2008

Contents

Abbreviations and Symbols

1, 2, 3-D	one, two, three dimensional
A	acceptor
AFE	antiferroelectric
AFM	antiferromagnetic
AFMR	antiferromagnetic Resonance
AO	anion ordering
AZ interaction	anisotropic Zeeman interaction
BEDT-TTF	bisethylenedithio-tetrathiafulvalene [$(CH_2)_4C_6S_8$]
B_{c1}	lower critical magnetic field
B_{c2}	upper critical magnetic field
BCS	Bardeen, Cooper and Schrieffer (theory)
CDW	charge density wave
CO	charge order
CW	continuous wave
d_1	intradimer distance
d_2	interdimer distance
D	donor
DC	direct current
DPPH	1,1-diphenyl- 2-picryl- hydrazyl
EAT-model	Eggert, Affleck and Takahashi-model
ESR	electron spin resonance
FE	ferroelectric
g	g-value
$g_{\parallel}$	in-plane g-value
H_1	microwave magnetic field
H_o	static magnetic field

Abbreviations and Symbols

H_{c1}	Lower critical magnetic field
H_{c2}	Upper critical magnetic field
HOMO	highest occupied molecular orbital
H_{res}	resonance magnetic field
HWHM	half width at half maximum
J	antiferromagnetic exchange constant
J_1	intradimer antiferromagnetic exchange constant
J_2	interdimer antiferromagnetic exchange constant
J'	Inter-chain exchange constant
k_F	Fermi wave vector
loc	localized state
M_2	Second magnetic moment
MF	mean field (theory)
m^*	effective mass
NMR	nuclear magnetic resonance
P_{abs}	absorbed microwave power
PP	peak-to-peak
q_{AO}	anion ordering wave vector
SC	superconductivity
SDW	spin density wave
SP	spin-Peierls
SQUID	superconducting quantum interference device
T_1	spin lattice relaxation time
T_2	spin spin relaxation time
t_a, t_b, t_c	transfer integrals
T_{AO}	anion ordering transition temperature
T_c	superconducting transition temperature
T_{CO}	charge ordering transition temperature
TE	transverse electric (cavity mode)
T_g	glassy transition temperature

TMTSF	tetramethyltetraselenafulvalene [$(CH_3)_4C_6Se_4$].
TMTTF	tetramethyltetrathiafulvalene [$(CH_3)_4C_6S_4$].
TMT*C*F	TMTSF and TMTTF
T_F^*	effective Fermi temperature
T_N	antiferromagnetic transition temperature (Neel temperature)
T_{SP}	spin Peierls transition temperature
TTF	Tetrathiofulvalene
T_ρ	localization temperature
$t_\parallel$	transfer integral parallel to the highest conduction direction
$t_\perp$	transfer integral perpendicular to the highest conduction direction
U	on-site Coulomb repulsion
V	inter-site Coulomb repulsion
V_c	critical inter-site Coulomb repulsion
Δg	g-shift (g-2.002319)
ΔH	ESR linewidth (half width at half maximum)
ΔH_{CO}	ESR linewidth induced by the charge ordering
ΔH_{pp}	ESR linewidth (peak to peak)
L	orbital angular momentum
Δ_ρ	localization energy gap
Δ_σ	singlet triplet energy gap
ε'	dielectric constant
λ_{SO}	spin-orbit coupling constant
ρ_{RT}	electrical resistivity at room temperature
$\rho_\parallel$	electrical resistivity parallel to the conduction plane
$\rho_\perp$	electrical resistivity perpendicular to the conduction plane
ρ_o	residual resistivity
σ	electrical conductivity
$\tau_\parallel$	on-chain scattering time
$\tau_\perp$	interchain tunnelling time
χ_s	spin susceptibility

Abbreviations and Symbols

$(\chi_s)_p$	spin susceptibility at constant pressure
$(\chi_s)_v$	spin susceptibility at constant volume
γ	Sommerfeld coefficient
ϕ_0	Magnetic flux quantum

Kurzfassung

Niedrigdimensionale organische Leiter sind sicherlich eines der interessantesten und fruchtbarsten Forschungsgebiete der modernen Festkörperphysik: die reduzierte Dimensionalität und die Konkurrenz zwischen elektronischen, magnetischen und Gitter-Freiheitsgraden führen zu Phasenübergängen in verschiedene Grundzustände wie z. B. Spin- und Ladungsordnung oder Supraleitung. Aufgrund der reduzierten Dimensionalität zeigen diese Materialien ein stark anisotropes Verhalten in einigen physikalischen Größen. Diese Anisotropie der physikalischen Größen entsteht durch die ungewöhnliche Gitterstruktur. Während die Moleküle in eindimensionalen Materialien kettenförmig angeordnet sind, bilden sie in zweidimensionalen Systemen Ebenen.

Wegweisende niedrigdimensionale Systeme sind die organischen Ladungstransfersalze, z. B. die quasi eindimensionalen $(TMTSF)_2X$ und $(TMTTF)_2X$ und die zweidimensionalen Metalle der $(BEDT\text{-}TTF)_2X$ Familie. Die physikalischen Eigenschaften und die Dimensionalität dieser Materialien kann leicht variiert werden, indem das Anion ausgetauscht oder äußerer Druck angelegt wird. Für diese Salze ergibt sich so ein reichhaltiges Phasendiagramm mit Phasenübergängen in diverse Grundzustände. Dies macht sie zu idealen Kandidaten zur Untersuchung der Physik niedrigdimensionaler Systeme.

Spin- und Ladungsordnung sind eines der faszinierenden Phänomene, die bei tiefen Temperaturen in den $(TMTTF)_2X$ Salzen beobachtet werden. Verschiedene Messungen, wie z.B. NMR [1], ESR [2,3], optische Reflektivität [4] und dielektrische Permeabilität [5,6], wurden in den letzten Jahren an den Verbindungen $(TMTTF)_2X$ (X = ReO_4, AsF_6, SbF_6) durchgeführt, um Spin- und Ladungsordnungsphänomene zu untersuchen. Kürzlich an unserem Institut durchgeführte X-Band ESR-Messungen an $(TMTTF)_2AsF_6$ und $(TMTTF)_2SbF_6$ [2] zeigten Anhaltspunkte für einen neuen Streuprozess im ladungsgeordneten Zustand, welcher auf magnetisch nicht äquivalente Gitterplätze hindeutet. Um dies genauer zu untersuchen, war es notwendig hochfrequente ESR-Messungen durchzuführen und die Ergebnisse mit denen von anionengeordneten TMTTF Salzen, wie z. B. $(TMTTF)_2ReO_4$, für welche eine andere Verteilung der Ladungsordnung vorhergesagt wurde, zu vergleichen.

Die Konkurrenz zwischen der antiferromagnetischen und der supraleitenden Phase bzw. den Mott-Isolatoren und der metallischen Phase führte in den letzten Jahren

ebenfalls zu intensiven Untersuchungen an der isostrukturellen Familie κ-(BEDT-TTF)$_2$Cu[N(CN)$_2$]*X*, mit X = Br, Cl, I [7,8]. Trotz vielfältiger experimenteller Anstrengungen die Eigenschaften dieser Salze zu ergründen, sind die Erkenntnisse aus den Experimenten bis zum jetzigen Zeitpunkt sehr begrenzt. Zudem beschränkten sich alle diese Studien darauf, äußeren Druck anzulegen, um den Bereich des Mott-Hubbard-Überganges im Phasendiagramm zu bestimmen [8,9]. Die Frage nach der Art der Anregung der Ladungsträger bei tiefen Temperaturen [8, 10] and den Relaxationsprozessen [11] machte weitere Untersuchungen an diesen Verbindungen sinnvoll und motivierte uns, die Erkenntnisse über dieses Material zu vertiefen.

Im Rahmen der vorliegenden Arbeit wurden ausführliche Multifrequenz (X-Band (9.5 GHz), Q-Band (34 GHz) and W-Band (95 GHz)) Elektronenspinresonanz (ESR) Untersuchungen an den quasi eindimensionalen organischen Spinketten (TMTTF)$_2$*X* (*X* = ReO_4, AsF_6 and SbF_6) durchgeführt, um den spin- und ladungsgeordneten Zustand zu untersuchen und die Natur der Relexationsprozesse bestimmen zu können. X-Band und W-Band ESR-Messungen wurden in den Laboren des 1. und 2. Physikalischen Institutes der Universität Stuttgart unter Verwendung der beiden kommerziellen CW-Spektrometer Bruker ESP 300 and Bruker Elexsys 680 durchgeführt. Für die Q-Band ESR-Messungen wurde das Bruker Elexsys 500 Spektrometer am Lehrstuhl für Experimentalphysik V der Universität Augsburg verwendet. Des Weiteren wurden während dieser Doktorarbeit Transport-, SQUID und X-Band ESR-Messungen an der Verbindungsserie κ-(BEDT-TTF)$_2$Cu[N(CN)$_2$]Br$_x$Cl$_{1-x}$ (x = 0%, 20%, 40%, 70%, 80%, 85%, 90% and 100%) ausgeführt, um das Phasendiagramm in der Nähe des Mott-Hubbard-Überganges in Abhängigkeit des Bromgehaltes (x) zu untersuchen.

Für die temperaturabhängigen ESR-Messungen im Temperaturbereich zwischen 4.3K und 300K wurde an allen Spektrometern ein Durchflusskryostat der Firma Oxford eingesetzt. Für alle Messungen reichten schon relative kleine Kristalle aus, um ein ausreichend starkes ESR-Signal zu erhalten. Um einen Einfluss der Probengröße auf die ESR-Linienbreite zu vermeiden, mussten daher sehr kleine Kristalle für die Q- und W-Band ESR-Messungen verwendet werden. Die orientierungsabhängigen Messungen wurden bei konstanter Temperatur mit Hilfe eines Goniometers durchgeführt. Für die temperaturabhängigen ESR-Messungen wurde ein statisches Magnetfeld H_o entlang einer der drei kristallographischen Achsen angelegt. Die Berechnung der Linienbreite und des Resonanzfeldes aus dem

ESR-Spektrum erfolgte mittels Anpassung mit der Methode der kleinsten Fehler Quadrate. Der Vergleich von Intensität und Resonanzfeld des gemessenen ESR-Signals mit denen von DPPH ergab die Spin-Suszeptibilität und den g-Wert. Auch wurden DC-Suszeptibilitätsmessungen an einem Quantum Design SQUID Magnetometer durchgeführt. Der elektrische Widerstand der Proben wurde unter Verwendung der Vierpunktmethode bestimmt. Kontaktiert wurde die Proben mit 25 μm dicken Gold-Drähten, die mit Carbon-Paint direkt auf die Kristalle aufgeklebt wurden. Um Heizeffekte zu vermeiden, wurde der die Probe durchfließende Strom auf maximal 10 μA begrenzt.

In der paramagnetischen Phase weisen sowohl *g*-Wert als auch Linienbreite von $(TMTTF)_2ReO_4$ eine deutliche Anisotropie auf. Dies wurde auch in den zuvor untersuchten $(TMTTF)_2X$-Salzen gefunden [2,12]. Der größte *g*-Wert und die höchste Linienbreite treten auf, wenn das statische Magnetfeld H_o parallel zur c^*-Achse liegt, was der longitudionalen Achse der TMTTF-Moleküle entspricht. Die kleinsten Werte für *g* und die Linienbreite zeigen sich für Magnetfelder parallel zur *a*-Achse. Damit ergibt sich für die Anisotropie der Linienbreite und des *g*-Wertes folgende Beziehung: $\Delta H_{c^*} > \Delta H_{b'} > \Delta H_a$ und $g_{c^*} > g_{b'} > g_a$. Die Ursache der Anisotropie des g-Wertes liegt in der Kopplung zwischen Spin-Drehmoment und orbitalem Drehmoment (spin-orbit coupling). Der Tensor der *g*-Werte (g_a, $g_{b'}$ und g_{c^*}) wird durch die molekulare Struktur bestimmt. Die Linienbreite hat dieselbe Anisotropie aufgrund der Symmetrieeinschränkungen des Materials. Sie ergibt sich aus den Spin-Bahn gekoppelten elektronischen Übergängen im Donator-Leitungsband des organischen Leiters, welche durch Rotationsschwingungen der Donator-Moleküle um ihre lange, in der Ebene liegende, Achse angeregt werden. Die Tatsache, dass *g*-Wert und Linienbreite die gleiche Anisotropie zeigen, deutet auf Spin-Phonon-Wechselwirkungen als dominierenden Relaxationsprozess bei hohen Temperaturen hin. Die Winkelabhängigkeit des g-Wertes und der Linienbreite bei konstanter Temperatur kann durch die Beziehung

$$\Delta H(\theta) = \left[\Delta H^2(0^o)\cos^2(\theta) + \Delta H^2(90^o)\sin^2(\theta) \right]^{1/2} \quad (1)$$

$$g(\theta) = \left[g^2(0^o)\cos^2(\theta) + g^2(90^o)\sin^2(\theta) \right]^{1/2} \quad (2)$$

beschrieben werden. Hierbei ist θ der Winkel zwischen dem statischen Magnetfeld H_o und derjenigen kristallographischen Achse, für die die Linienbreite und der *g*-Wert am kleinsten sind. $\Delta H(0^o)$ and $g(0^o)$ stehen für die *g*-Werte und die

Linienbreite für die das Minimum beobachtet wird, wohingegen $\Delta H(90^{o})$ and $g(90^{o})$ die des Maximums beschreiben.
Im paramagnetischen Zustand, wird ein nahezu linearer Abfall der Linienbreite für sinkende Temperaturen bis hin zum Anionen-Ordungs-Übergang bei T_{AO} = 157 K beobachtet. Der g-Wert hingegen ist Temperatur unabhängig. Am Ladungs-Ordnungs-Übergang bei T_{CO} = 227 K tritt keinerlei Anomalie in der Linienbreite auf.
Die Temperaturabhängigkeit der Spin-Suszeptibilität für konstantes Volumen $(\chi_s)_v$ kann bei Temperaturen T > 160 K durch die theoretischen Modelle von Bonner und Fisher [13] bzw. Eggert, Affleck und Takahashi (EAT-Model) [14] für antiferromagnetische S = 1/2 Spinketten beschrieben werden. Unter Verwendung dieser Modelle ergibt sich für die antiferromagnetische Austauschwechselwirkung $|J|$ ein Wert von 425 K.
Bei T_{AO} wird ein stufenartiger Abfall der Linienbreite beobachtet, auf welchen ein Anstieg der Linienbreite für fallende Temperaturen folgt. Unterhalb von T_{AO} ändert sich die Anisotropie der Linienbreite hin zu $\Delta H_a > \Delta H_{b'} > \Delta H_{c^*}$. Diese Änderung kann den durch die Anionenordnung induzierten Verlust des äquivalenten elektrostatischen Potentials (Coulomb-Potential), welches die Leitungselektronen sehen, verursacht werden. Des Weiteren, sinkt die Spin-Suszeptibilität exponentiell für fallende Temperaturen bis 120K, wo das ESR-Spektrum schließlich vollständig verschwindet. Dieser Abfall der Spin-Suszeptibilität entspricht dem Entstehen eines Spin-Singulett Grundzustand und lässt sich in diesem Temperaturbereich durch das Aktivierungsgesetz

$$[\chi_s]_v(T) = \frac{A}{T}\exp\left(\frac{-\Delta_\sigma}{T}\right) \tag{3}$$

beschreiben. Für die Anregungsenergie Δ_σ des Spin-Triplett-Zustands im anionen-geordneten Zustand ergibt sich mit obiger Anpassung der Wert Δ_σ = 1100 K. Diese sehr große Anregungsenergie weist darauf hin, dass $|J_1| >> |J_2|$ gilt, wobei J_1 und J_2 für die AFM-Austauschwechselwirkung innerhalb bzw. zwischen den Dimeren stehen. Dieses Ergebnis gibt einen Hinweis darauf, dass die Ladung entlang der Stapelrichtung von der Form –o-O-O-o– ist. Hierbei stehen “o” und “O” für eine ladungsarme bzw. ladungsreiche Verteilung auf den einzelnen Plätzen.
Im anionengeordneten Zustand ändert sich die winkelabhängige Linienbreite nicht mit der Frequenz. Dies lässt darauf schließen, dass der Relaxationsprozess durch Dipol-Dipol-Wechselwirkungen dominiert wird.

Der Übergang in den ladungsgeordneten Zustand (CO) und die Art der Relaxationsprozesse in diesem Zustand wurde an $(TMTTF)_2AsF_6$ und $(TMTTF)_2SbF_6$ mittels Q-Band und W-Band ESR-Messungen untersucht. Die resultierenden Q- und W-Band Spektren für alle drei Kristallrichtungen zeigen für alle Temperaturen eine symmetrische lorenzförmige Linienbreite, was ebenfalls in X-Band ESR-Messungen beobachtet wurde [2]. Die temperaturabhängige Q- bzw. W-Band Linienbreite und der *g*-Wert von $(TMTTF)_2AsF_6$ und $(TMTTF)_2SbF_6$ entlang der drei magnetischen Hauptachsen (*a*, *b´* and c^*) sind frequenzunabhängig und vergleichbar mit den Ergebnissen der X-Band ESR-Spektren [2]. Diese Frequenzunabhängigkeit von ΔH ist im Rahmen des Mechanismus der Spinrelaxation an Torsionsschwingungen der Moleküle verständlich [118]. In beiden Verbindungen tritt am Ladungs-Ordnungs-Übergang (T_{CO} = 105 K in $(TMTTF)_2AsF_6$ und T_{CO} =156 K in $(TMTTF)_2SbF_6$) eine Anomalie in der Linienbreite für alle drei Kristallrichtungen auf. In $(TMTTF)_2SbF_6$ ist diese Anomalie deutlicher ausgeprägt. Unterhalb von T_{CO} verändert sich die Anisotropie in der Linienbreite für tiefe Temperaturen hin zu $\Delta H_{c^*} > \Delta H_{b'} \approx \Delta H_a$.

Innerhalb der *ab*`-Ebene zeigen sowohl die Q- und W-Band als auch die X-Band Linienbreite [2] für beide Verbindungen eine vergleichbare Winkelabhängigkeit, d.h. das Maximum befindet sich entlang der Diagonalen zwischen der *a* und *b´* Richtung (45^o und 135^o). Für alle Messungen wird eine Verdopplung der Periodizität beobachtet. Der winkelabhängige Anstieg der Linienbreite lässt sich durch die Beziehung

$$\Delta H(\theta) = \Delta H(45^o)\left|\sin(2\theta)\right| \tag{4}$$

beschreiben. ΔH_{45^o} steht für die Linienbreite entlang der 45^o –Richtung innerhalb der *ab´*-Ebene. Unterhalb von T_{CO} ist die Summe der Gleichungen (1) und (4) zur Beschreibung der Winkelabhängigkeit der Linienbreite geeignet. Hierbei sind $\Delta H(0^o)$ und $\Delta H(90^o)$ die Linienbreiten entlang *a* und *b´* Achse, welche durch die Spin-Phonon-Wechselwirkung entlang der *a*- bzw. *b´*-Richtung entstehen. θ ist der Winkel zwischen dem Magnetfeld H_o und der *a*-Achse. Die erhöhte Linienbreite $\Delta H_{enhanced}$ für den 45^o -Winkel in der *ab´*-Ebene kann für alle drei gemessenen Frequenzbänder mit der Gleichung

$$\Delta H_{enhanced} = \Delta H_{45^o} - \left(\frac{\Delta H_a + \Delta H_{b'}}{2}\right). \tag{5}$$

berechnet werden. Für Temperaturen unterhalb T_{CO} ist die Linienbreite entlang der 45°-Richtung abhängig vom Quadrat der Frequenz, d.h. $\Delta H_{\mathbf{enhanced}} \propto \nu^2$. Dieses Ergebnis deutet auf die anisotrope Zeeman-Wechselwirkung (AZ) als Relaxationsprozess hin. Unterhalb des Ladungs-Ordnungs-Überganges liegen somit zwei magnetisch nicht äquivalente Gitterplätze vor.
Der Unterschied des *g*-Tensors (Δg) von zwei magnetisch nicht äquivalenten Gitterplätzen lässt sich mittels der folgenden Gleichung [15] abschätzen:

$$\Delta H_{AZ}(10^4\,\mathrm{Oe}) \approx \frac{\mu_B H_0^2}{g_e k_B |J'|}\sqrt{\frac{\pi}{8}}\,|\Delta g|^2 . \tag{6}$$

Die Abschätzung ergibt Δg = 0.012 mit $\Delta H_{AZ} \rightarrow \Delta H_{enhanced}$ = 1.55 Oe für $(TMTTF)_2SbF_6$ bei T ≈ 60 K unter Verwendung von J' = 2.2 K. Dieser Wert weicht geringfügig von dem aus der Differenz der *g*-Werte entlang der *a*- und *b*-Achse ($g_b - g_a$ = 0.008) berechneten ab. Dies bedeutet, dass der *g*-Tensor der beiden zu magnetisch verschiedenen Gitterplätzen gehörenden Spins eine charakteristische Anisotropie aufweist. Die Anisotropie des *g*-Wertes kann für jeden magnetischen Gitterplatz durch die nachfolgende Gleichung gut beschrieben werden:

$$\begin{aligned} g_1 &= \sqrt{g_{\max}^2 \cos^2(\theta-\varphi) + g_{\min}^2 \sin^2(\theta-\varphi)} \\ g_2 &= \sqrt{g_{\max}^2 \cos^2(\theta+\varphi) + g_{\min}^2 \sin^2(\theta+\varphi)}\,. \end{aligned} \tag{7}$$

Hierbei sind g_1 und g_2 die *g*-Tensoren der beiden unterschiedlichen Spins 1 und 2 und 2φ ist der Winkel zwischen beiden. g_{max} und g_{min} stehen für das Maximum bzw. Minimum der *g*-Werte für die beiden im Winkel φ zueinander stehenden Spins. Unter Verwendung von Gleichung (7) ergibt sich ein Winkel von 2φ = 56° zwischen den magnetisch nicht äquivalenten Gitterplätzen, welcher ein Δg = 0.012 bei θ = 45° bedingt, wenn g_{max} = 2.0126 und g_{min} = 1.9982 beträgt. Das heißt, dass es, abhängig von g_{max}, g_{min} und φ, verschiedene Möglichkeiten der Variation des *g*-Wertes von zwei magnetisch nicht äquivalenten Gitterplätzen gibt, die denselben Wert für Δg ergeben. Die Frage der Anisotropie des *g*-Tensors der zwei magnetisch nicht äquivalenten Gitterplätze im ladungsgeordneten Zustand bietet somit Raum für weitere magnetische Resonanzuntersuchungen and theoretische Berechnungen.

Die anisotrope Zeeman-Wechselwirkung resultiert in zwei verschiedenen Signalen bei zwei unterschiedlichen magnetischen Resonanzfeldern, falls das Austauschfeld J' deutlich kleiner als das Resonanzfeld H_o ist. In $(TMTTF)_2SbF_6$ ist das Austauschfeld mit 16.4 kG (≈ 2.2 K) [16] etwas kleiner als das Resonanzfeld mit 33.6 kG. Dadurch lässt sich erklären, warum nur eine verbreiterte Linie beobachtet wird. Die Verzerrung der ESR-Linie bei 45^o könnte auf eine Aufspaltung bei höheren Feldern hinweisen. Möglicherweise ist aber auch der Beitrag anderer Mechanismen zur Linienbreite die Ursache, der die Auflösung in zwei getrennte Signale überdeckt. Analysen haben ergeben, dass $\Delta H_{\text{enhanced}}$ auch durch die kubische Frequenzabhängigkeit $\Delta H_{\text{enhanced}} \propto \nu^3$ beschrieben werden kann. Somit könnte der Waller-Prozess (direkter Prozess) einer der Relaxationsprozesse im ladungsgeordneten Zustand sein.
Der Anstieg der ESR-Linienbreite in $(TMTTF)_2SbF_6$ für Temperaturen in der Nähe des AFM-Überganges ist auf magnetische Fluktuationen zurückzuführen. In diesem Bereich zeigt sich die Linienbreite proportional zu $(T - T_N)^{-\mu}$ [17]. Die theoretische Analyse der AFM-Fluktuationen basiert auf der Hypothese, dass in diesem Temperaturbereich die Dipol-Dipol-Wechselwirkungen den dominanten Relaxationsprozess darstellen. Im Rahmen der vorliegenden Arbeit konnte die Frequenzunabhängigkeit dieser Wechselwirkung gezeigt werden. Somit ergibt sich, dass die AFM-Fluktuationen ebenfalls frequenzunabhängig sind. Diese Schlussfolgerung wird bestätigt dadurch, dass sich derselbe Wert μ = 0.5 für Messungen bei verschiedenen ESR-Frequenzen ergibt.

DC-Widerstandsmessungen wurden an Einkristallen der Verbindungsserie κ-$(BEDT\text{-}TTF)_2Cu[N(CN)_2]Br_xCl_{1-x}$ (x = 20%, 40% 70%, 80%, 85% and 90 %) durchgeführt. Der spezifische Widerstand für alle untersuchten Proben lag bei Zimmertemperatur im Bereich zwischen 0.3 bis 5 Ωcm. Das Verhältnis von $\rho_\perp/\rho_\parallel$ = 25 bei Zimmertemperatur für die Proben mit 90% Bromanteil lässt deutlich den zweidimensionalen Charakter der Kristalle erkennen. Im Temperaturbereich von 300 K bis 100 K zeigen alle Proben die Temperaturabhängigkeit eines Halbleiters. Eine deutliche Abhängigkeit des spezifischen Widerstandes vom Br/Cl-Verhältnis tritt beim Abkühlen der Proben unter 100K auf. Die Kristalle mit 20% und 40 % Bromanteil durchlaufen bei 50K einen Mott-Hubbard Übergang. Im Temperaturbereich 300K bis 25K zeigt der Verlauf des spezifischen Widerstandes ein thermisch aktiviertes Verhalten der Form $\rho \propto \exp(\Delta / k_B T)$ mit einer deutlichen Änderung der Temperaturabhängigkeit im Bereich um T = 50K. Die Aktivierungsenergie für Temperaturen kleiner 50 K liegt bei 600 K bzw. 400 K für x

= 0.2 und x = 0.4. Für Temperaturen oberhalb des Mott-Hubbard Überganges ergibt sich für beide Proben eine Aktivierungsenergie von Δ=200K. Unterhalb von 25 K kann das Temperaturverhalten des spezifischen Widerstandes mittels Variable-Range-Hopping (VHR) $\rho(T) = \rho_o \exp(T_{hop}/T)^{1/3}$ beschrieben werden [18]. Dieses Verhalten bestätigt die Existenz von lokalisierten Zuständen bei tiefen Temperaturen. In den Kristallen mit $x \geq 0.7$ tritt im Bereich 80-100K ein breites Maximum auf. Für niedrigere Temperaturen ist der Widerstandsverlauf, bis hin zum starken Abfall beim Eintritt in die Supraleitung bei $T_c \approx 12$ K, der eines Metalls. Die supraleitenden Proben zeigen hier zwischen 12 K und 30 K eine quadratische Temperaturabhängigkeit, welche durch die Gleichung

$$\rho(T) = \rho_o + AT^2 \tag{8}$$

beschrieben werden kann. Hierbei ist ρ_o der Restwiderstand und A der Vorfaktor von T^2. Diese quadratische Abhängigkeit des spezifischen Widerstandes gilt in den untersuchten Proben bis hin zu der charakteristischen Temperatur T_o. Das Produkt $A(x)\times[T_o(x)]^2$ ist in Übereinstimmung mit der Theorie der Fermiflüssigkeit nahezu konstant, d.h. unabhängig vom Bromgehalt. Daraus lässt sich schließen, dass die Elektron-Elektron-Streuung die Ursache der quadratischen Temperaturabhängigkeit ist. Diese Resultate werden bestätigt durch Infrarot-Messungen an diesen Verbindungen [19] und sie entsprechen auch denen von Jacko *et al*. aufgestellten Skalierungsverhalten der Verbindungen die Fermiflüssigkeitsverhalten zeigen [20].

Die Form der ESR-Linie bei Zimmertemperatur hängt von der Orientierung der Probe im Resonator bezüglich des Magnetfeldes H_1 der Mikrowelle ab. Wenn die leitende Ebene (*ac*-Ebene) der Probe senkrecht zu H_1 verläuft, so tritt im ESR-Spektrum eine asymmetrische dysonförmig Linie auf. Ist die *ac*-Ebene parallel zu H_1 orientiert, so zeigt sich die Linie lorentzförmig. Die asymmetrische Linienform steht mit dem Skin-Effekt in Verbindung. Sie wird durch die Abschirmung der eingestrahlten Mikrowelle durch die Leitungselektronen erzeugt. In den isolierenden Proben ändert sich für Temperaturen unterhalb von 50 K die dysonförmige Linie allmählich hin zu einer symmetrischen lorentzförmigen. Dies liegt an der Zunahme der Skintiefe. Die aus der Linienform berechnete Mikrowellenleitfähigkeit stimmt qualitativ mit den Ergebnissen der DC-Messungen überein.
Für die Anisotropie der ESR-Linienbreite und des *g*-Wertes gilt $\Delta H_a > \Delta H_c > \Delta H_b$ und $g_b > g_c > g_a$. Der *g*-Wert aller Kristalle folgt derselben Winkelabhängigkeit und ist für die Hauptachsen nahezu unabhängig vom Dotierungsgehalt. Für den mittleren

g-Wert entlang der drei Hauptachsen ergeben sich die Werte g_a = 2.0044, g_b = 2.0069 and g_c = 2.0031. Die mittlere gefundenen Linienbreite bei Zimmertemperatur entlang der der Hauptachsen sind ΔH_a = 54 Oe, ΔH_b = 49 Oe and ΔH_c = 65 Oe.
Die Temperaturabhängigkeit der ESR-Linienbreite für alle Bromkonzentrationen ist nahezu identisch. Ausgehend von 300 K steigt die Linienbreite für fallende Temperaturen an, erreicht ein breites Maximum bei 60 – 80 K und fällt anschließend für tiefe Temperaturen stark ab. Für die isolierenden Proben verschwindet das ESR-Spektrum für beide Richtungen völlig beim Übergang in den antiferromagnetischen Grundzustand bei 22 K. In den supraleitenden Kristallen ist aufgrund der Formierung von Cooperpaaren einige Kelvin unterhalb der Sprungtemperatur kein ESR-Signal mehr detektierbar. Die Linienverbreiterung wird durch die Streuung der Leitungselektronen an den Vibrationen der Ethylen-Endgruppen der BEDT-TTF Molekülen verursacht. Diese sind bei hohen Temperaturen thermisch aktiviert. Durch Kühlen werden ihre Vibrationen langsamer und frieren schließlich am Glasübergang bei $T_g \approx 77$ K aus [diese Arbeit, 139]. Das breite Maximum in der Linienbreite ist dadurch erklärbar, dass bei hohen Temperaturen diese Vibrationsfrequenz größer ist als die typische ESR-Frequenz von 9.5 GHz. Daher ist der Relaxationseffekt der Vibrationen auf die Leitungselektronen nicht sehr stark. Für niedrigere Temperaturen sinkt die Vibrationsfrequenz, erreicht schließlich die ESR-Frequenz, und die Streuung der Leitungselektronen nimmt zu. Dies führt zu einem breiten Maximum in der Linienbreite ΔH.
Allerdings verschiebt sich das Maximum der Linienbreite hin zu niedrigeren Temperaturen T kleiner T_g. Die Ursache hierfür können die antiferromagnetischen Fluktuationen sein, welche stärker in den Proben mit hohem Bromgehalt vertreten sind. Im gesamten untersuchten Temperaturbereich und entlang aller drei Richtungen verhält sich der *g*-Wert temperaturunabhängig.
Die Spin-Suszeptibilität liegt bei 300 K und für alle Proben im Bereich $(4 – 8) \times 10^{-4}$ emu/mole. Die Temperaturabhängigkeit der Spin-Suszeptibilität ist in den Proben mit 0%, 20% und 40% Bromanteil im Temperaturbereich 300 K – 40 K nahezu nicht vorhanden, passend zur Pauli Spin-Suszeptibilität eines Metalls. Unterhalb von 40K bis hin zu 22K fällt die Suszeptibilität stark ab, d.h. für $x \geq 0.7$ und für Temperaturen T > 100 K ist sie vergleichbar mit der von Proben mit niedrigerem Bromgehalt. Unterhalb von 100 K verringert sich die Suszeptibilität mit der Temperatur und fällt von 50 K bis hin zu 8 K stark ab. Im Allgemeinen wird der Rückgang der Suszeptibilität bei niedrigen Temperaturen der geringeren Zustandsdichte an der Fermikante $N(E_F)$ zugeschrieben, welche durch die Vibrationen der Ethylene-Endgruppen verursacht wird. Die Temperaturabhängigkeit

der Spin-Suszeptibilität in den supraleitenden Proben wird durch ein Modell mit zwei Energielücken beschrieben [11]:

$$\chi(T) = (A_1 / T)\exp(-\Delta_1 / k_B T) + (A_2 / T)\exp(-\Delta_2 / k_B T) \qquad (9)$$

wobei Δ_1, Δ_2 für die Energielücken und A_1, A_2 für die Fit-Parameter stehen. Die so bestimmte Energielücke Δ_1 ist nicht konstant, sondern verändert sich zufällig von Probe zu Probe. Möglicherweise ist diese Energielücke der Mittelwert über die zufällig verteilten Energielücken, welche durch Störstellen verursacht werden. Die Aktivierungsenergie Δ_2 für tiefe Temperaturen entspricht der supraleitenden Energielücke, welche auch im Rahmen der BCS-Theorie für diese organischen Leiter erwartet wird. Der Übergang in den supraleitenden Zustand wird durch das Abschirmsignal, welches die Messungen mit dem Squid-Magnetometer zeigen, bestätigt.

In den hoch dotierten Bromproben ist das halbleiterartige Bild der Spin-Suszeptibilität und das metallische Verhalten des DC-Widerstandes bei tiefen Temperaturen dem Pseudo-Gap in der Zustandsdichte an der Fermikante zuzuschreiben, welches in κ-(BEDT-TTF)$_2$Cu[N(CN)$_2$]Br [21] gefunden wurde.

Die Ergebnisse der vorliegenden Arbeit ermöglichen die Darstellung der Übergangstemperaturen des Metall-Isolator-Überganges und der Phasenübergänge in den antiferromagnetischen bzw. supraleitenden Zustand für die verschiedenen Bromkonzentrationen in einem Phasendiagramm.

Introduction

Low-dimensional organic conductors have led to one of the most interesting and fruitful chapters in modern solid state science: due to the reduced dimension and the competition between electric, magnetic and lattice degrees of freedom, phase transitions into different ground states like spin order, charge order or superconductivity can be observed, which are missed in three dimensional systems.
Benchmark systems for low-dimensional materials are organic charge-transfer salts, like the quasi one-dimensional salts $(TMTSF)_2X$ and $(TMTTF)_2X$ and the two-dimensional metals from the BEDT-TTF family. The physical properties and the dimensionality of these materials can be easily changed by exchanging the monovalent anion X or by applying external pressure. Therefore, these salts have a rich phase diagram where they undergo phase transitions into different grounds states, which make them ideal candidates for investigating the physics of low-dimensional systems.
Electron spin resonance (ESR) spectroscopy has been proven to be a very powerful method to explore the different regions of the phase diagram. The high sensitivity of this method gives the possibility to investigate the paramagnetic high-temperature regions as well as the diverse ground state properties. From the temperature dependence of the spin susceptibility, among other things information on the magnetic exchange interaction, spin fluctuations, or charge carriers dynamics can be obtained. The anisotropy as well as temperature and frequency dependence of the linewidth and the g-value provide information on the dominating mechanism of exchange interaction, local charge order phenomena, and the dimensionality of the electronic system.
The spin and charge ordering transition is one of the exciting phenomena in the quasi one-dimensional organic conductors $(TMTTF)_2X$ which has been investigated experimentally and theoretically. Most of the ESR studies on these compounds were limited to standard (X-band) ESR spectrometer. Recently, detailed studies on the spin and charge ordering transition in our institute were performed by X-band ESR. The obtained results did not give a complete story, and performing high frequency ESR measurements in the spin and charge ordered state was necessary to accomplish this story. Therefore, multi-frequency ESR investigations are performed in this part of project in order to explore the frequency and temperature dependence of the ESR

parameters in the spin and charge ordered states in the quasi one-dimensional salts $(TMTTF)_2X$ salts (X = ReO_4, AsF_6 and SbF_6).
The isostructural charge-transfer salts κ-$(BEDT\text{-}TTF)_2Cu[N(CN)_2]X$ (X = Br, Cl, I) has a strong competition between magnetically ordered and superconducting phases. Previous studies on these compounds showed that their physical properties have a great sensitivity to the hydrostatic pressure or chemical pressure, i.e, anion size. Interestingly, the type of the excitation of the charge carriers and the relaxation mechanism at low temperatures in these compounds was a controversial topic in these studies. Here, a comprehensive transport and magnetic measurements on the alloyed series κ-$(BEDT\text{-}TTF)_2Cu[N(CN)_2]Br_xCl_{1-x}$ (x = 0%, 20%, 40%, 70%, 80%, 85%, 90% and 100%) by dc, ESR and SQUID are performed in order to explore the most interesting region in the phase diagram of these compounds and to understand the physics behind it.

This thesis is organized as follow:
The first chapter presents a general introduction about the phase diagram, the crystal structure, and the electrical and magnetic properties of the studied materials from the low-dimensional organic conductors $(TMTTF)_2X$ and κ-$(BEDT\text{-}TTF)_2X$. For a deep understanding of this work, the necessary theoretical models for the electronic and magnetic properties of low-dimensional systems are introduced in chapter two. In chapter three, the experimental techniques (X-, Q- and W-band ESR, the SQUID magnetometer and the dc resistivity setup) used in this work, the information deduced from these techniques and the detailed measurement procedures are given. Detailed multi-frequency (X-, Q- and W-band) ESR measurements of three $(TMTTF)_2X$ salts (X = ReO_4, AsF_6 and SbF_6) are reported in chapter four. In this chapter the general behavior of $(TMTTF)_2ReO_4$ at high temperature and detailed measurements in the anion ordered state will be discussed and explained. A comprehensive investigation of the frequency dependence of the ESR parameters (the linewidth and the g-value) of $(TMTTF)_2AsF_6$ and $(TMTTF)_2SbF_6$ at high temperatures and in the charge ordered state will be presented and discussed. In chapter five, the transport and the magnetic properties of the alloyed series κ-$(BEDT\text{-}TTF)_2Cu[N(CN)_2]Br_xCl_{1-x}$ (x = 0%, 20%, 40%, 70%, 80%, 85%, 90% and 100%) investigated by means of dc, ESR and SQUID will be presented and discussed. Finally, the summary of the thesis and the outlook will be presented in chapter six.

Chapter 1

Low-Dimensional Organic Conductors and Superconductors

Low-dimensional materials exhibit large anisotropic ratios in some distinctive physical properties. For example, one-dimensional (1-D) conductors are much better conducting in one direction with respect to the orthogonal directions. This anisotropy in the physical properties comes from the unusual lattice structure of low-dimensional materials. While 1-D materials resemble chains in their lattice structures, 2-D materials have a layered structure. Low-dimensionality and anisotropy play an important role in many areas of condensed-matter physics. The unique properties and the novel ground states of these low-dimensional materials have attracted much attention during the last decades by the physicists, chemists, and material scientists.

Organic charge-transfer salts are one of those classes of materials that have been studied intensively as a model of low-dimensional materials. Besides their low dimensionality, they are also interestingly because they can show considerable values of conductivity $\sigma \geq 1\ \Omega^{-1}\text{cm}^{-1}$ and a metallic temperature dependence of $\sigma(T)$. Some charge-transfer salts are even superconductors at very low temperature. Because organic conductors can have electronic properties typical for metals, sometimes they are referred to as *synthetic metals*. This work investigates the electronic and the magnetic properties of quasi 1-D organic conductors from the TMTTF-family[I] which is called Fabre salts and quasi 2-D organic superconductor from the (BEDT-TTF)-family[II], specifically κ-(BEDT-TTF)$_2$Cu[N(CN)$_2$]Br$_x$Cl$_{1-x}$. In this chapter, first the phase diagram, the crystal structure, and the electrical and magnetic properties will be discussed in section 1.1. The phase diagram of the κ-phase family and the crystal structure of κ-(BEDT-TTF)$_2$Cu[N(CN)$_2$]Br$_x$Cl$_{1-x}$ are introduced in section 1.2.

[I] TMTTF stands for tetramethyltetraselenafulvalene and has a chemical composition $(CH_3)_4C_6S_4$.

[II] BEDT-TTF which is known also as ET stands for Bisethylenedithio-tetrathiafulvalene and has a chemical composition $(CH_2)_4C_6S_8$.

1.1 Fabre Salts $(TMTTF)_2X$

The organic charge-transfer salts $(TMTTF)_2X$, where X is an inorganic monovalent anion like PF_6^-, AsF_6^-, ReO_4^-, BF_4^-, SbF_6^-, etc, was first synthesized in the late 1970's by J. M. Fabre [22]. Fabre salts are the sulfur analogous of the Bechgaard salts $(TMTSF)_2X$ [23], where the selenium (Se) atoms in the Bechgaard salts are replaced by the sulfur (S) atoms in the Fabre salts as shown in Figure 1.1. The TMTTF molecule is a flat molecule and has a structure similar to the TMTSF molecule. For this reason, Fabre and Bechgaard salts form together a group of quasi 1-D organic conductors which is denoted by $(TMTCF)_2X$ salts (C = S or Se).

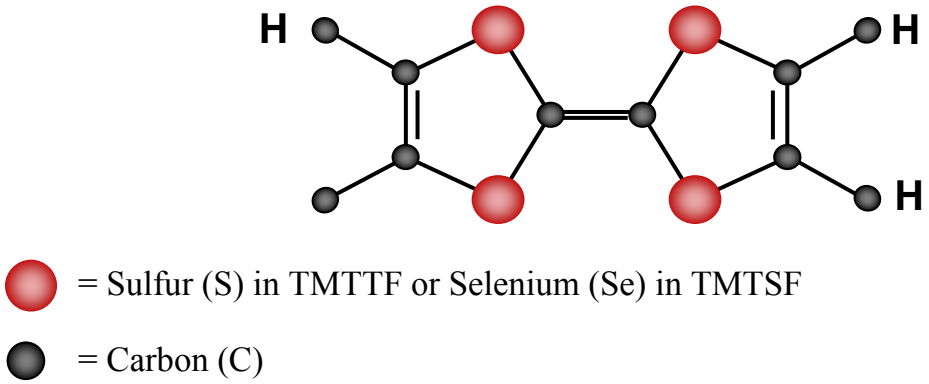

Figure 1.1: The structure of the TMT*C*F molecule (*C* = S or Se).

The $(TMTCF)_2X$ salts have electronic and/or magnetic instabilities when the system is cooled down to low temperatures and thus the system undergoes phase transitions resulting in a rich phase diagram with several ground states [24,25]. The ground state of these salts depends strongly on the chemical composition of the organic molecule TMT*C*F or inorganic anion X. For example, $(TMTTF)_2AsF_6$ has a spin-Peierls ground state. When the anion AsF_6^- is replaced by the anion SbF_6^-, the ground state of the resultant compound $(TMTTF)_2SbF_6$ becomes antiferromagnetic (AFM). The ground states (spin-Peierls, spin-density waves, and superconductivity) are tunable by chemical pressure (i.e. size of the anion X and/or the chalgogen atom (Se or S)) and/or external pressure [12]. The phase diagram in Figure 2.1 displays this variety of the ground states found in Fabre and Bechgaard salts. Since this work investigates TMTTF salts, our discussion will be restricted on these salts and a detailed description about the physics of the ground states observed in these salts is given in the next chapter "Physics of Low-dimensional Systems".

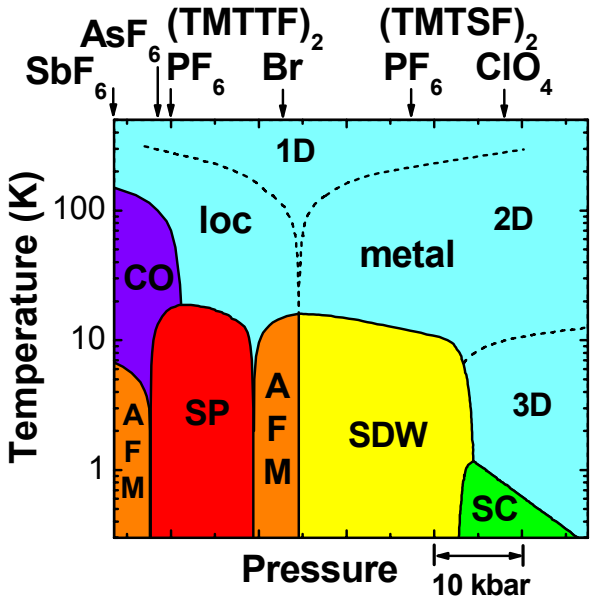

Figure 1.2: Generalized phase diagram for (TMT*C*F)$_2$*X* salts. The notations loc, SP, AFM, SDW and SC refer to Mott localized, spin-Peierls, antiferromagnetic (commensurate SDW), spin density wave (incommensurate), and superconducting ground states, respectively. The ambient pressure positions of the different compounds in the phase diagram are indicated by the arrows. The dimensionality of the compounds crosses over from one-dimensional (1D) to two-dimensional (2D) and three-dimensional (3D) with increasing pressure. Adopted from [2].

1.1.1 Crystal Structure

All (TMT*C*F)$_2$*X* salts are isostructural compounds. The crystals are grown in the electrochemical reaction [26]. They crystallize in the triclinic $P\bar{1}$ space group. The unit cell is composed out of two TMT*C*F molecules and one inorganic anion *X* (see Figure 1.3). The unit cell dimensions for the studied Fabre salts (TMTTF)$_2$ReO$_4$, (TMTTF)$_2$SbF$_6$ and (TMTTF)$_2$AsF$_6$ are listed in Table 1.1.

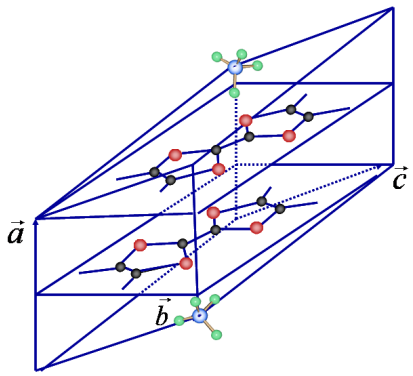

Figure 1.3: The triclinic unit cell of (TMT*C*F)$_2$*X* salt with tetrahedral anion.

X	ReO_4	SbF_6	AsF_6
Symmetry	Tetrahedral	Octahedral	Octahedral
a (Å)	7.151	7.195	7.178
b (Å)	7.618	7.622	7.610
c (Å)	13.244	13.45	13.317
α (^{o})	82.711	81.19	82.03
β (^{o})	84.622	96.65	95.75
γ (^{o})	71.723	106.19	107.11
V_{cell} (Å^3)	678.5	698.1	687.2
M (g/mol)	770.9	756.6	709.8
ρ (g/cm^3)	1.89	1.80	1.72
Reference	[27]	[28]	[28]

Table 1.1: The unit cell dimensions for several Fabre salts at room temperature. Labels *a*, *b*, and *c* are the unit cell dimensions along the respective crystallographic axis. Labels $\alpha = \widehat{(b,c)}$, $\beta = \widehat{(a,c)}$, and $\gamma = \widehat{(a,b)}$ are the angles of a unit cell of volume V_{cell}.

In $(TMTTF)_2X$, the organic molecules are stacked along *a*-axis and form layers in the *a*-*b* plane which alternate with the anion *X* along *c*-axis as shown in Figure 1.4. Along the stacking axis, the mean distance between the molecules is $a_s \approx 3.6$ Å, and it is smaller than the double distance of the van der Waals radius of the *C*-atoms (*C* = S or Se), suggesting a large overlap of the molecular wave functions in the direction of the π-orbitals and formation of a band structure along the molecule chains.

In all Fabre salts the stacking axis has a «zig-zag» configuration and the distances between TMTTF molecules along the stacks are not regular but are slightly dimerized. This means that there are two different distances (d_1 and d_2) between consecutive molecules in the same stack. This dimerization is quantified by the calculation of the intermolecular transfer integrals t_{a1} and t_{a2} along the d_1 and d_2 defined in Figure 1.4a. The transfer integrals are a direct measure of the overlap of the molecular orbitals between neighboring molecules, they strongly depend on the arrangement of the molecules in the crystal structure. Table 1.2 gives these values for the investigated TMTTF salts which were calculated in the framework of the extended Hückel model when the anionic potential is neglected [29]. The relative ratio between the transfer integrals $\Delta t_a/t_a = 2(t_{a1} - t_{a2})/(t_{a2} + t_{a2})$ gives the degree of dimerization along the stacks.

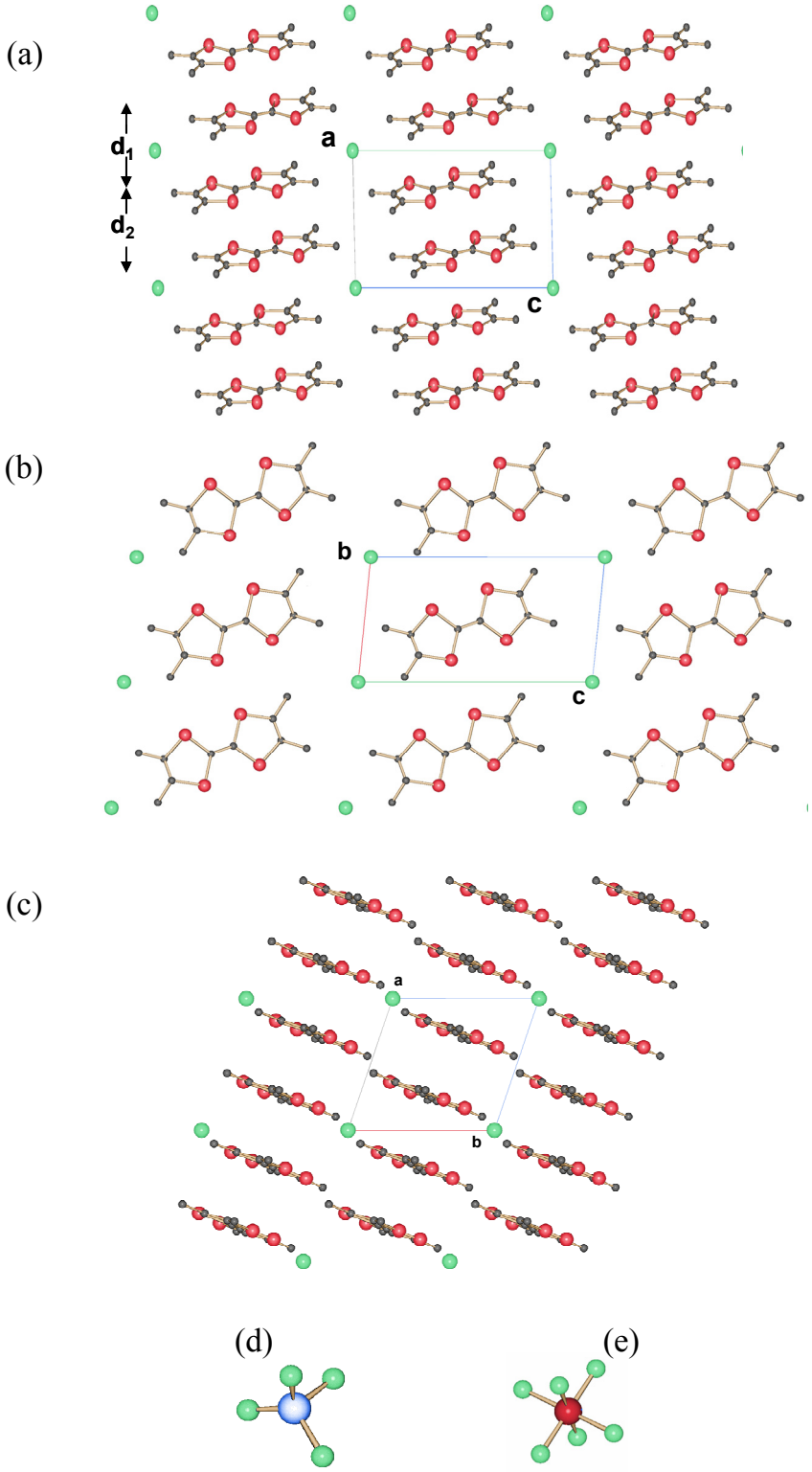

Figure 1.4: Projection of the crystal structure of $(TMTTF)_2X$ on the *a-c* plane (a), *b-c* plane (b) and (c) *a-b* plane. The green spheres between TMTTF molecules denote the anions. The tetrahedral and octahedral anions are shown in c and d, respectively. d_1 and d_2 are the intradimer and interdimer spacing, respectively where $d_1 > d_2$ (see table 1.2).

	$(TMTTF)_2X$		
	$X = ReO_4$	$X = SbF_6$	$X = AsF_6$
t_{a1} (meV)	87	88	81
t_{a2} (meV)	119	131	119
t_a (meV)	103	110	100
$\Delta t_a/t_a$	0.31	0.39	0.39
t_b (meV)	-	12.2	13.9
t_a/t_b	-	9.01	7.19
Reference	[29,30]	[31]	[31]

Table 1.2: The transfer integrals for different TMTTF salts at room temperature and ambient pressure. t_{a1}, t_{a2} and t_a are the intrachain transfer integrals and the average transfer integral, respectively. $\Delta t_a/t_a$ is the calculated degree of dimerization. t_b is the transfer integral along *b*-direction.

Along *b*-axis, the shortest S-S distance is larger than the double of the van der Walls radius of the sulfur atom which means that the transfer integral along *b*-axis is much less than the transfer integral along *a*-axis. The highly different overlap of the orbital along *a*-, *b*-, and *c*-axis leads to the anisotropy in the transfer integrals and consequently anisotropy in the physical properties. Along the *c*-axis the transfer integral of $(TMTTF)_2X$ amounts to $t_c \approx 0.65$ meV [32].

Most of the charge transfer salts consist of donor acceptor (D-A) complexes. In the Fabre salts, the organic TMTTF molecules function as a donor and the inorganic anions as an acceptor. They form D_2A complexes which means that each two TMTTF molecules donate one electron to one anion resulting in a 3/4-filled band by electrons (1/4-filled band by holes) along the stack direction. Due to the structural dimerization where each two TMTTF molecules form a dimer a gap opens, thereby splitting the conduction band which is formed by the donor's HOMO. Therefore, the band is effectively 1/2 filled [7].

The symmetry of the anions plays a crucial role. Because of the «zig-zag» configuration of the compounds the anions are placed in cavities at a centre of symmetry of the room temperature $P\bar{1}$ crystallographic structure. When the anions are non-centrosymmetrical, the symmetry has to be restored by a statistical disorder of the anions and order-disorder phase transitions are generally observed at low temperature [29]. For centrosymmetrical anions, the statistical disorder is no longer necessary to keep the inversion centre of the high temperature structure [33]. The role of the anion ordering is considered explicitly in the next chapter.

1.1.2 Electronic properties

The Fabre and Bechgaard salts show a pronounced variation in their electrical resistivity although they have the same structure. This variation is attributed to the difference in the interchain coupling[I] which is an important parameter in varying the dimensionality of the system as well the electronic properties. While TMTTF salts are one-dimensional, TMTSF salts are more two-dimensional due to the increasing interaction in the second direction (See Figure 1.2). However, the crucial difference between TMTTF and TMTSF salts can be observed in the electrical resistivity as follows:

1. $(TMTTF)_2X$ are one dimensional metals at high temperatures. At normal pressure (p = 1 bar) their resistivity shows a minimum in the temperature range 100 – 300 K as shown in Figure 1.5. Below the localization temperature T_ρ, the resistivity increases upon cooling and changes into a thermally-activated low temperature behaviour $(d\rho/dT < 0)$ with activation energy Δ_ρ in the range (500 – 800) K (see Table 1.3) [34].

2. $(TMTSF)_2X$ are good conductors in a broad temperature range with very high anisotropy ($\rho_c/\rho_a \approx 30000$) [35]. They have a very low room temperature resistivity (about 10^{-2} Ωcm) (see Figure 1.5) and show a metallic conductivity down to about 20 K where most of TMTSF salts undergo a metal-insulator phase transition due to one-dimensional instabilities [36]. $(TMTSF)_2ClO_4$ is the only compound which at ambient pressure stays metallic down to 1 K if it is cooled down slowly where it becomes superconducting [37]. However, Many of TMTSF and TMTTF salts can be driven into the superconducting phase by applying an external pressure [38,39].

The opening the energy gap Δ_ρ in TMTTF salts is attributed to the larger effective on-site Coulomb repulsion U and the stronger dimerization which drives the electrons to be localized at high temperature. Therefore, TMTTF salts are regarded as dimer-Mott insulators (see section 2.2). Experimental and theoretical studies showed that Δ_ρ associated with the charge localization increases with increasing the degree of dimerization $\Delta t_a/t_a$ and with increasing effective on-site Coulomb repulsion U [2,39]. Δ_ρ was calculated in the framework of the 1-D dimerized

[I] The strength of the interchain coupling can be characterized by the value of the transfer integral t_b. TMTSF salts have higher values of t_b than TMTTF salts. This means the interchain coupling in TMTSF salts is stronger than TMTTF salts.

Hubbard model at 1/4 band filling, the energy gap is estimated using the alternating hopping integrals model [40] to be $\Delta_\rho \approx 0.05 t_{a1} \approx 150$ K in $(TMTSF)_2PF_6$ and $\Delta_\rho \approx 0.3 t_{a1} \approx 500$ K in $(TMTTF)_2PF_6$[I]. The estimated value of Δ_ρ for $(TMTTF)_2PF_6$ is found comparable to the value obtained by dc-measurements [41]. However, recent theoretical calculations using the Density-matrix renormalization-group (DMRG) technique by Nishimoto *et al* [42] showed that the nearest-neighbour Coulomb repulsion V has pronounced influence on Δ_ρ which must be taken into account.

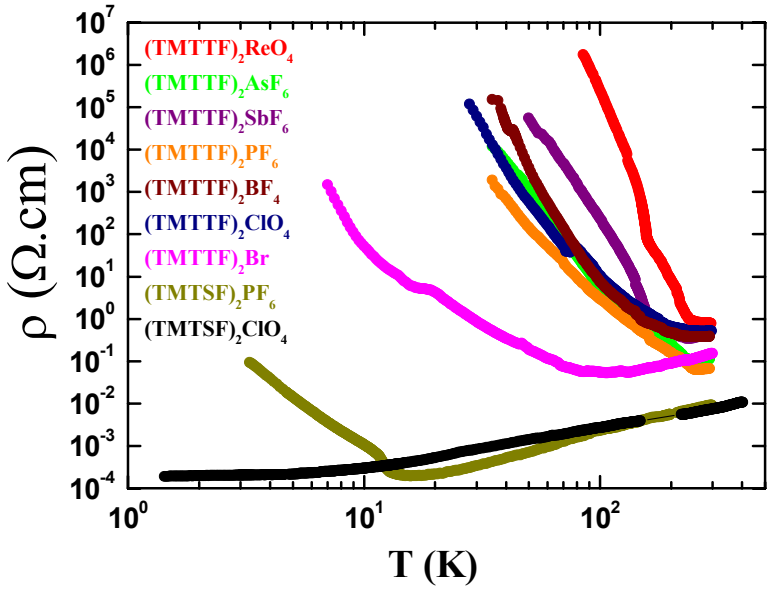

Figure 1.5: Temperature dependence of the electrical resistivity of selected TMT*C*F salts at normal pressure (p = 1 bar). From Ref. [2,41].

	$(TMTTF)_2X$		
X	ReO_4	SbF_6	AsF_6
$\sigma_{RT}^{\parallel}(1/\Omega\text{cm})$	1.27	2.27	8.83
T_ρ(K)	290	250	250
Δ_ρ(K)	800	400	550

Table 1.3: The conductivity at room temperature parallel to the stacking direction, the localization temperature and the localization energy gap of the investigated Fabre salts [41,43].

[I] The intrachain transfer integral t_{a1} for $(TMTSF)_2PF_6$ and $(TMTTF)_2PF_6$ is 252 meV and 137 meV, respectively [12].

1.1.3 Magnetic properties

The magnetic properties of TMT*C*F salts were investigated intensively by different techniques, such as static susceptibility, electron spin resonance (ESR), nuclear spin resonance (NMR) and muon-spin rotation (μSR). These techniques were able to detect the phase transitions into the magnetic and non magnetic ground states in TMT*C*F salts. Table 1.4 summarize the magnetic properties of the investigated Fabre salts where T_c is the transition temperature to the ground state.

	$(TMTTF)_2X$		
X	ReO_4	AsF_6	SbF_6
$T > T_c$	S = 1/2 AFM spin chain		
$T < T_c$	non-magnetic		AFM
Ground state	AO	SP	AFM
T_c (K)	156	13	6

Table 1.4: Magnetic properties of the investigated $(TMTTF)_2X$ above ($T > T_c$) and below ($T < T_c$) the phase transition into the ground state at atmospheric pressure. AFM stand for antiferromagnetic, AO for anion ordering and SP for Spin-Peirls.

Most of the electron spin resonance studies on $(TMTTF)_2X$ were done by *X*-Band ESR spectrometers[I] [2,44,45]. The ESR linewidth ΔH at room temperature is about 3 – 5 Oe which is significantly narrower than that of the selenium compounds[II] and decreases linearly with decreasing temperature with a slight and smooth change in the slope below about 200 K. ΔH is highest along c^*-axis and lowest along a-axis. The g-value has the same anisotropy as ΔH. Multi-frequency ESR studies (X-Band, Q-Band and W-Band ESR) on $(TMTTF)_2X$ in order to study the frequency dependence of the ESR parameters (linewidth and g-value) were not done so far and they are the goal of this work.

Figure 1.6 shows the spin susceptibility χ_s measured by SQUID for $(TMTTF)_2AsF_6$ and $(TMTTF)_2SbF_6$ [2]. At room temperature, the spin susceptibility of TMTTF salts is nearly independent of the counterion and it is in the range of $6-8\times10^{-9}$ m^3/mol. At T ≥ 100 K the spin susceptibility for both compounds are described by Bonner-Fisher model for S = 1/2 antiferromagnetic (AFM) spin chain [13] (see section 2.4.1) and the AFM exchange constant $|J|$ for $(TMTTF)_2AsF_6$ and

[I] The microwave frequency in the X-Band ESR spectrometer is 9.5 GHz.
[II] The room temperature ESR-linewidth of TMTSF salts is from 150 – 300 Oe.

$(TMTTF)_2SbF_6$ was found 410 K and 400 K, respectively. In $(TMTTF)_2AsF_6$ at T ≈ 13 K χ_s strongly decreases with decreasing the temperature which is a clear indication for the non magnetic spin-Peierls ground state. Contrary, there is slight increase in the susceptibility of $(TMTTF)_2SbF_6$ below the phase transition (T ≈ 6 K) which is comparable to the one observed in the antiferromagnetic (AFM) ground state of $(TMTTF)_2Br$ [46]. Coulon *et al.* investigated the AFM ground state in $(TMTTF)_2SbF_6$ using antiferromagnetic resonance. They found the easy axis close to the *b*`-axis, the intermediate axis around c^* and the hard axis around *a* [47].

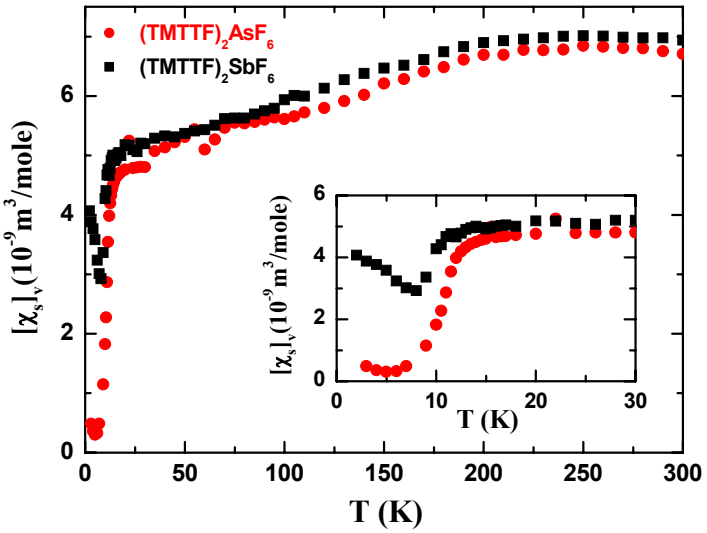

Figure 1.6: Temperature dependence of the spin susceptibility χ_s measured by SQUID at constant volume for $(TMTTF)_2AsF_6$ and $(TMTTF)_2SbF_6$. From Ref. [2].

Beside these magnetic and non-magnetic phase transitions, thermopower studies have detected a structureless phase transition in $(TMTTF)_2ReO_4$, $(TMTTF)SbF_6$ and $(TMTTF)_2AsF_6$ at 227 K, 156 K and 106 K, respectively [48]. This transition was referred to as a structureless phase transition because X-ray analysis failed to detect any distortion in the crystal structure due to this transition [33]. Also no anomaly in the magnetic susceptibility at these temperatures is observed. This transition stayed mysterious for a long period of time until it was recognized that it is due to "charge ordering" (CO) (and also called charge disproportionation). This transition has been identified by several experimental techniques. The first identification came from nuclear magnetic resonance (NMR) measurements. By using one- and two-dimensional ^{13}C spin labelled NMR spectroscopy [1], two distinct spectral lines were observed above the CO transition temperature T_{CO} (T_{CO} = 103 K for AsF_6, 156 K for SbF_6 and 227 K for ReO_4) [1,49,50]. Since all the TMTTF molecules are

equivalent, the two spectral lines originate from two inequivalent inner and outer ^{13}C nuclei of the TMTTF molecules (see Figure 1.4) which have inequivalent hyperfine coupling. Upon cooling the two lines remain unchanged down to T_{CO}. Below T_{CO} the two peaks splits into four peaks with equal absorption strength as shown in Figure 1.7 for the $(TMTTF)_2AsF_6$. This splitting is direct evidence that the TMTTF molecules are not equivalent below T_{CO} due to charge disproportionation developing between two TMTTF molecules, where these two molecules have two different molecular environments, one with slightly larger electron density (rich charged site) and one with a reduced electron density (poor charged site).

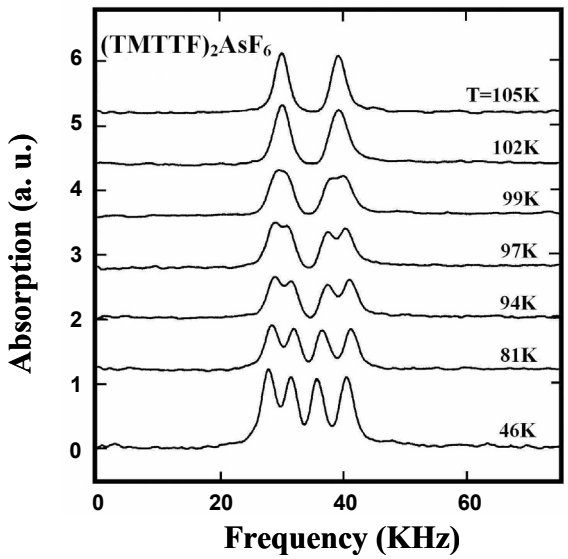

Figure 1.7: ^{13}C NMR spectra for $(TMTTF)_2AsF_6$ recorded at different temperatures. From. Ref. [51].

Charge ordering is quantified by the degree of the charge disproportionation $\Delta\rho_{CO} = |\rho_a - \rho_b|/(\rho_a + \rho_b)$, where ρ_a and ρ_b are the molecular charge densities for the rich charged site and the poor charged site, respectively. This ratio can be estimated from the spin-lattice relaxation rates T_1^{-1} obtained from NMR experiment by assuming that $T_{1a}^{-1}/T_{1b}^{-1} = \rho_a^2/\rho_b^2$ [51] where T_{1a}^{-1} and T_{1b}^{-1} are the spin-lattice relaxation rates of the rich and poor site, respectively. It was found from spin-lattice relaxation rates by applying the equation that the charge disproportionation $\Delta\rho_{CO}$ in $(TMTTF)_2AsF_6$, $(TMTTF)_2SbF_6$ and $(TMTTF)_2ReO_4$ is 0.26, 0.50 and 0.33, respectively [1,50,51].

Direct evidence of the charge ordering came from dielectric measurements. The dielectric permittivity ε´ measurements were performed on $(TMTTF)_2X$ (X = AsF_6, SbF_6, ReO_4) in the temperature range 10 – 300 K and the frequency range 100 kHz – 10 MHz [5,6]. It was observed that ε´ of all salts has a sharp growth as the temperature approaches T_{CO} with a tendency to diverge at T_{CO} (see Figure 1.8). In the ReO_4 salt, a sharp decrease of ε´ was observed near the anion ordering with q = (1/2,1/2,1/2) at 156 K. In the salts with centrosymmetrical anions (AsF_6 and SbF_6) and also the non-centrosymmetrical ReO_4, the charge ordering transition was shown to have a "ferroelectric" behaviour[I] (FE) with a second order phase transition character. Such a phase transition is normally described by the Curie law $\varepsilon' = A/|T - T_{CO}|$ [5,52]. Due to the charge ordering, the density of charges on TMTTF molecules alternates by $\pm\rho$ causing a permanent dipole moment and thus the ferroelectric ground state.

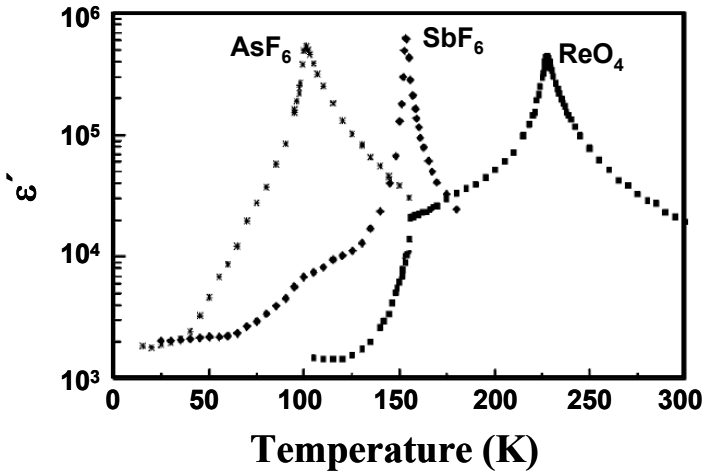

Figure 1.8: Temperature dependence of the real part of the dielectric permittivity ε`at frequency 1 MHz in semilogarithmic scale for $(TMTTF)_2X$ with X = AsF_6, SbF_6 and ReO_4. From Ref. [5].

The charge order in $(TMTTF)_2X$ was also investigated by infrared spectroscopy in our setup. It was found that:

- The electron-molecular-vibration (emv) coupled intermolecular $a_g(\nu_3)$ mode splits below T_{CO} as shown in Figure 1.9 for $(TMTTF)_2AsF_6$. Since the frequency of this mode depends on the charge on the molecule, the amount of

[I] In $(TMTTF)_2SCN$ the charge ordering transition at $T_{CO} \approx 169$ K is accompanied by an anion ordering transition, and due to the finite transverse component of q = (0,1/2,1/2) each anion chain can move in the opposite direction to the neighboring chains. Therefore, its transition has "antiferroelectric" (AFE) character [5].

charge disproportionation $\Delta\rho_{CO}$ could be estimated from these experiments in PF_6 and AsF_6. It was found that $\Delta\rho_{CO} = 0.12$ in PF_6 and $\Delta\rho_{CO} = 0.26$ in AsF_6.

- Below 100 cm^{-1}, the intermolecular modes of the $(TMTTF)_2$ dimers become IR active along all three crystal axes due to the charge disproportionation along the molecular stacks.

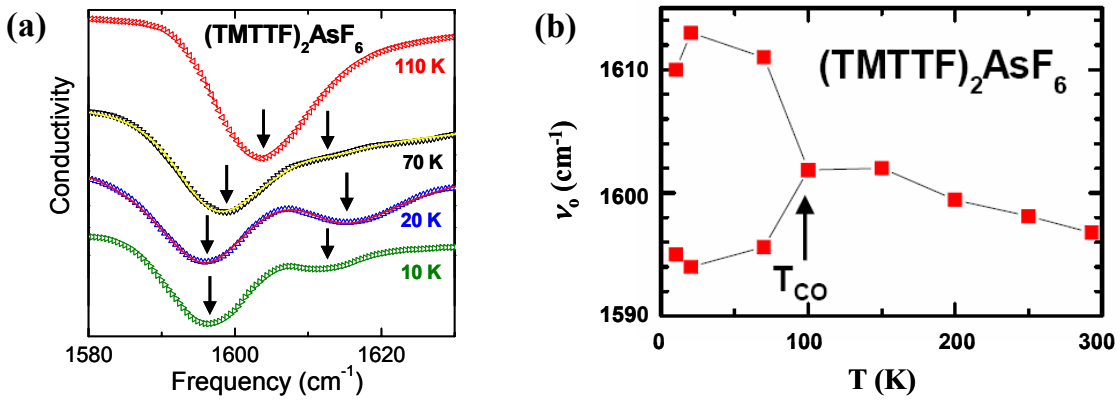

Figure 1.9: (a) Temperature dependent evolution of the emv coupled totally symmetric intramolecular $a_g(\nu_3)$ mode. The arrows indicate the positions of the antiresonance dips. (b) Temperature dependence of the antiresonance mode ν_o. From Ref. [4].

The effect of pressure on the charge ordering transition and on the ground state in $(TMTTF)_2AsF_6$ and $(TMTTF)_2SbF_6$ was studied using ^{13}C NMR spectroscopy [51]. It was found that T_{CO} decreases with increasing pressure and the CO phase can be suppressed easily with a moderate pressure of 1.5 kbar for $(TMTTF)_2AsF_6$ and 5 kbar for $(TMTTF)_2SbF_6$. It was demonstrated that the CO and spin-Peierls (SP) order parameters are competing in $(TMTTF)_2AsF_6$, and increasing the pressure reduces the amplitude of the CO and restores the SP state, while in $(TMTTF)_2SbF_6$ it was found that the AF state is stabilized when the CO parameter is large. By these experiments the temperature-pressure phase diagram of $(TMTTF)_2AsF_6$ and $(TMTTF)_2SbF_6$ was determined as shown in Figure 1.10.
The same experiment was repeated at ambient pressure on $(TMTTF)_2AsF_6$ in the low temperature region down to the SP state [53]. It was found below the SP transition that the splitted lines of the NMR spectra again merge by a charge origin. This result was interpreted as a redistribution of the charge densities at the SP transition. The same behaviour also was observed in $(TMTTF)_2ReO_4$ when a transition into anion ordered (AO) state occurs [50].

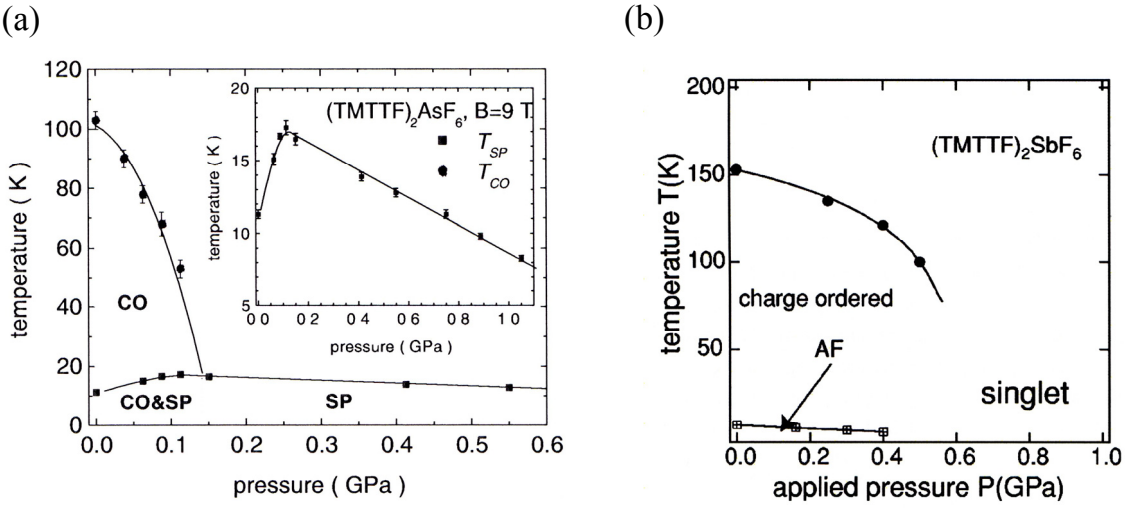

Figure 1.10: Pressure-temperature phase diagram for (a) $(TMTTF)_2AsF_6$ and (b) $(TMTTF)_2SbF_6$. From Ref. [49, 51].

Charge ordering was also studied through dielectric permittivity measurements on deuterated samples of $(TMTTF)_2X$ (AsF_6, SbF_6, ReO_4) [54]. It was found that the deuteration yields an increase of the characteristic temperatures for charge localization T_ρ and for charge ordering T_{CO}. This increase of T_{CO} was claimed to be due to the increased distance between TMTTF molecules along the molecular chains induced by deuteration.

1.1.4 Thermal expansion

Bechgaard and Fabre salts have a large thermal expansion coefficient. For example, when a single crystal of $(TMTSF)_2PF_6$ was heated up from low temperature ($T \approx 4$ K) to room temperature ($T \approx 300$ K), it was found that the crystal expands differently along the crystal directions and has the largest expansion coefficient ($\Delta a/a$) along the a-axis which increases linearly with increasing temperature above 100 K with a slope $(\Delta a/a)/T = 10^{-4}$ K^{-1} [55]. Recently, M. de Souza *et al* [56] performed high-resolution thermal expansion measurements on $(TMTTF)_2AsF_6$ and $(TMTTF)_2PF_6$ in the temperature range 4 K – 200 K. They showed that the expansion coefficient along the three orthogonal axes is strongly influenced with the phase transitions in these compounds. It was found a distinct lattice effects at T_{CO} in the uniaxial expansivity along the c^*-axis.

Most of the experimental measurements on (TMT*C*F)$_2$*X* are performed at constant pressure (p = 1 bar) while the theoretical models are derived at constant volume. Therefore, to compare the theoretical calculations with the experimental results the effect of the temperature dependence of the volume changes of the unit cell due to the thermal expansion must be evaluated. For the spin susceptibility which mostly is measured at constant pressure, the difference between its values at constant pressure $(\chi_s)_p$ and at constant volume $(\chi_s)_v$ is given by the relation [57]:

$$\Delta\chi_s \equiv (\chi_s)_p - (\chi_s)_v = \int_0^T dT \left(\frac{\partial\chi_s}{\partial p}\right)_T \left(\frac{a\partial p}{\partial a}\right)_T \left(\frac{\partial a}{a\partial T}\right)_p \tag{1.1}$$

where a is the unit cell parameter. The second and the third factor in equation 1.1 represent the compressibility and the thermal expansion coefficient of the salt which are known for (TMTSF)$_2$PF$_6$ from the structural studies [58]. The first factor can be determined by measuring the temperature and pressure dependence of the spin susceptibility. The experimental data for the first factor is not available up to now. However, the data of the first factor can be obtained using scaling relation which was derived by Bourbonnais and is valid at high temperature (T > 50 K) [59]:

$$\frac{1}{\sqrt{T_1 T}} \propto \chi_s(T) \tag{1.2}$$

where T_1 is the nuclear spin-lattice relaxation time. Using the data which was obtained by NMR measurements on (TMTSF)$_2$PF$_6$ by Wzietek *et al*. [57] and the X-ray under pressure measurements, the spin susceptibility at constant volume can be calculated [58]. Figure 1.11 shows the calculated temperature dependence of $(T_1\mathrm{T})^{-1/2}$ for (TMTSF)$_2$PF$_6$ at constant volume using the numerical integration of equation 1.1 and the measured values at constant pressure. $(\chi_s)_v$ has a much weaker temperature dependence than $(\chi_s)_p$. From the ratio $(\chi_s)_v/(\chi_s)_p$ using figure 1.12 and the measured susceptibility at constant pressure, the susceptibility at constant volume can be calculated. In (TMTTF)$_2$*X*, the *X*-ray under pressure measurements is still not available, therefore a direct determination of $(\chi_s)_v$ is not possible. However, by taking the assumption that the substitution of selenium by sulphur and changing the inorganic anion has no influence on the expansion coefficient of the material [2] the same ratio $(\chi_s)_v/(\chi_s)_p$ is used to rescale the susceptibility data for the TMTTF salts.

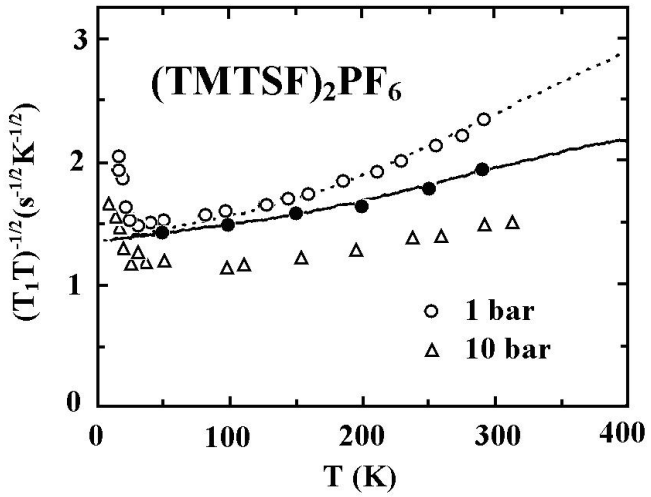

Figure 1.11: Temperature dependence of $(T_1T)^{-1/2}$ for ^{77}Se of $(TMTSF)_2PF_6$ under hydrostatic pressure of 1 bar and 10 bar. The closed symbols represent the corrected data for constant volume [2].

1.2 (BEDT-TTF)-Salts

Attempts for synthesizing high-temperature organic superconductors were stimulated by the prediction of W. Little [60] who proposed that the coupling of the electrons to Cooper pairs by an *excitonic mechanisms* could yield superconductors with transition temperatures T_c above room temperature where most of the synthesized 1-D organic compounds showed a metal-insulator transition. However, although these attempts did not reach the target of finding high-temperature organic superconductors, the metal-insulator transition temperature successfully was decreased in several organic compounds by modifying the atoms in the organic molecule. In order to overcome this transition and to achieve ambient-pressure organic superconductivity with a potentially high transition temperature, it is necessary to increase their dimensionally from 1-D to 2-D to avoid the dimensional instabilities and hence enhance T_c. This strategy was achieved in 1978 by synthesizing the new nonplanar electron donor molecule BEDT-TTF (Bisethylenedithiotetrathiafulvalene) by Mizuno *et al* [61]. The underlying idea of synthesizing the BEDT-TTF molecule depicted in Figure 1.12 was to enhance the overlap between the π-orbitals of adjacent molecules by enlarging the π-electron system on each molecule, and this has been accomplished by adding rings of carbon and sulfur atoms at the outer ends of the TTF skeleton.

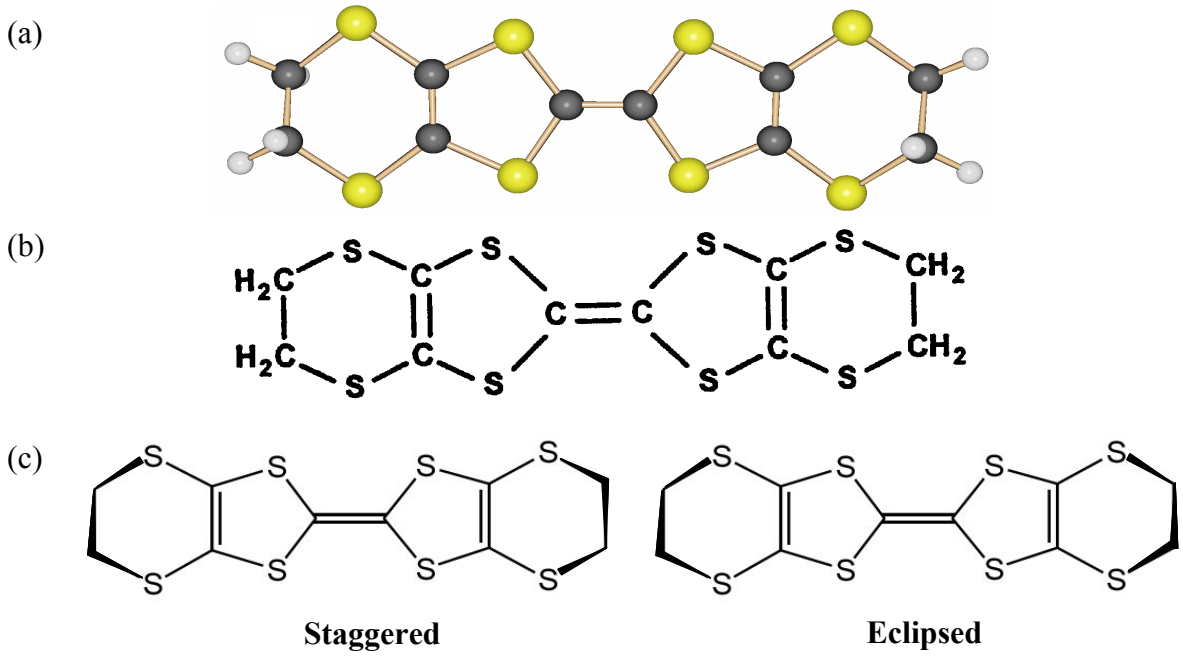

Figure 1.12: The Structure of the BEDT-TTF molecule (a) and (b). The main conformations of the terminal ethylene groups [$(CH_2)_2$] of the BEDT-TTF molecule are shown in (c).

The neutral BEDT-TTF molecule is nonplanar, it is twisted at the central double C=C bond. When this molecule forms the charge-transfer complex, the molecule fairly untwists, the central fragment of two C and four S atoms flattens to a plane but the outer rings remain nonplanar. The terminal ethylene groups [$(CH_2)_2$] are thermally disordered at high temperature and they can take on one of two degenerate out-of-plane conformations where they can be either staggered or eclipsed (Figure 1.12.c). Below a certain temperature, these groups become ordered and this kind of the structural difference has a noticeable effect on the electronic properties of the crystal. The nonplanar structure of the BEDT-TTF molecule together with the large disorder of the terminal ethylene groups have a subtle influence on the physical properties of the ET-complexes. It acts against building good overlap of π-orbitals of adjacent molecules. The S…S contacts increase the side-by-side intermolecular interaction and these two competing factors determine the dimensionality of the crystal.

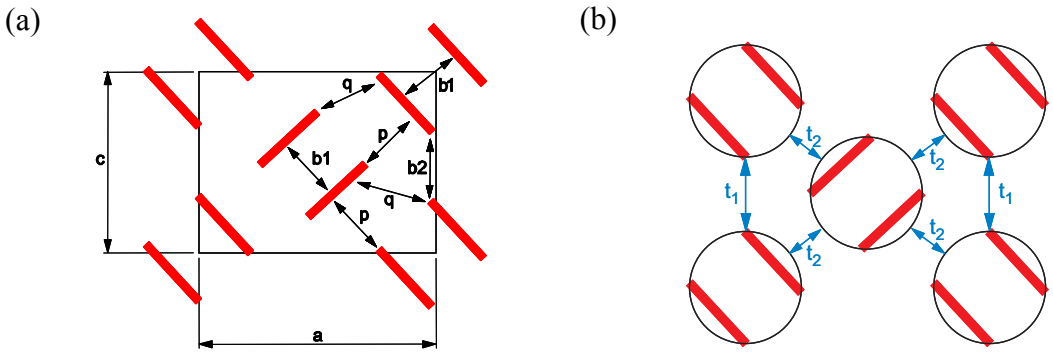

Figure 1.13: (a) Structural arrangement of the BEDT-TTF molecules in κ-phase (view along the molecular long axis). The red rectangles and the black ones represent the BEDT-TTF molecules and the unit cell, respectively. b1 is the intradimer overlap integral. b2, p and q are the interdimer overlap integrals. (b) Anisotropic triangular lattice modelling in-plane structure with two types of transfer integral t_1 and t_2, where t_1 = b2/2 and $t_2 = (p - q)/2$. The circles represent the dimers from BEDT-TTF molecules. From Ref. [62,63,64].

BEDT-TTF salts have several crystal structures depending on the spatial arrangement of BEDT-TTF molecules in the crystal, which determine the electronic structure of the salt. They are classified into α, β, Θ, κ, phases etc. The κ-phase salts (see Figure 1.13) are of particular interest, not only because they exhibit the highest superconducting transition temperature of all organic superconductors [25,65] but also owning to certain similarities in their normal- and superconducting-state properties with those of the high-temperature cuprate superconductors [66].

1.2.1 κ-(BEDT-TTF)$_2X$

In the κ-phase of the BEDT-TTF salts, the crystals are composed out of conducting layers of BEDT-TTF molecules which are separated by layers of monovalent anions *X*. As depicted in Figure 1.13.a, the BEDT-TTF$^{+0.5}$ molecules forms confacial dimers and due to this dimerization the conduction band is half filled.

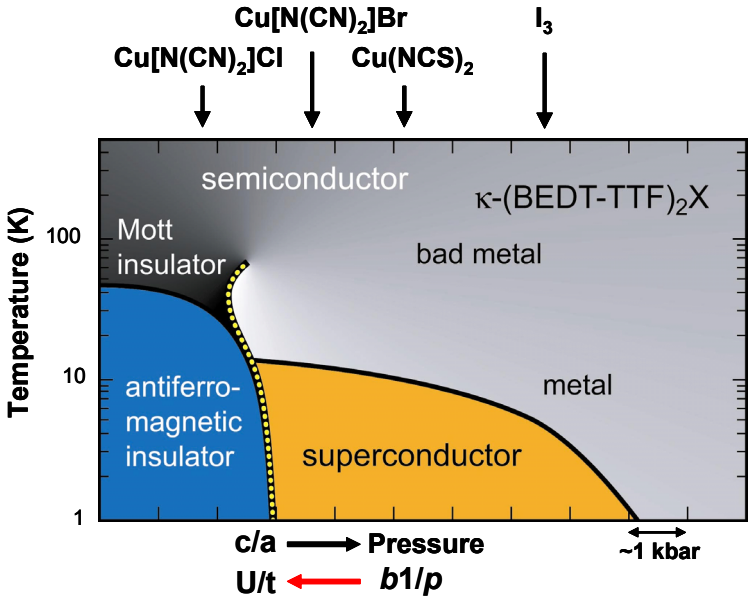

Figure 1.14: Generalized temperature-pressure phase diagram for the κ-(BEDT-TTF)$_2$*X* salts. The ambient pressure position of the different compounds in the phase diagram is indicated by the arrows. *c* and *a* are the lattice parameters; *b*1 and *p* indicate the transfer integrals according to Figure 1.13. *U*/*t* is the on-site Coulomb repulsion with respect to the hopping integral *t*. From Ref. [63].

The anion size sensitively influences the physical properties of the system very similar to the variation of pressure, since it defines the spacing between the molecules and thus the width of the conduction band. Quantitatively, increasing the anion size will increase the lattice parameter ratio *c*/*a* and this will decrease the ratio between the on-site Coulomb repulsion *U* and the hopping integral *t*, i.e. *U*/*t*. For this reason, the ground state which the κ-phase materials eventually prefer depends very sensitively on the chosen anion. However, different external parameters like pressure, cooling rate and even the chosen isotope can also change the ground state [67]. Figure 1.14 shows the generalized temperature-pressure phase diagram for the κ-(BEDT-TTF)$_2$*X* salts. The ground state of these salts can be switched between an antiferromagnetic insulating, a superconducting and a metallic state. It clear in Figure 1.14 that the most interesting region in this phase diagram is located between pure Cl and Br salts.

Several transport and magnetic studies were performed on the pristine organic conductor compounds κ-(BEDT-TTF)$_2$Cu[N(CN)$_2$]Br and κ-(BEDT-TTF)$_2$-Cu[N(CN)$_2$]Cl over the last years [25,8,117,68,69,70,71,72,73], while few experimental results on alloyed compounds from κ-(BEDT-TTF)$_2$Cu[N(CN)$_2$]-Br$_x$Cl$_{1-x}$ were reported [25,74,75]. It was shown that while κ-(BEDT-TTF)$_2$Cu-[N(CN)$_2$]Br is a superconductor, replacement of Br by the *slightly smaller* Cl results

in an antiferromagnetic (AFM) insulating ground state. On the other hand, the application of hydrostatic pressure of only about 0.3 kbar drives κ-(BEDT-TTF)$_2$Cu[N(CN)$_2$]Cl to a superconductor with a T_c of 12.8 K [25,7,68], suggesting that this material is an insulator closely situated in the metallic or superconducting states. P. Limelette *et al*. [8] recently studied the transport properties of κ-(BEDT-TTF)$_2$Cu[N(CN)$_2$]Cl. They could identify four transport regimes as a function of temperature and pressure which enabled to map the phase diagram shown in the Figure 1.15.b. In the left side of the phase diagram, at moderate temperatures the compound is semiconducting and around 50 K a phase transition into a Mott insulating state is observed (see Figure 1.15), followed by anti-ferromagnetic insulating (AFM) ground state below 25 K. At high pressures, the material shows so-called "bad metal"[I] behaviour [76] below about 100 K. However, at low temperatures (30 – 40 K) a phase transition to "Fermi liquid" state appears (T^2 dependence of ρ(T)) (Figure 1.15.a), and below around 12 K the compound becomes a superconductor (not shown in Figure 1.15). As seen in Figure 1.16 [72], κ-(BEDT-TTF)$_2$Cu[N(CN)$_2$]Cl is of two-dimensional nature, where the ratio of the out-of-plane resistivity $\rho_\perp$ to the in-plane resistivity $\rho_\parallel$ was found $\sim 10^2$ at room temperature and becomes $\sim 10^4$ below 25 K. The transport measurements at ambient pressure on alloyed compounds of κ-(BEDT-TTF)$_2$Cu[N(CN)$_2$]Br$_x$Cl$_{1-x}$ showed that the superconducting state appears in the compounds with $x \geq 0.5$ where below this value an insulating state is observed [25,74,75]. In all the superconducting samples a hump in the resistivity at around 100 K was observed and followed by a strong decrease of the resistivity with a T^2 dependence below 40 K before a sharp drop at the superconducting transition [8,69,75]. The pressure dependence of the resistivity of the pristine Br compound showed a decreasing T_c with increasing pressure [7,69]. Souza *et al* [9] studied the Mott metal-insulator transition on deuterated crystals of κ-(BEDT-TTF)$_2$Cu[N(CN)$_2$]Br using transport and thermal expansion experiments. They could identify the critical points at the boundary of metal-insulator transition of the phase diagram. As shown in Figure 1.17, this compound showed "Percolative" superconducting ground state and not bulk superconductivity. Percolative superconductivity was also observed in pure Cl compounds measured by microwave conductivity [77].

[I] They are called "bad metal" because their resistance has a metallic temperature dependence but at sufficiently high temperature, the mean free path *l* of the charge carriers would be less than its de Broglie wavelength, hence Boltzmann transport theory can not be applied.

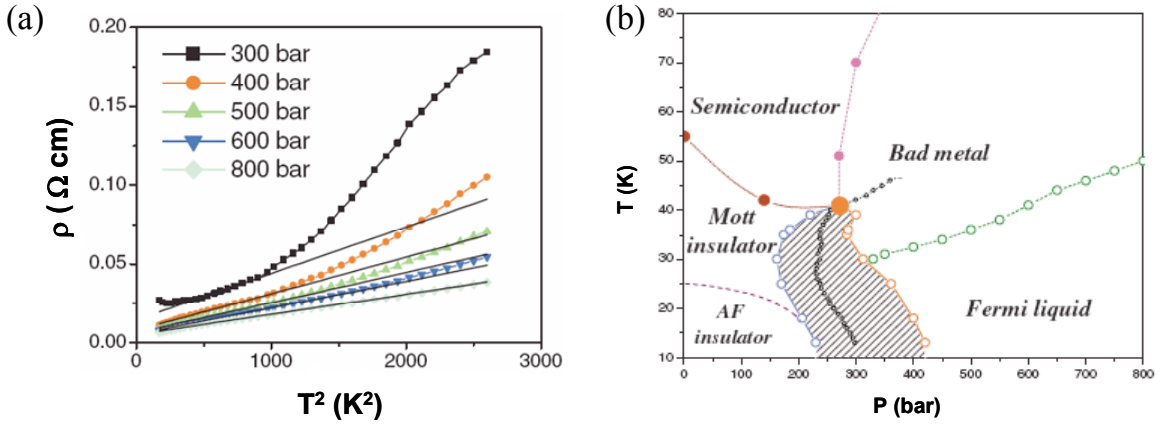

Figure 1.15: (a) Plot of resistivity ρ versus T^2 at different pressures for κ-(BEDT-TTF)$_2$Cu[N(CN)$_2$]Cl. (b) Pressure-temperature phase diagram of κ-(BEDT-TTF)$_2$Cu[N(CN)$_2$]Cl [8].

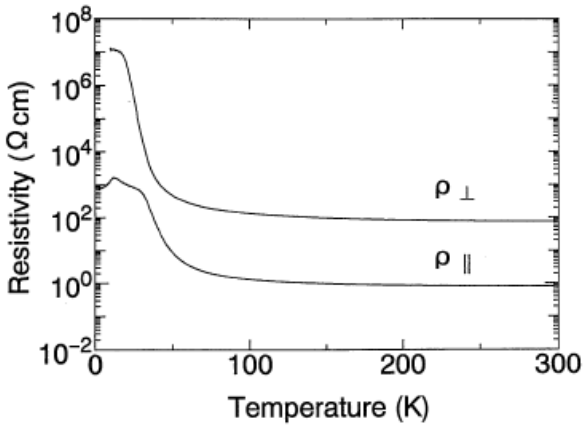

Figure 1.16: The temperature dependence of resistivity of κ-(BEDT-TTF)$_2$Cu[N(CN)$_2$]Cl in direction parallel $\rho_{\parallel}$ and perpendicular $\rho_{\perp}$ to the conduction plane [72].

In case of the magnetic investigations, most of the ESR measurements were done on the pristine Br and Cl compounds. The ESR linewidth at room temperature was between 50 and 80 Oe depending on the crystal orientation. Both compounds showed a maximum in the linewidth around 80 – 100 K and then a steep decrease down to low temperatures [11,70,71,72]. In pristine Cl compound, the linewidth is observed to increase below 25 K with decreasing temperature (see Figure 1.18) indicating the AFM phase transition [71].

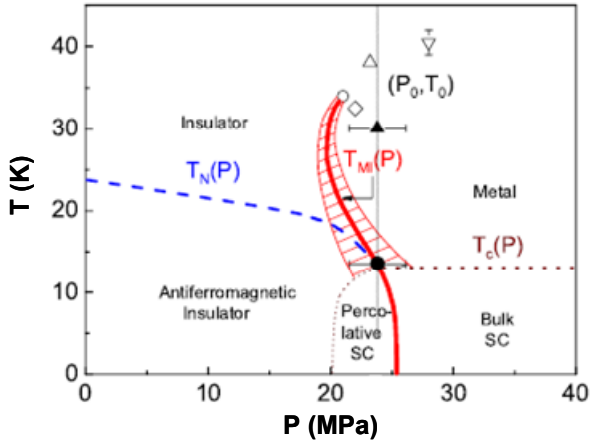

Figure 1.17: Pressure-temperature phase diagram of deuterated κ-(BEDT-TTF)$_2$Cu[N(CN)$_2$]Br [9]. The zero pressure indicates the position of κ-(BEDT-TTF)$_2$Cu[N(CN)$_2$]Cl.

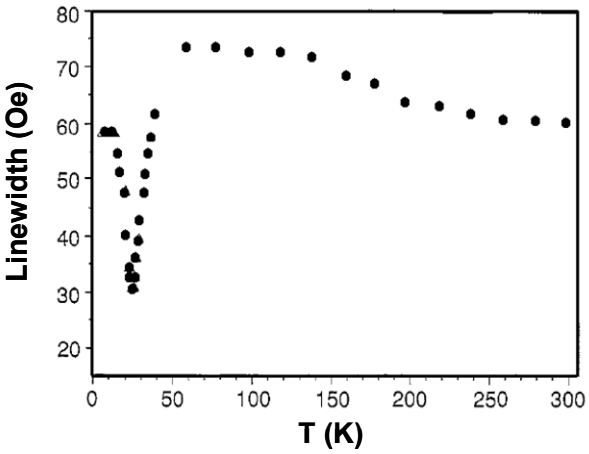

Figure 1.18: Temperature dependence of ESR linewidth of κ-(BEDT-TTF)$_2$Cu[N(CN)$_2$]Cl [71].

The origin of the metal-insulator transition of the κ-type compounds was also investigated by studying the magnetic properties of κ-(BEDT-TTF)$_2$Cu[N(CN)$_2$]Cl. NMR measurements have shown that this material undergoes an antiferromagnetic order below T_N = 27 K with a commensurate magnetic structure of essentially localized spins [78]. The magnetization measurements showed a weak ferromagnetic moment below T = 23 K when an external magnetic field was applied parallel to the *a*-*c* plane [79]. These measurements suggested that the easy axis is perpendicular to the ac-plane. However, determining the easy axis of κ-(BEDT-TTF)$_2$Cu[N(CN)$_2$]*X* compounds is under debate up to now. While antiferromagnetic resonance (AFMR) measurements on deuterated κ-(BEDT-TTF)$_2$Cu[N(CN)$_2$]Cl by Kubota *et al* [80] considered that the easy axis is along *b*-axis, the same experiment on deuterated κ-

(BEDT-TTF)$_2$Cu[N(CN)$_2$]Br by Ito and Ishiguro [81] showed that *a*, *b* and *c* axes are easy, hard and intermediate axes, respectively. Interestingly, AFMR so far were only observed in deuterated samples.

Figure 1.19 shows the magnetic susceptibility of κ-(BEDT-TTF)$_2$Cu[N(CN)$_2$]Cl, κ-(BEDT-TTF)$_2$Cu[N(CN)$_2$]Br and d8-κ-(BEDT-TTF)$_2$Cu[N(CN)$_2$]Br at a magnetic field B_o = 1 T [82]. Above ~35 K, the three compounds trace nearly the same susceptibility curve, which is characterized by the steep decrease at lower temperatures. The metallic Cu[N(CN)$_2$]Br salt has a kink at 35 K, while the nonmetallic Cu[N(CN)$_2$]Cl salt exhibits a huge increase below 30 K, which is attributed to spin canting in the antiferromagnetically ordered state. The d8-[N(CN)$_2$]Br salt, which is just on the Mott boundary [9] shows a similar behavior to the Cu[N(CN)$_2$]Cl salt except that the increase occurs at around 16 K.

The superconducting properties of κ-(BEDT-TTF)$_2$Cu[N(CN)$_2$]Br were found to resemble in many respects the behavior known from the layered superconductors like cuprates [66]. It was shown that this compound is a strongly anisotropic type-II superconductors with lower critical fields B_{c1} of only a few mT (about 3 mT at T = 0) and upper critical fields B_{c2} of typically a few tesla (about 8 T at T = 0) for fields perpendicular to the conduction plane [67]. For field parallel to the conduction plane, B_{c1} in κ-(BEDT-TTF)$_2$I$_3$ was found smaller than the earth's field (0.05 mT) and B_{c2} about 7 T [67,83].

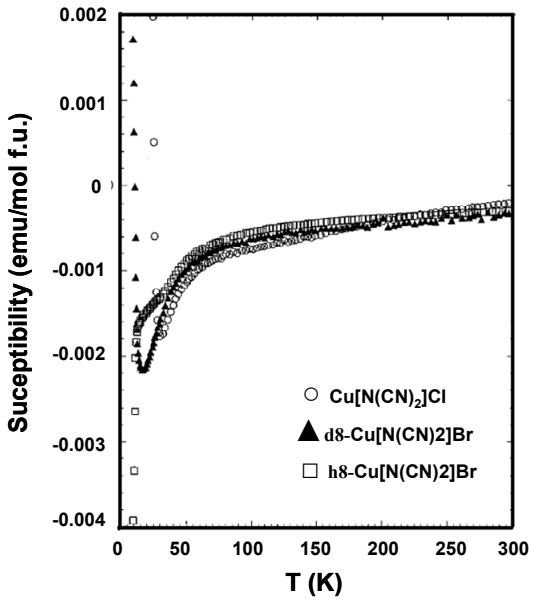

Figure 1.19: Temperature dependence of the dc susceptibility of κ-(BEDT-TTF)$_2$*X* at a magnetic field B_o = 1 T [82].

1.2.2 Crystal structure of κ-(BEDT-TTF)$_2$Cu[N(CN)$_2$]Br$_x$Cl$_{1-x}$

The single crystals of κ-(BEDT-TTF)$_2$Cu[N(CN)$_2$]Br$_x$Cl$_{1-x}$ crystallize in orthorhombic symmetry[I] with a unit cell containing four dimers. The dimers on the corners are oriented in a different direction from that on the centers (see Figure 1.13). The angle between these two kinds of dimers is very close to 90^o. The interaction between the BEDT-TTF molecules is characterized by the intradimer overlap integral $b1$ and the interdimer overlap integrals $b2$, p and q. As shown in Figure 1.13.b, these overlap integrals are reduced to two interdimer transfer integrals, t_1 and t_2 by modeling the lattice of dimers to an anisotropic triangular lattice whose anisotropy t_2/t_1 depends on the anion X where $t_1 = b2/2$ and $t_2 = (p - q)/2$ [64]. The room temperature unit cell parameters and the overlap integrals at 127 K of κ-(BEDT-TTF)$_2$Cu[N(CN)$_2$]Br$_x$Cl$_{1-x}$ for $x = 1$ and $x = 0$ are listed in Table 1.5. Figure 1.20 shows the 3D view of the crystal structure of κ-(BEDT-TTF)$_2$Cu[N(CN)$_2$]Br [84]. The BEDT-TTF molecules form conducting layers in *a*-*c* plane which are separated by anionic layers along *b*-axis.

	κ-(BEDT-TTF)$_2X$	
X	Cu[N(CN)$_2$]Br	Cu[N(CN)$_2$]Cl
a (Å)	12.942	12.977
b (Å)	30.016	29.979
c (Å)	8.539	8.480
V (Å^3)	3317	3299
$b1$ (eV)	0.265	0.273
$b2$ (eV)	0.098	0.104
p (eV)	0.109	0.105
q (eV)	0.038	0.039
t_1 (eV)	0.049	0.052
t_2 (eV)	0.036	0.033

Table 1.5: Unit cell parameters of κ-(BEDT-TTF)$_2X$ (X = Cu[N(CN)$_2$]Br and Cu[N(CN)$_2$]Cl) at room temperature and their overlap integrals at T = 127 K [62,64].

[I] In the orthorhombic symmetry, the three perpendicular crystal axes and the unit cell coordinates are the same and thus $(a,b`,c^*) \equiv (a,b,c)$.

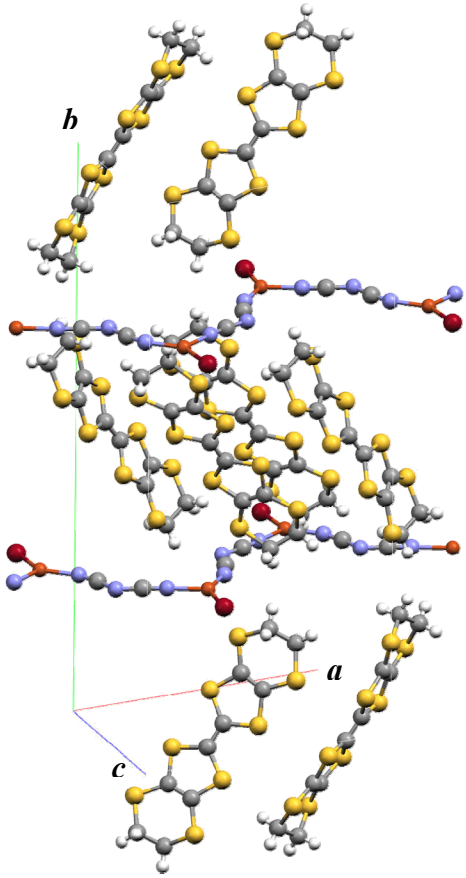

Figure 1.20: 3D view of the crystal Structure of κ-(BEDT-TTF)$_2$Cu[N(CN)$_2$]Br [84].

Chapter 2

Physics of Low-Dimensional Systems

Physics in low-dimensional systems is a fascinating topic in condensed matter. Due to the reduced dimensionality the electrons in these materials are strongly correlated, i.e., the interaction between the electrons is not neglected as in case of three dimensional conductors. Therefore, several exciting physical phenomena can be observed in 1-D and 2-D systems due to competition between spin and charge degrees of freedom which are absent in 3-D systems. Furthermore, many problems can be solved exactly while approximations are introduced in the theoretical models of 3-D systems. In this chapter a general description about the physics in low-dimensional systems will be given.

2.1 Electronic Structure

It was shown in chapter one that the formation of the band structure in $(TMTTF)_2X$ and κ-$(BEDT\text{-}TTF)_2X$ salts results from the overlapping of the π-molecular orbitals. The electrons in these orbitals can tunnel (hop) from one orbital to a nearest neighbor with strength t (called the transfer integral). The value of the transfer integral depends on the overlapping size of the molecular wave functions in the direction of the π-orbitals. Since the π-orbitals are directional (depending on the molecular structure), the transfer integral are anisotropic. Generally, the electron band structure of organic conductors can be described within the tight-binding single electron Hamiltonian. The linearized energy desperation is given by the relation [65]:

$$\varepsilon(\vec{k}) = -2t_a \cos(k_a \cdot a) - 2t_b \cos(k_b \cdot b) - 2t_c \cos(k_c \cdot c) \qquad (2.1)$$

where t_a, t_b, and t_c are the transfer integrals between nearest-neighbor molecules along the a, b, and c-axis of the crystal lattice respectively, k_i is the electron wave vector in the i^{th} direction. The differences in the ratio between the transfer integrals

along the three different crystallographic directions can map the Fermi surface in different shapes for 1-D, 2-D and 3-D conductors as illustrated in Figure 2.1.

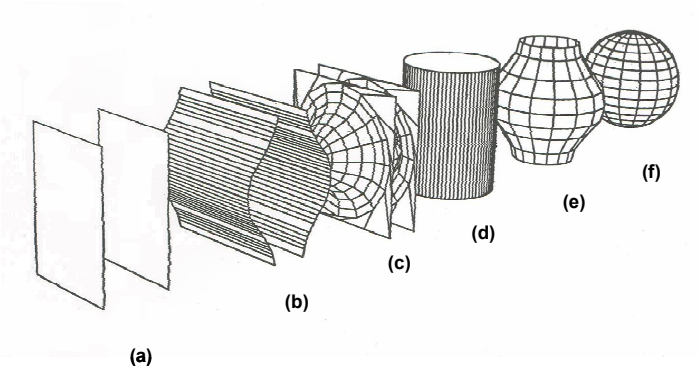

Figure 2.1: The shape of Fermi surface depending on the dimensionality: (a) one-dimensional ($t_a \gg t_b, t_c$), (b) quasi-one-dimensional ($t_a > t_b \gg t_c$), (c) transverse isotropic quasi-one-dimensional ($t_a > t_b \approx t_c$), (d) isotropic two-dimensional ($t_a \approx t_b \gg t_c$), (e) quasi-two-dimensional ($t_a \approx t_b > t_c$), (f) isotropic three-dimensional ($t_a \approx t_b \approx t_c$). From Ref. [85].

The dimensionality of the system increases from 1-D to 2-D with increasing the ratio t_b/t_a. It was shown in (TMT*C*F)$_2X$ that increasing the ratio t_b/t_a stabilizes the metallic state and the system will not undergo a metal-insulator phase transition at low temperatures [2]. However, in addition to the transfer integral, metal-insulator phase transition is strongly correlated with the Coulomb interaction between electrons which is described in the framework of the Hubbard model in the next section.

2.2 Mott Transition (Metal-Insulator Transition)

It is well known from the band theory of solids that completely filled and empty bands give insulating behavior while partially filled bands have metallic conduction [86]. Mott and Hubbard have shown that an incompletely filled band will not necessarily show metallic conduction and a metal-insulator transition can occur under critical conditions [87,88,89]. They argued that strong electronic correlations drive the system into the insulating state. Unlike the 3-D metals, the electronic interactions in one-dimensional systems are more relevant. Therefore, the Coulomb interaction U between two electrons on the same site ("on-site") beside the transfer integrals is considered. Many of the charge-transfer salts tend toward the dimerization along the molecular chains, and they can be described by the one-dimensional dimerized Hubbard model defined by the Hamiltonian [40]:

$$\hat{H} = -t_1 \sum_{i,\sigma} \left(c^{\dagger}_{2i,\sigma} c^{\dagger}_{2i+1,\sigma} + h.c. \right) - t_2 \sum_{i,\sigma} \left(c^{\dagger}_{2i-1,\sigma} c_{2i,\sigma} + h.c. \right) + U \sum_{i=1} n_{i,\uparrow} n_{i,\downarrow} \tag{2.2}$$

where σ is a spin index which takes $\uparrow$ and $\downarrow$, $c^{\dagger}_{i\sigma}$ and $c_{i\sigma}$ are the creation and the annihilation operators of the electron at the ith site and $n_i = c^{\dagger}_{i\sigma} c_{i\sigma}$. U is the on-site Coulomb interaction. In order to determine the dispersion energy of one electron band, the following cases are distinguished:

- When the crystal lattice of the one-dimensional conductor is not dimerized, i. e. $t_{a1} = t_{a2} = t_a$ and there are no interactions between the electrons ($U = 0$), the one electron band dispersion energy is given by $\varepsilon(k) = \sqrt{2t_a^2 + 2t_a^2 \cos(ka)}$ (see Figure 2.2). In this case the material has a metallic conductivity along the *a*-direction for all finite band fillings. If there are interactions between the electrons ($U > 0$), the on-site repulsion interaction in half-filled band of one dimensional systems leads to the opening of an energy gap Δ_ρ (charge gap) at the Fermi level [90].

- In dimerized crystal lattice with non-interacting electrons ($t_{a1} > t_{a2}$ and $U = 0$), the relation of the dispersion energy of one electron band becomes:

$$\varepsilon(k) = \sqrt{2t_{a1}^2 + 2t_{a2}^2 + 2t_{a1}^2 t_{a2}^2 \cos(ka)} \tag{2.3}$$

  At the Brillouin zone boundary, the dimerization energy gap $\Delta_D = 2(t_{a1} - t_{a2})$ opens due to the finite dimerization along the chain direction (see Figure 2.2) and the total bandwidth is $W = 2(t_{a1} + t_{a2})$ [40].

- In case of interactive electrons in a dimerized lattice ($U > 0$ and $t_{a1} > t_{a2}$), equation 2.3 still is valid. Due to the dimerization the energy band splits into two sub-bands. If one of these sub-bands is half filled, an energy gap Δ_ρ at Fermi level opens induced by a finite value of the on-site Coulomb energy [40].

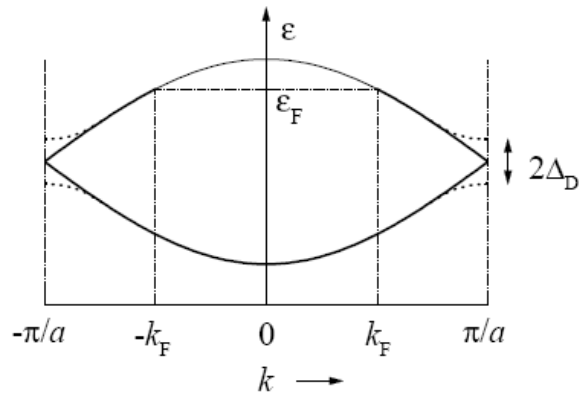

Figure 2.2: Schematic representation of the one electron band dispersion energy of 1-D system along the chain direction in the extended Hubbard model with $U = 0$. The band structure is folded at $\pm\pi/a$ because of the stack dimerization. The dotted lines indicate the opening of the energy gap $2\Delta_D$ at the Brillouin zone boundary due to the finite dimerization in the chain. The thick line sketches the zone for the 3/4 filled conduction band.

In the Hubbard model, the two important parameters responsible for driving the metal-to insulator transition are the electron correlation strength U/t and the band filling n. In the case of half-filled band ($n = 1$), the change of U/t drives the metal-to-insulator transition at a critical value. To clarify how the ratio U/t drives the metal-to-insulator transition, two limiting cases are considered as shown in Figure 2.3 for the 2-D organic conductor as an example:

- For $U \neq 0$ (or $U >> t$), some energy has to be paid for double occupancy. Therefore, the electrons are equally distributed and the system is insulating.

- For $U = 0$ (or $U < t$), the system is metallic, since the electrons are free to move.

The Mott-insulator transition in a 2-D lattice has been predicted theoretically[I] [91]. It was shown that this transition typically occurs when U (the electrostatic repulsion (e^2/r_{12}) between a pair of electrons) is comparable to the band width $W = 8t$ ($U_{eff}/t = 8$) [63,91,92]. The band gap Δ is predicted to change discontinuously from zero to some positive value as U/W changes. Opening this gap gives raise to an activated electrical conductivity $\sigma = \sigma_0 \exp(-E_a / k_B T)$, where E_a is the activation energy [92].

[I] The metal-to-insulator transition occurs in $(TMTCF)_2X$ salts when U is comparable to the band width $W = 4t_a$, where t_a is the transfer integral parallel to the stacking direction.

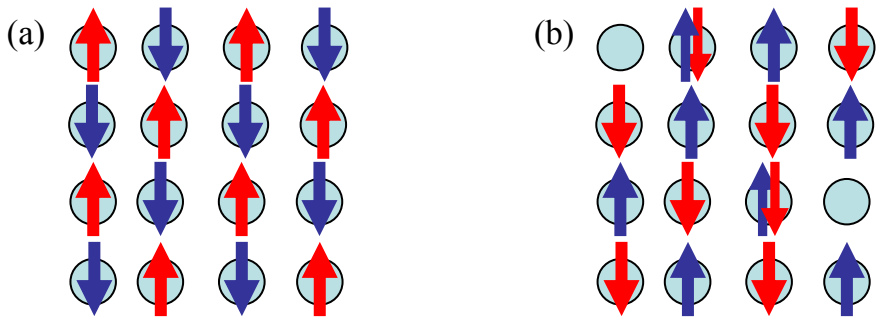

Figure 2.3: (a) Ordered arrays of radicals with one unpaired electron per each site (half-filled band) exists when $U \neq 0$ (or $U >> t$). (b) The case of double occupancy of a single site exists when $U = 0$ (or $U < t$).

2.3 Electrical Conductivity of Low-Dimensional Organic Conductors

While some of low-dimensional organic conductors show semiconducting temperature dependence as discussed in the last paragraph, others show metallic temperature dependence. The strong interaction between the electrons leads to a diverse in their electronic behavior. Therefore, two important concepts correlated with the interactive electrons in low-dimensional organic conductors are introduced below.

2.3.1 Fermi liquid

In conventional metals, the electrons do not significantly interact with each other, they are just scattered at defects or lattice vibrations (phonons). Thus they can be described by the Drude-Sommerfeld model (free electron gas model). In the case of narrow bands or reduced dimensions, the electronic density is enhanced and the electronic correlations (electron-electron interaction) can not be neglected any more. In 1957, Landau introduced Fermi liquid theory describing the effects of the interactions between the electrons in systems with dimensionality $d \geq 2$ [93]. Since the electrons are highly charged particles, the interaction between themselves has to be taken into account. In this case they behave like free electrons but have enhanced mass and they are so-called *quasi-particles*[I]. In simple systems such as elementary metals, it is possible to apply the models derived for non-interacting electrons on quasi-particles with an enhanced effective mass, where all complications are

[I] The quasi-particles have the same quantum numbers as the original free particles and also obey Fermi-Dirac statistics.

absorbed in the renormalized effective mass. The effective mass m^* of the quasi-particles is determined by [94]:

$$m^* \approx (1 + F)\, m_\lambda = (1 + F)\,(1 + \lambda)\, m_b \tag{2.4}$$

where F is a constant known as a Fermi liquid parameter, m_λ is the dynamical mass resulting from the interaction between the electron and the lattice, λ is an electron-phonon coupling constant (in many substances, λ is between 0.1 and 1) and m_b is the mass calculated in the band structure calculations. The electrical conductivity in a Fermi liquid is given by [94]:

$$\sigma_{dc} = \frac{Ne^2\tau^*}{m^*} \tag{2.5}$$

Equation 2.5 is the classic equation of Drude if the effective mass m^* is replaced by the free mass m_e of electrons. N is the carrier density and e the electronic charge. τ^* is the life time of the quasi particles and defined as

$$\tau^* = \tau \frac{m^*}{m_e} \tag{2.6}$$

In electron-electron interaction, the temperature and the frequency dependence of the scattering rate of the quasi-particles is given by:

$$1/\tau(\omega,T) \propto (2\pi k_B T)^2 + (\hbar\omega)^2 \tag{2.7}$$

It is clear from equation 2.7 that when the electron-electron scattering dominates, the resistivity varies as T^2, which is often taken as an experimental check for Fermi liquid behavior (in addition to the linear temperature-dependence of the specific heat).

2.3.2 Superconductivity

Superconductivity occurs due to an attractive interaction between electrons, which in general is mediated by phonons. Superconductivity was described microscopically in 1957 by Barden, Cooper and Schrieffer [95,96], presently known as BCS theory. According to this theory, electrons travel in pairs with momentum equal to zero (known as Cooper pairs), interacting with each other through lattice vibrations or

phonons. The pairing of the electrons occurs because the attraction between two electrons is greater than that of Coulomb repulsion. The attractive interactions between electrons lead to a ground state separated from excited states by an energy gap Δ:

$$2\Delta(0) = 3.54 k_B T_c \tag{2.8}$$

where k_B is the Boltzmann constant and T_c is the superconducting transition temperature.

Superconducting materials interact with magnetic fields. In the superconducting state, a superconducting material will tend to exclude all magnetic fields, a phenomenon known as the *Meissner effect*. However, if the magnetic field strength intensifies beyond a critical level H_c, the superconducting material will be rendered non-superconductive. In other words, superconducting materials will lose their superconductivity if exposed to a magnetic field $H > H_c$. In fact, the presence of any magnetic field tends to lower the critical temperature of any superconducting material. Superconductors fall into two classes depending on the way in which the transition from the superconducting to the normal state proceed when the applied magnetic field exceeds H_c: **type-I** and **type-II** superconductor (see Figure 2.4). The principal difference between them is that the **type-I** superconductor possess a single well defined critical field whereas the **type-II** has two critical fields, the lower of which (H_{c1}) defines the field below which magnetic flux is substantially excluded from the material (the Meissner effect). For fields above H_{c1} but below the upper critical field (H_{c2}) the superconductor is in the Shubnikov phase. Here, any penetrating magnetic flux is confined within narrow flux vortex lines each of which is associated a quantum of magnetic flux Φ_0 ($\Phi_0 = h/2e = 2 \times 10^{-15}$ Wb).

The superconducting properties of the organic conductors resemble in many respects the behavior known from the cuprate superconductors. The organic superconductors are **type-II** superconductors with low critical fields H_{c1} of only a few mT and upper critical fields H_{c2} of a few T [67] (see section 1.2.1).

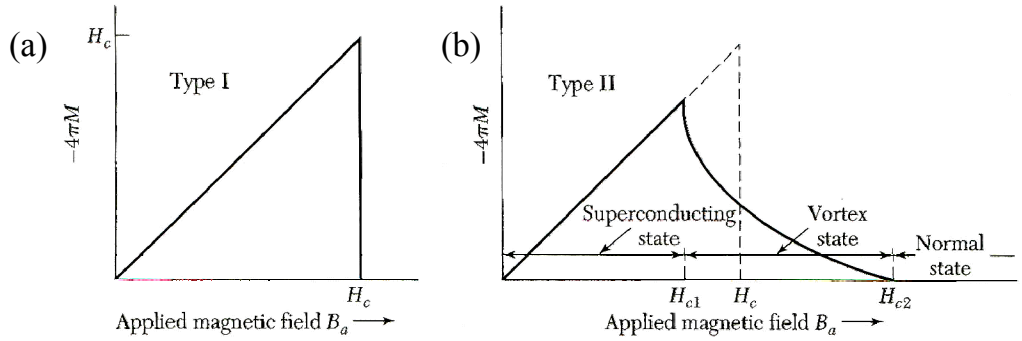

Figure 2.4: (a) Magnetization versus applied magnetic field for a bulk superconductor exhibiting a complete Meissner effect (perfect diamagnetism). (b) Superconducting magnetization curve of a type II superconductor. The flux starts to penetrate the specimen at a field H_{c1} lower than the thermodynamic critical field H_c (see text). From Ref [97].

2.4 Magnetism of Organic Conductors

Magnetism is based on the magnetic moment of the electron, which in turn is attributed to the spin (S = 1/2) of the electron. Magnetism is a bulk property and it results from the nonzero net vector sum of all the individual spin magnetic moments which can be induced by application of an external magnetic field H on a material. The strength of the response of the spins to the applied magnetic field is described by the spin susceptibility χ_s:

$$\chi_s = M/H \tag{2.9}$$

where M is the magnetization density (the spin magnetic moment per unit volume). In conventional metals, the spin susceptibility is temperature independent within the free-electron Fermi model, and is called Pauli susceptibility [98]:

$$\chi_{Pauli} = \frac{\mu_0 N g^2 \mu_B^2}{2} D(E_F) \tag{2.10}$$

$D(E_F)$ is the density of states at the Fermi level ($D(E_F) = mk_F / 2\pi^2\hbar^2$). In low-dimensional systems the interaction between the spins is accounted due to the strong correlations between the electrons. The exchange interaction between two spins operators at sites i and j can (S_i and S_j) is described by the Ising-Heisenberg Hamiltonian:

$$\hat{H} = -J\sum_{i=1}^{n-1}\left[S_i^z S_{i+1}^z + \xi\left(S_i^x S_{i+1}^x + S_i^y S_{i+1}^y\right)\right] - g\mu_B\sum_{i=1}^{n}\vec{H}\bullet\vec{S}_i \qquad (2.11)$$

where J is the coupling constant of the exchange interaction between the two spins operator S_i and S_{i+1}. J is positive in case of ferromagnetism (spins are aligned parallel) while it is negative in case of antiferromagnetism (spin are aligned anti-parallel). ξ is a measure of the magnetic anisotropy. In case of completely anisotropic exchange interaction $\xi = 0$ (Ising model) and for isotropic interaction $\xi = 1$ (Heisenberg model) [98].

In the TMTTF salts, at high temperatures the spins form a $S = 1/2$ AFM Heisenberg chain while in κ-(BEDT-TTF)$_2$Cu[N(CN)$_2$]Br$_x$Cl$_{1-x}$ the arrangement of the spins can be mapped as a 2-D dimensional $S = 1/2$ Heisenberg AFM on square lattice as shown in Figure 2.5.

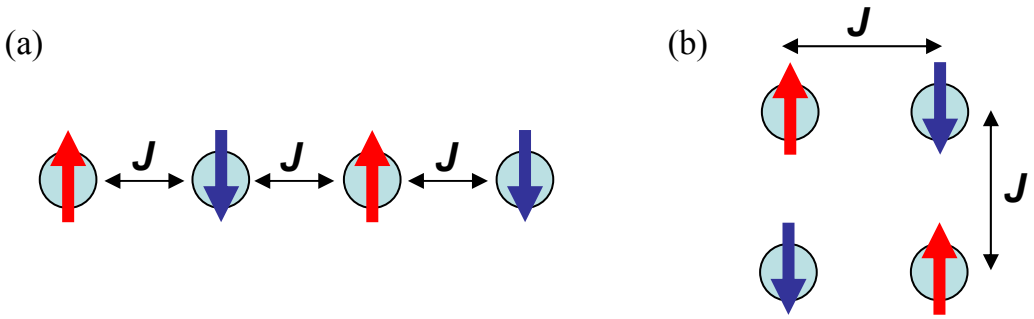

Figure 2.5: Schematic view of the isotropic $S = 1/2$ Heisenberg chain of localized electrons with AFM coupling constant J (a), and 2-D dimensional S = 1/2 Heisenberg AFM on square lattice with AFM coupling constant J (b).

2.4.1 $S = 1/2$ antiferromagnetic Heisenberg chain

At high temperatures, the TMTTF molecules form isotropic antiferromagnetic (AFM) $S = 1/2$ chains. If a magnetic field $\vec{H}$ is applied on the AFM Heisenberg chain of N spins $\vec{S}_i$, the effect can be described by the Heisenberg Hamiltonian:

$$\hat{H} = -J\sum_{i=1}^{N}\vec{S}_i\bullet\vec{S}_{i+1} - g\mu_B\sum_{i=1}^{N}\vec{H}\bullet\vec{S}_i \qquad (2.12)$$

By using analytical methods, Bonner and Fisher [13] were calculated numerically the temperature dependence of the spin susceptibility of an isotropic finite spin chain with $N \leq 11$ and the results were extrapolated for $N \rightarrow \infty$. The temperature dependence of the spin susceptibility $\chi_s(T)$ for the infinite chain is shown in Figure

2.6. The χ_s has a smooth maximum value of $\chi_{max} = 0.1469\Gamma / |J|$ at $T_{max} / |J| = 0.641$ where $\Gamma = \mu_0 N g^2 \mu_B / k_B$ [12] and in the most of the theoretical papers $\Gamma = 1$. Below the maximum, χ_s decreases with decreasing temperature down to low temperatures to approach a finite non-zero value at zero Kelvin $\chi(T \to 0) = \Gamma / \pi^2 |J|$.

The temperature dependence of the spin susceptibility of the S = 1/2 Heisenberg AFM chain at low temperatures (J < 0.25J) were calculated more accurately by Eggert, Affleck and Takahasi (EAT-model) [14]. As shown in Figure 2.6, the spin susceptibility of this model at low temperatures is larger than that of the Bonner-Fisher model.

For both models, the spin susceptibility at high temperatures (T > 0.3J) can be approximated numerically using the following relation [99] with $x = |J| / T$:

$$\chi(T) = \frac{\Gamma}{T} \frac{0.25 + 0.74975x + 0.075235x^2}{1.0 + 0.9931x + 0.172135x^2 + 0.757825x^3} \tag{2.13}$$

The AFM exchange constant J for a spin chain can be obtained independently from χ_{max} or by fitting the behavior of the spin susceptibility using equation 2.13.

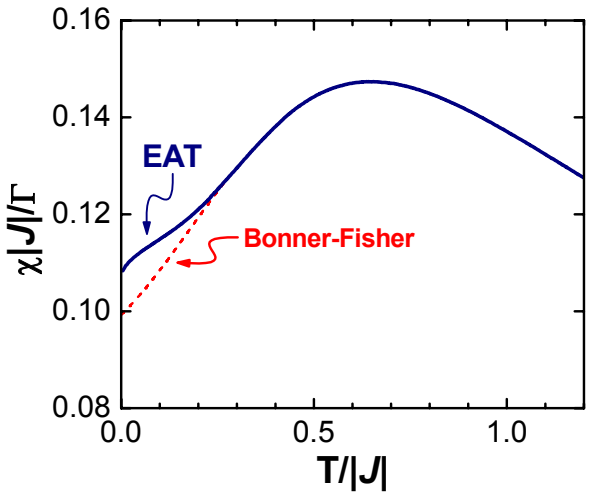

Figure 2.6: Temperature dependence of the spin susceptibility for S = 1/2 antiferromagnetic spin chain obtained by the Bonner-Fisher model [13] and EAT model (Eggert, Affleck and Takahashi) [14].

2.4.2 S = 1/2 Heisenberg AFM on square lattice

The spin susceptibility at high temperature for 2-D spin-1/2 Heisenberg AFM on square lattice[I] was calculated using Monte Carlo simulation [100,101]. Simulation were done on linear size of 128 × 128 lattice, in the temperature range from $T = 2.0J$ to $T = 0.25J$. The data of the uniform susceptibility are presented in Figure 2.7. The susceptibility saturates around $T \approx |J|$ then decreases with decreasing temperature down to $T = 0.25J$.

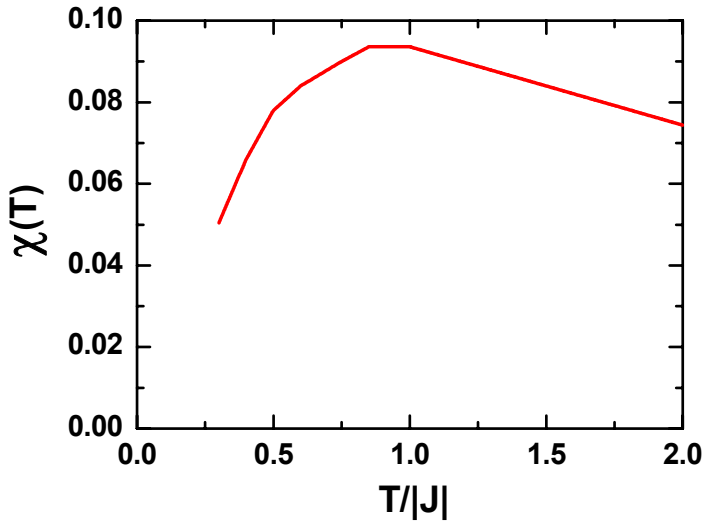

Figure 2.7: Temperature dependence of the spin susceptibility for S = 1/2 Heisenberg AFM on square lattice model [100,101].

2.4.3 Quasi low-dimensional antiferromagnets

Strictly one dimensional (1-D) and two-dimensional (2-D) antiferromagnetic Heisenberg systems cannot display long-range order (LRO) except at zero temperature [102]. In real materials, weak interchain or interlayer couplings J' lead to a finite Néel temperature T_N. The Néel temperature of quasi 1-D and quasi 2-D antiferromagnetic Heisenberg systems on cubic lattice as a function of interchain (interlayer) to intrachain (intralayer) coupling J'/J was calculated by Yasuda *et al* [16] using Monte Carlo simulations. The Hamiltonian of the quasi 1-D and quasi 2-D antiferromagnetic Heisenberg systems is defined on an anisotropic simple cubic lattice:

$$\hat{H} = \sum_{i,j,k} (J_x \vec{S}_{i,j,k} \bullet \vec{S}_{i+1,j,k} + J_y \vec{S}_{i,j,k} \bullet \vec{S}_{i,j+1,k} + J_z \vec{S}_{i,j,k} \bullet \vec{S}_{i,j,k+1}) \qquad (2.14)$$

[I] The Hamiltonian of this model is similar to the Hamiltonian given in equation 2.12.

where the summation $\sum_{i,j,k}$ runs over all the lattice sites on an $L_x \times L_y \times L_z$ cubic lattice and $\vec{S}_{i,j,k}$ is the spin operator at site (i, j, k). $J_x = J_y = J'$ and $J_z = J$ for the quasi 1-D system and $J_x = J_y = J$ and $J_z = J'$ for the quasi 2-D system with $J > 0$ and $0 \le J' \le J$.

For the $S = 1/2$ quasi 1-D system, the derived formula for $J'(T_N)$ is [16]:

$$J' = T_N \Big/ \left[4c \sqrt{\ln\left(\frac{\lambda J}{T_N}\right) + \frac{1}{2}\ln\ln\left(\frac{\lambda J}{T_N}\right)} \right] \tag{2.15}$$

where $c = 0.233$ and $\lambda = 2.6$. The formula 2.15 can be used to analyze experimental results of J'/J down to $J'/J \cong 10^{-2}$. For the quasi 2-D system, the derived formula for $J'(T_N)$ is:

$$T_N = 4\pi\rho_s \Big/ \left[b - \ln\left(J'/J\right) \right] \tag{2.16}$$

with $\rho_s/J = 0.183$ and $b = 2.43$ for $S = 1/2$, and $\rho_s/J = 0.68$ and $b = 3.12$ for S = 1. This expression describes T_N in the range $0.001 \le J'/J \le 1$. The obtained T_N dependence of $T_N/JS(S+1)$ for the quasi 1-D systems (Q1D), and the quasi 2-D systems (Q2D) estimated from the expressions 2.15 and 2.16 is shown in Figure 2.8. It is clear that T_N increases with increasing J', and this explains why the T_N is higher in the Q2D systems than in the Q1D systems due to increasing the interchain or interlayer couplings with increasing the dimensionality.

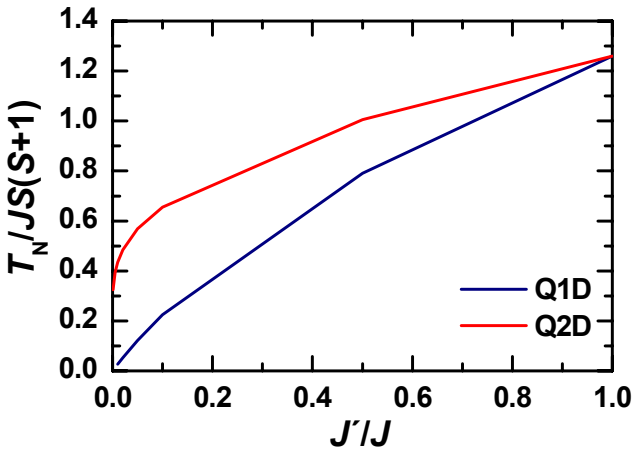

Figure 2.8: J' dependence of $T_N/JS(S+1)$ for the quasi 1-D systems (Q1D), and the quasi 2-D systems (Q2D). The data is taken from the Ref. [16].

2.4.4 Spin-Peierls transition

Spin-Peierls (SP) transition is a magneto-elastic transition that occurs in a regular $S = 1/2$ Heisenberg antiferromagnetic chain at a critical temperature $T = T_{SP}$ when the magnetic free energy decrease due to the formation of singlet spin pairs outweighs the increase in the lattice free energy occurring as a result of the dimerization of the regular array.

In TMTTF salts this transition is depicted in Figure 2.9. At high temperatures ($T > T_{SP}$) the spins are arranged in a regular chain of dimers with one spin per dimer (Figure 2.9.a). Below the SP transition the spin chain forms singlet pairs (due to the teramerization of the molecular chain (dimerization of the dimers)) by alternating the spacing between the spins forming two different AFM exchange constants J_1 and J_2 (Figure 2.9.b). Here J_1 and J_2 are the intradimer and interdimer exchange constant, respectively, and $|J_1| > |J_2|$.

This transition can be detected by measuring the temperature dependence of the spin susceptibility where below T_{SP} the spin susceptibility decreases exponentially and approaches zero as $T \rightarrow 0$.

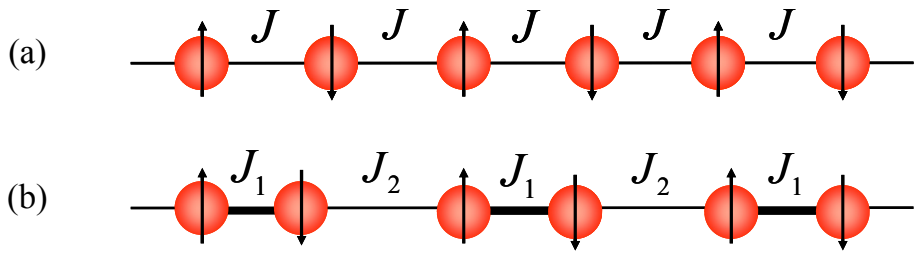

Figure 2.9: The equidistant AFM Heisenberg spin chain with a uniform coupling constant J (a), and the distorted chain below T_{SP} with two different AFM exchange constant J_1 and J_2 (b).

2.5 Charge Ordering (CO) in Fabre Salts

Charge order (CO) is a self organization of the charge carriers in a distinct pattern. It is one of several phase transitions (ground states) observed in charge-transfer salts at low temperatures. CO is a typical consequence of such strong correlation, namely, large electron-electron Coulomb repulsion compared to the kinetic energy, especially due to the long-range nature of this Coulomb force.

In TMTTF salts, the effect of the Coulomb repulsion is studied theoretically by introducing the intersite Coulomb repulsion V. This is done by the 1-D dimerized extended Hubbard model for a quarter filled system (two electrons per four sites as schematically shown in Figure 2.10) [103]:

$$\hat{H} = -t_1 \sum_{i,\sigma} \left(c^{\dagger}_{2i,\sigma} c^{\dagger}_{2i+1,\sigma} + h.c. \right) - t_2 \sum_{i,\sigma} \left(c^{\dagger}_{2i-1,\sigma} c_{2i,\sigma} + h.c. \right) + U \sum_{i=1} n_{i,\uparrow} n_{i,\downarrow} + V \sum_{i=1} n_i n_{i+1} \qquad (2.17)$$

Using the Hamiltonian and the "mean field approximation", the charge ordering in TMTTF was predicted theoretically [103]. These calculations were carried out at T = 0 and fixed electron density at quarter filling. It is assumed that $t_1 \geq t_2$, so that each pair of molecules forms dimer.

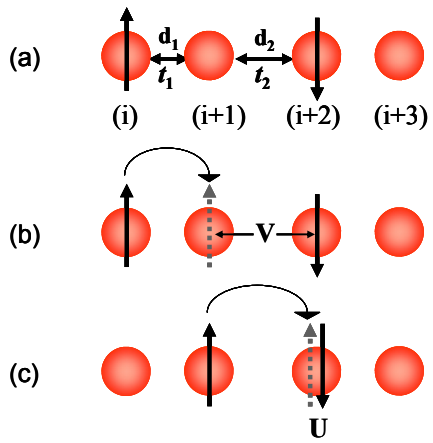

Figure 2.10: Schematic view of the quarter-filled dimerized one-dimensional antiferromagnetic spin chain (a), the sites 1 and 2 form one dimer; t_1 and t_2 are the intradimer and interdimer transfer integral, respectively. The intersite (V) and the onsite (U) Coulomb interactions are represented in (b) and (c), respectively.

In this model, two limiting cases were considered:

1. When V is small (i.e. $t_1 >> V$), the electron will be able to move within the dimer. This means the spin moment in each site $S_z(i)$ will be the same ($S_z(1) = S_z(2) = -S_z(3) = -S_z(4)$), and also the charge is equally distributed between the sites (each TMTTF molecule has 0.5e charge) as depicted in Figure 2.11.a.

2. At critical value of V ($V = V_c$) and for a fixed value of the reduced onsite repulsion ($U/t_2 = 5$), it was shown that a phase transition occurs between two different types of the spin distributions and charge disproportionation δ accompanies this transition. As shown in Figure 2.12, above the critical Coulomb repulsion value (V_c) the charge disproportionation δ grows and the absolute magnitudes of the spin moments on the two molecules within the dimer are different. This means some molecules will have a charge of 0.5 + δ (rich charge sites) and other molecules 0.5 - δ (poor charge sites) (see Figure 2.11.b).

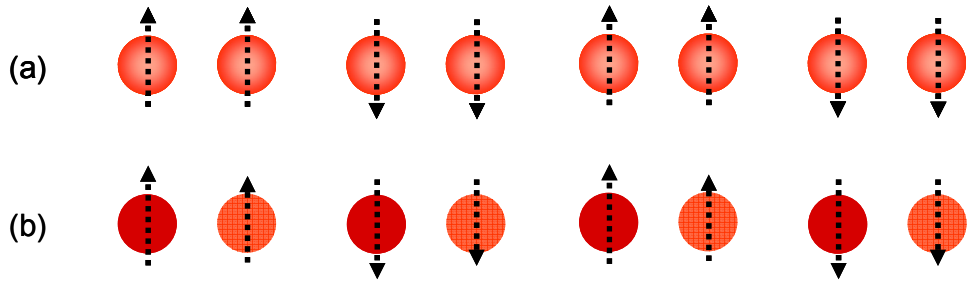

Figure 2.11: (a) Schematic view of the quarter-filled dimerized one dimensional antiferromagnetic spin chain if the intersite Coulomb interaction is zero ($V = 0$). (b) Schematic presentation of the 1010 (rich poor rich poor) type charge ordering for $V > V_c$ and $U/t_2 = 5$, the length of the arrow represents the spin density on the site and the darkness of the circle represent the charge density where the charge of the dark red sites is 0.5 + δ and the light blue ones is 0.5 - δ.

This theoretical model was developed by Seo and Fukuyama [103]. It successfully described the experimental results of TMTTF compounds, where the theoretical calculations is employed on TMTTF salts with onsite interaction $U \approx 1$ eV and $t_2 \approx 0.2$ eV, thus the reduced onsite interaction $U/t_2 \approx 5$. Moreover, it is important to note that the value of V_c where the phase transition occurs gets larger when the degree of dimerization t_1/t_2 increases.

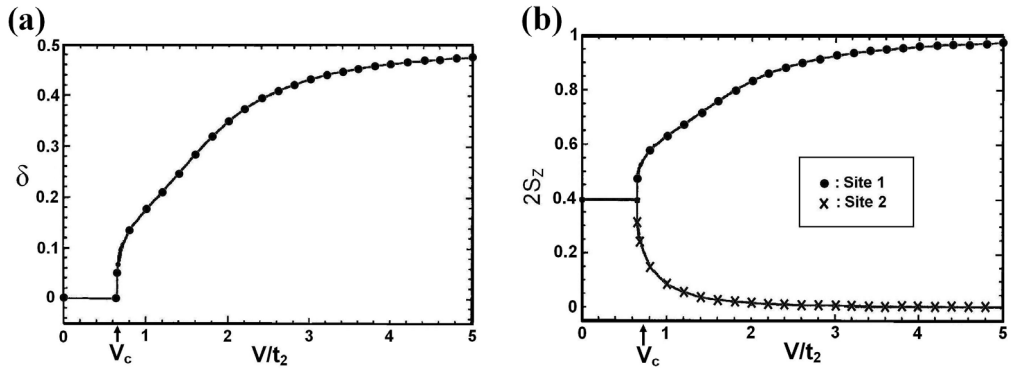

Figure 2.12: The charge disproportionation δ (a) and the absolute magnitude of the spin moment per molecule S_z (b) as a functions of the reduced intersite Coulomb interaction (V/t_2) for a fixed value of the reduced onsite Coulomb repulsion ($U/t_2 = 5$) and for $t_1/t_2 = 1.1$. From Ref. [103].

2.6 Anion Ordering (AO) Transition

TMTSF and TMTTF salts with non-centrosymmetrical anions undergo a structural phase transition at low temperature. This transition is correlated with the non-centrosymmetrical anions in these salts. The methyl groups of the organic TMT*C*F molecules delimit centrosymmetrical cavities where the anions are located. The average position of the anions is on the inversion centers at least at room temperature (RT). At RT, compounds with non-centrosymmetrical anions such as ReO_4, ClO_4, BF_4, SCN and NO_3 have orientational disorder, where they have two (or more) equivalent orientations corresponding to short and long contacts between the Se or S atoms of the TMTSF or TMTTF molecule, respectively as shown in Figure 2.13.a for a tetrahedral anion. This orientational disorder of the anions at RT is a unique property of the TMT*C*F salts because of the weak anion-donor interactions. Due to this weak interaction, the anion experiences a local potential from its surrounding. This local potential is composed from two symmetrical potential wells. Therefore, at RT the orientation of the tetrahedral anion is confined between one of two orientations, labelled I and II in Figure 2.13.a. The anion will be able to change its orientation if it can overcome the barrier potential V_o (i.e. $T >> V_o$) as depicted in Figure 2.13.b. Upon cooling, the kinetic energy associated to individual reorientations ($k_B T_{AO}$) gets much less than V_o and this will induce the anion ordering (AO) transition. Therefore, the orientational ordering of the anions generally occurs at low temperature [104,105]. This ordering is achieved by the formation of superstructures through a structural phase transition (anion ordering transition).

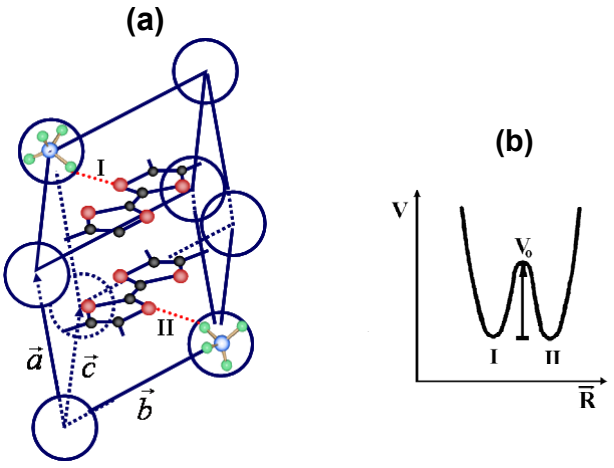

Figure 2.13: Two possible orientations of a tetrahedral anion in TMTTF salt (a), and schematical representation of the potential experienced by such an anion from its surrounding (b). I and II denotes the two inversion symmetry related orientations of the anion. From Ref. [29].

The superstructure achieved by the AO transition is characterized by the anion ordering critical wave vector q_{AO} and is stabilized below the anion ordering transition temperature T_{AO} [29]. In $(TMTTF)_2ReO_4$, the AO transition is a first order phase transition with q_{AO} = (1/2,1/2,1/2) and $T_{AO} \approx 157$ K [27,44].
Structural studies have shown that anion ordering transition is accompanied by a shift (~0.1 Å) of the anion from the center of the cavity delimited by the organic molecules. In the case of (1/2,1/2,1/2) AO wave vector superstructure, a sizable tetramerization (molecular displacements of about 0.1 Å) of the organic stacks accompanies the anion ordering [29]. This means that the crystals are perturbed along the stacking direction. In addition, an elastic deformation of the $P\bar{1}$ symmetry of the triclinic lattice and variations of the lattice parameters occurs below this transition [106].
The AO transition affects strongly the electronic structure, and pronounced influences on the electronic and magnetic properties can be observed. For example, in the AO with (1/2,1/2,1/2) AO wave vector (as in ReO_4, BF_4 and ClO_4), the stacks are tetramerized (dimerization of the dimers) and this leads to considerable deformation of the organic stacks with $d_1 \sim 3.45$ Å, $d_2' \sim 3.60$ Å and $d_2'' \sim 3.48$ Å [27] as shown in Figures 2.14 and 2.15. The tetramerization of the donor stacks leads to an exponential decrease of the spin susceptibility below T_{AO} because each two TMTTF dimers with spin 1/2 will be coupled and system will go into non-magnetic $S = 0$ ground state. Consequently, a singlet triplet energy gap Δ_σ opens. Moreover, displacement of the anion can induce redistribution of charge density on the TMTTF molecules due to Coulomb interaction between the anion and the charge on the TMTTF molecules which produce a significant charge pattern along the stacks [3].

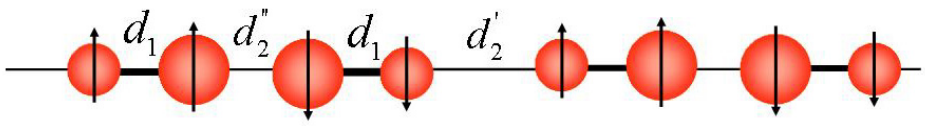

Figure 2.14: Schematic representation of one-dimensional spin chain at the (1/2,1/2,1/2) anion ordering. d_1, d_2' and d_2'' are the distances between the TMTTF molecules along the stacking direction. The short and long arrow represents one spin per dimer. The large circles mean that they have much larger charge density than the small ones.

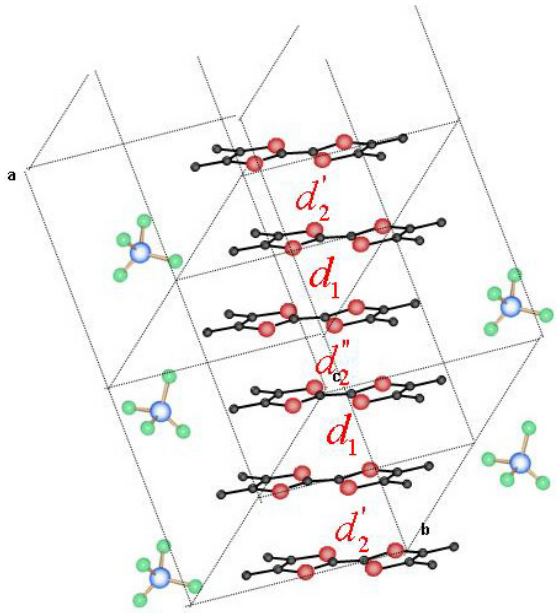

Figure 2.15: 3D view of the crystal structure of $(TMTTF)_2ReO_4$ at the (1/2,1/2,1/2) anion ordering. d_1, d_2' and d_2'' are the distances between the TMTTF molecules along the stacking direction.

Chapter 3

Experimental Techniques

This chapter presents an overview of the experimental techniques which were used to investigate the electronic and magnetic properties of low-dimensional organic conductors (within the scope of this thesis). Electron spin resonance (ESR) at standard and high fields is the main technique used in this work, so this chapter starts out with an introduction to ESR and the spectrometers that were used. Later on, a short description of the dc-measurements and static susceptibility measurements will be given.

3.1 Electron Spin Resonance

Electron spin resonance is a branch of spectroscopy which deals with the interaction of electromagnetic radiation with the intrinsic magnetic moment of electrons arising from their spins. The electromagnetic radiation is absorbed by the magnetic moment of unpaired electrons in the molecules, ions, or atoms.
ESR spectroscopy has been proven to be a very convenient contactless technique in studying the magnetic properties from the microscopic point of view. Abundant literature on the underlying principles of this method can be found for example in the references [107-108]. Therefore the following sections concentrate on the main topics which are necessary for this work.

3.1.1 Fundamentals

The phenomenon of electron spin resonance can be explained by considering the behavior of free electron. The spin $\vec{S}$ of the charged electron results in a magnetic moment

$$\vec{\mu} = -\frac{g\mu_B}{\hbar}\vec{S} \tag{3.1}$$

where g is the electronic g-value[I], μ_B is the Bohr magneton[II], and $\hbar$ is the Planck constant h divided by 2π. In the absence of an external magnetic field the two possible spin states with spin quantum numbers $m_s = +1/2$ and $m_s = -1/2$ will have the same energy and are equally populated. If an external magnetic field $\vec{H}_0 = H_0 \cdot \vec{e}_z$ is applied the degeneracy of the spin states is lifted, the so-called Zeeman splitting (Figure 3.1). The energy difference between the two states becomes $\Delta E = E_{+1/2} - E_{-1/2} = g\mu_B H_0$.

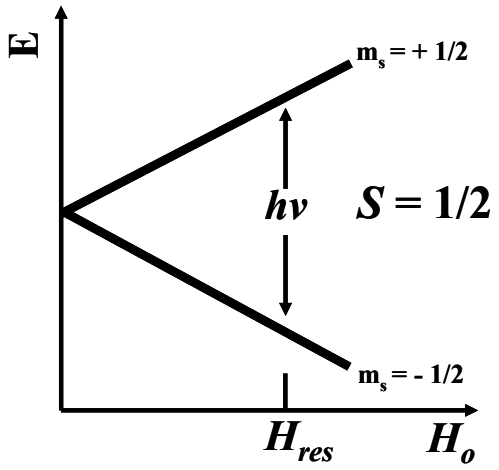

Figure 3.1: Energy level splitting of the free electron spin levels in an external static magnetic field H_0.

If an oscillating magnetic field $\vec{H}_1$ of a frequency v is applied perpendicular to the static external magnetic field H_0, transitions between the energy levels are induced when the energy of the oscillating magnetic field matches the energy difference between the two states. This is described in equation 3.2.

$$hv = \Delta E = g\mu_B H_0 \tag{3.2}$$

When equation 3.2 is fulfilled in any ESR experiment, an ESR absorption signal can be detected. In thermal equilibrium the spin populations in the energy levels exhibit slight population differences due to the Boltzmann law. The population ratio of these states can be expressed using the following equation:

[I] $g = g_e = 2.002319$ for a free electron.

[II] $\mu_B = -\frac{e\hbar}{2m} = 9.2741 \times 10^{-24}$ J/T

$$\frac{N_{+1/2}}{N_{-1/2}} = e^{-\Delta E/k_B T} = e^{-g\mu_B H_0/k_B T} \tag{3.3}$$

where k_B is the Boltzmann constant and T is the absolute temperature. Since ESR probes the net absorption that results from the transitions between the energy levels, and depends on their population ratio, the sensitivity of the ESR signal can be tuned by controlling the population difference between the energy states. Equation 3.3 shows that ESR sensitivity rises with decreasing temperature T and with increasing magnetic field H_0. Because the magnetic field is proportional to microwave frequency, different frequency bands are used in ESR spectrometers in order to increase sensitivity of ESR signal. Table 3.1 summarizes some of the typical frequency bands in ESR spectroscopy for $g = g_e$ designations.

Band	Frequency (GHz)	Magnetic field (T)
X	9.5	0.34
K	24	0.86
Q	35	1.25
W	95	3.4

Table 3.1: Summary of some of the typical frequency bands in ESR spectroscopy for $g = g_e$ designations.

3.1.2 ESR Spectrometer

The X-Band and W-Band ESR measurements presented in this work were performed in the ESR labs at the 1. Physikalisches Institut and 2. Physikalisches Institut of the Universität Stuttgart. The Q-Band ESR measurements were done at the Lehrstuhl für Experimentalphysik V of the Universität Augsburg. Three different commercial continuous wave (cw) ESR spectrometers were used for all measurements:

- Continuous wave (cw) X-Band (9.5 GHz) spectrometer (Bruker ESP 300) with a rectangular TE_{102} cavity mode. The microwave source of this setup is a Gunn diode with a maximum power output 200 mW. The magnetic field strength can be swept from 50 to 13000 Oe by an electromagnet. More details about the setup can be found in Ref. [2].

- Continuous wave (cw) Q-Band (34 GHz) spectrometer (Bruker Elexsys 500) with a cylindrical cavity. The microwave source of this system works with an ultra-low noise dual Gunn diode which has a maximum microwave power output at 34 GHz of 80 mW. The electromagnet allows sweeping the magnetic field from -60 Oe to 2 T [109,110].

- Continuous wave (cw) W-Band (95 GHz) spectrometer (Bruker Elexsys 680). Figure 3.2 shows the general layout of this spectrometer. The microwave source is a superheterodyne design with an intermediary frequency (I.F.) of ≈ 9.5 GHz (X-Band frequency) produced by a Gunn oscillator. In the I.F. bridge the microwave power is passed through an attenuator to the converter unit. The converter unit converts the 9.5 GHz to 95 GHz by an additional local oscillator and mixers that are physically separated from the microwave bridge. This allows to place the microwave closer to the probehead and thereby to reduce losses in the waveguides. In the I.F. bridge two detectors are installed and the I.F. signal is superimposed to a reference signal derived from the Gunn oscillator. This converting process gives a maximum microwave power output ~5 mW. The absorption of the microwaves by the sample can be detected as a decrease in the d.c. current produced by the detector diode which employed inside the microwave bridge. The microwave bridge is also equipped with a *lock-in* amplifier which eliminates the noise of the modulated signal[I], thus enhancing the signal-to-noise ratio. The sample is placed in a cylindrical resonator which is driven in TE_{011} mode.

  The magnetic field produced by a superconducting magnet allows fields up to 6 T controlled by the field controller. The magnetic field is achieved by using a superconducting coil (in order to avoid the high energy consumption and heat dissipation) which is split into two halves in a "Helmholtz-like" arrangement, resulting in easy access to the region of highest field and best homogeneity. The magnet is put into persistent field mode via a superconducting short circuit to avoid unnecessary boil-off of the cryogen (liquid helium) resulting from the dissipation in the connection to an external power supply. The magnet can be swept by the facility of the "heater switch" which connects the superconducting coil to an external power supply. This is done by heating the superconducting short over its critical temperature. In most of the experiments, only small variations of the static magnetic field are required. Therefore, the

[I] The detected signal is modulated by the modulation of the magnetic field, consequently the detected signal appears as a first derivative of the absorption signal.

superconducting coil is complemented by a pair of resistive auxiliary coils that superimpose an additional magnetic field of -40…+40 mT. Using these coils greatly reduces the liquid helium consumption of the system and allows for significantly faster sweeps. However, the superconducting coils tend to lose some current due to relaxation of the flux lattice[I] [86] leading to a difference between the actual magnetic field and the measured ones. Therefore, throughout this work, the magnetic field is calibrated by comparing the ESR signal with that one of DPPH[II]. The magnetic field is oriented horizontally, so that the probehead allows turning samples about the vertical axis. This gives the possibility to measure ESR spectra as a function of the sample orientation with respect to the magnetic field. The computer is used for coordinating the units required for acquiring a spectrum. Finally it should be noted that the W-band spectrometer is also equipped for pulsed ESR measurements.

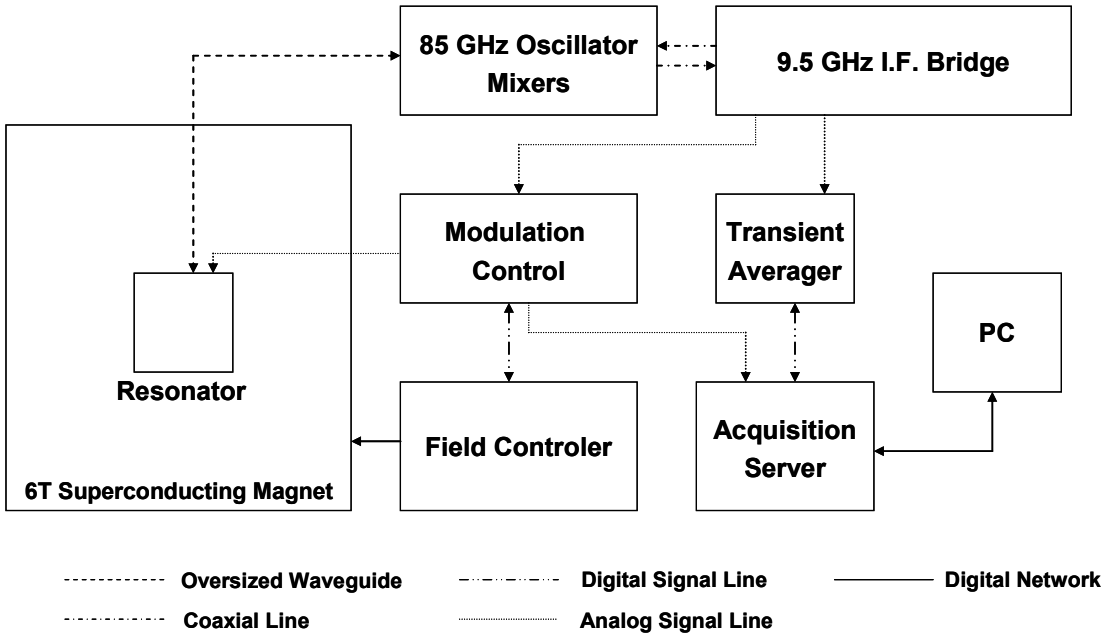

Figure 3.2: Simplified block diagram of the ESR Bruker Elexsys 680 95 GHz spectrometer.

[I] Above the lower critical field of a type II superconductors vortices penetrate the system forming a vortex/flux lattice.
[II] DPPH stands for 1,1-Diphenyl-2-Picryl-Hydrazyl.

All spectrometers were equipped with an Oxford continuous helium flow cryostat which allows temperature variations between 4.2 K and 320 K for temperature dependent measurements:

- In the X-band spectrometer an Oxford ESR 900 cryostat is used (see Figure 3.3). The advantages of this cryostat are that it has satisfactory stability ($\Delta T \approx \pm$ 0.1 K) and also one can do very sensitive measurements of the spin susceptibility. The temperature sensor was fixed very close to the sample, thus good accuracy of temperature measurements (about 0.3 %)[I] is obtained during the measurements. The temperatures were collected from the LakeShore 340 temperature controller.

- In the Q-band and W-band spectrometers, an Oxford CF935 cryostat is used. The main feature of this cryostat is the high stability of the temperature which reaches to $\Delta T \approx$ 0.01 K. The temperatures were recorded by Oxford a temperature controller.

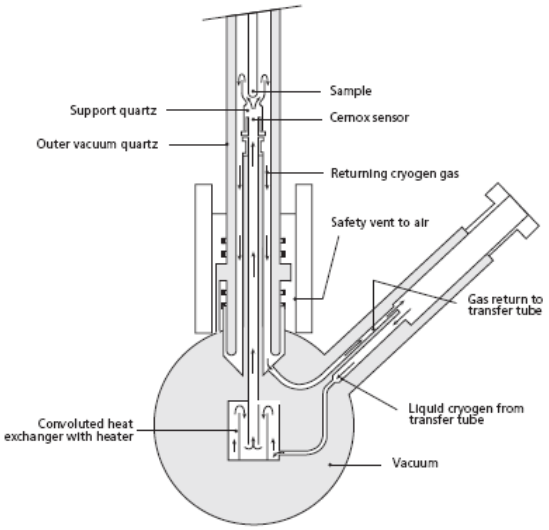

Figure 3.3: Oxford ESR 900 cryostat for X-band ESR spectrometer. A heat exchanger located in the base of the cryostat is used to regulate the cryogen temperature. A controlled flow of temperature stabilized cryogen from the heat exchanger exits a capillary within the sample support quartz that is immediately below the sample position. A Cernox sensor located at the capillary exit is used for accurate temperature measurement. The liquid/gas flows directly over the sample before exhausting back down the inside of the vacuum insulated quartz tube.

[I] This was checked by measuring the spin density wave (SDW) transition temperature for a $(TMTSF)_2PF_6$ sample (T_{SDW} = 12 K).

The dimension of the resonator is inverse proportionate with the frequency band used. This means the dimension of the resonator decreases with going to high frequency bands, thus decreasing the effective sample volume inside the resonator. Therefore, the sample is mounted inside the resonator using different sizes of quartz tube: In X-Band measurements the single crystals were glued to a 4 mm quartz tube by vacuum grease (for BEDT-TTF salts) or paraffin (for the $(TMTTF)_2X$ salts) in order to ensure good thermal contact, then covered by 5 mm quartz tube to avoid soiling the cavity. In Q-Band and W-Band measurements the single crystals from $(TMTTF)_2X$ salts were mounted inside the cavity using 0.9 and 0.4 mm fibre quartz and covered by 1.2 and 0.5 mm quartz tube, respectively (see Figure 3.4). The samples were oriented along their *a*, *b´*, or c^* axis by using a goniometer. In order to perform orientation dependent measurements along all three crystal planes, the samples were fixed to the quartz tube in different ways as shown in Figure 3.5.

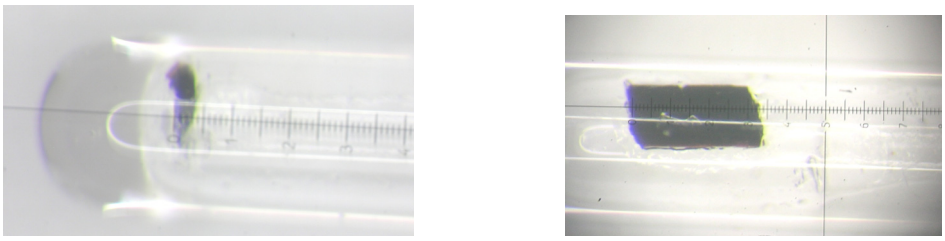

Figure 3.4: Mounting the single crystals from $(TMTTF)_2X$ salts inside the Q- and W-band quartz tube in two different orientations.

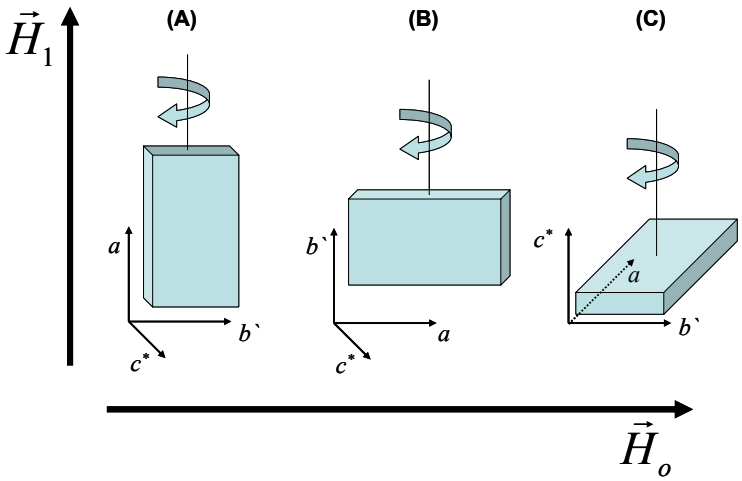

Figure 3.5: Orientation of the single crystal in static magnetic field $\vec{H}_0$ and the microwave magnetic field $\vec{H}_1$. The principle magnetic axes of the $(TMTTF)_2X$ single crystal are shown in (A). The single crystal can be rotated in *b´-c plane (A), *a-c** plane (B) and *a-b´* plane (C).**

In the W-band ESR measurements, the size of the crystal is one of the main problems encountered in this part of work. The size of the crystal is very important to get an accurate value for the ESR linewidth. Due to the volume of the W-band resonator, the spatial distribution of the magnetic field inside the resonator is confined to a very small region. Therefore, for a large sample, inhomogeneous broadening for the linewidth can be observed due to the inhomogeneous magnetic field through the sample. For this reason the measurements is repeated many times on many different sample size in order to avoid this effect as much as possible. Moreover, the coupling of the microwave to the resonator is strongly influenced by the sample size as well as the orientation of the crystal with respect to the magnetic field inside the cavity. Since the sample changes the impedance of the resonator, increasing the sample size or changing its orientation inside the resonator will change the resonance mode of the resonator as well as the coupling state. Therefore, critically coupling was achieved after each run in order to optimise the signal to noise ratio. As a consequence, each experiment took more than the usual time in X- or Q-band spectrometers.

3.1.3 Spectroscopic aspects

In electron spin resonance the signal of the absorption of the microwave power gives valuable information about the studied system. For example, in organic conductors the ESR signal yields information about the electron localization, dimensionality, and the electron spin interactions with the lattice or other spins. Practically, the ESR signal is detected as the first derivative with respect to the magnetic field dP_{abs}/dH. By integration of the signal the absorbed microwave power P_{abs} is obtained. Four main characteristics can be deduced from the ESR signal:

- The lineshape, which can be Lorentzian, Gaussian or Dysonian. In the later case, from the asymmetry of the lineshape the microwave conductivity σ_{ac} can be obtained.
- The resonance field H_{res}, and directly by the relation $g = h\nu/\mu_B H_{res}$ the g-factor.
- The linewidth ΔH.
- Intensity I which is proportional to the spin susceptibility χ_s.

3.1.3.1 The lineshape

The ESR lineshape contains useful information about the nature of the exchange interaction in the investigated systems. For example, most of organic conductors have a symmetric Lorentzian shape (Figure 3.6). This is due to the strong exchange narrowing in these materials.

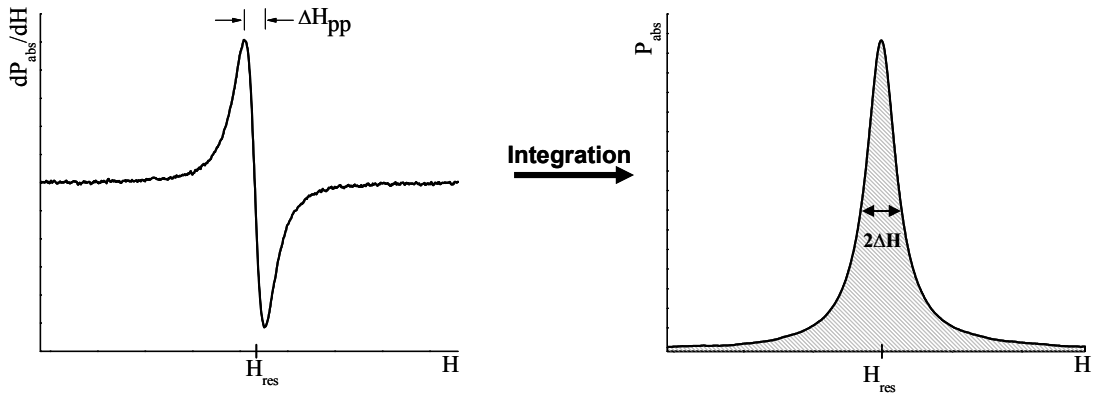

Figure 3.6: The first derivative of the absorbed microwave power dP_{abs}/dH (left) as measured by ESR spectrometer and through the integration the absorbed microwave power P_{abs} (right) is obtained as a function of the static magnetic field H. For a Lorentzian line the relation between half width half maximum line (HWHM) ΔH and the peak to peak linewidth (ΔH_{pp}) is $\Delta H = \sqrt{3}\Delta H_{pp}/2$.

When an ESR experiment is performed on a metallic or highly conducting big sample, it can be observed that the detected ESR signal has an asymmetric lineshape, known as Dysonian line. This lineshape was predicted theoretically by Dyson [111], and was demonstrated experimentally by Feher and Kip in metals [112]. The physical reason for this Dysonian lineshape is due to the skin effect resulting from the screening of the incident microwave field by the conduction electrons. As consequence the microwave field penetrates only into a certain depth inside the conductive sample called the skin depth (δ)

$$\delta = \sqrt{\rho/(\pi\mu_0\nu)} \tag{3.4}$$

Here ρ is the electrical resistivity of the material, μ_0 the permeability of the free space[I] and ν stands for the frequency of the microwave.

[I] $\mu_0 = 4\pi\times10^{-7}$ (Henries/m).

The Dysonian lineshape is a combination of the absorption and dispersion components of a symmetric Lorentzian lineshape as shown in Figure 3.7. Therefore, the absorption and dispersion is included into the fitting formula for the ESR signal, which is given by:

$$P_{abs}(H) \propto \frac{\Delta H + \alpha(H - H_{res})}{(H - H_{res})^2 + \Delta H^2} \tag{3.5}$$

where α denotes the dispersion-to-absorption ratio, which is called asymmetry factor and it has the values $0 \le \alpha \le 1$. When the dispersion term vanishes $(\alpha = 0)$, equation 3.5 reduces to the Lorentzian lineshape.

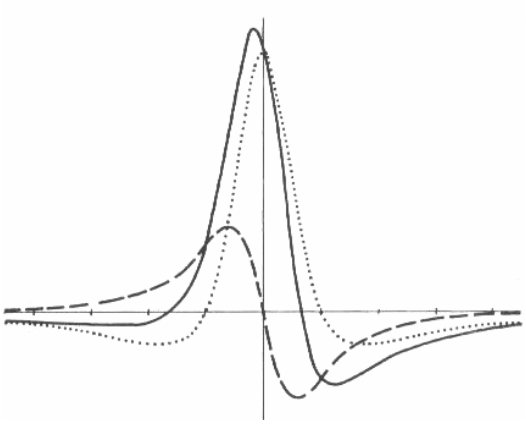

Figure 3.7: Superposition of the derivative of a Lorentzian absorption curve (dashed) and a dispersion curve (dotted) to give a typical Dysonian lineshape (solid).

The microwave conductivity of highly conductive samples can be extracted from the Dysonian lineshape. The Dysonian absorption (W) is described as a linear combination of the absorption (χ'') and dispersion (χ') of the sample as follows [113]:

$$W = \beta(\chi' + \alpha\chi'') \tag{3.6}$$

where β is a constant and α is an asymmetric factor defined in equation 3.5. α and β can be determined experimentally from the Dysonian lineshape analysis. For a flat plate sample of thickness $2t$ the microwave conductivity is extracted according to the equation [113,114]:

$$\sigma = \frac{c^2}{2\pi\nu\delta^2} = \frac{c^2}{2\pi\nu\left(\frac{2t}{p}\right)^2} \tag{3.7}$$

Here c is the speed of light, δ is the skin depth and p is the ratio between the sample thickness and the skin depth $(2t/\delta)$. From the correlation between the p and the asymmetry factor α which has been derived analytically for flat plate samples [113] (see Figure 3.8) the relative microwave conductivity can be calculated by the equation

$$\frac{\sigma}{\sigma_0} = \left(\frac{p}{p_0}\right)^2 \tag{3.8}$$

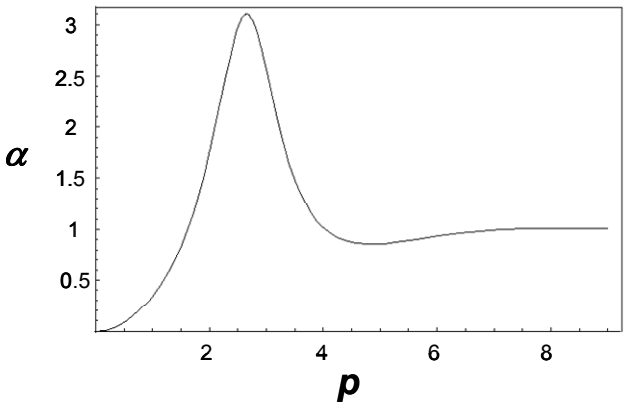

Figure 3.8: Plot of the analytical relation between the p and the asymmetry factor α for flat plate samples [113].

3.1.3.2 The *g*-factor

In most of ESR experiments, the measured g-value differs from the *g*-value for the free electron g_e = 2.002319. This is due to the fact that the local magnetic field $\vec{H}_{loc}$ arising from the orbital motion of the electrons is added to the applied magnetic field $\vec{H}$. By this the effective magnetic $\vec{H}_{eff}$ field experienced by the electrons differs from the applied one as shown in the following equation.

$$\vec{H}_{eff} = \vec{H} + \vec{H}_{loc} = \frac{g}{g_e}\vec{H} \tag{3.9}$$

The measured g-value in the ESR experiment is often called the g-factor. Therefore the shift in the g-value $\Delta g\,(g - g_e)$ is used as a probe for the electronic environment of the unpaired spins.

In single crystals with monoclinic, orthorhombic or triclinic symmetry ($a \neq b \neq c$) the *g*-factor is anisotropic, which means that its magnitude depends on the orientation of the molecule with respect to the applied magnetic field. This anisotropy guides the g-factor to be a tensor, which in its eigensystem is diagonal and described by its principal values g_x, g_y, and g_z. In this case the g-factor for the crystal in terms of *g*-tensors in spherical coordinates is given by:

$$g = \sqrt{g_x^2 \sin^2\theta\cos^2\phi + g_y^2 \sin^2\theta\sin^2\phi + g_z^2 \cos^2\theta} \tag{3.10}$$

where θ is the azimuthal angle in the xy-plane with $0 \leq \theta < 2\pi$ and ϕ is the polar angle from the z-axis with $0 \leq \phi \leq \pi$. This equation indicates that the rotation pattern for the g-factor in any specific plane will give $\cos^2\theta$ dependence. For example if the crystal is rotated in xy-plane and if the angle between the applied magnetic field and x-axis is θ, then one obtains

$$g = \sqrt{g_x^2 \cos^2\theta + g_y^2 \sin^2\theta} \tag{3.11}$$

3.1.3.3 The linewidth

The linewidth of the ESR-signal provides useful information about the relaxation rates of processes related to the molecules in the investigated sample. The relaxation rates can be realized by the fact that at the resonance the spins have a finite lifetime in the excited energy state, and at the equilibrium these spins relax back to their ground state. During the relaxation process a given spin interacts with its surrounding (neighbouring spins, lattice), which gives the relaxation processes a finite time. This leads to a finite linewidth in the ESR signal.

To quantify this finite linewidth of the ESR signal, the relaxation rates, which were proposed by Bloch [115] is considered as follows:

$$\frac{d\vec{M}_z}{dt} = -\left(\vec{M} \times \gamma_e \vec{H}\right)_z + \frac{\vec{M}_o - \vec{M}_z}{T_1} \tag{3.12}$$

and, for $i = x$ or y:

$$\frac{d\vec{M}_i}{dt} = -\left(\vec{M} \times \gamma_e \vec{H}\right)_i - \frac{\vec{M}_i}{T_2} \tag{3.13}$$

where T_1 and T_2 are the spin-lattice and the spin-spin relaxation times, respectively. γ_e is the gyromagnetic ratio[I] and $\vec{M}_o$ is the equilibrium magnetization. These equations which are well known as "Bloch equations" describe the time dependence of the magnetization components ($\vec{M}_x, \vec{M}_y$ and $\vec{M}_z$) in terms of T_1 and T_2 assuming that the static magnetic field H_0 is applied parallel to the z-axis. The total relaxation rate $1/T_2'$ determines the total linewidth of the ESR signal, which generally consists from two contributions [116]: one equal to $1/2T_1$ comes from the spin-lattice relaxation rate and the other equal to $1/T_2$ comes from the energy fluctuation (spin-spin relaxation rate).

3.1.3.4 The intensity and the spin susceptibility

One of the main advantages of the ESR technique is that the spin susceptibility χ_s^e of a conduction electron can be measured. While the magnetization techniques measure the total susceptibility of all the paramagnetic states in the sample, ESR can separate contributions from conduction electrons and localized spins from the ones of impurities if the lines are well separated.

The intensity of the ESR-line is the area under the ESR absorption signal. By integrating the first derivative of the ESR absorption signal twice (see Figure 3.4) the intensity can be obtained. For a Lorentzian absorption the intensity is given by [107]:

$$I = \frac{8\pi}{3\sqrt{3}} y'_{\max} \Delta H^2 \tag{3.14}$$

ΔH is the linewidth and $y'_{\max}$ is the maximum amplitude of the derivative of the ESR absorption signal. For a paramagnetic sample in a resonant cavity of frequency $\omega_0 = 2\pi\nu_0$ the power absorbed by the sample per unit volume is given by:

$$P_{abs} = \frac{\omega_0}{2} H_1^2 \chi''(\omega) \propto \chi''(\omega) \tag{3.15}$$

[I] $\gamma_e = \frac{g\mu_B}{\hbar}$.

where H_1 is the amplitude of the microwave magnetic field at the sample and χ'' is the imaginary part of the conduction electron spin susceptibility. From the Kramers-Kronig relation we get for the electron spin susceptibility χ_s^e [108,117]

$$\chi_s^e = \frac{2}{\pi H_{res}} \int_0^\infty \chi''(H)\,dH \propto \int_0^\infty P_{abs}(H)\,dH = I \tag{3.16}$$

which is in direct proportional to the intensity of the ESR absorption line. In this work the absolute values of the spin susceptibility measured by ESR are determined by comparing the intensity of the ESR signal with that of DPPH. Also SQUID magnetometer measurements were performed in order to obtain accurate values of the spin susceptibility at the phase transitions.

3.2 Broadening Mechanisms of the ESR Linewidth

The linewidth of a Lorentzian absorption ESR line is given by the relation [15,118]:

$$\Delta H \approx \frac{\hbar^2}{g\mu_B |J|} M_2 \tag{3.17}$$

where M_2 is the second magnetic moment and J is the anisotropic exchange coupling constant. The main factors which contribute in the broadening of the ESR absorption line are:

3.2.1 Magnetic dipolar interaction

The classical interaction energy E between two magnetic dipole moments $\vec{\mu}_1$ and $\vec{\mu}_2$ separated by a distance vector $\vec{r}$ is [98]:

$$E = \frac{\mu_0}{4\pi}\left(\frac{\vec{\mu}_1 \bullet \vec{\mu}_2}{r^3} - \frac{3(\vec{\mu}_1 \bullet \vec{r})(\vec{\mu}_2 \bullet \vec{r})}{r^5}\right) \tag{3.18}$$

The dipolar interaction between two electron spins S_1 and S_2 can be rewritten in terms of spin operators $\hat{S}_1$ and $\hat{S}_2$. It is not trivial what magnetic moment has to be associated with them. For large distances, the dipole moment is given by the moment of the electron and its environment as a whole, i.e. $\vec{\mu}_{1,2} = < \mathbf{g}_{1,2}\vec{S}_{1,2} >$. Thus, the quantum mechanical Hamiltonian of the dipolar interaction is given by:

$$\hat{H}_{dd} = \frac{\mu_0 \mu_B g_1 g_2}{4\pi} \left(\frac{\vec{S}_1 \bullet \vec{S}_2}{r^3} - \frac{3(\vec{S}_1 \bullet \vec{r})(\vec{S}_2 \bullet \vec{r})}{r^5} \right) \tag{3.19}$$

When the electrons are close to each other, they see each other "*freely*" and their *g*-values are used as g_e. However, in many cases the g-factors differ only slightly from the g_e, and $g_1 g_2$ in equation 3.19 can be replaced by g_e^2.
The contribution of the magnetic dipole-dipole interaction to the broadening of the linewidth is expressed by the equation [15]:

$$\Delta H_{d-d} \left(10^4 \text{ Oe}\right) \approx \frac{\mu_o^2 \mu_B^3 g_e^3}{4\pi |J| d^6} = 4.6381 \frac{1}{|J(K)| \left[d(\text{Å}) \right]^6} \tag{3.20}$$

where J and d are the exchange constant and the distance between the two dipoles in the chain direction, respectively. The presence of the exchange constant J in equation 3.20 yields to an exchange narrowing of the ESR spectrum. For one spin chain, the linewidth has the angular dependence $\left(3\cos^2\theta - 1\right)^{4/3}$ if the exchange energy is less than Zeeman energy and has the angular dependence $\left(1 + \cos^2\theta\right)^{2/3}$ if the exchange energy larger than Zeeman energy [119]. In two-dimensional systems the linewidth has the angular dependence $\left(3\cos^2\theta - 1\right)^2$ [120]. θ is the angle between the direction of a one one-dimensional magnetic chain and H_o for d = 1, while θ is the angle between the direction of a normal axis and H_o for d = 2.

3.2.2 Hyperfine interaction

The hyperfine interaction is the magnetic interaction between the magnetic moment of a nucleus $\vec{\mu}_n$ and the magnetic moment of an electron $\vec{\mu}_e$. The interaction is caused by the magnetic field produced by the magnetic moment of the electron and by the motion of the electron about the nucleus. The hyperfine interaction is described by the Hamiltonian [121]:

$$\hat{H}_{h.f} = \sum_{i=1}^{N} \vec{S} \bullet \mathbf{A}_i \bullet \vec{I}_i \tag{3.21}$$

where the sum is over all the magnetic nuclei. I_i is the angular momentum operator of the nucleus i, and A_i is the tensor describing the electron-nucleus magnetic interaction. Actually, equation 3.21 is the sum of three contributions, namely the contact, the dipolar and the pseudocontact term. The contact term is given by the

electron spin density on the magnetic nucleus, the dipolar interaction is given by the magnetic dipolar interaction between the electron spin and the nuclear spin, and the pseudocontact term is given by the magnetic dipolar interaction between the orbital of the electron and the nuclear spin. In ESR experiment, the contribution of the hyperfine interaction to the relaxation process is [15]:

$$\Delta H_{h.f.}\left(10^4\ \mathrm{Oe}\right) \approx \frac{A_{\parallel}^2}{g_e \mu_B |J|} = 1.71156 \times 10^9 \times \frac{\left[A_{\parallel}\left(\mathrm{MHz}\right)\right]^2}{\left|J\left(K\right)\right|} \tag{3.22}$$

$A_{\parallel}$ is the anisotropic hyperfine interaction constant of the relevant nucleus.

3.2.3 Anisotropic Zeeman interaction

The second term of equation 2.12 is called Zeeman term (see section 2.4.1), and describes the interaction of the magnetic field with each individual spin. When the *g*-value is anisotropic and two inequivalent magnetic sites exist in the material, the interaction becomes anisotropic (so-called anisotropic Zeeman (AZ) interaction). The two magnetic sites can be distinguished by their different orientations of the *g*-tensor of their spins, and the Zeeman Hamiltonian is given by [15]:

$$\hat{H}_{AZ} = \mu_B H_0 \sum_{\mu=x,y,z} g_{z\mu}^{(1)} \sum_{i\in 1} \vec{S}_i^{\mu} + \mu_B H_0 \sum_{\mu=x,y,z} g_{z\mu}^{(2)} \sum_{i\in 2} \vec{S}_i^{\mu} \tag{3.23}$$

where H_0 is the applied magnetic field, and the sums $\sum_{i\in 1}$ and $\sum_{i\in 2}$ run over all spins of kind 1 and kind 2, respectively. If the magnetic field is applied along the z-direction, equation 3.23 can be rearranged in the following way:

$$\hat{H}_{AZ} = \mu_B H_0 \sum_{\mu=x,y,z} \frac{1}{2}\left(g_{z\mu}^{(1)} + g_{z\mu}^{(2)}\right) \sum_{i\in 1,2} \vec{S}_i^{\mu} + \mu_B H_0 \sum_{\mu=x,y,z} \frac{1}{2}\left(g_{z\mu}^{(1)} - g_{z\mu}^{(2)}\right)\left(\sum_{i\in 1} \vec{S}_i^{\mu} - \sum_{i\in 2} \vec{S}_j^{\mu}\right) \tag{3.24}$$

The first term on the right-hand side gives the usual Zeeman operator, which defines the position of the resonance line. The second term contains the difference between *g*-tensors of the site one and the site two, $\Delta g_{\mu z} = 1/2(g_{z\mu}^{(1)} - g_{z\mu}^{(2)})$, and determines the Zeeman contribution to the anisotropy of the ESR linewidth (see equation 3.25).
The AZ interaction has a pronounced effect on the relaxation rate of the conduction electrons. In case of sufficient exchange narrowing and for T >> $|J|/k_B$, the contribution of the AZ interaction to the ESR linewidth is expressed by [109]:

$$\Delta H_{AZ}(\text{kOe}) \approx \frac{g\mu_B H_0^2}{|J|}\left(\frac{\Delta g}{g}\right)^2 = \frac{h^2 v^2}{g\mu_B |J|}\left(\frac{\Delta g}{g}\right)^2 \tag{3.25}$$

where J is the exchange coupling constant, v is the frequency of the microwave field and Δg is the difference between the g-tensors of the two inequivalent magnetic sites. When the exchange coupling is strong, one resonance instead two corresponds for two g-tensors will be observed. Therefore, the linewidth increases with increasing magnetic field, due to the increasing ratio between the difference $H_0^{(1)} - H_0^{(2)}$ of the resonance fields of the two kinds of spin (increasing Δg) and J [15].

3.2.4 Anisotropic exchange interaction

It is an exchange interaction between the excited state of one ion produced by spin-orbit coupling and the ground state of the other ion. The Hamiltonian of the anisotropic exchange interaction is given by the sum [15]:

$$\begin{aligned}\hat{H}_{A.E} = \sum_{i\neq j}\frac{1}{4}A_0(ij)(3\vec{S}_i^z\vec{S}_j^z - \vec{S}_i \bullet \vec{S}_j) + \sum_{i\neq j} -\frac{3}{4}A_{\pm 1}(ij)(\vec{S}_i^{\pm}\vec{S}_j^z - \vec{S}_j^{\pm}\vec{S}_i^z) \\ + \sum_{i\neq j} -\frac{3}{8}A_{\pm 2}(ij)(\vec{S}_i^{\pm}\vec{S}_j^{\pm})\end{aligned} \tag{3.26}$$

The A_t ($t = 0, \pm 1, \pm 2$) denote the geometrical parameters of the anisotropic exchange, and $\vec{S}_i$ the individual spins. The coordinate x, y, z refer to a coordinate system in which the z-direction is defined by the direction of the applied magnetic field H_o. When only nearest-neighbor interactions are considered, the contribution of the antisymmetric anisotropic exchange (AE) interaction which is also known as Dzyaloshinsky-Moriya interaction [122] to the ESR linewidth is [15]:

$$\Delta H_{A.E.}\left(10^4 \text{ Oe}\right) \approx \frac{1}{g_e\mu_B}\left(\frac{\Delta g}{g_e}\right)^2 |J| = 0.012\left(\Delta g\right)^2 \left|J\left(K\right)\right| \tag{3.27}$$

In case of symmetric anisotropic exchange interaction $\Delta H \sim (\Delta g)^4 |J(\text{K})|$ [15,122].

3.2.5 Elliot Process

In three-dimensional isotropic metals, the conduction electron spin resonance (CESR) linewidth is correlated to the spin-orbit coupling (the g-shift) Δg and to the electron scattering rate τ^{-1} by use of Elliott formula [123]

$$\Delta H \propto \frac{(\Delta g)^2}{\tau} \tag{3.28}$$

The Elliott formula describes the temperature dependence of an ESR linewidth at a fixed orientation. In quasi-one dimensional (Q-1D) metals, on-chain scattering does not cause electron relaxation and the interchain tunnelling time plays the main role in the relaxation process. Consequently, in strictly 1D system, no spin relaxation can occur. Therefore, Elliott's relation is not valid for Q-1D metals because it does not take into account the interchain tunnelling time in the relaxation process. However, Elliott formula was modified later by Weger [124] taking the deviation from the one-dimensional behaviour into account in the spin relaxation mechanism, as shown in the following equation:

$$\Delta H \propto \frac{(\Delta g)^2}{\tau_{\|}} \frac{\tau_{\|}}{\tau_{\perp}} = \frac{(\Delta g)^2}{\tau_{\perp}} \tag{3.29}$$

where $\tau_{\|}$ is the on-chain scattering time and $\tau_{\perp}$ is the interchain tunnelling time. The ratio $(\Delta g)^2 / \Delta H$ is used as a measure of the interchain coupling, which probe the dimensionality of the materials.

3.2.6 Relaxation Process in Quasi 1-D Organic Conductors

Several theoretical studies were done to explain the relaxation mechanisms of the conduction electrons of the single chain quasi 1-D organic conductors [125,126]. Spin-orbit-coupled electronic transitions between donor conduction-band states of the organic conductors (TMT*C*F)$_2$X were shown to be the main relaxation process of the conduction electrons which contribute to the broadening of the ESR linewidth [126]. These transitions were suggested to be mediated by torsional oscillations of the donor molecules around their long in-plane axis (see Figure 3.9) which are thermally activated. These transitions break the symmetry restriction which forbids spin-orbit transitions within or between the donor stacks comprised of the same, identically oriented, centrosymmetrical molecules.

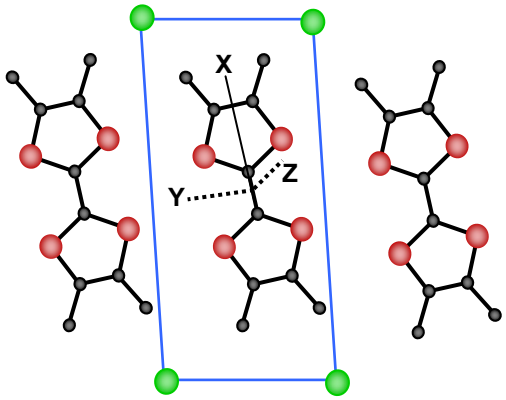

Figure 3.9: Crystal structure of the TMTTF salts showing the possible rotational axes of the TMTTF molecule, the x and y axes are parallel to the molecular plane and the z-axis is perpendicular to it. The green spheres represent the monovalent anions.

The spin-orbit interaction of the heavy chalcogen atom in the TMT*C*F molecule (S in TMTTF and Se in TMTSF) has a short-range nature. This nature limits the donor conduction-band states to couple via their valance π atomic orbitals only to the states containing the σ ones on the same chalcogen. Since these orbitals are perpendicular to each other, interstack interaction is important in the broadening mechanism of the ESR line because it leads to admixture of the chalcogen valence σ atomic orbitals into the acceptor orbitals. However, this mechanism which might produce spin-orbit scattering along the stacks comparable in magnitude to the interstack scattering is excluded by the following symmetry-based restriction [125]: Spin-orbit interactions can not cause electronic transitions within stacks of the same, identically oriented, centrosymmetrical donor molecules. This symmetry precludes the intrastack spin-orbit scattering in the (TMT*C*F) salts and this explains the observed anisotropy of the ESR linewidth. Furthermore, the anisotropy of the ESR linewidth can be understood by introducing the effective spin-orbit coupling magnetic field H_{eff}^{SO} which is given by the relation [125]:

$$H_{eff}^{SO} = \lambda l_c / \gamma_e \tag{3.30}$$

where l_c is the orbital momentum quantum number, λ is the spin-orbit coupling constant and γ_e is the electron magnetogyric ratio. H_{eff}^{SO} is anisotropic, it has the largest component along the molecular x-axis and the smallest along z-axis if the inversion symmetry is conserved (see Figure 3.9), and consequently, the relaxation rate and the ESR linewidth depend strongly on the orientation of the external magnetic field.

3.3 SQUID Magnetometer

A superconducting quantum interference device (SQUID) is considered as a very sensitive device which can explore the magnetic properties of materials. It uses the Josephson effect phenomena [127] to measure extremely small variations in the magnetic flux. Typically, a SQUID consists out of two Josephson junctions connected in parallel on a closed superconducting loop which can enclose magnetic flux only in multiples of a universal constant called the flux quantum ϕ_0 [I]. The SQUID functions as a magnetic flux-to-voltage transducer, because it converts the magnetic flux, which is hard to measure, into voltage which is easy to measure. When the sample moves inside the pickup loops, the magnetic flux change will be measured as a voltage oscillation at the two Josephson junctions, which depends on the change in the magnetic flux induced by the sample (see Figure 3.10). More details about the physical principles and the operation of SQUID magnetometer can be found in the literature (see for example [128]).

In this work a dc SQUID measurement were performed using a Quantum Design MPMS XL SQUID which allows measuring the magnetic moment of the sample at applied field of 0 to 7 tesla in the temperature range 1.8 K and 400 K.

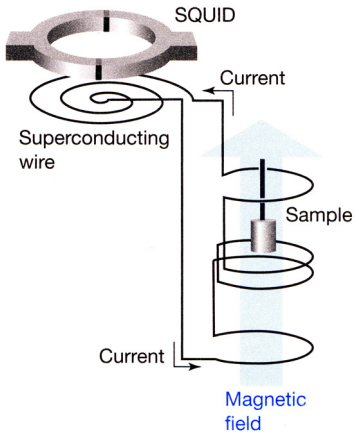

Figure 3.10: The basic structure of the SQUID magnetometer. The sample is moved upwards in small increments and the potential difference across the SQUID is measured [129].

3.4 DC Resistivity Measurements

The temperature dependence of the direct current (dc) resistivity is a good method to characterize the electronic properties of the materials. By using this method, one can determine whether the investigated material is metallic, semiconducting or

[I] $\phi_0 = h/2e = 2.0678\times10^{-15}$ tesla.m^2

insulating. In addition, the anisotropy of the electronic transport or phase transitions into ground states like superconductivity can be investigated. In this work dc resistivity measurements were performed using a conventional four point technique to eliminate the influence of the contact resistances. The contacts were made by pasting 25 μm gold wires with a small amount of carbon paint (see Figure 3.11) directly on the sample. Then the samples were mounted on a sapphire crystal[I] connected to a plug by gold wires and silver paint, and finally fixed on a sample holder.

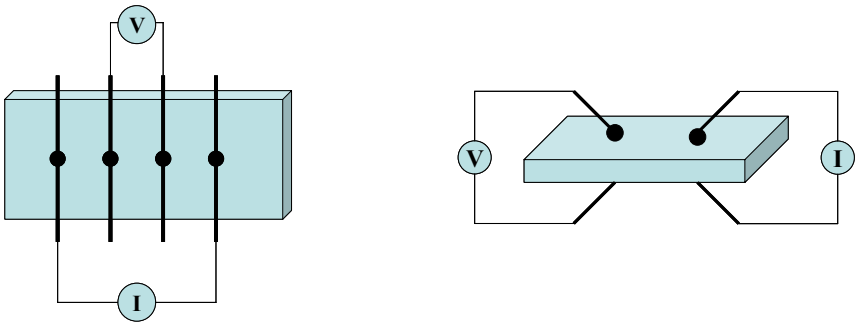

Figure 3.11: The four dc contacts along different directions of the single crystal.

For the temperature dependent measurements an exchange gas cryostat was used. Figure 3.12 shows a schematic representation of this ^{4}He cryostat. After inserting the sample holder into the sample chamber inside the cryostat, the nitrogen chamber is insulated from the surrounding and from the helium chamber by pumping the cryostat to around 6×10^{-3} mbar. For measuring down to 78 K nitrogen is sufficient for cooling. To reach 4.2 K, the helium chamber was filled with the helium and exchange gas was inserted to the sample chamber to get a better thermal coupling between the helium chamber and the sample. The samples were cooled down slowly to avoid cracks and ensure a good thermal equilibrium. The measurements are performed during the cooling and the heating of the sample within the temperature range from 300 K to 4.2 K. Temperature was stabilized by the heater at the end of the sample holder. The measurements processes are controlled by a "Labview" software program. After thermal stability of the sample is reached the computer creates step voltage signals from a regulated voltage source to the sample. Using a multimeter the current through the sample with a value of 5-10 μA and the voltage was measured. From these data and using the entered sample dimensions the computer calculates the electrical resistivity for each measured temperature point.

[I] Sapphire crystal is used because it is a good thermal conducting but insulating material.

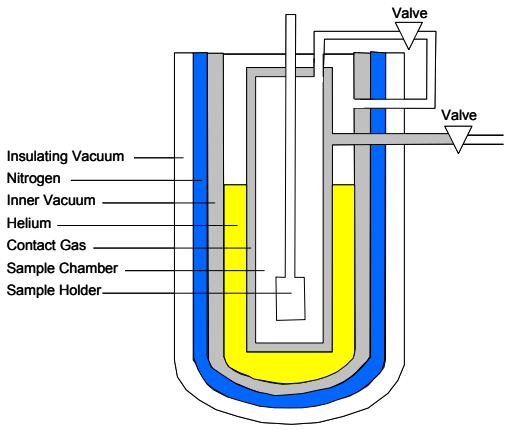

Figure 3.12: Schematic representation of the exchange gas cryostat. Adopted from [41].

Chapter 4

Spin and Charge Ordering Investigations on $(TMTTF)_2X$

The family of $(TMTTF)_2X$ salts represents a fertile ground for studying the competition between the electronic and magnetic ground states. Their rich phase diagram with unique physical properties such as spin and charge ordering are the focus of strong scientific research because many of those properties are not observed in three dimensional systems, but are exclusive of the reduced dimensionality of those structures. Electron spin resonance (ESR) spectroscopy has played a major role as a first step in investigating these salts. The high sensitivity of this method allows investigating the paramagnetic high-temperature region, probing the phase transitions and as well as the diverse ground state properties. Since standard ESR spectroscopy is a well established method to explore the magnetic properties and the charge dynamics of these salts, the observation of characteristic changes in the ESR linewidth of the TMTTF-salts with centrosymmetrical anions below the charge ordering transition temperature (T_{CO}) in previous studies [2] motivated us to perform high frequency ESR experiments in order to investigate the frequency dependence of the ESR parameters (linewidth and g-value) in this state as well as the anion ordered state, and the physics behind it.

4.1 Investigated Materials

In this work, comprehensive multi-frequency (X-, Q- and W-Band) ESR experiments were performed on single crystals of the quasi-one dimensional organic charge transfer salts $(TMTTF)_2X$ (X = ReO_4, AsF_6 and SbF_6). All the investigated crystals were grown in the crystal growth laboratory of the 1. Physikalisches Institut, Universität Stuttgart by Mrs. Gabriele Untereiner. The TMTTF molecules were synthesized in the group of Prof. H. J. Keller at the University of Heidelberg and by Prof. L. K. Montgomery from Department of Chemistry, Indiana University, USA. Samples with a typical size of $2 \times 0.5 \times 0.1$ mm^3 were used in the X-Band ESR

measurements, while very small samples with a typical size of less than $0.4 \times 0.4 \times 0.05$ mm^3 were used in the Q- and W-Band ESR measurements to avoid any sample size effect which can lead to a broadening of the linewidth [130]. The ESR spectra were collected from the three commercial ESR spectrometers introduced in section 3.1.2. The least-square method was performed for calculating the linewidth and the resonance field from the observed ESR spectra[I]. The spin susceptibility and the *g*-value were determined by comparing the intensity and the resonance field of the measured ESR signal with that of DPPH[II].

4.2 X-Band ESR investigation of $(TMTTF)_2ReO_4$

The title compound undergoes an anion order (AO) transition at $T_{AO} = 156$ K. The physical properties of this compound are strongly influenced by this transition [29,41]. X-Band ESR experiments were performed on this compound in order to investigate the effect of this transition on the ESR linewidth, the *g*-value and the spin susceptibility.

4.2.1 Room temperature ESR measurements

The principle magnetic axes (*a*, *b´* and c^*) of the single crystal of $(TMTTF)_2ReO_4$ are determined by performing ESR measurements at room temperature and studying the angular dependence of the ESR linewidth and the *g*-value when the single crystal is rotated around the three principle (*a*, *b´* and c^*). At room temperature a single conduction electron ESR signal ($g \approx 2$) with a symmetric Lorentzian lineshape along all directions is observed. Figure 4.1 shows the typical ESR spectra observed at room temperature when the static magnetic field H_o is applied parallel to the three crystal axes.

The *g*-value and the linewidth have a distinct anisotropy which was also observed in other $(TMTCF)_2X$ compounds [12,2]. The *g*-value and the linewidth have a maximum value for $H_o \parallel c^*$ (parallel to the long axis of the TMTTF molecules) and a minimum for $H_o \parallel a$ (perpendicular to the molecular plane of TMTTF).

[I] The ESR spectra are fitted using "Meascom" software which was provided by T. Kurz and H. A. Krug von Nidda from the Institut für Experimental Physik V of the Universität Augsburg.
[II] The density of spins of DPPH is 1.52714×10^{18} spin/g.

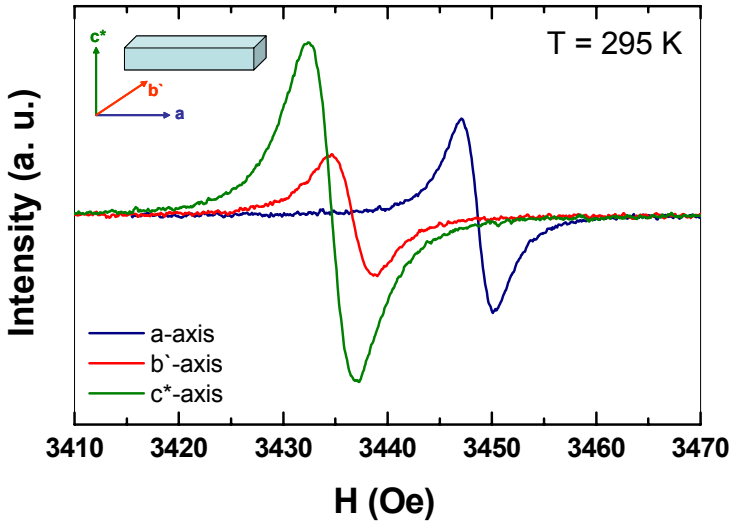

Figure 4.1: ESR spectra of $(TMTTF)_2ReO_4$ single crystal at room temperature when the static magnetic field (H_o) is applied parallel to the three crystal axis *a*, *b`* and *c (see the insert).**

The angular dependence of the *g*-value and the linewidth when the crystal is rotated around the *a*-axis (H_o // *b`*-$c^*$ plane) and around the *b`*-axis (H_o // *a*-c^* plane) at room temperature are shown in Figure 4.2. The values obtained from the angular dependence of the *g*-value and the linewidth are listed in table 4.1. The linewidth and the *g*-value have the same anisotropy which indicates that the spin-phonon interaction is the main relaxation process at high temperatures. The angular dependence of the *g*-value and the linewidth is fitted using the relations:

$$\Delta H(\theta) = \left[\Delta H^2(0^o)\cos^2(\theta) + \Delta H^2(90^o)\sin^2(\theta)\right]^{1/2} \tag{4.1}$$

$$g(\theta) = \left[g^2(0^o)\cos^2(\theta) + g^2(90^o)\sin^2(\theta)\right]^{1/2} \tag{4.2}$$

where θ is the angle between the static magnetic field (H_o) and the *a*-axis (in the case of rotation around the c^*-axis and *b`*-axis).

$(TMTTF)_2ReO_4$				
Δg (10^{-3})	a	-0.81	$\overline{\Delta g^2}$ (10^{-6})	29.01
	$b`$	5.57		
	c^*	7.44		
ΔH (Oe)	a	2.70	$\overline{\Delta H}$ (Oe)	3.38
	$b`$	3.54		
	c^*	3.91		
$\overline{\Delta H}/\overline{\Delta g^2}$ (kOe)		116.63		

Table 4.1: The obtained ESR linewidth and the g-shift for $(TMTTF)_2ReO_4$ at room temperature, where $\overline{\Delta H} = (\Delta H_a + \Delta H_{b`} + \Delta H_{c^*})/3$ and $\overline{\Delta g^2} = (\Delta g_a^2 + \Delta g_{b`}^2 + \Delta g_{c^*}^2)/3$.

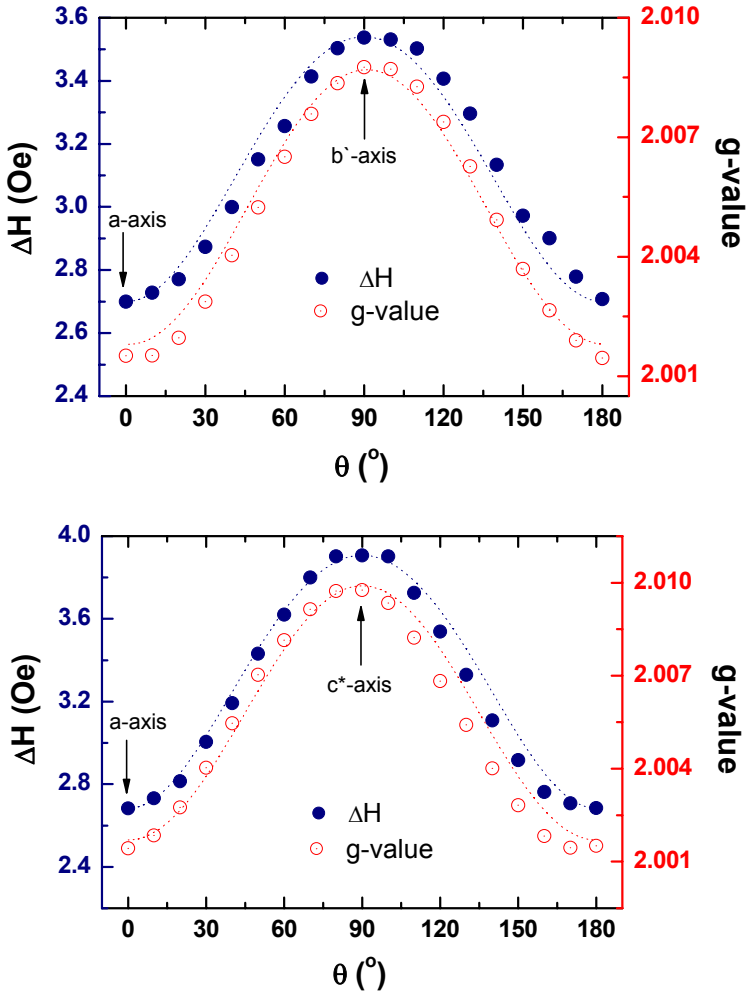

Figure 4.2: Angular dependence of the ESR linewidth ΔH (closed circles) and the g-value (open circles) for $(TMTTF)_2ReO_4$ at room temperature when the static magnetic field (H_o) is applied parallel to a-$b`$ plane (up) and $a$-$c^*$ plane (down). The least-square fits of the linewidth and the $g$-value are shown by the dotted lines. The fit parameters are $\Delta H_a$ = 2.70 Oe, $\Delta H_{b`}$ = 3.54 Oe, ΔH_{c^*} = 3.91 Oe, g_a = 2.00180, $g_{b`}$ = 2.00865 and g_{c^*} = 2.00990.

The origin of the anisotropy in the *g*-value comes from the coupling of the spin angular momentum to the orbital angular momentum (spin-orbit coupling) [131]. The tensors of the *g*-value (g_a, $g_{b`}$ and g_{c*}) are determined by the molecular structure. Since the spin-orbit coupling depends on the molecular symmetry and the orbital angular momentum L depends on the position vector of the electron (r) relative to the origin ($L = r \times p$) [132], the spin-orbit coupling has the largest value (largest g-shift) when H_o is applied parallel to the long molecular axis and the smallest value (smallest *g*-shift) along the shortest molecular axis. This means for the TMTTF molecule that the *g*-value has the largest value along the c^*-axis (the long molecular axis), the intermediate value along the $b`$-axis (the intermediate molecular axis) and the smallest value along the *a*-axis (the shortest molecular axis) as shown in Figure 4.1.

The broadening mechanism of the ESR linewidth and the anisotropy in $(TMTTF)_2ReO_4$ are similar to those known from other $(TMTCF)_2X$ compounds. The linewidth originates from the spin-orbit-coupled electronic transitions between donor conduction-band of the organic conductors, which are activated by torsional oscillations of the donor molecules around their long in-plane axis [126,2] (for more details see section 3.2.6). This argument is supported by recent ESR results on quasi 1-D organic conductor $(EDT\text{-}TTF\text{-}CONMe_2)AsF_6$[I] [133,134]. It was observed that at high temperatures (T > 50 K) the linewidth is temperature independent, which was explained due to the locking of the terminal ethylene group conformation by the hydrogen bonds which make the organic molecule rigid, thus no torsional oscillations can occur.

4.2.2 Temperature dependent measurements

The temperature dependence of the ESR linewidth, the *g*-value and the spin susceptibility for $(TMTTF)_2ReO_4$ was studied from room temperature down to low temperatures until its ESR spectrum vanished. The measurements were performed with the static magnetic field H_o applied parallel to the three orthogonal magnetic axes *a*, $b`$ and c^*. In the whole temperature range and along all orientations a single symmetric Lorentzian line is observed.

Figure 4.3 shows the temperature dependence of the linewidth ΔH, the *g*-shift ($\Delta g = g_e - 2.002319$) and the spin susceptibility normalized to the room temperature value $\chi_s/(\chi_s)_{RT}$ along the three crystal axes of $(TMTTF)_2ReO_4$. In the high temperatures region, the ΔH is largest along the c^*-axis and smallest along the *a*-axis. The

[I] $EDT\text{-}TTF\text{-}CONMe_2$ stands for tertiary amide-functionalized etyleneedithiotetrathiafulvalene.

linewidth decreases almost linearly as the temperature decreases for all direction. No anomaly or change in the slope of the linewidth is observed at the charge ordering transition temperature (T_{CO} = 227 K). At the anion ordering transition temperature (T_{AO} = 156 K), the linewidth shows a sudden step-like decrease along the three directions. Below about 150 K, the linewidth starts to increase with decreasing temperature down to the lowest temperature. Below T_{AO}, the anisotropy of the linewidth is $\Delta H_a > \Delta H_{b`} > \Delta H_{c*}$. At 120 K, the ESR lines vanish totally for all the three directions.

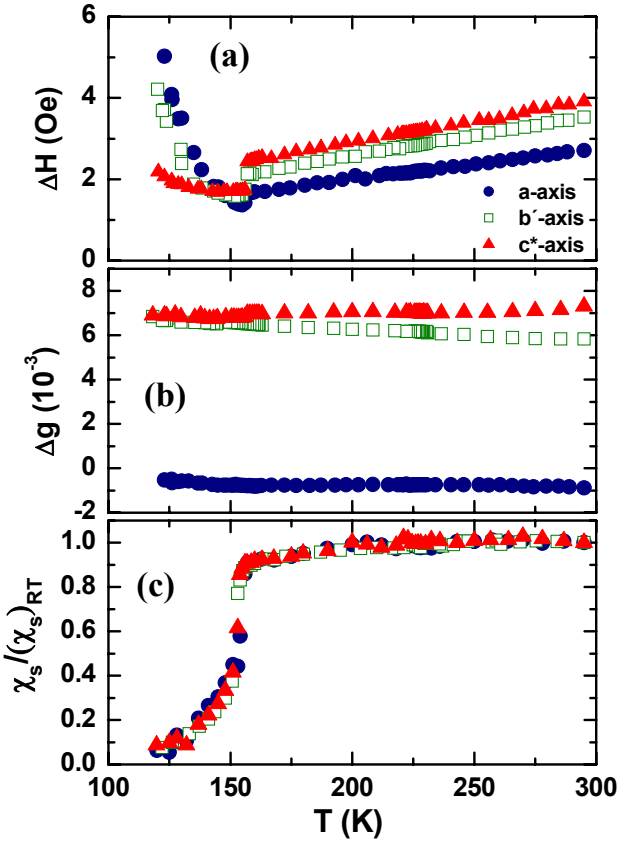

Figure 4.3: Temperature dependence of (a) the linewidth, (b) the *g*-shift (Δg) and (c) the spin susceptibility normalized to the room temperature value $[\chi_s/(\chi_s)_{RT}]$ in the three crystal directions of $(TMTTF)_2ReO_4$.

The *g*-shift for the three crystal axes is approximately temperature independent with very pronounced anisotropy (the anisotropy is the same as the linewidth). The values of Δg for the three crystal axes are very small ($-1 \times 10^{-3} - 8 \times 10^{-3}$), and are very similar to the absolute values found for $(TMTTF)_2X$ (X = AsF_6, SbF_6, BF_4, and SCN) [2]. Δg has a negative values along *a*-axis and positive values along *b*`- and *c*\*-axes. The anisotropy of $\Delta g$ between the *b*`- and *c**-axes decreases with decreasing

temperature and below T_{AO} $g_{b'} \cong g_{c*}$. No obvious effect at the anion ordering transition is observed on the *g*-value.

The spin susceptibility is isotropic for the three axes in the whole temperature range as expected. It shows very weak temperature dependence, where it decreases weakly with decreasing temperature down to the anion order transition (T_{AO} = 156 K) with a smooth anomaly at the charge ordering temperature (T_{CO} = 227 K). At T_{AO} the susceptibility shows a step-like decrease indicating a first order phase transition below which an exponential decrease of the spin susceptibility is observed corresponding for a phase transition to a non-magnetic ground state.

A decrease of the linewidth with decreasing temperature is a common characteristics of TTF-based organic conductors in the metallic regions [3] which indicates that spin-phonon interaction dominates to the electron spin relaxation. However, the increase of the linewidth with increasing temperature in $(TMTTF)_2X$ salts is correlated with the thermally activated torsional vibrations of TMTTF molecules which activate spin-orbit-coupled electronic transitions (as discussed in section 3.2.6).

The change of the anisotropy of the linewidth below the anion ordering AO transition in $(TMTTF)_2ReO_4$ is similar to that found in previous studies of $(TMTTF)_2X$ salts with non-centrosymmetrical anions[I] [12,2,3]. Above the AO transition all conduction electrons experience an equivalent electrostatic potential (Coulomb potential) along the donor stacks induced by the anions. The elastic deformation of the $P\bar{1}$ triclinic lattice and variations of the lattice parameters caused by the AO transition [29] break this equivalency and lead to changes in the electrostatic potential seen by the conduction electrons along the donor stacks which can be the reason the different anisotropy of the linewidth below T_{AO}. Additionally, the anion ordering transition was found to have a pronounced effect on the charge distribution in the AO state [3]. The influence of the anion potential on the charge distribution has been studied theoretically [135]. It was shown that a small displacement of the anions can change the charge distribution along the stacks (charge ordering). NMR results on $(TMTTF)_2ReO_4$ found an evidence of the redistribution of the charge density in the AO state [50]. Nakamura [3] have proposed the possible charge ordering pattern in the CO state depending on the anisotropy of the linewidth. He pointed that the linewidth has a higher value along the axis which has a higher charge density. Since our results are found comparable to Nakamura's results, this imply that the possible charge ordering (CO) pattern in the CO state is that one shown in Figure 4.4. The estimated huge spin gap from the

[I] We mean here non-centrosymmetrical anions with tetrahedral shape.

spin susceptibility in the AO state (see text below) confirms this assumption of the CO pattern in the AO state.

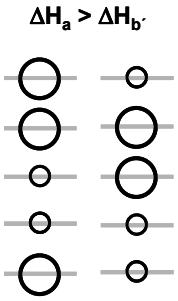

Figure 4.4: Schematic possible charge-ordering pattern in the conducting *a-b´* plane of $(TMTTF)_2ReO_4$. The large circles mean rich charge density and the small ones poor charge density.

The spin susceptibility at room temperature for $(TMTTF)_2ReO_4$ is found equal to 6×10^{-9} m^3/mole, which is approximately similar to the values found in other TMTTF salts [12,2]. Due to the large thermal expansion coefficient of TMTTF salts along the chain direction, our experimental results for the spin susceptibility which are measured at constant pressure $[\chi_s]_p$ have to be transformed to the spin susceptibility at constant volume $[\chi_s]_v$ in order to compare it with the theoretical models as discussed in section 1.1.4.

The temperature dependence of $[\chi_s]_p$ and $[\chi_s]_v$ from room temperature down to 120 K is shown in Figure 4.5. $[\chi_s]_v$ has a smooth maximum at about 273 K. The spin susceptibility at constant volume $[\chi_s]_v$ resembles the behavior of a spin-1/2 Heisenberg chain with AFM coupling, which can be fitted using the theoretical models of Bonner and Fisher [13] and Eggert, Affleck and Takahashi (EAT-model) [14] as discussed in section 2.4.1. Using this model, the $[\chi_s]_v$ of $(TMTTF)_2ReO_4$ for $T > 160$ K[I] can be modeled numerically using equation 2.14 [99] with $|J| = 425$ K. From the obtained J value the spin susceptibility at zero temperature $[(\chi_s)_v\ (T \rightarrow 0)]$ can be calculated using the relation $\chi_s(T \rightarrow 0) = \Gamma/\pi^2|J|$, which gives $\chi_s(T \rightarrow 0) = 4.5 \times 10^{-9}$ m^3/mole. The maximum of the spin susceptibility is calculated using the relation $\chi_{max} = 0.1469\Gamma/|J|$ and is found to equal 6.5×10^{-9} m^3/mole.

[I] This because $(TMTTF)_2ReO_4$ has high transition temperature ($T_{AO} = 157$ K) which leads to sharp decrease in the spin susceptibility, where the above theoretical models are valid only above the phase transition.

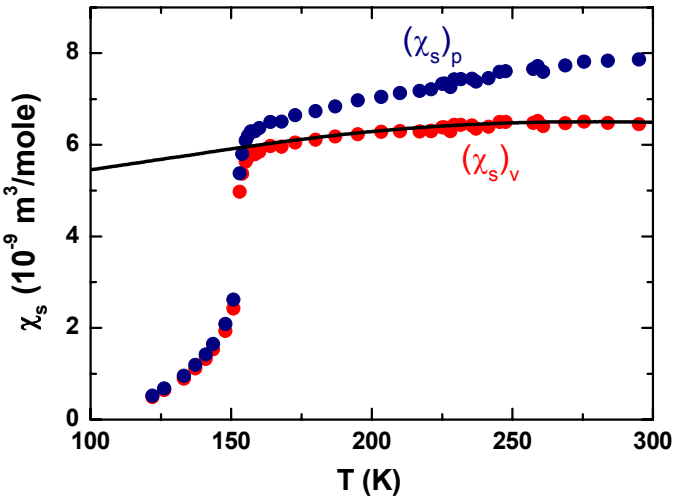

Figure 4.5: Temperature dependence of the spin susceptibility at constant pressure $(\chi_s)_p$ (blue circles) and at constant volume $(\chi_s)_v$ (red circles) of $(TMTTF)_2ReO_4$ calculated from the intensity of the ESR spectra along the stacking direction (a-axis). The line corresponds to a fit using the Bonner-Fisher model for a S = 1/2 AFM Heisenberg chain [13] with $|J|$ = 425 K. The maximum value of $(\chi_s)_v$ was calculated using the relation $\chi_{max} = 0.1469\mu_0 Ng^2\mu_B^2 / k_B|J|$.

4.2.3 Anion ordering transition

The anion ordering of $(TMTTF)_2ReO_4$ is achieved by the formation of a superstructure due to the structural transition with critical anion ordering wave vector q_{AO} = (1/2,1/2,1/2) as it was discussed in section 2.6. This transition is accompanied by a tetramerization of the donor stacks (dimerization of the spin chain) and the system will go into non-magnetic (S = 0) ground state with $J_1 >> J_2$. This explains the exponential decrease in the spin susceptibility below T_{AO} (see Figure 4.6). Due to this transition, a singlet-triplet spin gap Δ_σ opens in the AO state. The magnitude of this gap is estimated from spin susceptibility data assuming that $[\chi_s]_v$ below T_{AO} obeys an activated law [44]:

$$[\chi_s]_v(T) = \frac{A}{T}\exp\left(\frac{-\Delta_\sigma}{T}\right) \tag{4.3}$$

where A is the fit parameter. Using A = 491111 m^3K/mole, the singlet-triplet spin gap gives Δ_σ = 1100 K. This value agrees well with the value obtained from magnetization and the x-ray spectroscopy measurements [44,106].

The observed huge singlet-triplet spin gap in the AO state can be understood if this transition is accompanied with a charge redistribution along the stacks with such a

pattern that makes $J_1 >> J_2$ (this means enhancing the value of Δ_σ)[I]. Since the attraction (increasing the coupling) between any two neighbouring anti-parallel spins increases with increasing their charge density (Lorentz force law) [136], the charge ordering pattern –o-O-O-o– along the stacks (see Figure 4.4) leads to $d_2'' < d_2'$ (see Figure 2.14) and yields $J_1 >> J_2$ with a very large value of Δ_σ as it is observed.

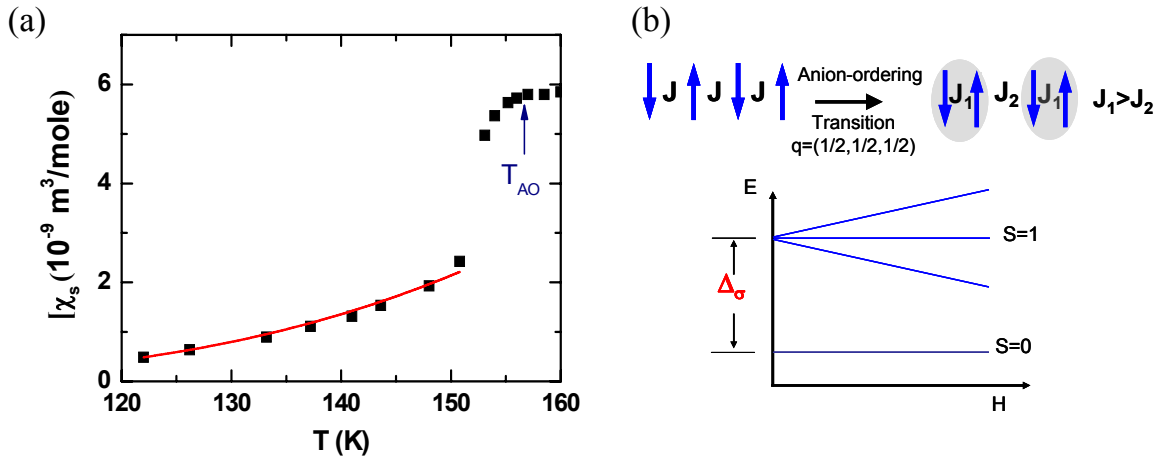

Figure 4.6: (a) Temperature dependence of the spin susceptibility of $(TMTTF)_2ReO_4$ in the low-temperature region calculated from the ESR spectra. At T_{AO} = 156 K a step-like drop in the spin susceptibility is observed below which the spin susceptibility decreases exponentially, indicating a transition to a non-magnetic ground state (b). The line corresponds to the fit by an activation behaviour model using equation 4.3. The fit parameters are A = 491111 m^3K/mole and Δ_σ = 1100 K.

The electronic state of the low temperature non-magnetic insulating phase and the origin of the linewidth in that phase are investigated through the angular dependence of the ESR linewidth along the three planes. Figure 4.7 shows the angular dependence of the linewidth along *a*-*b*` plane at T = 123 K[II] (the region of the non-magnetic ground state) measured by X-band and W-band ESR. The broadest line is measured along the *a*-direction ($\theta = 0^o$) and the narrowest line at $55^o$. Along the *b*`-direction ($\theta = 90^o$) the linewidth has an intermediate value. The minimum near the magic angle ($\theta = 54.7^o$) indicates that the dipole-dipole interaction contribute to the relaxation process in this temperature range. The angular dependence of the linewidth in one-dimensional systems governed by dipole-dipole interactions is given by:

[I] Bulaevskii's model for an alternating spin chain [12,2] showed that the singlet triplet spin gap Δ_σ can be obtained using the equation $\Delta_\sigma(0) = 0.43075(|J_1| + |J_2|)\delta^{2/3}$, where $(|J_1|+|J_2|)/2 = |J|$. Although this model is only valid in case of small degree of dimerization, it agrees well with our argument concerning the relation between Δ_σ and the exchange constants J_1 and J_2.

[II] The measured ESR spectra at this temperature are due to the thermally activated unpaired spins.

$$\Delta H_{\text{d-d}}(\theta) = \Delta H_{b`}\left[3\cos^2(\theta) - 1\right]^{4/3} \tag{4.4}$$

As seen in Figure 4.7, the angular dependence of the linewidth is fitted with the sum of the contributions of the dipole-dipole interaction using equation 4.4 with the fitting parameter $\Delta H_{b'}$ = 1.61 Oe and the spin-phonon interaction using equation 4.1 with the fitting parameters $\Delta H(0^{\circ})$ = 1.22 Oe and $\Delta H(90^{\circ})$ = 1.29 Oe. This means that the relaxation process in the non-magnetic ground state of $(TMTTF)_2ReO_4$ is governed by both interactions. Since the contribution of the spin-phonon interaction to the relaxation process decreases with decreasing temperature due to decreasing the number of phonons, it clear from the fitting parameters that the dipole-dipole interaction at low temperatures has more contribution to the relaxation process. In agreement with equation 3.20, the relaxation process is frequency independent (Figure 4.7). Moreover, the absence of the strong frequency dependence of the linewidth at 45° between *a*- and *b´*-axis which is observed in $(TMTTF)_2AsF_6$ and $(TMTTF)_2SbF_6$ at low temperatures (see section 4.3.1) indicates that the $(TMTTF)_2ReO_4$ has a different type of charge ordering in the AO state. In the *a*-c^* plane, the same angular dependence of the linewidth as in the *a*-*b´* plane is observed.

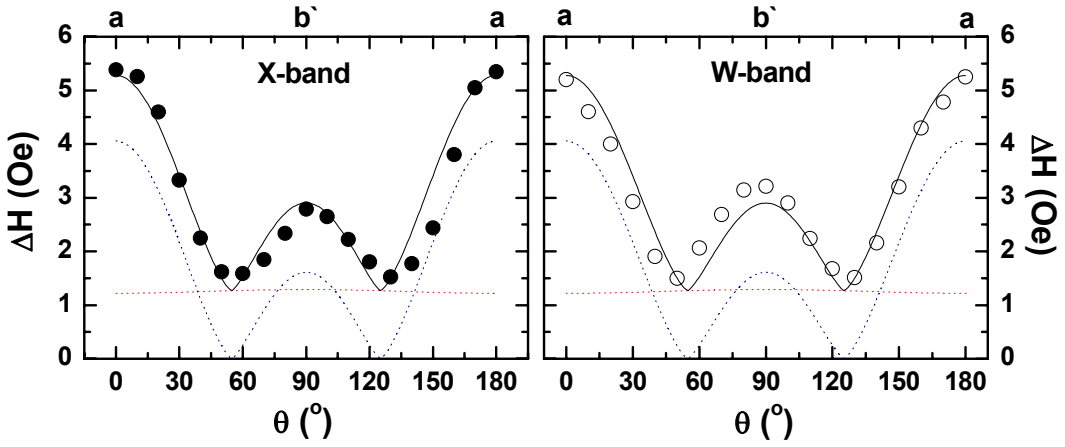

Figure 4.7: Angular dependence of the linewidth ΔH of $(TMTTF)_2ReO_4$ along *a*-*b`* plane in the anion ordered region (T = 123 K) measured by X-band (left) and W-band (right) ESR. The points are the measured data, the blue line represents a fit with equation 4.4 (dipole-dipole interaction), the red line a fit with equation 4.1 (spin-phonon interaction) and the black line is the sum of both.

Contrary, in *b`*-$c^*$ plane, a different angular dependence of the linewidth occurs below the anion ordering transition temperature ($T_{AO}$ = 157 K) as depicted in Figure 4.8. Above $T_{AO}$, the maximum and the minimum of the linewidth is observed along $c^*$-axis and *b`*-axis, respectively. The maximum and the minimum start to shift from

the crystal axes below T_{AO}, and at very low temperatures the maximum of the linewidth is observed along the b`-axis and the minimum along the c^*-axis. The angular dependence of the linewidth at all temperature is fitted using the following equation:

$$\Delta H(\theta) = \left[\Delta H_{\min}^{2} \cos^2(\theta+\varphi) + \Delta H_{\max}^{2} \sin^2(\theta+\varphi) \right]^{1/2} \tag{4.5}$$

where φ is the angle where the minimum value of the linewidth is observed.
The shift of the linewidth in b`-c^* plane was also found in $(TMTTF)_2SCN$ [2] which has anion ordering critical wave vector q_{AO} = (0,1/2,1/2) [29]. In this compound the shift of the linewidth was attributed to the anion ordering transition, where the unit cell is doubled along b and c-axes due to the movement of the anion in this plane at T_{AO}. In case of $(TMTTF)_2ReO_4$ the transition is accompanied by a small displacement of the anion with q_{AO} = (1/2,1/2,1/2) [29]. This means that the unit cell is doubled along the three crystal axes. Therefore, the shift of the maximum and the minimum of the linewidth cannot be explained as in $(TMTTF)_2SCN$. Since the linewidth along each axis should be independent from which plane is measured, the shift of the maximum and the minimum of the linewidth can be due to AO transition as a consequence of domination the dipole-dipole interaction in a-b' and a-c^* plane which leads to change in the anisotropy of the dipole-dipole interaction in b'- c^* plane.
It was shown in Figure 4.3 that the linewidth increases sharply with decreasing temperature after the step-like decrease at T_{AO}. This increase was observed also in $(TMTTF)_2ClO_4$[I] [12]. It was found that the linewidth can be fitted with a power law $\Delta H \propto T^{-1.5}$ along b'-axis. This result was taken as a hint of possible antiferro-magnetic (AFM) fluctuations (see section 4.4). In $(TMTTF)_2ReO_4$ the temperature dependence of the linewidth is fitted with a power law $\Delta H \propto T^{-x}$ along the three directions as shown in Figure 4.9. The linewidth fits along a- and b'-axis with $\Delta H \propto T^{-6.2}$ and along c^*-axis with $\Delta H \propto T^{-1.5}$. AFM fluctuations should show the same power law with x = 1.5 along the three directions, the power law in $(TMTTF)_2ReO_4$ cannot be correlated as a hint for AFM fluctuations and it is more or less inhomogeneous broadening of the linewidth due to the anion ordering transition.

[I] $(TMTTF)_2ClO_4$ has anion ordering transition at T_{AO} = 70 K with q_{AO} = (1/2,1/2,1/2) [29].

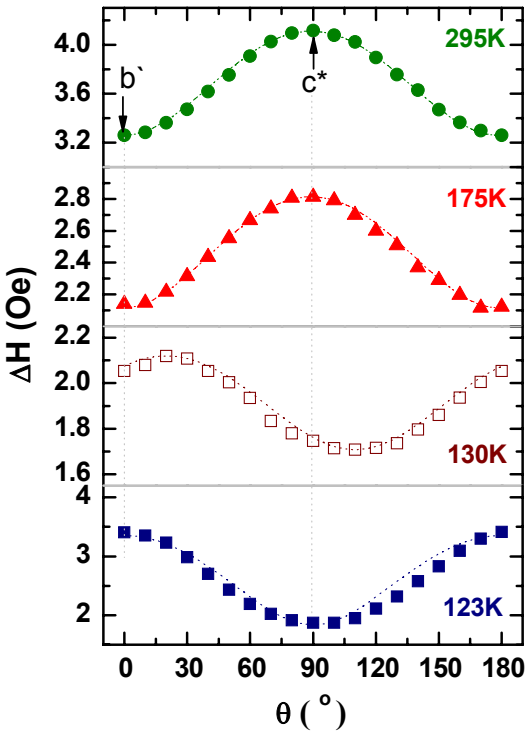

Figure 4.8: Angular dependence of the linewidth ΔH of $(TMTTF)_2ReO_4$ along b`-c* plane above and below T_{AO}. The symbols represent the measured data and the dotted lines represent the least-square fit using equation 4.5. The values of φ used in the fit are: 0^o for 295 K and 175 K, 110^o for 130 K and 90^o for 123 K.

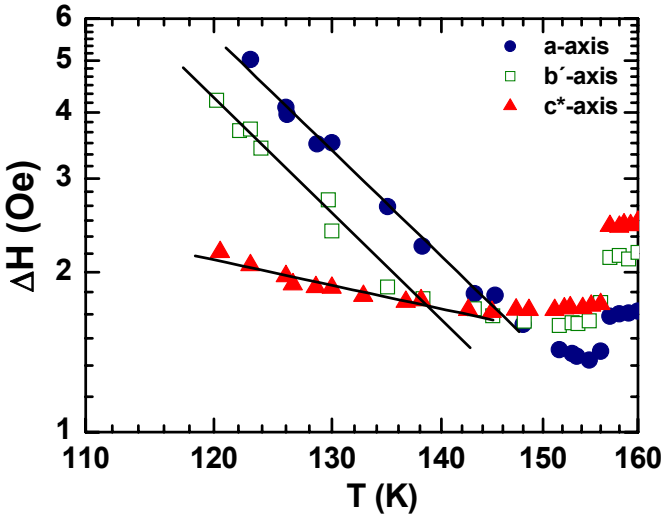

Figure 4.9: Double-logarithmic plot of the linewidth versus temperature of $(TMTTF)_2ReO_4$ along different directions in the AO state. The lines represent the linear fit with a slope x = 6.2 along a- and b´-axes and x = 1.5 along c*-axis (see text).

4.3 High frequency ESR investigations of $(TMTTF)_2AsF_6$ and $(TMTTF)_2SbF_6$ in the charge ordered (CO) state

The charge ordered (CO) state in $(TMTTF)_2AsF_6$ and $(TMTTF)_2SbF_6$ was investigated at our institute by X-band ESR spectroscopy [2]. It was shown that the CO leads to an increase of the linewidth with decreasing temperature below the charge ordering transition temperature T_{CO}, where $T_{CO} \approx 105$ K for X = AsF_6 and 156 K for X = SbF_6 (see Figure 4.10). Moreover, the angular dependence of the linewidth in *a*-*b´* plane of $(TMTTF)_2AsF_6$ and $(TMTTF)_2SbF_6$ showed characteristic changes in the charge order region [2]: two peaks at 45° and 135° were observed instead of one peak at 90°. It was suggested that this effect is due to the coexistence of two inequivalent magnetic TMTTF sites in the CO region. In this case two ESR signals should show up in the CO region. It was claimed that X-band frequencies are too low to resolve two lines. On this ground, a comprehensive Q-band (34 GHz) and W-band (95 GHz) measurements were performed on $(TMTTF)_2AsF_6$ and $(TMTTF)_2SbF_6$ in order to study the frequency dependence of the ESR parameters (the *g*-value and the linewidth) in the charge ordered state as well as to find the physical reason(s) for the characteristic changes of the linewidth.

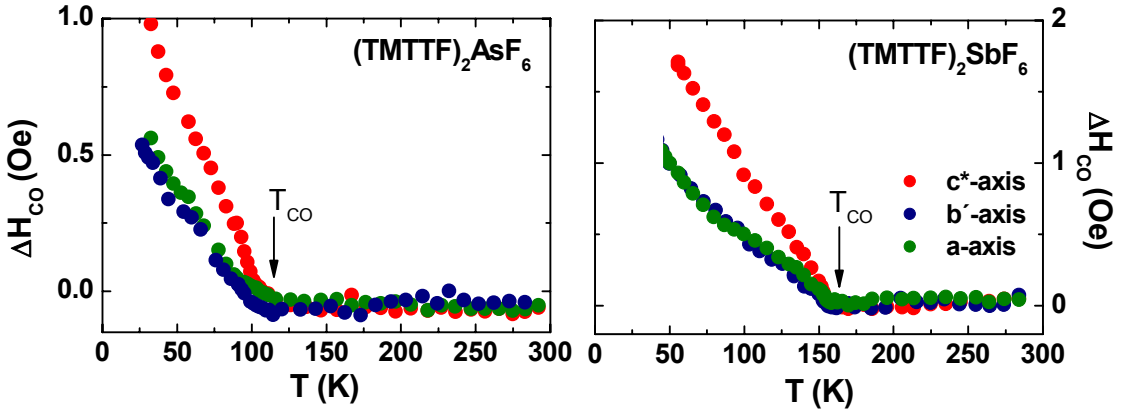

Figure 4.10: The calculated charge ordering ESR linewidth (ΔH_{CO}) for $(TMTTF)_2AsF_6$ and $(TMTTF)_2SbF_6$ along the three crystal axes using the equation $\Delta H_{CO}(x) = \Delta H(x) - \Delta H_{model}(x)$, where $\Delta H(x)$ is the measured linewidth along the *x*-axis ($x = a$, $b´$ and c^*) and $\Delta H_{model}(x)$ is the linewidth of $(TMTTF)_2PF_6$ salt along the same direction normalized to the room temperature value of the linewidth of the investigated salt. Adopted from Ref. [2].

4.3.1 Q-band and W-band ESR measurements

In the first step, room temperature investigations were performed to determine the principle magnetic axes of $(TMTTF)_2AsF_6$ and $(TMTTF)_2SbF_6$ in the same way it has been done before for $(TMTTF)_2ReO_4$ by X-band ESR. The resulting Q- and W-band spectra for all orientations revealed a symmetric Lorentzian lineshape and coincide with those observed by X-band ESR measurements [2]. The typical observed ESR spectra at room temperature for $(TMTTF)_2AsF_6$ along *a*-axis are shown in Figure 4.11 as an example.

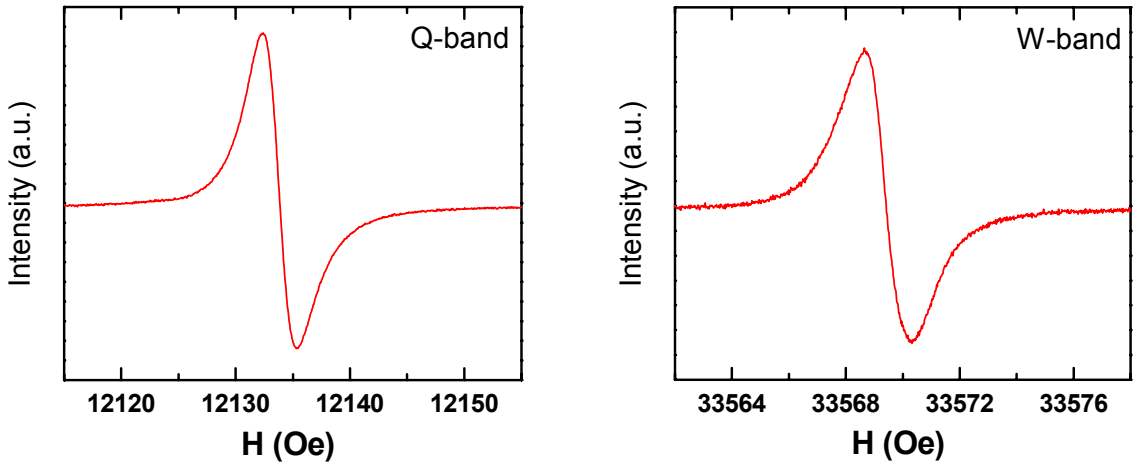

Figure 4.11: Q-band and W-band ESR spectra of $(TMTTF)_2AsF_6$ single crystal at room temperature when the static magnetic field H_o is applied parallel to the *a*-axis.

The angular dependence of the linewidth and the *g*-value along *a*-*b*′ and *b*′-c^* plane at room temperature for both compounds are shown in Figures 4.12 and 4.13. The anisotropy and the absolute values of the linewidth and the *g*-value are similar to the X-band ESR results [2]. The largest linewidth and *g*-value is observed when the static magnetic field (H_o) is applied parallel to c^*-axis, and the smallest linewidth and *g*-value when H_o is applied parallel to the *a*-axis. The origin of the anisotropy of the *g*-value and the linewidth, and the mechanism of the broadening of the linewidth can be explained similarly to the case of $(TMTTF)_2ReO_4$ which was discussed in section 4.2.1. Since the anisotropy of the *g*-value originates from the spin-orbit coupling [131] which is intrinsically quantified by the spin-orbit coupling constant λ ($\lambda = 3.8 \times 10^{14}$ s^{-1} for the sulphur atom [137]), no frequency dependence of the *g*-value is observed as expected.

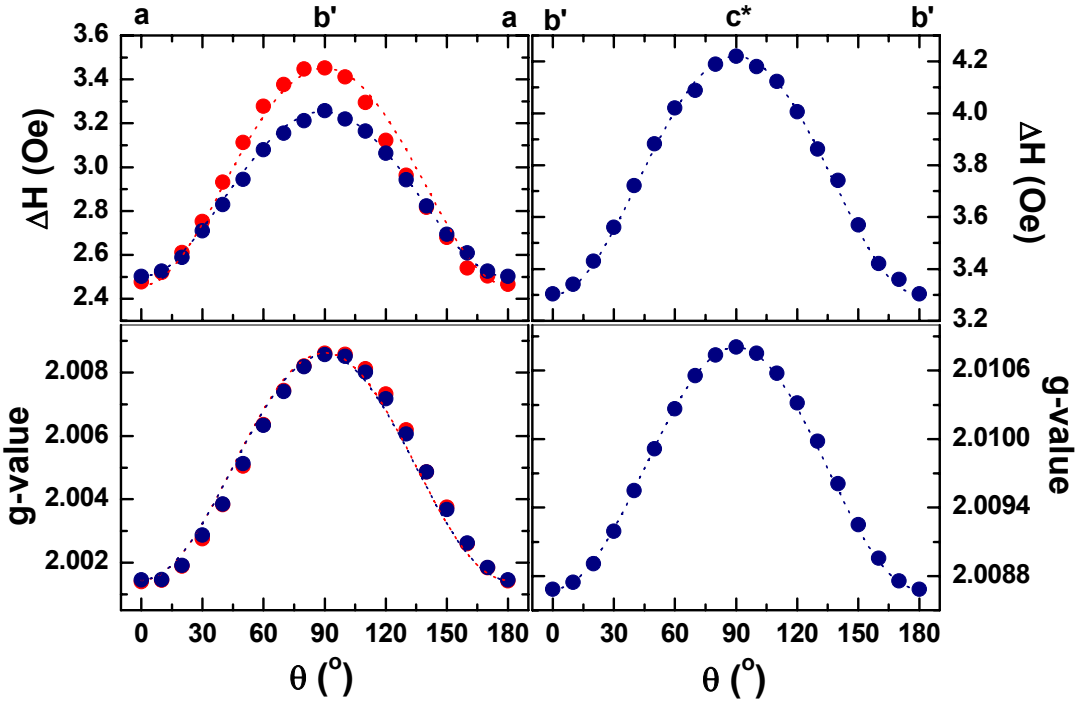

Figure 4.12: Angular dependence of the ESR linewidth ΔH and the g-value at room temperature for $(TMTTF)_2AsF_6$ measured at Q-band (red circles) when the static magnetic field (H_o) is applied parallel to a-b` and W-band (blue circles) when $H_o$ is applied parallel to $a$-$b$` plane (left), and to b'-c* plane (right). The least-square fittings of the linewidth and the g-value are shown by the dotted lines. The fit parameters are $(\Delta H_a)_{Q\text{-band}}$ = 2.46 Oe, $(\Delta H_{b'})_{Q\text{-band}}$ = 3.45 Oe, $(\Delta H_a)_{W\text{-band}}$ = 2.50 Oe, $(\Delta H_{b'})_{W\text{-band}}$ = 3.25 Oe, $(\Delta H_{c^*})_{W\text{-band}}$ = 4.22 Oe, g_a = 2.00146, $g_{b'}$ = 2.00856 and g_{c^*} = 2.01080.

The observed frequency independent linewidth[I] along the three crystal axes is due to the fact that the torsional oscillations of the TMTTF molecule which have the symmetry restrictions and cause the broadening of the linewidth are only induced thermally [126], also the anisotropy of the linewidth is correlated with the effective spin-orbit coupling magnetic field H_{eff}^{SO}, and this field is anisotropic and depends directly on the strength of the spin-orbit coupling as it was discussed in section 3.2.6.

[I] A small difference in the absolute value of the linewidth measured by Q-band and W-band is observed due to the sample size effect.

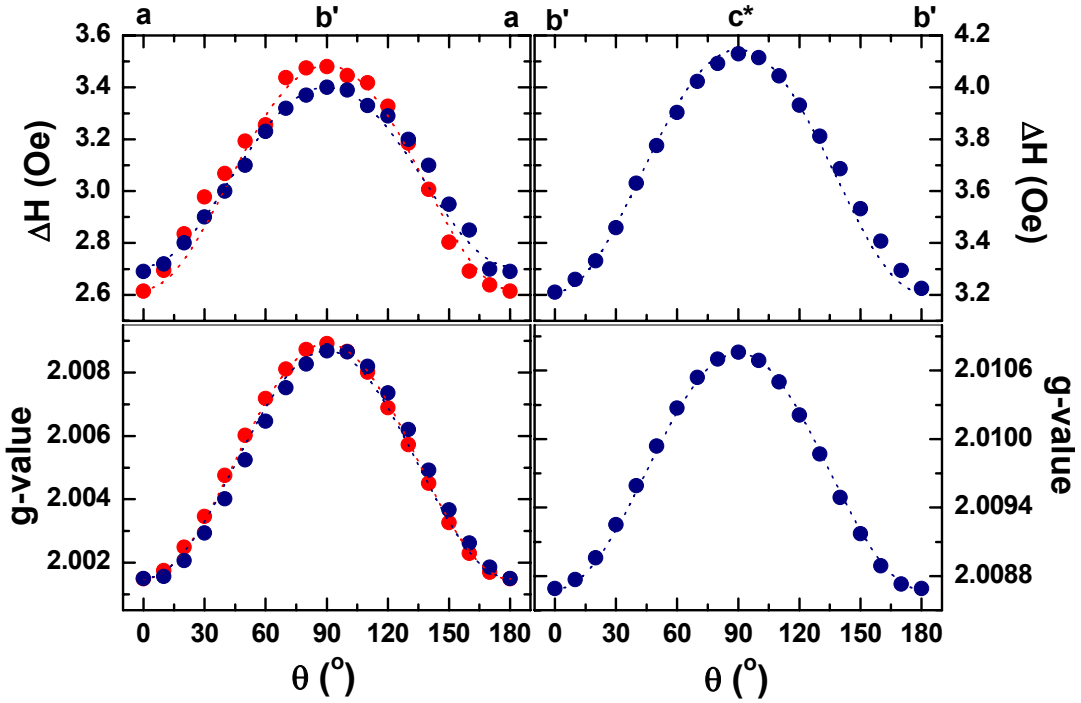

Figure 4.13: Angular dependence of the ESR linewidth ΔH and the g-value at room temperature for $(TMTTF)_2SbF_6$ measured at Q-band (red circles) when the static magnetic field (H_o) is applied parallel to a-b` and W-band (blue circles) when $H_o$ is applied parallel to $a$-$b$` plane (left), and to b'-c^* plane (right). The least-square fittings of the linewidth and the g-value are shown by the dotted lines. The fit parameters are $(\Delta H_a)_{Q\text{-band}}$ = 2.62 Oe, $(\Delta H_{b'})_{Q\text{-band}}$ = 3.49 Oe, $(\Delta H_a)_{W\text{-band}}$ = 2.71 Oe, $(\Delta H_{b'})_{W\text{-band}}$ = 3.40 Oe, $(\Delta H_{c^*})_{W\text{-band}}$ = 4.15 Oe, g_a = 2.00150, $g_{b'}$ = 2.00868 and g_{c^*} = 2.01075.

The temperature dependence of the W-band ESR linewidth and the g-shift ($\Delta g = g - 2.002319$) along the three principle magnetic axes a, $b'$and c^*, and the X-, Q- and W-band ESR linewidth and the g-shift along a-axis of $(TMTTF)_2AsF_6$ and $(TMTTF)_2SbF_6$ are shown in Figures 4.14 and 4.15, respectively. The behaviour and the absolute values of the linewidth and the g-shift for both compounds in the whole temperature range (300 K – 4.2 K) do not show any frequency dependence and they are similar to the results measured by X-band ESR spectrometer [2].

In $(TMTTF)_2AsF_6$, the linewidth decreases almost linearly as the temperature decreases for all directions with a distinct anisotropy $\Delta H_{c^*} > \Delta H_{b'} > \Delta H_a$ (as discussed before) down to the charge ordering transition temperature (T_{CO} = 105 K) at which a smooth hump in the linewidth for all directions is observed which is more pronounced along c^*-axis. Below T_{CO} the linewidth shows a smooth anomaly and the anisotropy starts to change to $\Delta H_{c^*} > \Delta H_{b'} \approx \Delta H_a$ at low temperatures. At 35 K the linewidth begins to increase with lowering the temperature and starts to fluctuate

below about 15 K. The temperature dependence of the *g*-shift along the three crystal axes down to 5 K is similar to that found in $(TMTTF)_2ReO_4$.

In $(TMTTF)_2SbF_6$, the ESR results at high temperatures are very similar to the results of $(TMTTF)_2AsF_6$, even the absolute values of the linewidth and the *g*-shift. At T_{CO} = 156 K a clear anomaly in the linewidth for the three directions is observed. Below T_{CO}, the linewidth has same change as in $(TMTTF)_2AsF_6$, where the decrease of the linewidth with decreasing temperature becomes slower and the anisotropy of the linewidth starts to change in the same way as in $(TMTTF)_2AsF_6$ ($\Delta H_{c^*} > \Delta H_{b'} \approx \Delta H_a$). At around 45 K, the linewidth starts to increase with lowering temperature down to T_N = 8 K where the ESR spectra vanish totally for the three directions due to a phase transition to AFM ground state. This phase transition is accompanied by a decrease in the *g*-shift along *b´* and c^*-directions and an increase in *a*-direction when $T \rightarrow T_N$.

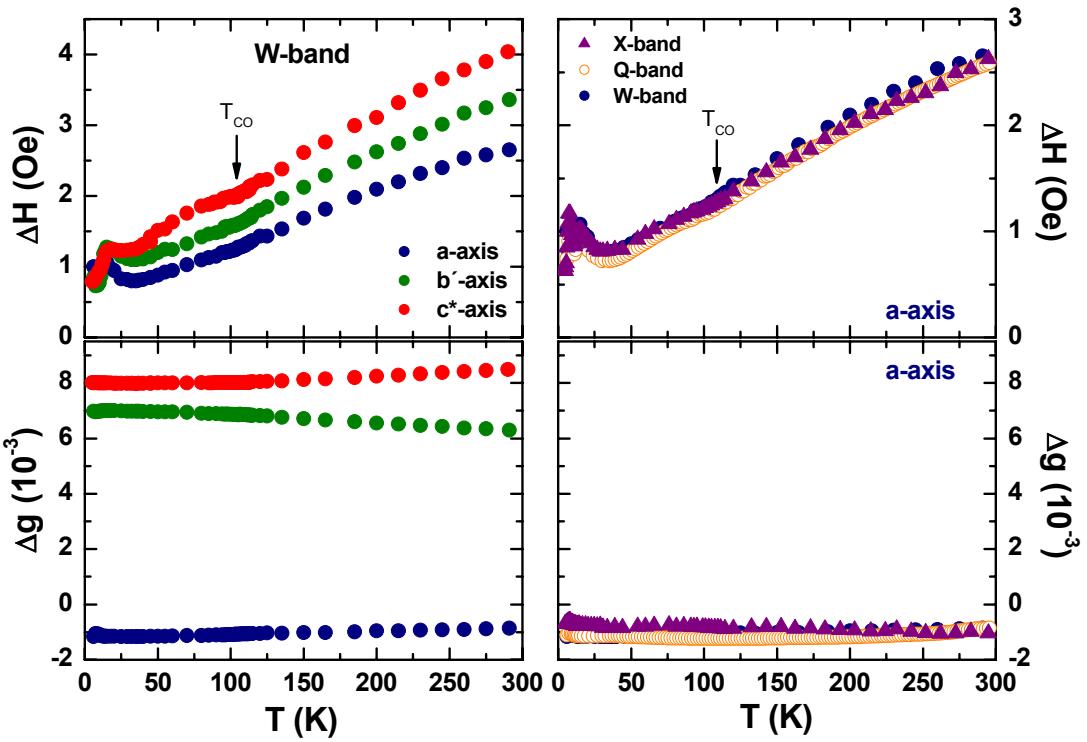

Figure 4.14: Temperature dependence of the linewidth and the *g*-shift (Δg) measured at W-band in the three crystal directions (left), and the X-, Q- and W-band ESR linewidth and the Δg along *a*-axis (right) of $(TMTTF)_2AsF_6$. Data of X-band from Ref. [2].

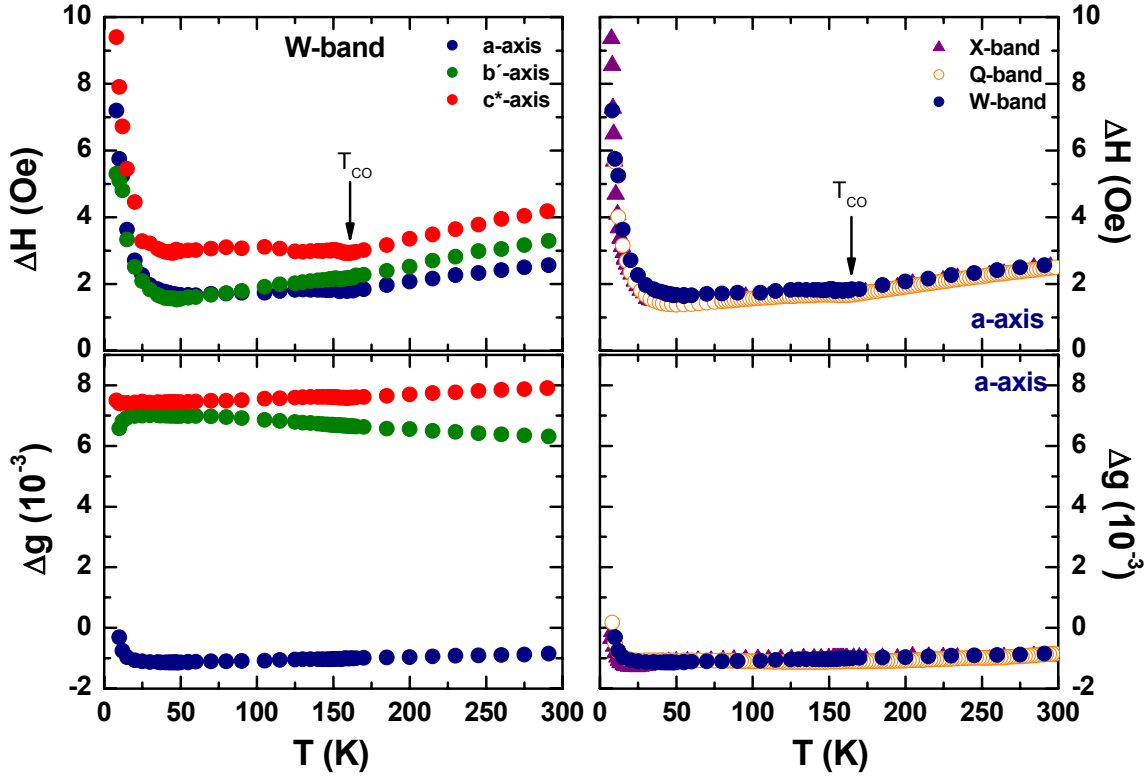

Figure 4.15: Temperature dependence of the linewidth and the *g*-shift (Δg) measured at W-band in the three crystal directions (left), and the X-, Q- and W-band ESR linewidth and the Δg along *a*-axis (right) of $(TMTTF)_2SbF_6$. Data of X-band from Ref. [2].

So far, it was shown that there is no frequency dependence of the ESR parameters along the three principle crystal axes and they are completely similar to the X-band ESR results [2]. Since the characteristic changes were observed in the angular dependence, detailed angular dependent investigations of the linewidth and the *g*-value were performed along *a*-*b´* and *b´*-*c** planes[I]. In the whole temperature range and along all the orientations, a single absorption line is observed[II]. Figure 4.16 shows the W-band ESR spectra with the Lorentzian fit at different temperatures when the static magnetic field H_o is applied parallel to the 0^o (*a*-axis), 45^o and 90^o (*b*`-axis) in *a*-*b´* plane for $(TMTTF)_2SbF_6$ as an example. Above T_{CO}, the ESR spectra show a symmetric Lorentzian line along all the orientations while below T_{CO}, a slight distortion in the ESR spectra along 45^o is observed.

[I] No characteristic changes were observed in the angular dependence of the linewidth along *a*-*c** plane which was measured by X-band ESR.
[II] Throughout the experiment full magnetic field sweep was performed in order to check the possibility of the existence of a second ESR signal.

The angular dependence of the *g*-value along *a*-*b*´ and *b*´-*c** planes does not change with decreasing temperature and has the same orientation pattern as at room temperature. Figure 4.17 shows the angular dependence of the *g*-value at different temperatures in *a*-*b*´ plane for both salts measured by W-band ESR. The values of the *g*-value are comparable to the values measured by X-band ESR [2].

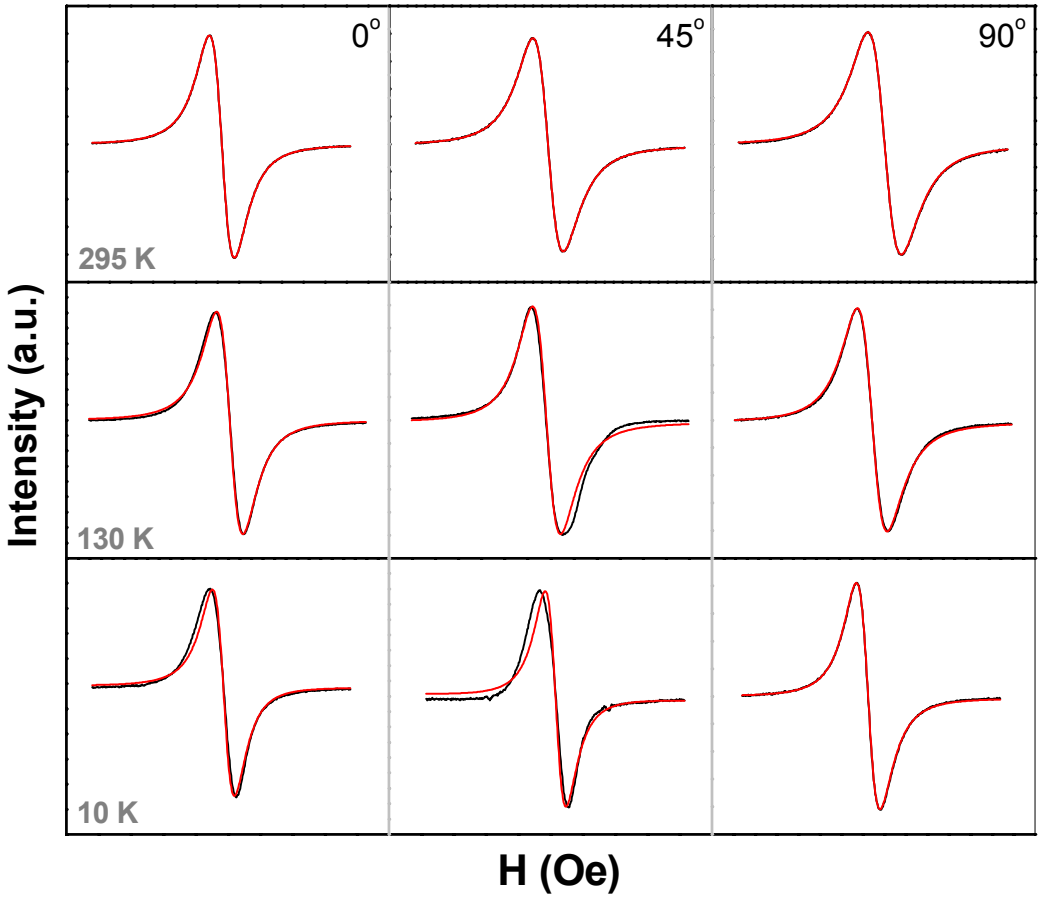

Figure 4.16: W-band ESR spectra of $(TMTTF)_2SbF_6$ single crystal at different temperatures when the static magnetic field H_o is applied parallel to the 0° (*a*-axis), 45° and 90° (*b*`-axis) in *a*-*b*´ plane. The black lines are the ESR spectra and the red ones are the Lorentzian fitting curves. The tiny signal at the tail of the real signal along 45° at 10 K is due to impurities in the resonator.

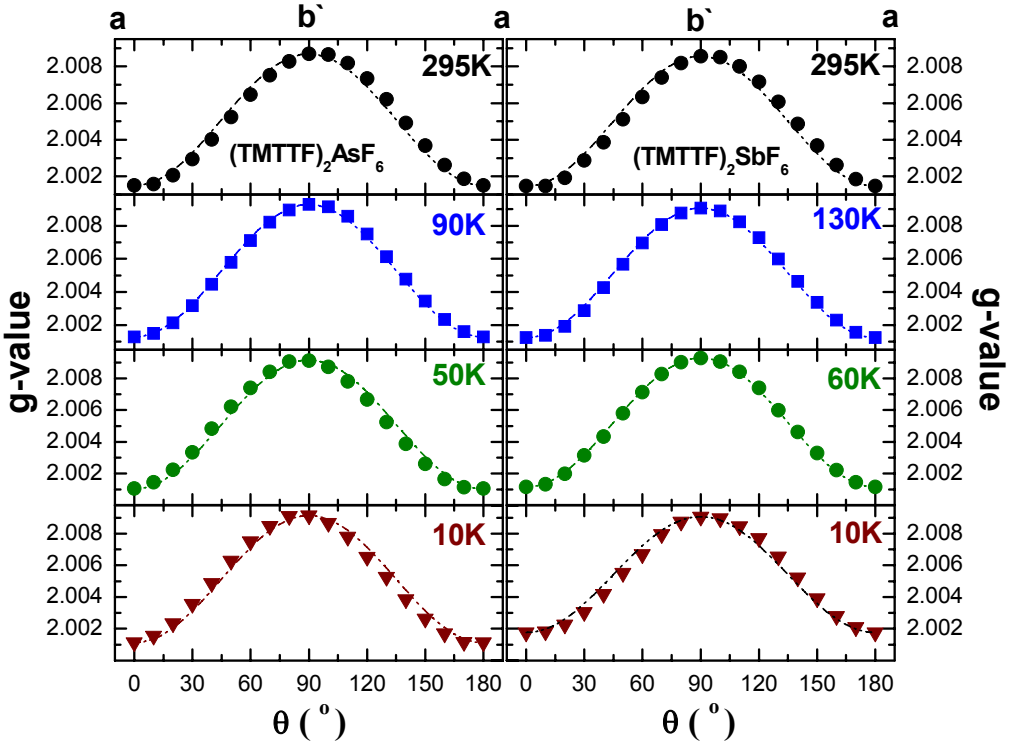

Figure 4.17: Angular dependence of the *g*-value measured at W-band for $(TMTTF)_2AsF_6$ and $(TMTTF)_2SbF_6$ at different temperatures when the static magnetic field (H_o) is applied parallel to *a*-*b*` plane. The least-square fittings of the linewidth are shown by the dotted lines.

The angular dependence of the X-[I], Q- and W-band ESR linewidth along *a*-*b*´ plane at different temperatures for $(TMTTF)_2AsF_6$ and $(TMTTF)_2SbF_6$ is shown in Figures 4.18 and 4.19, respectively. Above T_{CO}, the linewidth has the same orientation pattern as at room temperature and has no frequency dependence. The angular dependence of the linewidth for the two salts can be fitted by equation 4.6 as was discussed in section 4.2.1.

$$\Delta H_{sp}(\theta) = \left[\Delta H_{sp}^2(a)\cos^2(\theta) + \Delta H_{sp}^2(b')\sin^2(\theta)\right]^{1/2} \tag{4.6}$$

where $\Delta H_{sp}(a)$ and $\Delta H_{sp}(b')$ are the linewidths induced by spin phonon interaction along *a*- and *b*´-axes, respectively and θ is the angle between H_o and the *a*-axis. Below T_{CO} the angular dependence of the Q- and W-band linewidth shows the same characteristic changes as observed in the X-band; while the linewidth along the *a*- and *b*´-axes is frequency independent, it has a pronounced enhancement for the Q- and W-band measurements along the two peaks at 45° and 135°. The angular

[I] Adopted from Ref. [2].

dependence of the linewidth corresponding to this enhancement can be modelled by the relation:

$$\Delta H(\theta) = \Delta H(45^{o})\left|\sin(2\theta)\right| \tag{4.7}$$

where ΔH (45^{o}) is the linewidth at 45^{o}. Below T_{CO} the orientation dependence of the linewidth can be fitted by sum of equation 4.6 and 4.7. The fit parameters used in modelling the orientation dependence of the linewidth at different temperatures are listed in Table 4.2. The frequency dependence of the linewidth along 45^{o} and 135^{o} in *a-b´* plane exists only below T_{CO}. This means that the new scattering process which causes the doubling of the periodicity of the linewidth along *a-b´* plane is a function of frequency.

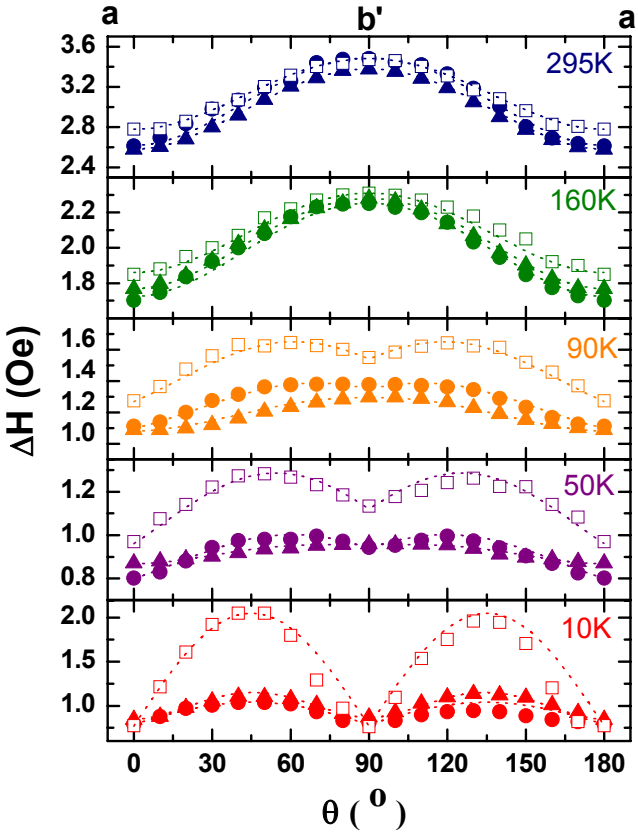

Figure 4.18: Angular dependence of the ESR linewidth ΔH measured at X-band (filled triangles), Q-band (filled circles) and W-band (open rectangles) for $(TMTTF)_2AsF_6$ at different temperatures when the static magnetic field (H_o) is applied parallel to *a-b`* plane. The least-square fittings of the linewidth are shown by the dotted lines. The fit parameters used are tabulated in Table 4.2. Data of X-band was taken from Ref. [2].

T (K)	$(TMTTF)_2AsF_6$			T (K)	$(TMTTF)_2SbF_6$		
	Q-band				Q-band		
	ΔH (a)	ΔH (b')	ΔH (45^o)		ΔH (a)	ΔH (b')	ΔH (45^o)
295	2.62	3.49	0	295	2.46	3.45	0
160	1.73	2.25	0	130	1.61	1.99	0.13
90	1.10	1.35	0.10	60	1.37	1.48	0.18
50	0.80	0.94	0.11	10	4.69	4.69	2.13
10	0.79	0.79	0.25				
	W-band				W-band		
295	2.78	3.48	0	295	2.50	3.25	0
160	1.86	2.31	0	130	1.69	1.95	1.02
90	1.27	1.54	0.20	60	1.48	1.60	1.55
50	0.96	1.12	0.23	10	4.90	4.90	9.35
10	0.77	0.77	1.28				

Table 4.2: The fit parameters for the orientation dependence of the linewidth along *a-b´* plane of $(TMTTF)_2AsF_6$ and $(TMTTF)_2SbF_6$ using equations 4.6 and 4.7.

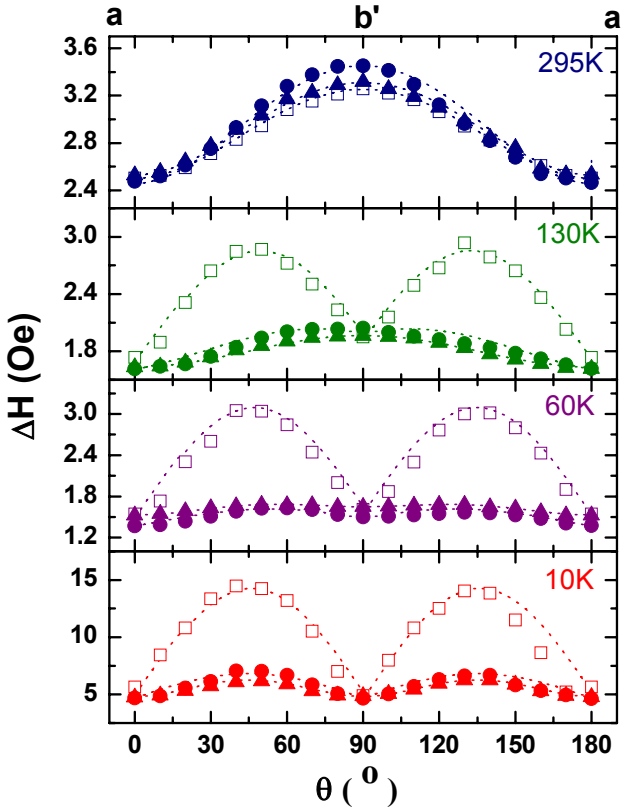

Figure 4.19: Angular dependence of the ESR linewidth ΔH measured at X-band (filled triangles), Q-band (filled circles) and W-band (open rectangles) for $(TMTTF)_2SbF_6$ at different temperatures when the static magnetic field (H_o) is applied parallel to *a-b`* plane. The least-square fittings of the linewidth are shown by the dotted lines. The fit parameters used are tabulated in Table 4.2. Data of X-band was obtained from Ref. [2].

4.3.2 Analysis and discussion

In order to clarify the nature of the relaxation process in the charge ordered state, the enhanced linewidth $\Delta H_{\text{enhanced}}$[I] along 45° in *a*-*b*′ plane for the X-, Q- and W-band measurements is calculated using equation 4.8 for $(TMTTF)_2AsF_6$ at 10 K and 50 K, and for $(TMTTF)_2SbF_6$ at 10 K, 60K and 130 K:

$$\Delta H_{enhanced} = \Delta H_{45^o} - \left(\frac{\Delta H_a + \Delta H_{b'}}{2} \right) \tag{4.8}$$

where ΔH_{45^o} is the linewidth along 45° in *a*-*b*′ plane. The calculated values of $\Delta H_{\text{enhanced}}$ for both salts are plotted versus the frequency in Figure 4.20. In both compounds the $\Delta H_{\text{enhanced}}$ increases slightly when the frequency increases from 9.5 GHz (X-band) to 34 GHz (Q-band), while increases sharply at 95 GHz (W-band).

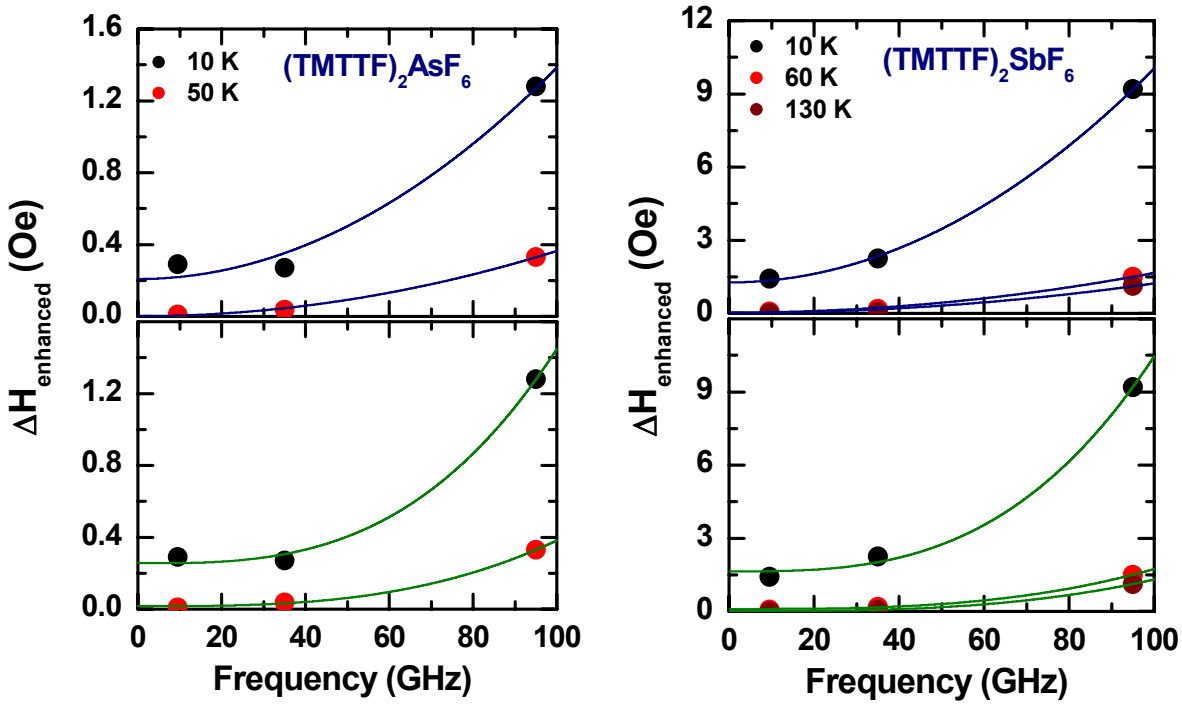

Figure 4.20: Frequency dependence of the enhanced ESR linewidth $\Delta H_{\text{enhanced}}$ along 45° in *a*-*b*′ plane for $(TMTTF)_2AsF_6$ at 10 K and 50 K, and $(TMTTF)_2SbF_6$ at 10 K, 60 K and 130 K. The circles are the experimental data. The blue and green curves are the fitting lines using equations 4.9 and 4.11, respectively (see text).

[I] The enhanced linewidth ($\Delta H_{\text{enhanced}}$) for the Q- and W-band measurements is calculated by weighting their linewidths along *a*- and *b*′-axes to the ones of the X-band measurements in order to cancel any sample size effect in our calculations.

The doubling in the periodicity of the linewidth was observed in the quasi one-dimensional S = 1/2 AFM Heisenberg inorganic systems $CuGeO_3$ by Pilawa [15] and $CuSb_2O_6$ by Heinrich *et al* [109]. They attributed this observation due to coexistence of two magnetically inequivalent Cu^{2+} sites in the system. Riera and Poilblanc [135] have suggested that the observed charge ordering in TMTTF salts is due to a cooperative effect between the Coulomb interaction and the coupling of the electronic stacks to the anions, and small displacements of the anions (along some arbitrary directions) lead to local changes of the on-site electronic energies which produces non-equivalent magnetic sites. This means that the angular dependence of the linewidth observed in *a-b´* plane might be due to anisotropic Zeeman (AZ) interaction. As shown in Figure 4.20 (upper panel) the enhanced linewidth $\Delta H_{\text{enhanced}}$ at different temperatures below T_{CO} for both compounds shows fairly v^2 dependence which is fitted using the empirical equation:

$$\Delta H_{\text{enhanced}}(v) = \alpha + \beta v^2 \tag{4.9}$$

where α and β are the fit parameters. This result is a strong indication that the doubling in the periodicity of the linewidth and the frequency dependence of the linewidth is due to AZ interaction. To verify this indication, the theory of AZ interaction introduced in section 3.2.3 is used. According to our results, using equation 3.25, at W-band frequency with a resonance field of about 33.6 kOe and with $|J| \approx 410$ K [2] and $\overline{\Delta g^2} = 33 \times 10^{-6}$ at 10 K (see Figures 4.14 and 4.15) we obtain $\Delta H_{\text{AZ}} \approx 3 \times 10^{-3}$ Oe. It is clear that this value much smaller than the measured linewidth of $(TMTTF)_2AsF_6$ and $(TMTTF)_2SbF_6$ even at low temperatures along the directions of 45° and 135° in *a-b´* plane. This discrepancy between the calculated value of ΔH_{AZ} and the measured one can be due to the fact that the two magnetic inequvalent sites which produce AZ interaction exist along the two neighbouring chains of TMTTF molecules while the used values of J and Δg are the exchange constant between two spins along the chain and the average of the g-tensors along the principle axes, respectively. Pilawa [15] has shown that the contribution of the anisotropic Zeeman interaction in $CuGeO_3$ to the ESR linewidth is due to interactions between neighbouring chains, thus the interaction exchange constant J' has to be considered. The corresponding linewidth due to the AZ interaction with $J \to J'$ is given by the following equation [15]:

$$\Delta H_{AZ}(10^4\,\text{Oe}) \approx \frac{\mu_B H_0^2}{g_e k_B |J'|} \sqrt{\frac{\pi}{8}} |\Delta g|^2 \tag{4.10}$$

Using Figure 2.8 with T_N = 6 K for $(TMTTF)_2SbF_6$, the inter-chain exchange constant is estimated by J' = 2.2 K. The difference between the *g*-tensors of the two inequivalent magnetic sites (Δg) can be calculated using equation 4.10. Since they result from the charge ordering, Δg is calculated using $\Delta H_{AZ} \rightarrow \Delta H_{enhanced}$ = 1.55 Oe at $\theta = 45^{o}$ and T ≈ 60 K[I] (see Table 4.2 for $(TMTTF)_2SbF_6$), J' = 2.2 K and H_0 = 33600 Oe. By using these values in equation 4.10, we obtain Δg = 0.012. This value is slightly different from that one calculated from the difference between the *g*-value along the *a*- and *b*-axis ($g_b - g_a$ = 0.008). The maximum at 45^{o} and the finite value of Δg means that the *g*-tensors of the two spins corresponding to the two different magnetic sites do not coincide with the principle magnetic axes, and the two inequivalent magnetic sites make an angle 2φ with respect to each other. Therefore, the anisotropy of the *g*-value observed in *a*-*b*′ plane (see Figure 4.13) is an average result of the anisotropy of the two different magnetic sites. The anisotropy of the *g*-value for each magnetic site can be expressed by the equations:

$$g_1 = \sqrt{g_{max}^2 \cos^2(\theta - \varphi) + g_{min}^2 \sin^2(\theta - \varphi)}$$
$$g_2 = \sqrt{g_{max}^2 \cos^2(\theta + \varphi) + g_{min}^2 \sin^2(\theta + \varphi)} \qquad (4.11)$$

where g_1 and g_2 is the *g*-tensor of kind 1 and kind 2 of spins, respectively. 2φ is the angle between the two kinds of spins. g_{max} and g_{min} is the maximum and the minimum of the *g*-value for each kind of spins at the angle φ, respectively. As shown in Figure 4.21, the variation of the *g*-value of the two magnetically inequivalent sites which can produce Δg = 0.012 at $\theta = 45^{o}$ is obtained when g_{max} = 2.0126, g_{min} = 1.9982 and the angle between the two kinds of spins is $2\varphi = 56^{o}$. This means that there are different possibilities for this variation depending on g_{max}, g_{min} and φ. Therefore, the question of the anisotropy of the *g*-tensors of the two inequivalent magnetic sites in the charge ordered state is still an open question which needs further magnetic resonance investigations and also theoretical calculations.

Comparing the energy scale of J' (2.2 K) and the microwaves used in the experiment (95 GHz ≡ 4.5 K)[II], two resonance signals at quite different magnetic fields might be expected. Since the AZ interactions produces a maximal broadening effect in the direction where the maximal line splitting should appear [138] (at 45^{o} and 135^{o} in our case), the reason for the absence of the splitting can be due to the fact that the

[I] This value is used in order to exclude the antiferromagnetic fluctuation effect in our calculations.
[II] 1 Hz = 4.799×10^{-11} K.

W-band frequency still not sufficient to split the two expected ESR signals below T_{CO} due to the inter-chain exchange coupling J' between the two inequivalent magnetic sites or the two signals are not resolved due to contribution of another mechanisms to the broadening of the linewidth. It is known from previous studies [139] that the distortion of the signal is a precursor of the splitting. The slight distortion which is observed in the ESR spectra along 45^{o} and 135^{o} below T_{CO} (see Figure 4.16) supports this proposed scenario. Furthermore, if we compare our results with those of the quasi one-dimensional S = 1/2 AFM Heisenberg inorganic system $CuGeO_3$, a qualitative similarity can be observed. In $CuGeO_3$ [15], the two magnetically inequivalent Cu^{+2} sites have a large difference in the orientation of the *g*-tensors. This should result in two resonance signals at quite different magnetic fields, since the inter-chain exchange constant of the two magnetically inequivalent Cu^{+2} sites (J_{inter} = 4.2 K) is much smaller than the frequency used in the experiment (245 GHz ≡ 11.8 K). Nevertheless, no splitting of the ESR signal was observed. In our case, due to the parallel arrangement of the TMTTF molecules on neighbouring stacks, one would not expect the observed anisotropy of the linewidth. Additionally, it seems to be that observing the two resonance signals corresponding to AZ interaction is related to other parameters like the anisotropy of the *g*-tensors of the two inequivalent magnetic sites and contribution of other mechanisms to the relaxation process which can be responsible for that.

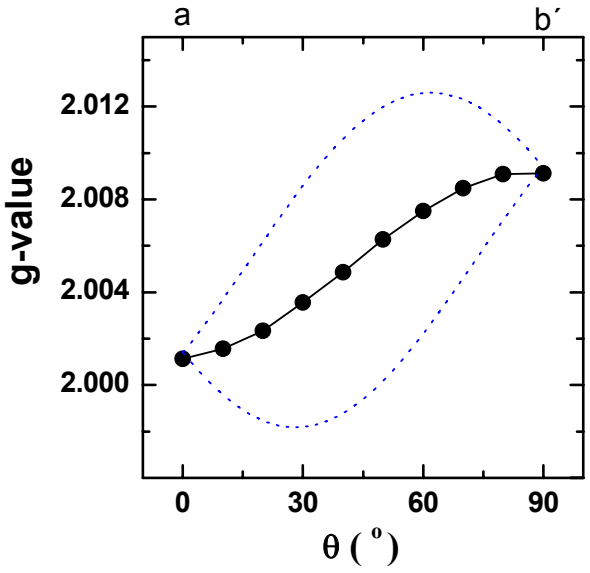

Figure 4.21: Angular dependence of the *g*-value at 10 K of $(TMTTF)_2SbF_6$ single crystal when the static magnetic field H_o is applied parallel to the *a-b´* plane. The doted blue lines indicate the calculated possible variation of the *g*-value of the two magnetically inequivalent sites (g_1 and g_2) using equation 4.11 with φ = 28°, g_{max} = 2.0126, g_{min} = 1.9982.

The measured angular dependence of the linewidth in a-c^* plane of $(TMTTF)_2SbF_6$ does not show any change in the orientation pattern of the linewidth and is similar to that one measured by X-band ESR [2], but interestingly, a clear distortion in the W-band ESR spectra is observed as the orientation gets closer from the 45^o direction in this plane as shown in Figure 4.22. This is a strong support to our argument that the non-equivalent magnetic sites are along the neighbouring chains.

In the previous discussion it was shown that the unresolved two ESR signals corresponding to AZ interaction can be due to contribution of other mechanisms. As shown in Figure 4.20 (lower panel) it is possible also to fit the calculated values of the enhanced linewidth $\Delta H_{\text{enhanced}}$ with cubic frequency dependence (v^3) using the empirical equation:

$$\Delta H_{\text{enhanced}}(v) = \alpha' + \beta' v^3 \tag{4.12}$$

where α' and β' are the fit parameters. The fit parameters used in fitting the frequency dependence of $\Delta H_{\text{enhanced}}$ using the equations 4.9 and 4.12 are listed in Table 4.3.

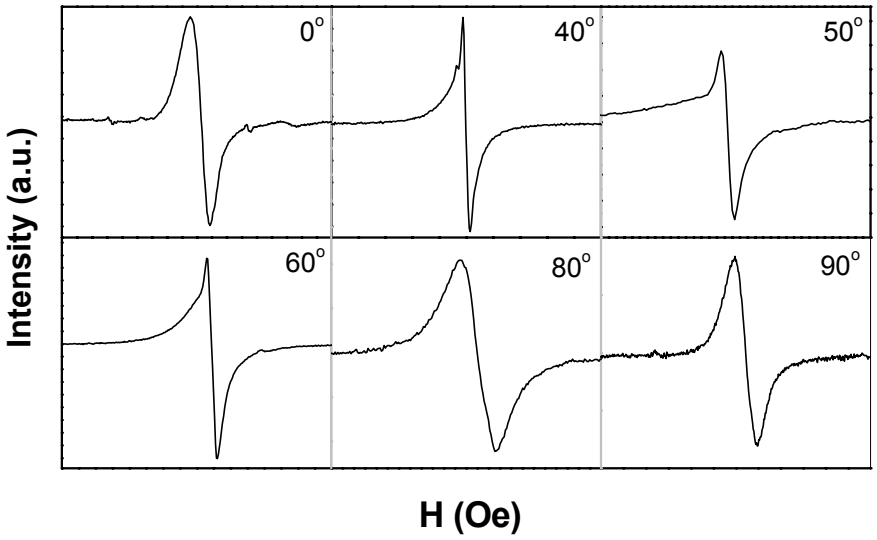

Figure 4.22: W-band ESR spectra of $(TMTTF)_2SbF_6$ single crystal at 10 K when the static magnetic field H_o is applied parallel to the 0^o (a-axis), 40^o, 50^o, 60^o, 80^o and 90^o(c^*-axis) in a-c^* plane. The tiny signals at the tail of the real signal are due to the resonator impurities.

	T (K)	$\Delta H_{enhanced}(v) = \alpha + \beta v^2$		$\Delta H_{enhanced}(v) = \alpha' + \beta' v^3$	
		α (Oe)	β Oe/(GHz)^2	α' (Oe)	β' Oe/(GHz)^3
$(TMTTF)_2AsF_6$	10	0.21	1.2×10^{-4}	0.25	1.19×10^{-6}
	50	0.001	4.0×10^{-4}	0.02	3.66×10^{-7}
$(TMTTF)_2SbF_6$	10	1.27	8.8×10^{-4}	1.64	8.82×10^{-6}
	60	0.03	1.6×10^{-4}	0.10	1.64×10^{-6}
	130	0.013	1.2×10^{-4}	0.01	1.30×10^{-6}

Table 4.3: The fit parameters for the frequency dependence of the enhanced linewidth along 45° in *a-b´* plane of $(TMTTF)_2AsF_6$ and $(TMTTF)_2SbF_6$ using equations 4.9 and 4.12.

Indeed, the cubic frequency dependence of the linewidth is a characteristic of Waller mechanism (direct process) [140]. According to this mechanism, the spin-spin interaction is modulated by the lattice waves which correspond to the lattice vibrations. This correlation leads to distance fluctuations between the spins under the action of the lattice vibrations. Consequently, the local magnetic field which exists at one spin because of the magnetic dipole on the neighbouring spin fluctuates, thus changing the total magnetic field seen by each spin. Zorko *et al* [141] have shown in pulsed ESR in $(TMTTF)_2Br$ that the temperature dependence of the spin-phonon relaxation rate can be described by the indirect Waller process which has no v^3 dependence. However, applying the direct Waller mechanism on our results poses the question why this mechanism should be active in the charge ordered state at low temperature where no thermal phonons are present and why only along 45° in *a-b´* plane. Therefore, further investigations using pulse ESR on a comparable compound like $(TMTTF)_2PF_6$[I] which has a narrow linewidth (less than 1 Oe) in the charge ordered state would be useful to resolve any contributions to the relaxation mechanisms. Moreover, performing high frequency ESR measurements (higher than 95 GHz) would be very important to verify the proposed mechanisms.
As in X-band results, no change in the orientation pattern of the W-band ESR linewidth is observed along *b´-c** plane for both salts as shown in Figure 4.23.

[I] $(TMTTF)_2PF_6$ has a charge ordering transition temperature at around 70 K [41].

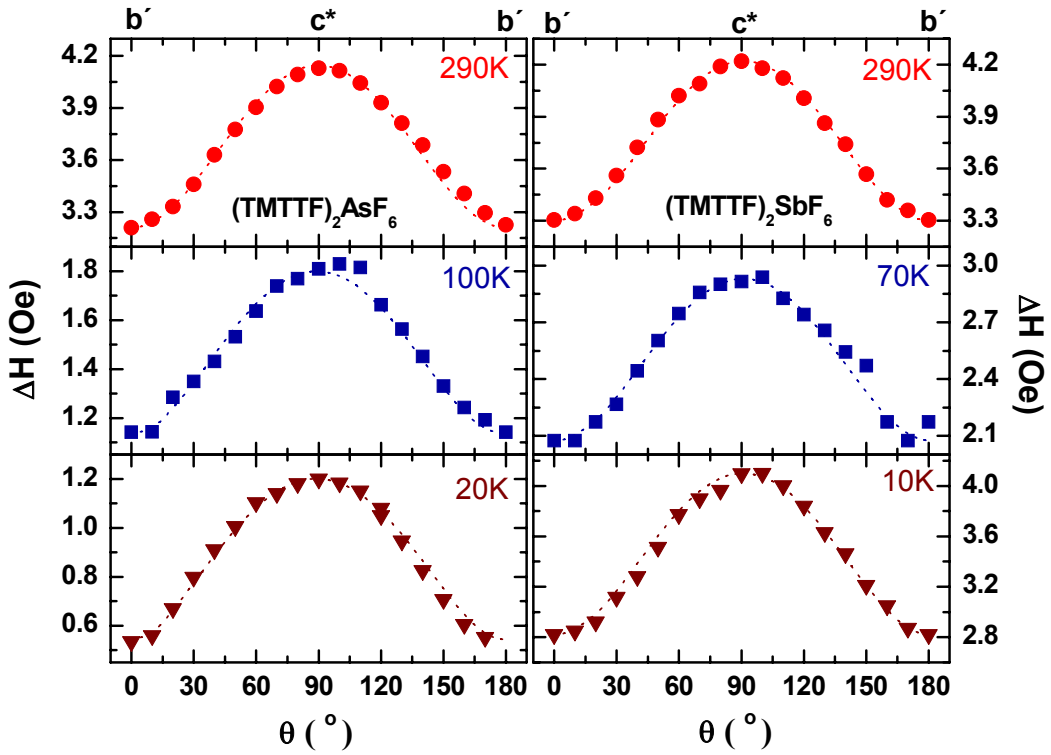

Figure 4.23: Angular dependence of the ESR linewidth ΔH measured at W-band for $(TMTTF)_2SbF_6$ and $(TMTTF)_2AsF_6$ at different temperatures when the static magnetic field (H_o) is applied parallel to $b`$-c^* plane. The least-square fittings of the linewidth are shown by the dotted lines.

It was shown in Figure 4.14 that the linewidth of $(TMTTF)_2AsF_6$ along the three directions starts to fluctuate below about 15 K where the compound is close to the spin-Peierls transition temperature (T_{sp} = 13 K). This fluctuation is absent when the linewidth is measured along 45° in *a*-*b´* plane. As shown in Figure 4.24 the linewidth starts to increase enormously below 13 K with decreasing temperature. This increase is assigned to the coexistence of two magnetic sites in the spin-Peierls state [135] which enhances the contribution to the relaxation process along this direction below T_{sp}, thus causes the broadening of the linewidth.

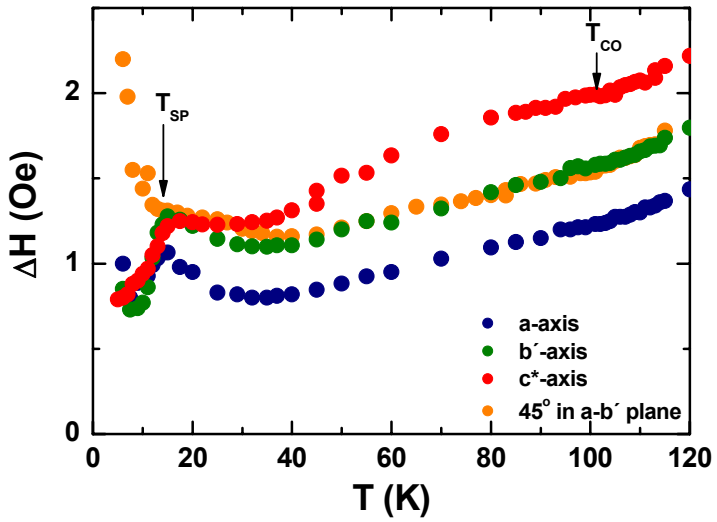

Figure 4.24: Temperature dependence of the linewidth measured by W-band with the static magnetic field (H_0) applied parallel the diagonal of the *a*-*b´* plane in $(TMTTF)_2AsF_6$. For comparison, the results along *a*, *b´* and *c are also plotted.**

4.4 Antiferromagnetic (AFM) fluctuations in $(TMTTF)_2SbF_6$

It was shown in Figure 4.15 that the linewidth of $(TMTTF)_2SbF_6$ along the three axes increases distinctively by lowering the temperature as the temperature approaches the AFM ordering temperature. This increase was studied theoretically [17]. It was shown that this singularity of the linewidth in the AFM fluctuation region is a signature for the magnetic character of the ordering, and in case of a small static magnetic field H_o the linewidth in the AFM fluctuation region follows the equation:

$$\Delta H(T \to T_N) = C r_{AFM}^{-\mu} \tag{4.12}$$

where C is a constant, $r_{AFM} = (T - T_N)/T_N$ and μ is a function of the critical indices, and the dimensionality of the AFM fluctuations d. If the dipole-dipole interaction is the dominant relaxation process in this critical region, μ is given by $\mu = 3 - d/2$. i.e. $\mu = 3/2$ for 3-D AFM fluctuations. Since the linewidth is found frequency independent along the three direction in the whole temperature range (see Figure 4.15), equation 4.12 is assumed to be valid also at high magnetic field. Figure 4.25 shows the plot of the linewidth versus (T-T_N) near the AFM phase transitions. The W-band ESR linewidth along the three directions and the Q-band ESR linewidth along a-axis is fitted by $\Delta H \propto (T - T_N)^{-\mu}$ with $\mu = 0.5$ (X-band data is added for comparison). This value is similar to the value of the X-band ESR linewidth [2]. Since the theoretical analysis bases on the hypothesis that the dipole-dipole

interaction is the dominant relaxation process in the AFM fluctuation region, and this interaction is found to be frequency independent (see Figure 4.7), this means AFM fluctuations is frequency independent which is confirmed by observing the same value of μ for all the ESR frequency bands.

The value of μ = 0.5 is found also in $(TMTSF)_2NO_3$ [142], while it was found μ = 1.5 in $(TMTTF)_2SCN$ [2], $(TMTSF)_2AsF_6$ and $(TMTTF)_2Br$ [39]. This difference in the value μ might be assigned due to the different anisotropy in the spin degrees of freedom, as well as to different magnitudes of the dipole-dipole interaction and spin-orbit coupling.

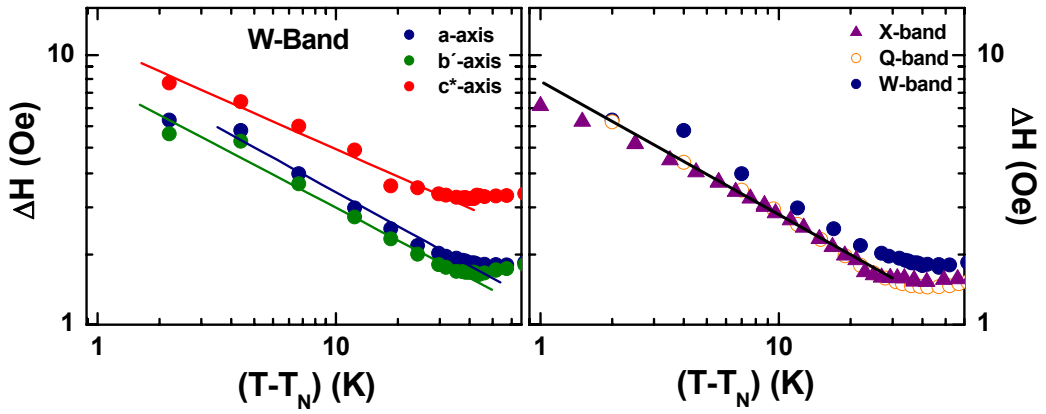

Figure 4.25: Double-logarithmic plot of the linewidth versus (T-T_N) of $(TMTTF)_2SbF_6$ along different directions measured by X-, Q- and W-band in the antiferromagnetic fluctuation region. The lines represent the linear fit with a slope μ = 0.5 ± 0.1, T_N = 8 K. Data of X-band from Ref. [2].

Chapter 5

Magnetic and Transport Studies on κ-(BEDT-TTF)$_2$Cu[N(CN)$_2$]Br$_x$Cl$_{1-x}$

The family of quasi two-dimensional κ-(BEDT-TTF)$_2$X provides an ideal example of strongly correlated electron systems which has attracted increasing attention in the recent years because of their unique physical properties. The competition between magnetically ordered antiferromagnetic and superconductivity phases, Mott metal-to-insulator (MI) transition and the structural transition stimulated an intensive study of the isostructural family κ-(BEDT-TTF)$_2$Cu[N(CN)$_2$]*X*, where *X* = Br, Cl, I. The physical properties of these compounds showed a great sensitivity to the hydrostatic pressure or chemical pressure, i.e, anion size [7,8]. As depicted in the phase diagram of κ-(BEDT-TTF)$_2$*X* (see Figure 1.14), the electronic and magnetic properties are strongly influenced by modifying the atom *X*. Despite the numerous experimental efforts recently expended on the properties of these salts, the information collected from experiments done under pressure remained until now limited by the selectivity of the experimental probe used. Moreover, all of the studies were confined to applying an external pressure in order to map the region of the Mott-Hubbard transition in the phase diagram [8,143]. The debate of determining the type of excitation of the charge carriers at low temperature [8,10] and the relaxation mechanism of these compounds [11] kept the doors opened for further investigations and it was a motivation for us to verify the story of this material. Therefore, we aimed to investigate the electronic and magnetic phase transitions in the phase diagram of κ-(BEDT-TTF)$_2$*X* between pure Cl and Br by performing ESR, transport and SQUID measurements on the alloyed series κ-(BEDT-TTF)$_2$Cu[N(CN)$_2$]Br$_x$Cl$_{1-x}$. We selected the amount of alloying *x* in a way that all relevant regions of the phase diagram could be probed.

5.1 Experimental

The single crystals of alloyed series κ-(BEDT-TTF)$_2$Cu[N(CN)$_2$]Br$_x$Cl$_{1-x}$ (x = 0%, 20%, 40%, 70%, 80%, 85%, 90% and 100%) have been synthesized by standard electrochemical growth method (see Sec. 1.2.2). The samples have naturally flat *a*-*c* surfaces (plate-like) with an average dimensions of 0.7 × 0.8 × 0.2 mm^3. The magnetic properties of the samples were investigated by the electron spin resonance (ESR) and SQUID magnetometer. The spin susceptibility and the *g*-value were determined by comparing the resonance position and the intensity of the measured ESR signal with that of DPPH.

The dc resistivity measurements were performed using the standard four probe method. The applied current is kept always less than 10 μA through the experiment to avoid heating the sample.

In the following sections we report transport and ESR results on the alloyed series κ-(BEDT-TTF)$_2$Cu[N(CN)$_2$]Br$_x$Cl$_{1-x}$. It will be shown that the dc resistivity and ESR parameters depends strongly on the ratio Br/Cl in the alloyed compound and the ration Br$_{0.7}$/Cl$_{0.3}$ is approximately the critical value for the insulating anti-ferromagnetic/superconducting transition in the phase diagram. Moreover, these results enabled us to map the critical temperatures of the metal-to-insulator, antiferromagnetic and superconducting transitions for different Br dopings. The interpretation of the data obtained and the discussion of the electronic structure will be given.

5.2 Transport Investigations

The temperature dependence of the resistivity from room temperature down to 4.2 K was measured parallel to the conduction plane for the alloyed series κ-(BEDT-TTF)$_2$Cu[N(CN)$_2$]Br$_x$Cl$_{1-x}$ for different Br doping x (x = 20%, 40%, 70%, 80%, 85% and 90%). All measurements were performed at a low cooling rate of 8 K/hour to guarantee thermal equilibrium and to minimize effects associated with disorder in the terminal ethylene groups which may arise from rapidly cooling through the ordering/disordering transition temperature[I] [10]. As displayed in Figure 5.1, at room temperature the resistivity for all measured samples is in the range (0.3 – 5) Ωcm. Between 300 K and 100 K, all samples show the same temperature

[I] The ordering/disordering transition temperature is known as "glassy" transition temperature ($T_g \approx 77$ K), below this temperature a certain disorder in the positional degrees of freedom of the terminal ethylene groups [(CH$_2$)$_2$] of the BEDT-TTF molecules is frozen in. The kinetics of the transition is strongly dependent on the cooling rate when the system crosses T_g and has effects on the physical properties and also the ground state of the system.

dependence of the resistivity. Upon cooling, the resistivity shows strong dependence on the Br/Cl ratio. For the samples with x = 20% and 40% the resistivity increases smoothly with decreasing temperature down to around 50 K, below this temperature a strong increase in the resistivity of many orders of magnitude is observed. This behavior is analogous to that reported in [25] for $x < 0.5$. In the samples with x = 80%, 85% and 90% the resistivity shows basically the same temperature dependence like the pristine Br specimen [69], it increases slightly below room temperature until it reaches a broad maximum around 80 – 100 K, and at lower temperatures the behavior becomes metallic and finally a superconducting transition takes place. In case x = 70%, the resistivity shows a pronounced increase below 80 K down to 50 K where a maximum appears then the behavior becomes metallic similar to x = 80%, 85% and 90% compounds and finally the superconducting transition occurs. This behavior reveals that this sample is very close to the border of the metal-insulator phase transition in the phase diagram. The resistivity measurements clearly demonstrate how the chemical pressure drives the system from a low-conductivity insulating regime at low chemical pressure ($x < 70\%$) to a high-conductivity metallic regime at high chemical pressure ($x \geq 70\%$).

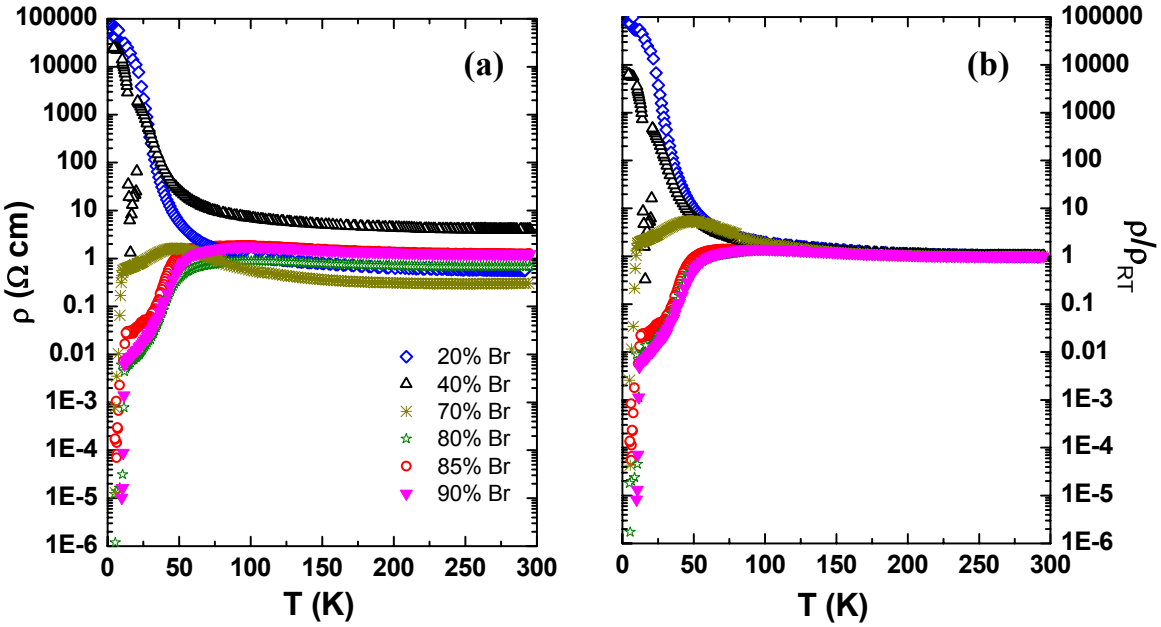

Figure 5.1: Temperature dependence of the dc resistivity parallel to the conduction plane (*a-c* plane) of single crystalline κ-(BEDT-TTF)$_2$Cu[N(CN)$_2$]Br$_x$Cl$_{1-x}$ for different Br doping (a), and when they normalized to their room temperature values (ρ/ρ$_{RT}$) (b). The results of x = 20% Br, 40% Br and 85% Br are taken from Ref. [144].

5.2.1 Analysis and discussion

The pronounced $\rho(T)$ maximum in the temperature range 80 – 100 K has been found in a number of (BEDT-TTF)$_2$X salts such as κ-(BEDT-TTF)$_2$Cu(NCS)$_2$ [145], the α-(BEDT-TTF)$_2$NH$_4$Hg(SCN)$_4$ [146] as well as κ-BETS[I] salts [147]. Several suggestions about the physical origin of the $\rho(T)$ maximum in κ-(BEDT-TTF)$_2$X have been reported including the formation of small polaron [148], a metal-metal phase transition [149], a valence instability of Cu^{+2} [150], as well as an order-disorder of the terminal ethylene groups of the BEDT-TTF molecules [151,152,153]. However, our measurement on two samples from the same batch indicates that this behavior is sample dependent. As shown in Figure 5.2, the $\rho(T)$ maximum in the first sample is five times less than the $\rho(T)$ maximum of the second sample. This is a clear indication that inhomogeneities or impurities have a substantial influence in these compounds. Moreover, it can be due to a slight difference in the doping concentration although they are from the same batch [154]. Montgomery *et al* [155] succeeded in preparing superconducting crystals which lack the anomalous resistance hump using different synthesis routes.

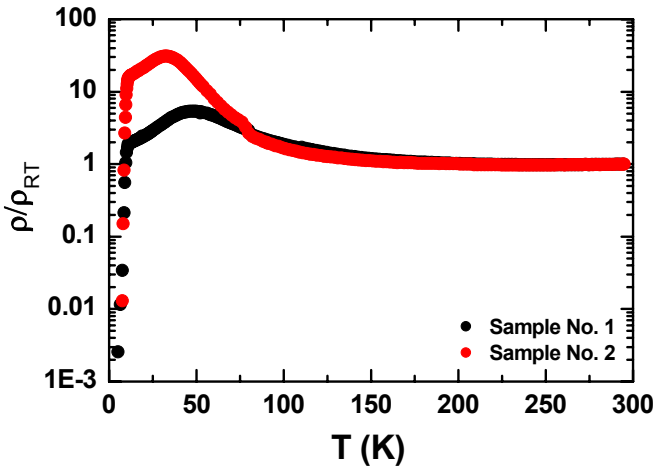

Figure 5.2: In-plane temperature dependence of the relative dc resistivity of κ-(BEDT-TTF)$_2$Cu[N(CN)$_2$]Br$_{0.7}$Cl$_{0.3}$ for two different samples.

Figure 5.3 shows the resistivity measurements in direction parallel and perpendicular to the conduction plane for a sample with x = 90%. The figure clarifies the dimensionality of the investigated system. The anisotropic ratio between the resistivities perpendicular and parallel to the conducting plane at room temperature

[I] BETS stands for bis(ethylenedithio)tetraselenafulvalene.

is $\rho_\perp / \rho_\parallel$ = 25 indicating two-dimensional electronic character. This ratio does not reflect the real anisotropy of the system, since it much less than the ratio measured for example by Ito *et al* [73] ($\rho_\perp / \rho_\parallel \approx 100$). This is due to the difficulty in determining the absolute value of in-plane resistivity[I]. At T ≈ 77 K a sharp dip is observed in $\rho(T)$ as shown in the insert in Figure 5.3. This anomaly is an assignment to a glass transition associated with a freezing of orientational degrees of freedom of the terminal ethylene groups [10,156].

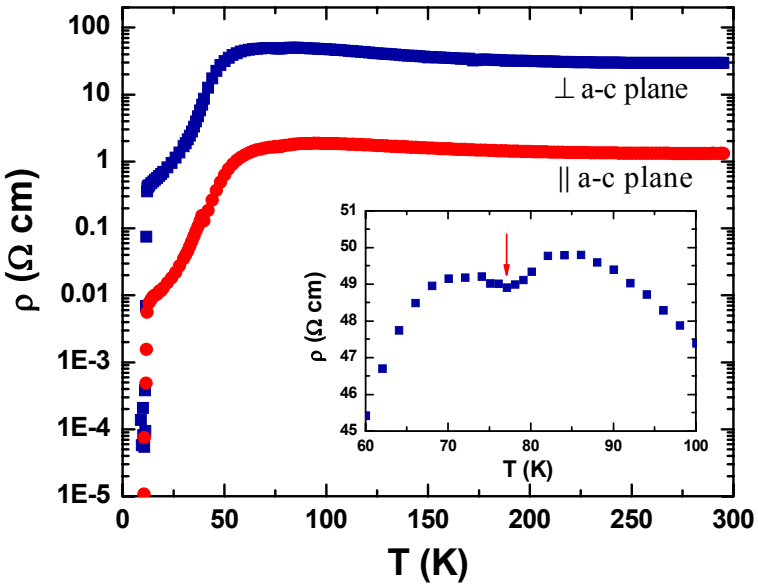

Figure 5.3: Temperature dependence of the dc resistivity of κ-(BEDT-TTF)$_2$Cu[N(CN)$_2$]Br$_{0.9}$Cl$_{0.1}$ for the current applied parallel (red circles) and perpendicular (blue rectangles) to the conduction plane (*a-c* plane). The insert shows the temperature dependence of the dc resistivity in reduced scale and the arrow points at the ordering temperature of the terminal ethylene groups.

5.2.1.1 Mott-insulating state

The temperature dependence of the resistivity of the insulating samples with x = 20% and 40% is analyzed in Figure 5.4. In the temperature range 300 – 25 K both samples can be described well by activation law $\rho \propto \exp(\Delta / k_B T)$ with strong change in the slope at around 50 K. This is clear from the energy gaps Δ obtained from the fitting lines using an activation law. In the temperature range 25 – 50 K the energy gap is 600 K and 400 K for 20% and 40% Br, respectively. From 50 K to 300 K the energy gap is found 200 K for both samples. These values agree well with the values

[I] In highly anisotropic samples it is difficult to determine the absolute value of the measured resistivity because the resistivity is hampered by the contributions from the other directions.

found in the reference [8]. Below 25 K the resistivity deviates from the fitting lines. Indeed, this activation law is limited to the temperature 300 – 25 K (paramagnetic insulator region) because below 25 K the system undergoes a phase transition into antiferromagnetic ground state [8,78]. As shown in Figure 5.5, the temperature dependence of the resistivity in the AFM ground state can be fitted by the variable-rang hopping (VRH) conduction law [18,157,158]:

$$\rho(T) = \rho_o \exp(T_{hop} / T)^{1/3} \tag{5.1}$$

The fit parameters are T_{hop} = 8.77 K, ρ_o = 1.19 × 10^4 Ω cm for 20% Br and T_{hop} = 7.14 K, ρ_o = 7.8 × 10^3 Ω cm for 40% Br. This fit gives conclusive evidence for the presence of localized electronic states, which can be the reason for the deviation of the activation law in this region of temperature.

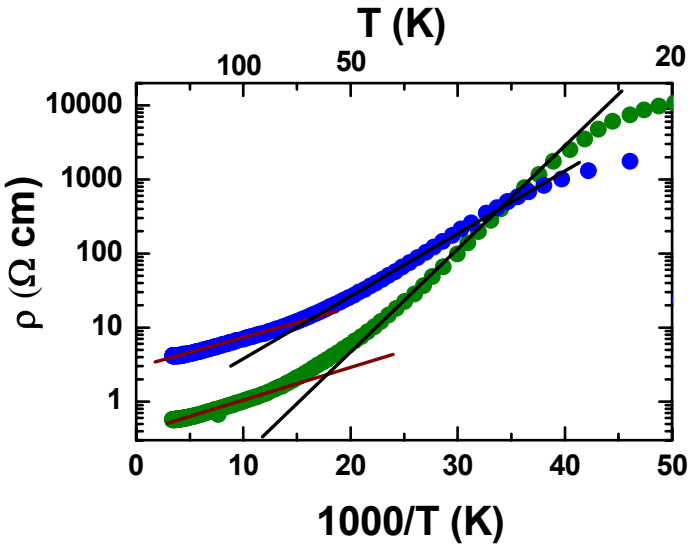

Figure 5.4: dc resistivity versus the inverse temperature for κ-(BEDT-TTF)$_2$Cu[N(CN)$_2$]Br$_{0.2}$Cl$_{0.8}$ (green circles) and κ-(BEDT-TTF)$_2$Cu[N(CN)$_2$]Br$_{0.4}$Cl$_{0.6}$ (blue circles). The solid straight lines are the fitting curves using an activation law.

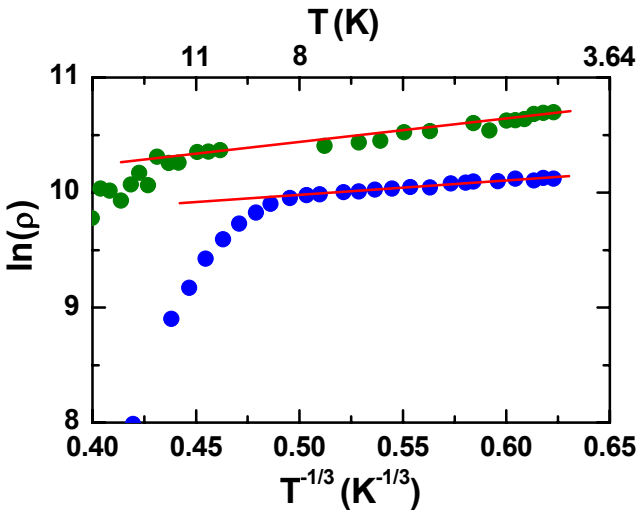

Figure 5.5: ln(ρ) versus T$^{-1/2}$ for κ-(BEDT-TTF)$_2$Cu[N(CN)$_2$]Br$_{0.2}$Cl$_{0.8}$ (green circles) and κ-(BEDT-TTF)$_2$Cu[N(CN)$_2$]Br$_{0.4}$Cl$_{0.6}$ (blue circles). The solid straight lines are the fitting curves using variable-rang hopping (VRH) conduction law (equation 5.1).

5.2.1.2 Fermi liquid state

At high Br dopings, i.e. $x \geq 70\%$, the superconducting transition is found to occur for 70%, 80%, 85% and 90% at 10.5 K, 12 K, 12.2 K and 12 K, respectively. Above the superconducting transition and at low temperatures, the samples are metallic (see Figure 5.1) and the resistivity in this regime can be described by the equation:

$$\rho(T) = \rho_o + AT^2 \qquad (5.2)$$

where ρ_o and A are the residual resistivity and the prefactor of T^2, respectively. Figure 5.6 shows the resistivity as a function of T^2 at low temperatures (T < 40 K) for the samples $x \geq 70\%$. Since the values of the in-plane resistivity are usually hampered by the contributions from the other directions which give a pronounced effect on the value of A, the fitting parameters are obtained after rescaling the values of the resistivity to their room temperature values (see Figure 5.1.b). As shown the results fit quite well with equation 5.2 from T$_c$ (superconducting transition temperature) to the coherence temperature T_o above which equation 5.2 is no longer valid. The fitting parameters of equation 5.2 are given in table 5.1. The residual resistivity values are determined by extrapolating the resistivity to T = 0.

	κ-(BEDT-TTF)$_2$Cu[N(CN)$_2$]Br$_x$Cl$_{1-x}$				
x	70 %	80%	85%	90%	90% (⊥)
ρ_o (Ω cm)	0.50	0.002	0.020	0.0026	0.180
$T_o(x)$ (K)	28	30	30	30	28
$A(x)$ (Ω cm K^{-2})	6.30×10^{-4}	2.85×10^{-5}	3.68×10^{-5}	2.17×10^{-5}	1.41×10^{-3}
$A(x)\times[T_o(x)]^2$ (Ω cm)	0.49	0.026	0.033	0.020	0.894

Table 5.1: The obtained parameters from the fitting equation 5.2 for different Br dopings after rescaling the values of the resistivity to their room temperature values (see Figure 5.1.b). ρ_o, T_o and A are the residual resistivity, the coherence temperature and the prefactor of the T^2, respectively. The last column is the obtained parameters for 90% Br when the resistivity measured in direction perpendicular to the conduction plane (see Figure 5.3).

The T^2 dependence of the resistivity is taken as an evidence of Fermi liquid behavior, which is characteristic of metals in which the dominant scattering mechanism is the interaction of the electrons with one another. This dependence has been observed in several materials as transition metals [159], various organic conductors [25] and heavy fermions [160]. In the electron-electron scattering process, the coefficient A is proportional with the effective carrier mass m^* and with the effective Fermi temperature T_F^* ($A \propto (m^*)^2 \propto (T_F^*)^{-2}$), the coefficient A scales with the square of the Sommerfeld coefficient $\gamma \propto m^* \propto (T_F^*)^{-1}$ of the electronic specific heat $C_{el} = \gamma T$, thus $A/\gamma^2 =$ constant. Such an $A/\gamma^2 =$ constant behavior within a given material class has been verified for different systems including heavy-fermion compounds and transition metals [161,162], the quasi-2D system Sr_2RuO_4 [163] and also for pressurized κ-(BEDT-TTF)$_2$Cu[N(CN)$_2$]Cl [8]. This scaling implies that upon variation of a control parameter x of the system, such as chemical pressure in our case, the product $A(x)\times[T_F^*(x)]^2$ should stay constant. Assuming that the T^2 dependence in Figure 5.6 is of electronic origin due to the low transition temperature, which means $A \propto (T_F^*)^{-2}$ and $T_o \simeq T_F^*$, the product $A(x)\times[T_o(x)]^2$ can be calculated (see Table 5.1). The values of the product $A(x)\times[T_o(x)]^2$ are approximately independent of the chemical pressure for $x \geq$ 80% Br implying that these findings correspond to a strongly correlated Fermi-liquid regime at low temperature. In 70% Br the value of $A(x)\times[T_o(x)]^2$ is much larger than the value of the other Br dopings. This is can be due to location of this compound very close from the border of Mott-transition.

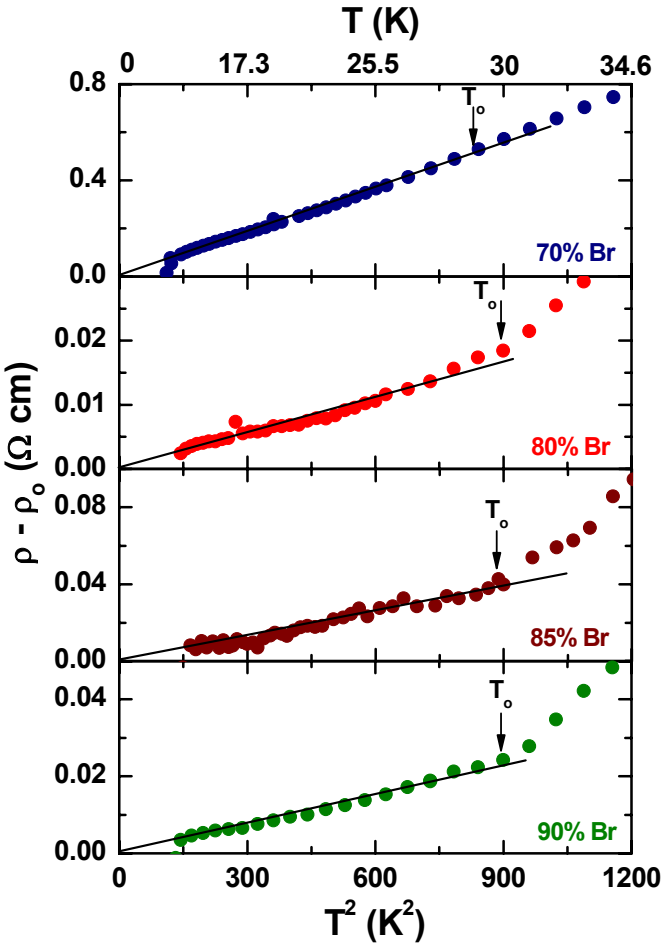

Figure 5.6: In-plane dc resistivity (ρ - ρ$_o$) as a function of T^2 in the low temperature region (T < 40 K) for κ-(BEDT-TTF)$_2$Cu[N(CN)$_2$]Br$_x$Cl$_{1-x}$ (x = 70%, 80%, 85% and 90%). The black lines are the fits of equation 5.2 and T$_o$ is the limit temperature of validation of equation 5.2.

As was discussed before, the ratio A/γ^2 (so called Kadowaki-Woods ratio KWR) is not universal, it takes different values for each class of materials which shows Fermi liquid behavior. For example, it was observed that in transition metals $A/\gamma^2 \approx a_{TM}$ = 0.4 μΩ cm mol^2 K^2/J^2 and in heavy fermion compounds $A/\gamma^2 \approx a_{HF}$ = 10 μΩ cm mol^2 K^2/J^2 [161,164]. Recently, Jacko *et al* [20] have introduced a new ratio, closely related to the KWR, that is universal and correctly describes data for heavy fermions, transition metals, organic charge transfer salts and transition metal oxides. This universal ratio which is given in equation 5.3 includes the effect of the carrier and spatial dimensionality.

$$\frac{Af_{dx}(n)}{\gamma^2} = \frac{81}{4\pi\hbar k_B^2 e^2} \tag{5.3}$$

For the isotropic materials where the electrons form a 3-D Fermi liquid (the heavy fermions, the transition metals, and Rb_3C_{60}) $f_{dx}(n) = f_{3x}(n) = \sqrt[3]{3n^7/\pi^4\hbar^6}$, and for layered compounds, $f_{dx}(n) = f_{2\perp}(n) = 2nm^{*2}t_\perp^{*2}/\pi^2\hbar^6$ in case the resistivity was measured perpendicular to the highly conducting plane and $f_{dx}(n) = f_{2\|}(n) = n^2/\pi c\hbar^2$ if the resistivity was measured parallel to it, where n is the electron density, m^* is the effective mass of the quasi particles, $t_\perp^*$ is the renormalized interlayer hopping integral and c is the interlayer spacing. Figure 5.7 shows the plot of $\gamma^2/f_{dx}(n)$ versus A for different classes of materials. We added our experimental results for κ-(BEDT-TTF)$_2$Cu[N(CN)$_2$]Br$_{0.9}$Cl$_{0.1}$ to this plot. It can be seen clearly that our results have a good agreement with the new universal line, which gives direct evidence that in our studied materials the electron-electron scattering is responsible for the quadratic term in the resistivity.

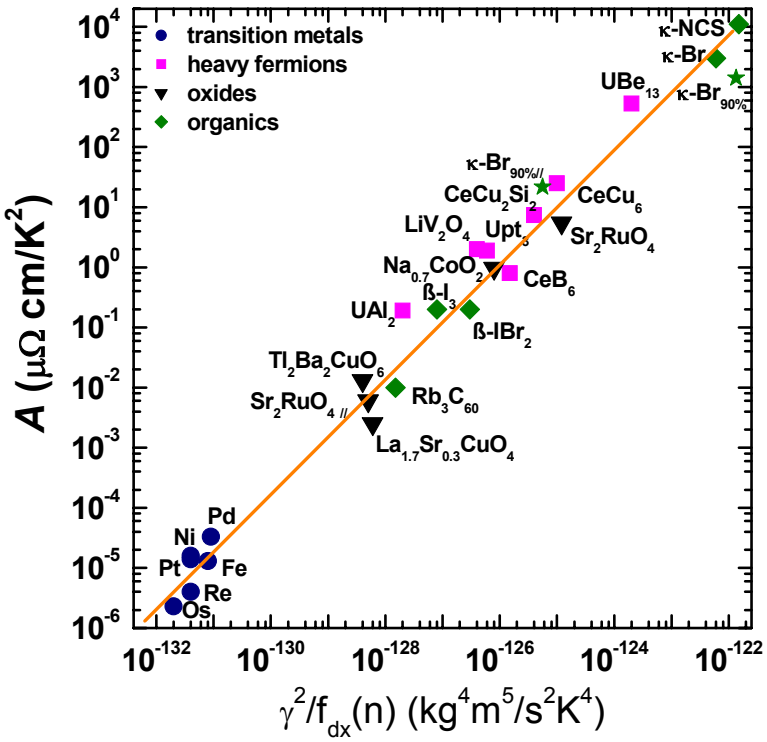

Figure 5.7: Plot of $\gamma^2/f_{dx}(n)$ versus A for several classes of materials including our experimental results for κ-(BEDT-TTF)$_2$Cu[N(CN)$_2$]Br$_{0.9}$Cl$_{0.1}$. The orange line is the new universal line introduced by Jacko *et al* [20]. $f_{2\perp}(n)$ is calculated by taking $m^*/m_e = 3$ [165], $t_\perp^* = 0.04$ meV and $c = 30.016$ Å [62]. We used $\gamma = 22$ mJmol/K^2 [166]. // stands for the resistivity data measured in the highly conducting plane. The original data for all the compounds except ours (green stars) is adopted from Ref. [20].

These findings agree with infrared measurements on the same compound with x = 73% and 85% [19] as shown in Figure 5.8 where the scattering rate has square frequency (ν^2) dependence at T = 20 K in agreement with Fermi liquid theory. This is in accord with dynamical mean-field (DMFT) calculations by J. Merino *et al* [167]. It has been found that the DMFT calculations fit with the infrared experimental results at relative Coulomb repulsion U/t = 10 and transfer integral t = 30 meV (see Figure 5.8).

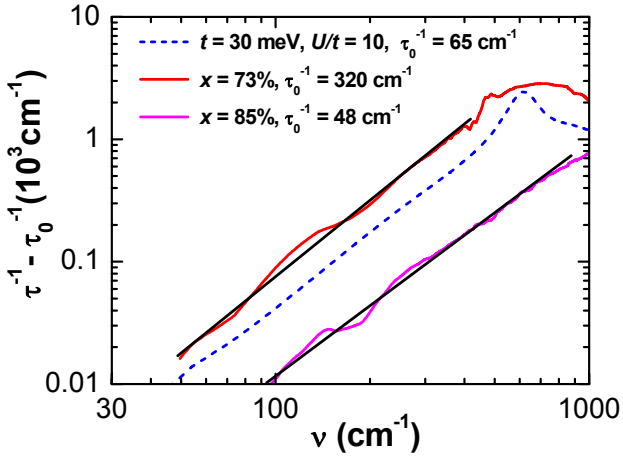

Figure 5.8: Frequency dependence of the scattering rate for κ-(BEDT-TTF)$_2$Cu[N(CN)$_2$]Br$_{0.73}$Cl$_{0.17}$ (red line) and κ-(BEDT-TTF)$_2$Cu[N(CN)$_2$]Br$_{0.85}$Cl$_{0.15}$ (pink line). The solid straight lines are the fitting curves using $\tau^{-1} - \tau_0^{-1} \propto \nu^2$. The dotted blue curve is the dynamical mean-field theory (DMFT) prediction with transfer integral t = 30 meV and relative Coulomb repulsion U/t = 10. τ_0^{-1} is the residual scattering rate [19].

As temperature is increased above T_o, a crossover from Fermi liquid to "bad metal" behavior occurs. Here the resistivity changes from the T^2 behavior to a regime which is characterized by very large values of the resistivity but a metal-like temperature dependence ($d\rho/dT > 0$) as depicted in Figure 5.9 for x = 80% and 90% Br[I]. In bad metal regime the resistivity increases with increasing temperature until a maximum is reached. Below the maximum in resistivity a semiconducting regime is entered ($d\rho/dT < 0$) (see Figure 5.9).

[I] In conventional metals transport occurs by quasiparticles, and their properties can be described by the Boltzmann equation. But if the scattering is sufficiently strong that the mean free path is comparable to a lattice constant ($l \sim a$) then $k_F l \sim \pi$ and the quasiparticle concept breaks down and this is often referred to as the "Mott-Ioffe-Regel limit". The material then is called a "bad metal".

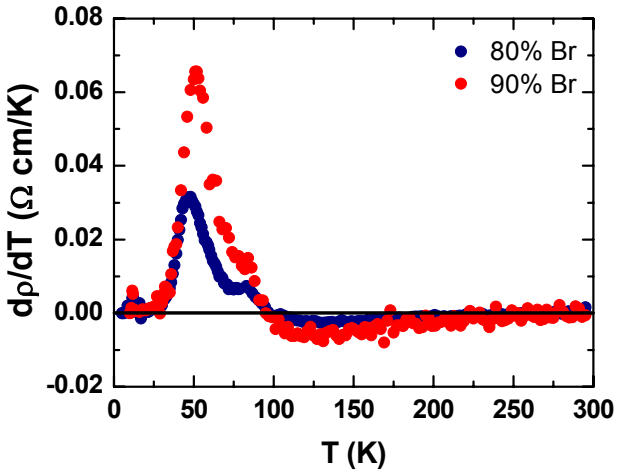

Figure 5.9: Temperature derivative of the in-plane resistivity for κ-(BEDT-TTF)$_2$Cu[N(CN)$_2$]Br$_{0.8}$Cl$_{0.2}$. and κ-(BEDT-TTF)$_2$Cu[N(CN)$_2$]Br$_{0.9}$Cl$_{0.1}$.

5.3 Magnetic Investigations

Electron spin resonance (ESR) and SQUID measurements were carried out on the alloyed series κ-(BEDT-TTF)$_2$Cu[N(CN)$_2$]Br$_x$Cl$_{1-x}$ (x = 0%, 20%, 40%, 70%, 80%, 90% and 100%) in order to understand the magnetic properties of this salt. The recorded ESR spectra for all the crystals along the different crystal directions and in the whole temperature range showed a single absorption line. The crystals were placed in the ESR cavity in direction parallel and perpendicular to the applied external magnetic field to demonstrate the orientation and the temperature dependence of the ESR lineshape, the g-value[I], the linewidth and the spin susceptibility.

5.3.1 Microwave conductivity

As depicted in Figure 5.10, the ESR lineshape at room temperature shows a strong dependence on the orientation of the sample in the cavity with respect to the microwave magnetic field H_1. When the conducting plane (a-c plane) of the sample is oriented perpendicular to H_1 the resulting ESR spectra had a Dysonian lineshape (Figure 5.10.I), while when the conducting plane was parallel to H_1, this means that the microwave electric field E_1 is perpendicular to the conduction plane, symmetric Lorentzian lineshapes were observed for all investigated crystals (Figure 5.10.II).

[I] Since κ-(BEDT-TTF)$_2$Cu[N(CN)$_2$]Br$_x$Cl$_{1-x}$ is orthorhombic two-layer system, the principle magnetic axes coincide with the principle axes of the crystal. This means $a = a$, $b' = b$ and $c^* = c$.

The Dysonian lineshape is observed for all investigated Br dopings when the microwave electric field E_1 is applied parallel to the conducting plane. This finding is attributed to the screening effect (see section 3.1.3.1) which is quantified by calculating the skin depth of the electromagnetic waves (equation 3.4). The calculated skin depths[I] are tabulated in table 5.2. Since the average size of the crystal plane for all used crystals is ≈ 0.7 × 0.8 mm^2 which is larger than the skin depth, a Dysonian line is observed. However, this is not the case when E_1 is applied perpendicular to the conducting plane as shown in Figure 5.10.II. The out-of-plane resistivity at room temperature ($\rho_\perp = \rho_y$) for x = 90% equals ~0.3 Ωm (see Figure 5.3). By using equation 3.4 and taking into account the orientation of the sample and the field geometry shown in Figure 5.10.II, the skin depth of the microwaves along z-direction is determined by the resistivity ρ_y and the skin depth along y-direction is determined by ρ_z. The skin depths δ_z and δ_y are found to equal 0.58 mm and 2.8 mm, respectively. The calculated skin depths δ_z and δ_y are much larger than the size of the *bc*-plane (0.2 × 0.8 mm^2) of the crystal, therefore no skin effect is expected for this case[II]. However, by lowering the temperature (this means increasing or decreasing the resistivity depending on the doping content x) the Lorentzian or Dysonian line changes, as will be discussed later.

κ-(BEDT-TTF)$_2$Cu[N(CN)$_2$]Br$_x$Cl$_{1-x}$				
x	20%	70%	80%	90%
$(\rho_{yz})_{RT} \times 10^{-3}$ (Ωm)	5.68	3.04	6.80	12.4
$(\delta_{yz})_{RT}$ (mm)	0.38	0.28	0.43	0.58

Table 5.2: The Room temperature resistivity and the calculated skin depth for several Br doping of κ-(BEDT-TTF)$_2$Cu[N(CN)$_2$]Br$_x$Cl$_{1-x}$.

[I] We assumed that the resistivity along the conduction plane is isotropic ($\rho_{\parallel} \equiv \rho_y = \rho_z = \rho_{yz}$) for all the crystals (see table 5.2). Consequently, $\delta_y = \delta_z = \delta_{yz}$.

[II] This effect is observed for all crystals since all of them have 2D electronic properties.

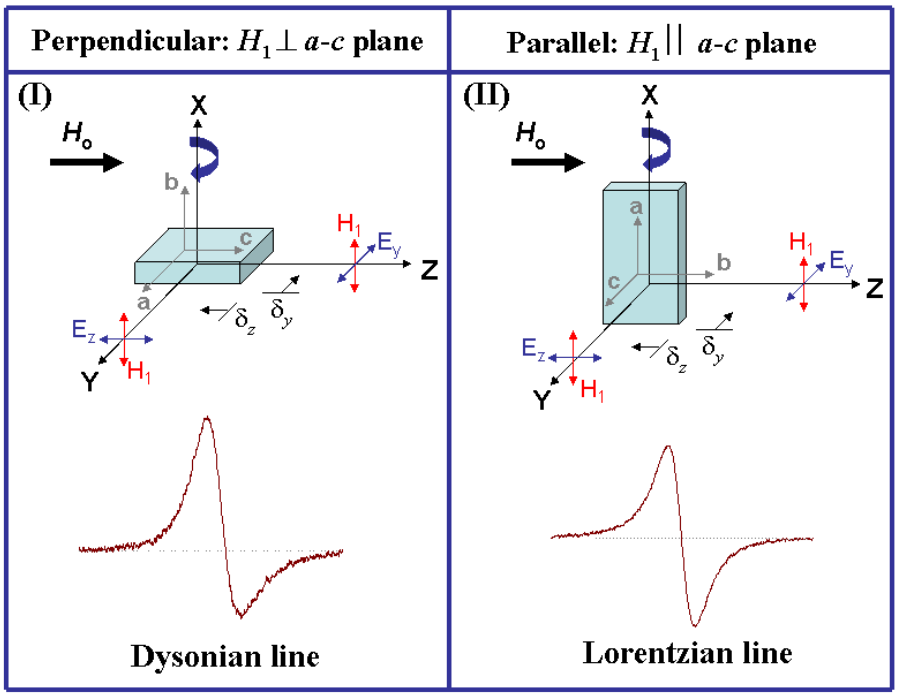

Figure 5.10: The geometrical crystal orientations in the ESR cavity and the corresponding ESR lineshapes of κ-(BEDT-TTF)$_2$Cu[N(CN)$_2$]Br$_x$Cl$_{1-x}$ (x = 0%, 20%, 40%, 70%, 80%, 90% and 100%) at room temperature. The grey axes represent the crystal axes and the black ones the field axes.

Since all κ-(BEDT-TTF)$_2$Cu[N(CN)$_2$]Br$_x$Cl$_{1-x}$ samples were plate-like crystals, the temperature dependence of the microwave (MW) conductivity at 9.5 GHz is evaluated from the ESR Dysonian lineshape analysis using a thin-slab calculation [113,114] (see section 3.1.3.1) as shown in Figure 5.11. For the samples with x < 70% the MW conductivity starts to decrease sharply towards lower temperatures at the Mott-transition around 50 K. At low temperatures below Mott-transition, the lineshape becomes Lorentzian and the MW conductivity can not be calculated. In case $x \geq$ 70% the MW conductivity starts to increase slightly below ≈70 K. The increase becomes stronger below 30 K due to the transition into Fermi liquid state. The qualitative behavior of the MW conductivity agrees with the dc-resistivity while the absolute values could not be calculated. This is because these measurements were performed in ESR cavity which has much less sensitivity than the MW cavity, and also the penetration depth in which the MW penetrate through it is strongly influenced with geometrical shape of the crystal [168]. However, it is important to point out that the qualitative behavior of the microwave conductivity of 100% Br is comparable to those measured by cavity perturbation techniques [169].

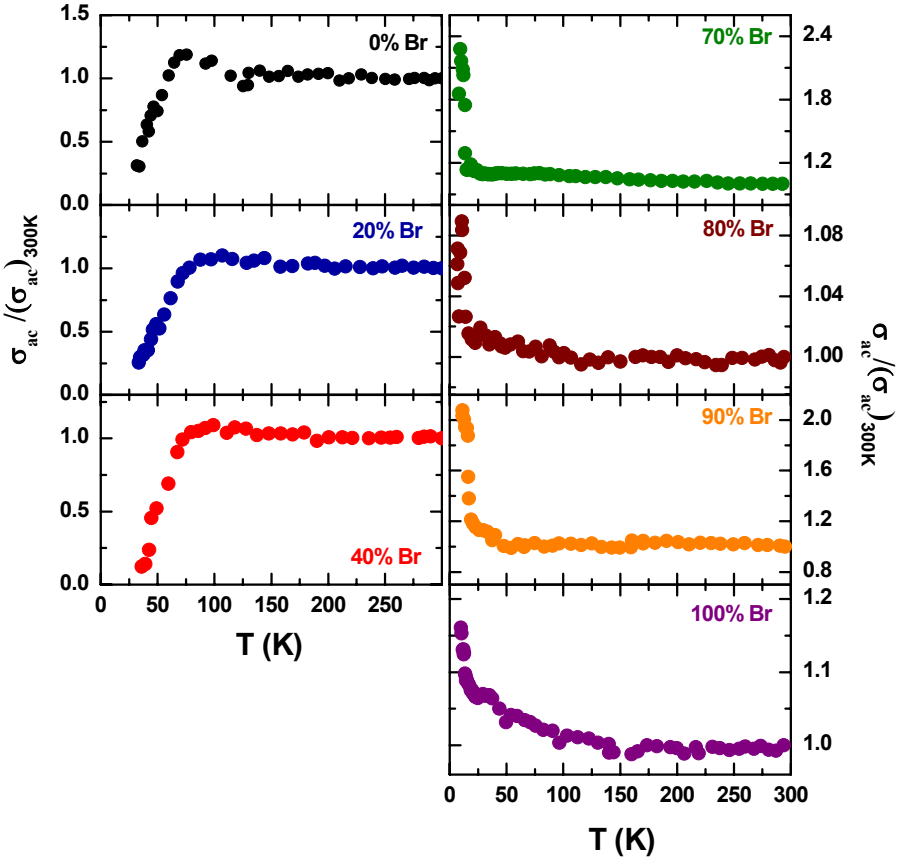

Figure 5.11: The normalized temperature dependence of the microwave (MW) conductivity $\sigma_{ac}/(\sigma_{ac})_{300K}$ at 9.5 GHz as evaluated from the ESR Dysonian line of κ-(BEDT-TTF)$_2$Cu[N(CN)$_2$]Br$_x$Cl$_{1-x}$.

5.3.2 Room temperature ESR results

Figures 5.12 and 5.13 show the angular dependence of the *g*-value and the linewidth at room temperature when the static magnetic field H_o is applied parallel and perpendicular to the conduction plane, respectively (see Figure 5.10)[I]. The dashed lines are least square fits of the measured data with the following equations:

$$\Delta H(\theta) = \left[\Delta H^2(0^o)\cos^2(\theta) + \Delta H^2(90^o)\sin^2(\theta)\right]^{1/2} \tag{5.4}$$

$$g(\theta) = \left[g^2(0^o)\cos^2(\theta) + g^2(90^o)\sin^2(\theta)\right]^{1/2} \tag{5.5}$$

The fitting parameters used in the previous equations to fit the data of the g-value and the linewidth are listed in table 5.3. The *g*-values of all crystals show the same angular dependence, and their values along the principle axes are nearly independent

[I] Here we show the results for x = 0%, 70% and 100% where the results for the other dopings are similar to these samples.

of the doping content x. When the static magnetic field is applied parallel to the conduction plane, the g-value exhibits a nearly isotropic nature with an average maximum value of 2.0044 along a-axis and a minimum value of 2.0031 along c-axis. The nearly isotropic nature of the g-value in this plane is due to the donor stacking pattern in which adjacent donor dimers from BEDT-TTF molecules are approximately perpendicular to each other. However, the small anisotropy in the conduction plane comes from the small incline of BEDT-TTF molecules toward a-axis. If we assume that the adjacent donor dimers from BEDT-TTF molecules are perfectly perpendicular to each other, the in-plane g-value can be evaluated as:

$$g_{//} = \left(\frac{g_a^2 + g_c^2}{2} \right)^{1/2} \tag{5.6}$$

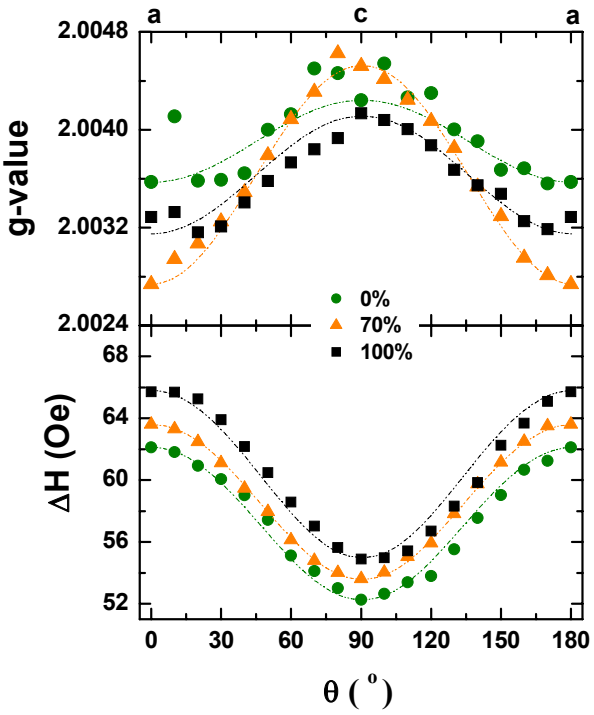

Figure 5.12: Angular dependence of the linewidth and the g-value along the a-c plane of κ-(BEDT-TTF)$_2$Cu[N(CN)$_2$]Br$_x$Cl$_{1-x}$ (with x = 0%, 70% and 100%) at room temperature. The least square fittings of the linewidth and the g-value are shown by the dashed lines.

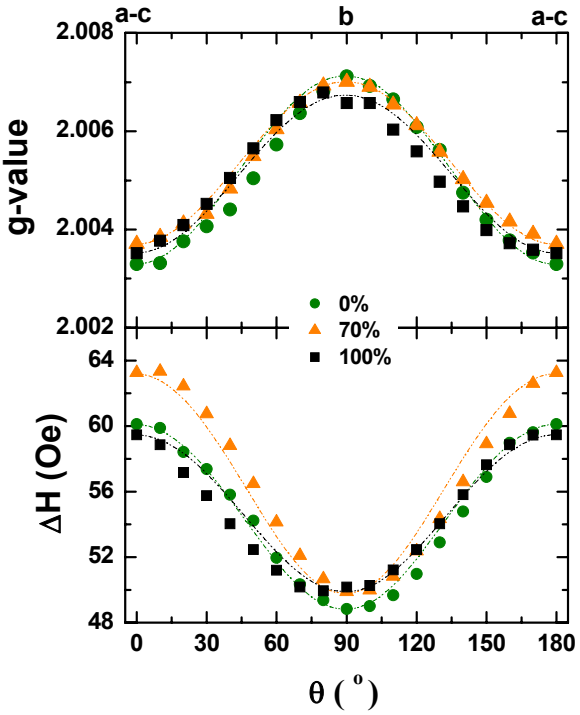

Figure 5.13: Angular dependence of the linewidth and the *g*-value along the *b-ac* plane of κ-(BEDT-TTF)$_2$Cu[N(CN)$_2$]Br$_x$Cl$_{1-x}$ (with x = 0%, 70%,and 100%) at room temperature. The least square fittings of the linewidth and the *g*-value are shown by the dashed lines.

Table 5.4 summarizes the calculated in-plane *g*-value for all the investigated crystals of κ-(BEDT-TTF)$_2$Cu[N(CN)$_2$]Br$_x$Cl$_{1-x}$. In the other case, when the static magnetic field is applied perpendicular to *a-c* plane, the *g*-value exhibits a clear anisotropic behaviour with a maximum average value of 2.0069 along *b*-axis. The *g*-value maximum corresponds to the orientation where the static magnetic field is approximately parallel to the long molecular axis (or central C=C double bond) of the BEDT-TTF molecule. The minimum is observed with an average value of 2.0036. This value does not belong to the value along *a*-axis or *c*-axis. We found that this value is comparable the calculated in-plane average *g*-value ($\bar{g}_{//}$ = 2.0037) (see table 5.4).

The angular dependence of the *g*-value of κ-(BEDT-TTF)$_2$Cu[N(CN)$_2$]Br$_x$Cl$_{1-x}$ was observed in many (BEDT-TTF)-based systems where the *g*-value is essentially determined by the coupling of the conduction electrons to the BEDT-TTF molecules [170]. The anisotropy of the *g*-value at room temperature originates from the coupling of the spin angular momentum to the orbital angular momentum as discussed in section 3.1.3.2, where the maximum *g*-value (g_x), the intermediate (g_y) and the minimum value (g_z) are expected to be along the molecular long axis, short

axis, and normal to the molecular plane of BEDT-TTF molecules, respectively. Due to the orthorhombic two-layer system of κ-(BEDT-TTF)$_2$Cu[N(CN)$_2$]Br$_x$Cl$_{1-x}$, the principle magnetic axes coincide with the principle axes of the crystal. Consequently, the principle *g*-tensor of the BEDT-TTF cations are $g_x = 2.0069$, $g_y = 2.0044$ and $g_z = 2.0031$. These values are in a good agreement with that determined for κ-(BEDT-TTF)$_2$Cu[N(CN)$_2$]Br [11,70]. This interpretation for the anisotropy of the *g*-value in terms of the BEDT-TTF cations explains also the independence of the observed *g*-value along each axis on the doping content *x* of κ-(BEDT-TTF)$_2$Cu-[N(CN)$_2$]Br$_x$Cl$_{1-x}$. Furthermore, the *g*-value along *b*-axis is much less than the value observed in other BEDT-TTF salts [2]. This is can be due to the dihedral angle between the donor plane and the anion plane in this compound which is about 56^o and this leads the *g*-value along *b*-axis to have a component along the short molecular axis and perpendicular to it.

κ-(BEDT-TTF)$_2$Cu[N(CN)$_2$]Br$_x$Cl$_{1-x}$							
x	0%	20%	40%	70%	80%	90%	100%
Δ*H*(*a*) Oe	52.28	53.60	52.00	53.60	54.97	54.98	55.00
Δ*H*(*b*) Oe	48.84	48.98	48.79	49.80	50.26	49.90	49.91
Δ*H*(*c*) Oe	62.12	64.80	62.55	63.60	66.12	66.40	65.80
ΔH(*a*-*c*) Oe	60.11	61.21	60.38	63.20	61.53	62.64	59.47
g(*a*)	2.0042	2.0049	2.0042	2.0045	2.0041	2.0046	2.0041
g(*b*)	2.0071	2.0070	2.0072	2.0070	2.0068	2.0069	2.0067
g(*c*)	2.0036	2.0034	2.0023	2.0027	2.0031	2.0036	2.0032
g(*a*-*c*)	2.0033	2.0038	2.0039	2.0037	2.0034	2.0037	2.0035

Table 5.3: The Fitting parameters for the orientation dependence of the linewidth and the *g*-value along *a*-*c* plane and *b*-*c* plane of κ-(BEDT-TTF)$_2$Cu[N(CN)$_2$]Br$_x$Cl$_{1-x}$ at room temperature using equations 5.4 and 5.5. The given fitting parameters Δ*H*(*c*) and *g*(*c*) are from the orientation dependence along *a*-*c* plane.

κ-(BEDT-TTF)$_2$Cu[N(CN)$_2$]Br$_x$Cl$_{1-x}$						
x	$g_{//}$	$g(a\text{-}c)$	g_b	$\Delta H_{//}$ (Oe)	$\Delta H(a\text{-}c)$ (Oe)	ΔH_b (Oe)
0%	2.0039	2.0033	2.0071	57.41	60.11	48.84
20%	2.0041	2.0038	2.0070	59.46	61.21	48.98
40%	2.0033	2.0039	2.0072	57.50	60.38	48.79
70%	2.0036	2.0037	2.0070	58.80	63.20	49.80
80%	2.0036	2.0037	2.0068	60.80	61.53	50.26
90%	2.0041	2.0037	2.0069	60.96	62.64	49.90
100%	2.0036	2.0035	2.0067	60.64	59.47	49.91

Table 5.4: A comparison between the calculated in-plane *g*-value and the linewidth using equations 5.6 and 5.8, and the measured ones along *a*-*c* plane and along *b*-axis of κ-(BEDT-TTF)$_2$Cu[N(CN)$_2$]Br$_x$Cl$_{1-x}$ at room temperature.

The measured angular dependence of the linewidth at room temperature is qualitatively not similar to that of the *g*-value as shown in Figures 5.12 and 5.13. In *a*-*c* plane, the linewidth shows anisotropic behavior with an average maximum value of 65 Oe along *c*-axis and a minimum value of 54 Oe along *a*-axis, while on the other plane, the linewidth shows a minimum average value of 49 Oe along *b*-axis and the maximum average value of 61 Oe which is comparable to the in-plane value of the linewidth (see table 5.4) that was calculated using equation 5.8. This result confirms the result of the *g*-value that in case the static magnetic field is applied perpendicular to *a*-*c* plane the measured angular dependence of the ESR parameters correspond to *b*-axis and *a*-*c* plane.

$$\Delta H_{//} = \left(\frac{\Delta H_a^2 + \Delta H_c^2}{2} \right)^{1/2} \tag{5.8}$$

The measured linewidth and its angular dependence shown in Figures 5.12 and 5.13 are in principal very similar to those shown by Nakamura *et al* [70]. The measured g-value is very close from the g-value of the free electron. Kataev *et al* [11] attributed the ESR signal in these compounds to the conduction electrons (CE). However, the broadening mechanism of the ESR linewidth in this compound can not be explained within the framework of the Elliot relaxation mechanism (see section 3.2.5) which is applicable to some quasi 1D organic metals and selected BEDT-TTF salts [170,171]. This is because that Elliot theory did not take into account the interchain scattering time $\tau_\perp$ which becomes important with increasing the

dimensionality, and has an anisotropic character which may be responsible to the observed difference in the anisotropy between the g-value and the linewidth. Bloch's theory [172] showed that with increasing the dimensionality from 1D to 2D the electron-phonon interaction should start to contribute to the linewidth. Since we have observed that the linewidths of κ-(BEDT-TTF)$_2$Cu[N(CN)$_2$]Br$_x$Cl$_{1-x}$ is more than one order of magnitude larger than that typical for 1D organic conductors [172], this means that the electron-phonon interaction takes part in the broadening mechanism of the linewidth in this compound. Moreover, the broadening mechanism of the linewidth seems to be correlated to the structural arrangement of the BEDT-TTF molecules. For example, the linewidth of κ-(BEDT-TTF)$_2$I$_3$ is similar to our results, and could not be explained within Elliot mechanism, while the linewidth of β-(BEDT-TTF)$_2$I$_3$ is 2 – 3 order of magnitude less than that observed in κ-salts and was explained within Elliot theory [2,71]. However, the broadening mechanism of the linewidth of κ-(BEDT-TTF)$_2$Cu[N(CN)$_2$]Br$_x$Cl$_{1-x}$ is attributed to structural reasons, where the vibration of the terminal ethylene groups at high temperature works as scattering centers for the conduction electrons, thus increasing the relaxation rate.

5.3.3 Low temperature investigations

Temperature dependent measurements of the ESR spectra of κ-(BEDT-TTF)$_2$Cu[N(CN)$_2$]Br$_x$Cl$_{1-x}$ were performed when the conduction plane of the sample was oriented in direction parallel to the magnetic field (H_o//*c*-axis) and perpendicular to it (H_o//*b*-axis) as depicted in Figure 5.10. For low Br dopings, $x < 70\%$, the ESR lineshape at room temperature has a Dysonian lineshape along *c*-axis and a symmetric Lorentzian lineshape along *b*-axis. The Dysonian line along *c*-axis is gradually converted to Lorentzian line with decreasing temperature below about 50 K and becomes symmetric by decreasing the temperature as shown in Figure 5.14 for κ-(BEDT-TTF)$_2$Cu[N(CN)$_2$]Br$_{0.2}$Cl$_{0.8}$. This conversion in the ESR lineshape is due the increase of the skin depth with decreasing temperature. The Lorentzian line along *b*-axis does not change with decreasing temperature as expected.

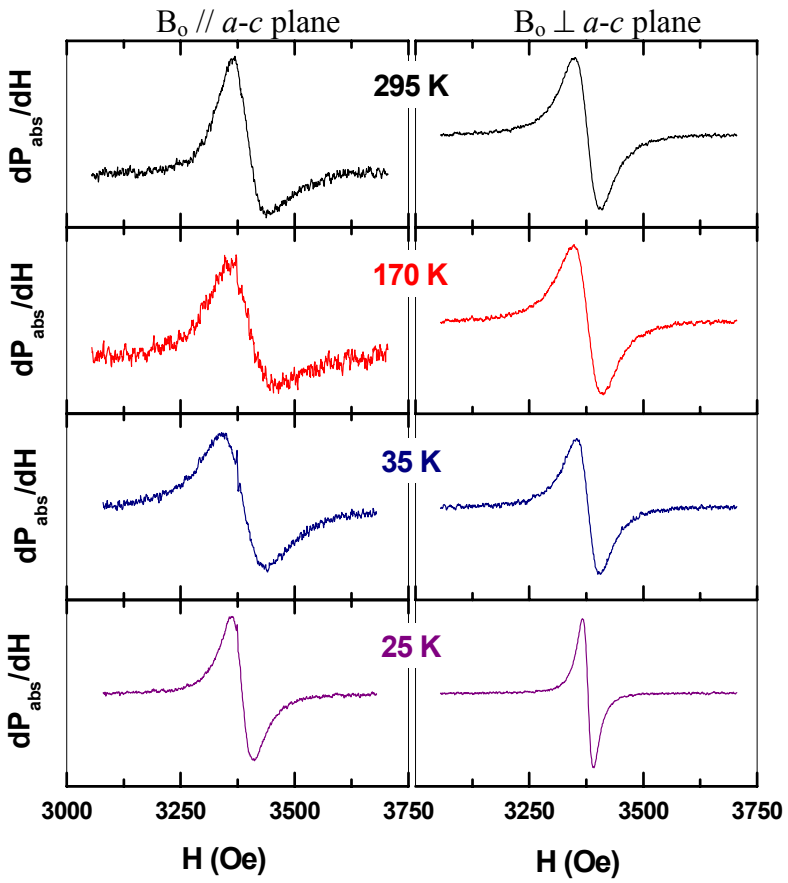

Figure 5.14: The ESR spectra of κ-(BEDT-TTF)$_2$Cu[N(CN)$_2$]Br$_{0.2}$Cl$_{0.8}$ at different temperatures when the magnetic field H_o is applied parallel and perpendicular to the conduction plane (*a*-*c* plane).

For high Br dopings, $x \geq 70\%$, the ESR spectra at room temperature has a Dysonian lineshape along *c*-axis and a symmetric Lorentzian lineshape along *b*-axis as was discussed above. With decreasing temperature the Dysonian line along *c*-axis stays always asymmetric down to low temperatures, while along *b*-axis the Lorentzian line is gradually converted to Dysonian below about 40 K due to a significant decrease of the skin depth (increase in conductivity) and becomes more asymmetric at low temperature as shown in Figure 5.15 for κ-(BEDT-TTF)$_2$Cu[N(CN)$_2$]-Br$_{0.8}$Cl$_{0.2}$.

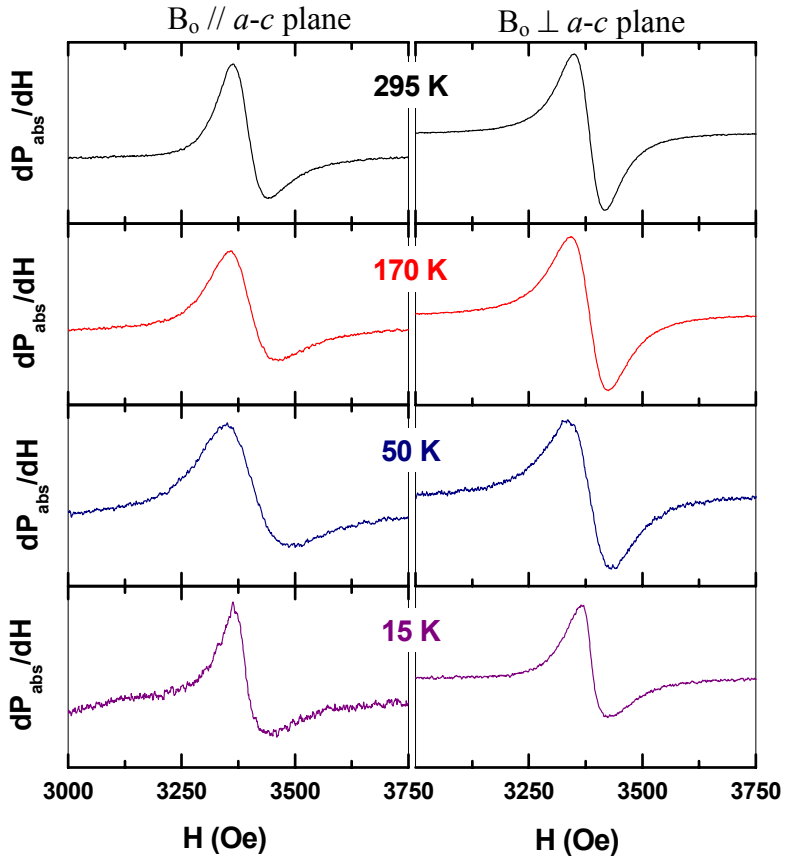

Figure 5.15: The ESR spectra of κ-(BEDT-TTF)$_2$Cu[N(CN)$_2$]Br$_{0.8}$Cl$_{0.2}$ at different temperatures when the magnetic field H_o is applied parallel and perpendicular to the conduction plane (*a*-*c* plane).

The temperature dependence of the linewidth and the *g*-value along *c*-axis (H$_o$//*a*-*c* plane) and *b*-axis (H$_o$⊥*a*-*c* plane) are shown in the Figures 5.16 and 5.17. The linewidth is not monotonic with temperature for all compounds of the series κ-(BEDT-TTF)$_2$Cu[N(CN)$_2$]Br$_x$Cl$_{1-x}$ and their temperature dependence is approximately identical. In the 0%, 20% and 40% Br samples, the linewidth increases from 62 Oe and 49 Oe at room temperature with decreasing temperature, reaches a broad maximum around 75 K to values of 95 Oe and 60 Oe along *c* and *b*-axis, respectively, then decreases sharply with decreasing the temperature down to 22 K where the ESR spectra vanish totally for both directions. In the samples with $x \geq 70\%$ the broad maximum of the linewidth shifts to lower temperatures around 60 K with linewidth values of 110 Oe and 70 Oe along both directions. Then, ΔH decreases sharply with decreasing temperature down to around 8 K where the ESR spectra vanish totally for both directions. The *g*-value along both directions in all compounds except the sample with 70% Br is temperature independent in the whole temperature range with a smooth anomaly at low temperatures. In the 70% Br

sample, the *g*-value increases below 20 K along *c*-axis while no change along *b*-axis is observed.

The observed non-monotonic change of the linewidth with temperature means that the relaxation mechanisms corresponding to spin-phonon scattering can not be accounted the main contribution to the linewidth; moreover the torsional oscillations of the BEDT-TTF$^+$ molecules, which have been found to dominate in ΔH(T) of (TMTSF)$_2$X, (TMTTF)$_2$X and some of BEDT-TTF salts [2,126] are not very significant in the κ-phase arrangement of BEDT-TTF because the structure of the cationic sheet has low symmetry and there is no symmetry limitation on the spin-orbit coupling between neighbouring BEDT-TTF molecules, where the linewidth is much less when there is a symmetry limitation as in case of TMTTF-salts. The increase of the linewidth with decreasing temperature is attributed to the scattering of the conduction electrons (CE) caused by vibrations of the terminal ethylene groups of the BEDT-TTF molecules which at high temperatures are disordered. With decreasing temperature their vibrations slow down until they freeze out at T = T_g [10]. The broad maximum of the linewidth can be explained by assuming that at high temperatures the frequency of these vibrations is higher than a typical ESR frequency (9.5 GHz), therefore they are not effective in the relaxation of the conduction electrons, but with lowering the temperature, the frequency of vibrations decreases, and when it starts to match the ESR frequency, the scattering of the conduction electrons becomes more effective leading to a broad maximum of ΔH. This means by performing high frequencies ESR experiments on these compounds in the temperature range 80 – 300 K one could estimate the frequency of the vibrations of the terminal ethylene groups and clarify the frequency dependence of the relaxation mechanism. The fast subsequent decrease of the linewidth with decreasing temperature is due to the rapid freezing out of the vibrations of the terminal ethylene groups which reduces the scattering rate of the conduction electrons.

The ordering of the terminal ethylene group was detected by X-ray measurements at low temperatures in κ-(BEDT-TTF)$_2$Cu[N(CN)$_2$]X (X = Cl, Br, I) [173] and also in our dc-measurements (see Figure 5.3) and found to occur at T = $T_g \approx 77$ K [10]. In our case, the observed maximum of the linewidth below T_g means that the broadening of the linewidth at low temperature is influenced by another mechanism than the vibration of the terminal ethylene groups. This mechanism can be due to the antiferromagnetic spin-fluctuation which has more pronounced effect in the high Br samples where the maximum of the linewidth drift more to lower temperatures. This observation is consistent with that found in the temperature dependence of the

nuclear-spin relaxation rate in κ-(BEDT-TTF)$_2$Cu[N(CN)$_2$]Br which is explained by using spin-fluctuation model [174] as shown in Figure 5.18.

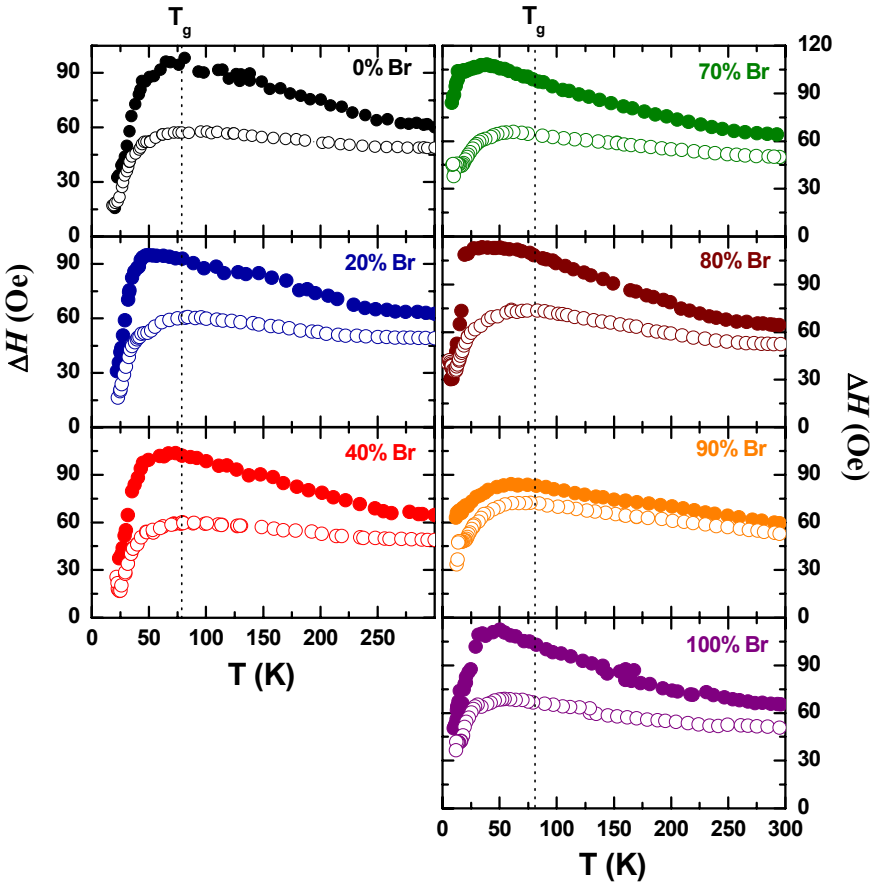

Figure 5.16: The temperature dependence of the linewidth of κ-(BEDT-TTF)$_2$Cu[N(CN)$_2$]Br$_x$Cl$_{1-x}$ when the static magnetic field H_o is applied parallel to the conduction plane along *c*-axis (filled circles) and perpendicular to it along *b*-axis (opened circles). The dotted line shows the T$_g$ transition temperature.

In the low Br doped samples, the vanishing of the ESR spectra below around 22 K is due to the transition into antiferromagnetic ground state which was detected by a NMR experiment in κ-(BEDT-TTF)$_2$Cu[N(CN)$_2$]Cl at T_N = 27 K [78], while at high Br dopings, it is associated with the transition into the superconducting ground state. The temperature independence of the *g*-value at low temperatures close to AFM transition is unusual because it is expected that the *g*-value increases/decreases due to the change of the internal magnetic field associated with the antiferromagnetic ordering. However, the change of the *g*-value might be small and occur in a very narrow temperature range and thus is not observable in the ESR spectra close to AFM transition. In the superconducting pure Br compound, it was shown by Kataev *et al* [11] that the *g*-value decreases below T_c due to decrease of the average internal

magnetic field. Since in our results the ESR spectra for the high Br samples vanish in a small temperature range below T_c, the decrease of the *g*-value could not be observed clearly. In the 70% Br sample, the strong shift in the *g*-value along *c*-axis could be due to antiferromagnetic fluctuations above the superconducting transition (as a result of the competition between the AFM and the superconductivity) where this sample is very close from the border of metal-to-insulator phase transition.
In all investigated samples of low Br dopings, antiferromagnetic resonance (AFMR) does not observed. This is can be due to the small size of the used crystals where the intensity of the AFMR modes are usually low and using large crystal is very necessarily to observe it.

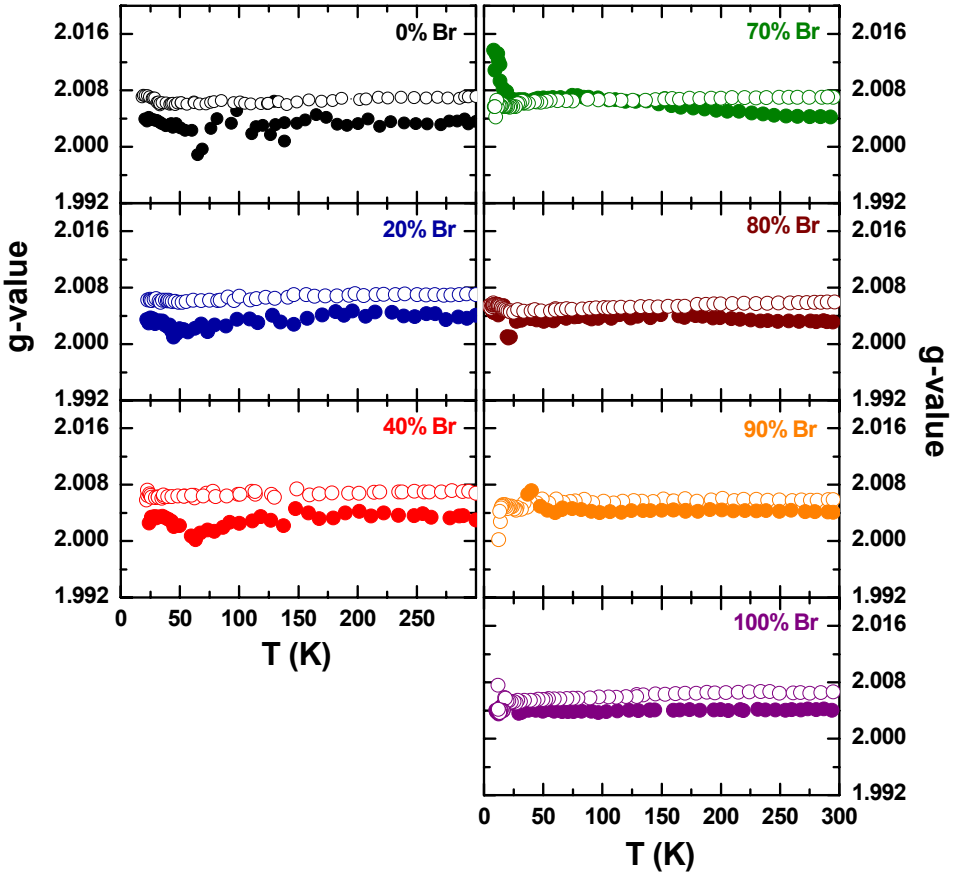

Figure 5.17: The temperature dependence of the *g*-value of κ-(BEDT-TTF)$_2$Cu[N(CN)$_2$]Br$_x$Cl$_{1-x}$ when the static magnetic field H_o is applied parallel to the conduction plane along *c*-axis (filled circles) and perpendicular to it along *b*-axis (opened circles).

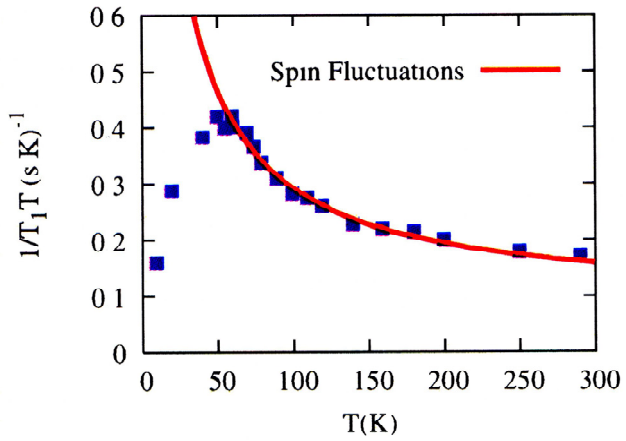

Figure 5.18: Comparison of the measured nuclear-spin relaxation rate per unit temperature, $1/T_1T$ (blue rectangles), with the prediction of the spin-fluctuation model (solid line) for κ-(BEDT-TTF)$_2$Cu[N(CN)$_2$]Br [174].

The spin susceptibility at room temperature was found the same for the pure Cl and pure Br compounds with a value of 5×10^{-4} emu/mol [70,80]. The temperature dependence of the spin susceptibilities for x = 0%, 20% and 40 % Br samples are shown in Figure 5.19. The temperature dependence of the spin susceptibility for all the samples is similar. It is nearly temperature independent from room temperature down to around 40 K as expected for the Pauli susceptibility of metals. Below 40 K down to 22K, the spin susceptibility decreases rapidly to a value which is five times smaller than the value at room temperature, below 22 K the ESR spectra vanish. These results are comparable to those published by Kubota *et al* [80] for κ-(BEDT-TTF)$_2$Cu[N(CN)$_2$]Cl. The rapid decrease of $\chi(T)$ below 40 K in parallel with increasing the linewidth below 25 K along *b*-axis for the sample with 40% Br (see the inset in Figure 5.19) is attributed to growing three-dimensional antiferromagnetic short range order, which can be due to exchange interactions between layers [175]. However, we did not observe any increase for the linewidth in both directions for the samples 0% and 20% Br.

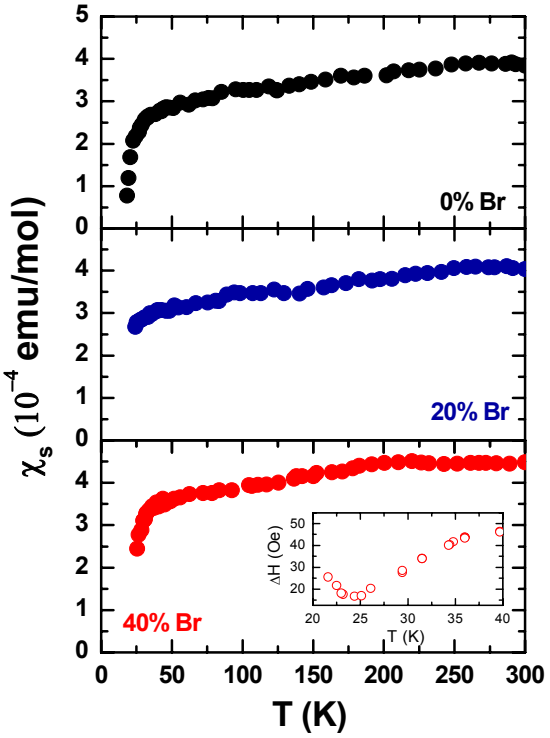

Figure 5.19: Temperature dependence of the spin susceptibility of κ-(BEDT-TTF)$_2$Cu[N(CN)$_2$]Br$_x$Cl$_{1-x}$ for x = 0%, 20% and 40%. The inset is the temperature dependence of the linewidth for x = 40% along *b*-axis at low temperatures. The absolute values of the spin susceptibility are obtained by comparing the intensity of the measured spectra with that of DDPH.

The antiferromagnetic ordering is suppressed with Br dopings. Lefebvre *et al* [143] found that the antiferromagnetic ordering at the Néel temperature T_N is gradually suppressed under the pressure with the value $dT_N/dP \cong$ -0.025 K/bar for the pressure coefficient.

For high Br dopings, i.e. $x \geq 70\%$, the spin susceptibility at T > 100 K more or less is similar to that observed for $x < 70\%$. As shown in Figure 5.20, the spin susceptibility for x = 70%, 80%, 90% and 100% Br decreases very smoothly from the room temperature down to around 100 K revealing more or less Pauli spin susceptibility in these compounds. Below 100 K the decrease of the spin susceptibility is more pronounced with decreasing temperature and at around 50 K a sharp drop can be observed down to 8 K, below this temperature the ESR spectra vanish. The decrease of the susceptibility for T < 100 K can be due to the decrease of the density of states at Fermi surface $N(E_F)$ induced by the vibrations of the terminal ethylene groups, which is proposed to play an important role in tuning the occupancy of the molecular energy levels [176]. Below T_c the formation of Cooper pairs results in a spin singlet ground state.

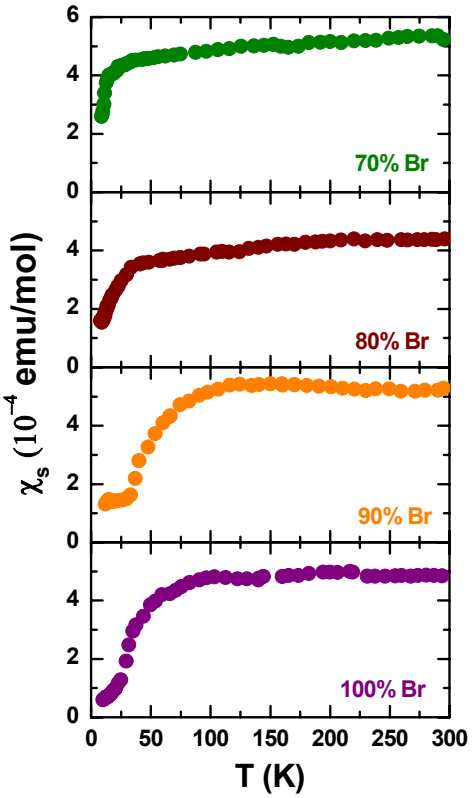

Figure 5.20: Temperature dependence of the spin susceptibility of κ-(BEDT-TTF)$_2$Cu[N(CN)$_2$]Br$_x$Cl$_{1-x}$ (with x = 70%, 80%, 90% and 100%). The absolute values of the spin susceptibility are obtained by comparing the intensity of the measured spectra with that of DDPH.

The temperature dependence of the spin susceptibility shown in Figure 5.20 can be fitted with a two-gap model using the following equation [11]:

$$\chi(T) = (A_1 / T)\exp(-\Delta_1 / k_B T) + (A_2 / T)\exp(-\Delta_2 / k_B T) \qquad (5.9)$$

where Δ_1, Δ_2 are the energy gaps and A_1, A_2 are the fitting parameters. The values of the energy gaps and the fitting parameters obtained from the linear fit of the logarithm of the temperature multiplied by the normalised spin susceptibility $\ln[T \times (\chi_s / (\chi_s)_{RT}]$ versus the inverse temperature $(1/T)$ as depicted in Figure 5.21 are tabulated in table 5.5. The energy gaps at high temperatures are much larger than those at low temperatures. Since the energy gap at high temperature is not constant and varies randomly from one sample to another, this can not be due to a complicated band structure with two gaps as supposed by Kataev *et al* [11]. We propose that this gap is an average of a random distribution of gaps comes from

impurities.[I] The smaller energy gaps at low temperature are approximately constant with an average value of 23.6 K. This value is comparable to the superconducting gap expected for these organic superconductors within BCS theory ($2\Delta \approx 19$ K at $T_c = 10.5$ K) [95,96].

κ-(BEDT-TTF)$_2$Cu[N(CN)$_2$]Br$_x$Cl$_{1-x}$				
x	70%	80%	90%	100%
A_1 (a. u)	487.2	427.4	2.4	347.2
Δ_1 (K)	233	196	33.4	115
A_2 (a. u)	57.8	45.3	3.9	5.7
Δ_2 (K)	25.4	26	21.1	21.8

Table 5.5: The obtained energy gaps Δ_1, Δ_2 and the fitting parameters A_1, A_2 from the fitting equation 5.7 for κ-(BEDT-TTF)$_2$Cu[N(CN)$_2$]Br$_x$Cl$_{1-x}$ (with x = 70%, 80%, 90% and 100%).

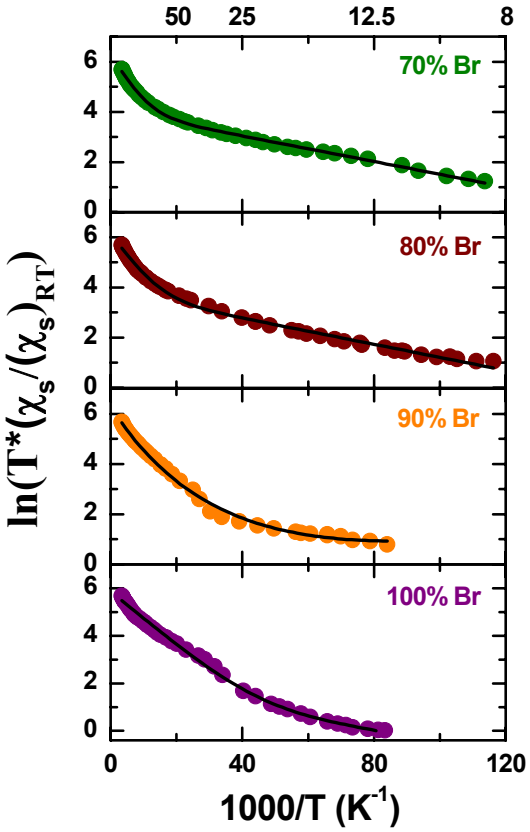

Figure 5.21: Plots of $\ln(T \times (\chi_s/(\chi_s)_{RT})$ versus $1/T$ of κ-(BEDT-TTF)$_2$Cu[N(CN)$_2$]Br$_x$Cl$_{1-x}$ (with x = 70%, 80%, 90% and 100%). The black lines are the fitting lines using equation 5.9.

[I] This assumption was checked by measuring the spin susceptibility for two single crystals of κ-(BEDT-TTF)$_2$Cu[N(CN)$_2$]Br$_{0.9}$Cl$_{0.1}$ and we found that the energy gap at high temperature is not the same.

The semiconducting-like picture of the spin susceptibility in the metallic regime of the dc resistivity at low temperatures in the highly doped Br samples can be due to presence of a sharp minimum in the density of states close to the Fermi level (pseudogap) which was found in κ-(BEDT-TTF)$_2$Cu[N(CN)$_2$]Br [21,177].

It was shown in chapter one that TMT*C*F salts are quasi one-dimensional organic conductors, and they can have a variation in their dimensionality due to the difference in the interchain coupling t_b. Although TMTSF salts are metallic, they could be described by a spin chain model. In two-dimensional systems, the lattice can be described by frustrated square or triangular lattice (see Figure 5.22). These lattices can be distinguished from the ratio t_2/t_1. While in the square lattice the ratio $t_2/t_1 \rightarrow 0$, it has a finite value in the triangular lattice. In Figure 1.14 the metallic and insulating phases in κ-(BEDT-TTF)$_2$*X* were shown in terms of a Mott transition with *U*/*t* as a controlling parameter. The lattice of this system can be modeled into a triangular lattice (see Figure 1.13) or a square lattice where the controlling parameter *U*/*t* influences on the ratio t_2/t_1. The antiferromagnet κ-(BEDT-TTF)$_2$Cu[N(CN)$_2$]Cl has an isotropy of t_2/t_1 = 0.64 at ambient pressure (see Table 1.5). This imply that one expect an agreement between the theoretical model of the spin susceptibility based on triangular lattice model [178] and the experimental data. Surprisingly, we could not to fit the spin susceptibility data with this model even if the anisotropy is considered. Another attempt to fit the spin susceptibility is done using *S* = 1/2 Heisenberg AFM on square lattice model [100,101] with |*J*| = 260 K for κ-(BEDT-TTF)$_2$Cu[N(CN)$_2$]Cl as shown in Figure 5.23. It is clear that this model does not fit the experimental results especially at low temperatures (T < 125 K) where the model deviates. This can be due to the fact that the calculations of this model were performed on a finite size with t_2/t_1 = 0 while the investigated system has infinite size with t_2/t_1 = 0.64; furthermore, the model does not account the magnetic fluctuations at low temperatures. Generally, the failure of both models in fitting the spin susceptibility data can be possibly because the system is situated very close from the Mott transition. Therefore, a further theoretical analysis using higher-order corrections or the Hubbard model is needed.

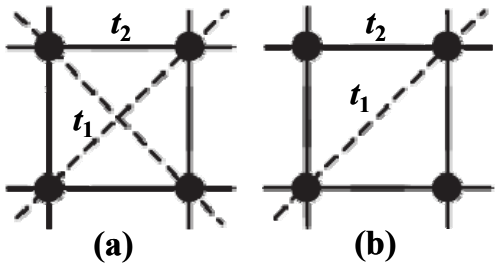

Figure 5.22: Lattice structure of geometrically frustrated lattices (a) on a square lattice and (b) on an anisotropic triangular lattice.

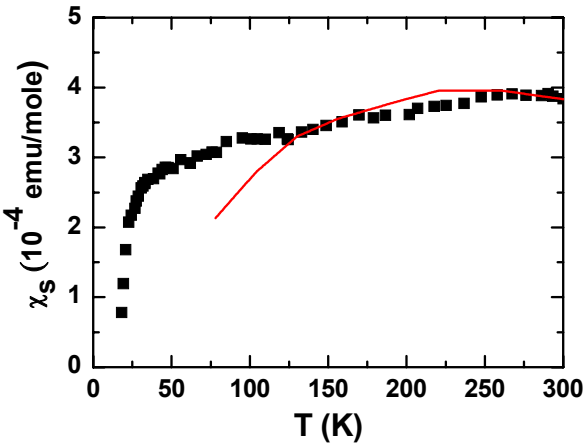

Figure 5.23: Temperature dependence of the spin susceptibility of κ-(BEDT-TTF)$_2$Cu[N(CN)$_2$]Cl. The line corresponds to a fit using S = 1/2 Heisenberg AFM on square lattice model [100,101] with $|J|$ = 260 K.

The superconducting transition in high Br doping was confirmed by observing the shielding signal in magnetization measurements as shown in Figure 5.24. The shielding signal was observed after cooling the sample slowly (6 K/hour) down to 1.8 K in zero magnetic field and then applying a magnetic field of 5 G perpendicular to the conduction plane. The measurements of the magnetic susceptibility were carried out during the heating[I]. In both samples the magnetic susceptibility shows a sharp drop at about 11.8 K, and the shielding signal has a broad transition for the 70% Br than 90% Br. However, the broad shielding signal for both samples indicates that the measured crystals are inhomogeneous [179].

[I] The shielding signal was very weak when the sample is cooled very fast (600 K/hour) or when the applied magnetic field was higher than 10 G.

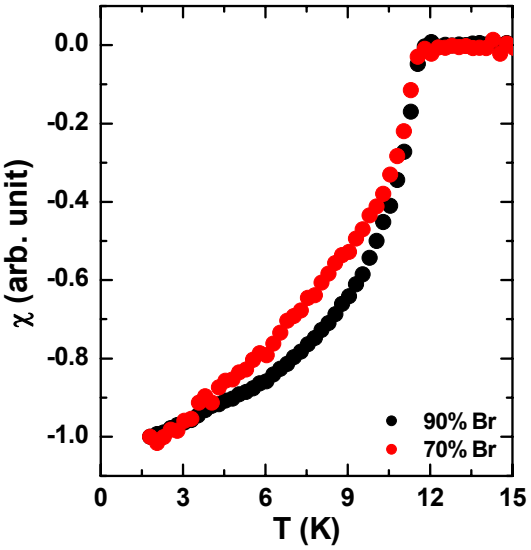

Figure 5.24: The temperature dependence of the magnetic susceptibility of κ-(BEDT-TTF)$_2$Cu[N(CN)$_2$]-Br$_x$Cl$_{1-x}$ for x = 70% and 90% . After cooling the sample in a cooling rate 6 K/min down to 1.8 K in zero magnetic field, a magnetic field of 5 G was applied perpendicular to the conduction plane and the magnetic susceptibility is measured during the heating.

5.3.4 The new phase diagram

The results of our dc, ESR and SQUID measurements on the alloyed series κ-(BEDT-TTF)$_2$Cu[N(CN)$_2$]Br$_x$Cl$_{1-x}$ enabled us to map the critical temperatures of the metal-to-insulator, antiferromagnetic and superconducting transitions for different Br dopings (see Table 5.6). Since each technique has a degree of sensitivity in detecting the transition temperature, differences in the transition temperature between the used techniques are observed. The temperature/Br-concentration phase diagram in the low temperature regime (T ≤ 60 K) is shown in Figure 5.25.

Our phase diagram summarises the phase transitions and the grounds states of κ-(BEDT-TTF)$_2$Cu[N(CN)$_2$]Br$_x$Cl$_{1-x}$. At high temperatures (T > 100 K), all the compounds are semiconductors and at low temperatures the state of the material is strongly influenced by the Br doping. Samples with x < 70% undergo to Mott-insulator transition followed by an antiferromagnetic ground state phase transition. For x > 70% they undergo a transition into Fermi liquid state, followed by a transition into superconducting ground state below around 12 K. The sample with 70% Br is locating very close from the border of Mott-transition.

	κ-(BEDT-TTF)$_2$Cu[N(CN)$_2$]Br$_x$Cl$_{1-x}$				
	Low Br dopings				
T (K)	0%		20%	40%	
$(T_{AFM})_{ESR}$	20.4		22.1	24	
$(T_{MI})_{ESR}$	54		56	55	
$(T_{MI})_{dc}$			50	50	
	High Br dopings				
T (K)	70%	80%	85%	90%	100%
$(T_c)_{ESR}$ (at 0.35 Tesla)	11.3	10.8		12.5	12.3
$(T_c)_{dc}$	10.5	12	12.2	12	
$(T_c)_{SQUID}$ (at 5 Gauss)	11.8			11.8	
$(T_{Fermi})_{ESR}$	28	27		29	29
$(T_{Fermi})_{dc}$	28	30	30	30	

Table 5.6: The critical temperatures of the metal-to-insulator (T_{MI}), antiferromagnetic (T_{AFM}), Fermi liquid (T_{Fermi}) and superconducting transitions (T_c) measured by dc, SQUID and ESR for different Br dopings of κ-(BEDT-TTF)$_2$Cu[N(CN)$_2$]Br$_x$Cl$_{1-x}$. The critical temperatures of T_{MI} and T_{Fermi} measured by ESR are estimated from the microwave conductivity results (see Figure 5.11).

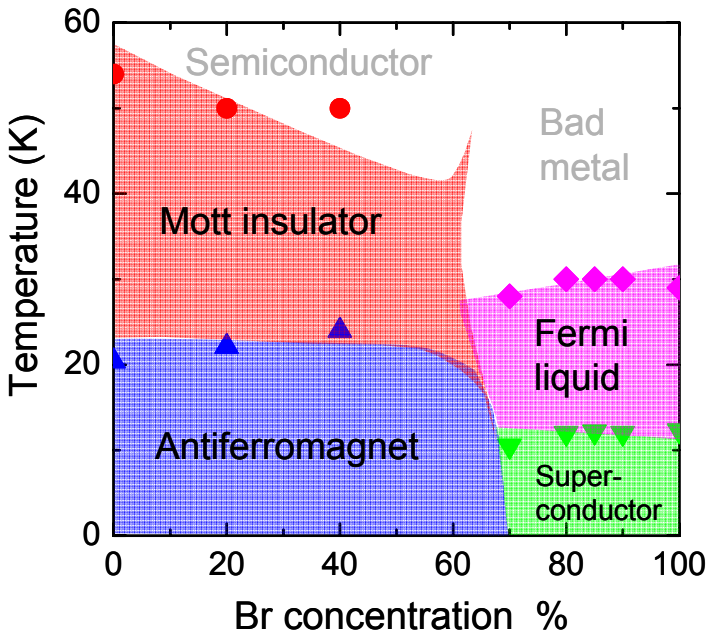

Figure 5.25: The temperature/Br concentration phase diagram determined from our dc-resistivity, ESR and SQUID experiments and after [8,9] for κ-(BEDT-TTF)$_2$Cu[N(CN)$_2$]Br$_x$Cl$_{1-x}$. The symbols are the experimental data from our measurements: the metal-to-insulator (T_{MI}) from the dc, the antiferromagnetic (T_{AFM}) and Fermi liquid (T_{Fermi}) from the ESR and the superconducting transitions (T_c) from the ESR and SQUID.

Chapter 6

Summary and Outlook

6.1 Results

In this work, detailed multi-frequency (X-band, Q-band and W-band) electron spin resonance (ESR) investigations of the quasi one-dimensional organic spin chain $(TMTTF)_2X$ (X = ReO_4, AsF_6 and SbF_6) were performed. The aim was to explore the spin and charge ordered state and to specify the nature of the relaxation processes. Furthermore, transport and X-band ESR measurements of the alloyed series κ-$(BEDT\text{-}TTF)_2Cu[N(CN)_2]Br_xCl_{1-x}$ (x = 0%, 20%, 40%, 70%, 80%, 85%, 90% and 100%) were carried out to study the phase diagram in the vicinity of the Mott-Hubbard transition as a function of the Bromine content (x).

The g-value and the ESR linewidth of $(TMTTF)_2ReO_4$ showed a distinct anisotropy similar to all previous studied $(TMTTF)_2X$ salts. In the high temperature region the g-value and the linewidth have the same anisotropy. The largest g-value and the linewidth are observed when the static magnetic field H_o is applied parallel to c^*-axis and the smallest linewidth and g-value when it is applied parallel to a-axis, i.e. $g_{c^*} > g_{b'} > g_a$ and $\Delta H_{c^*} > \Delta H_{b'} > \Delta H_a$. We observed that the linewidth along the three directions decreases nearly linearly from room temperature down to the anion ordering transition temperature (T_{AO} = 157 K). No anomaly is observed at the charge ordering transition temperature (T_{CO} = 227 K). The temperature dependence of the spin susceptibility at constant volume $(\chi_s)_v$ for T > 160 K can be modeled using the Bonner-Fisher model for S = 1/2 antiferromagnetic spin chain. From the fit, the calculated value of the AFM exchange constant $|J|$ is 425 K.

At T_{AO} a step-like decrease in the linewidth is observed, followed by an increase of the linewidth with decreasing temperature. Also the anisotropy of the linewidth changes below T_{AO} and becomes $\Delta H_a > \Delta H_{b'} > \Delta H_{c^*}$. From the angular dependence of the linewidth in the AO state, we found that the dipole-dipole interaction dominates as a relaxation process. Furthermore, in the AO state, no change with frequency is observed in the angular dependence of the linewidth.

The anion ordering transition of the low temperature non-magnetic insulating phase of $(TMTTF)_2ReO_4$ was studied. Below the AO transition, the spin susceptibility

decreases exponentially by lowering the temperature down to 120 K where the ESR spectra vanished. This decrease in the susceptibility corresponds to spin-singlet ground state. The spin susceptibility in this region can be described by an activation law. By this fit, the calculated singlet-triplet spin gap Δ_σ in the anion ordered state is 1100 K. This huge gap strongly indicates that $|J_1| >> |J_2|$, where J_1 and J_2 are the intradimer and the interdimer AFM exchange constant, respectively. This result was taken as a hint that the possible charge ordering pattern along the stacks is –o-O-O-o–, where "o" and "O" mean poor site and rich site, respectively.

The temperature dependences of the Q-band and W-band linewidth and the *g*-value of $(TMTTF)_2AsF_6$ and $(TMTTF)_2SbF_6$ along the three principle magnetic axes are frequency independent and their behaviors are similar to the results measured by X-band ESR spectrometer. The frequency independence of the linewidth along the three principle magnetic axes agrees with the theory of the torsional oscillation relaxation process. The angular dependence of the linewidth in *a*-*b*` plane in the charge ordered state for both compounds shows a doubling in the periodicity. Along the 45^o and 135^o directions the linewidth is strongly frequency dependent. The enhanced linewidth along 45^o in *a*-*b*´ plane at different temperatures below the charge ordering transition temperature (T_{CO}) shows square frequency dependence (ν^2). The ν^2 dependence of the linewidth is characteristic for anisotropic Zeeman (AZ) interaction. We conclude that the charge ordering transition in both compounds results in two inequivalent magnetic sites which cause the AZ interaction. Using AZ interaction theory, the difference in the *g*-value between the two inequivalent magnetic sites for $(TMTTF)_2SbF_6$ with $J' = 2.2$ K is calculated to be $\Delta g = 0.012$. The absence of the splitting of the ESR signal corresponds to AZ interaction is attributed to the inter-chain exchange coupling between the two inequivalent magnetic sites.

The increase of the ESR linewidth as the temperature approaches the AFM ordering temperature in $(TMTTF)_2SbF_6$ is due to AFM fluctuation. In this region the linewidth is proportional to $(T - T_N)^{-\mu}$. It is found that the AFM fluctuations are frequency independent where the same value of $\mu = 0.5$ is observed for all the ESR frequency bands.

The dc resistivity of κ-$(BEDT\text{-}TTF)_2Cu[N(CN)_2]Br_xCl_{1-x}$ showed a strong dependence on the Br/Cl ratio. At low Br dopings ($x < 70\%$), the resistivity has a semiconducting-like behavior from room temperatures down to around 50 K. Below T = 50 K the resistivity increases of many orders of magnitude due to a Mott-transition. At high Br dopings ($x \geq 70\%$), the resistivity showed a semiconducting-

like behavior with a broad maximum around 80 – 100 K, and at lower temperatures the behavior becomes metallic down to the superconducting transition temperature ($T_c \approx 12$ K) where the resistivity drops sharply.

The anisotropic ratio at room temperature in the 90% Br single crystal is found $\rho_\perp/\rho_\parallel = 25$, where $\rho_\perp$ is the resistivity perpendicular to the conduction plane and $\rho_\parallel$ is the resistivity parallel to the conduction plane. This ratio indicates the two-dimensional electronic character of the crystals. In the samples with x = 20% and 40%, the temperature dependence of the resistivity in the temperature range 300 – 25 K is found to follow an activation law $\rho \propto \exp(\Delta / k_B T)$ with strong change in the slope at 50 K. In the temperature range 25 – 50 K the obtained energy gap Δ is 600 K and 400 K for 20 % and 40%, respectively. From 50 K to 300 K the energy gap is found to be 200 K for both samples. The change in the energy gap above and below 50 K is a strong indication of a Mott-transition at this temperature. The temperature dependence of the resistivity in the high Br dopings (x = 70%, 80%, 85% and 90%) above the superconducting transition and at low temperatures in the metallic regime ($12\,\mathrm{K} < T < 30\,\mathrm{K}$) is described by $\rho(T) = \rho_o + AT^2$, where ρ_o and A is the residual resistivity and the prefactor of T^2, respectively. The quadratic temperature dependence of resistivity is found to be valid to a limiting temperature T_o. We found the product $A(x) \times [T_o(x)]^2$ is approximately constant independent of the chemical pressure for $x \geq 80\%$ Br. This result let us to conclude that this behavior corresponds to a strongly correlated Fermi liquid regime at low temperature.

The anisotropy of the ESR linewidth and the g-value is found $\Delta H_a > \Delta H_c > \Delta H_b$ and $g_b > g_c > g_a$, respectively. In all Br doping compounds, the temperature dependence of their ESR linewidth is approximately identical. The linewidth increases from room temperature with decreasing temperature, reaches a broad maximum around 75 K, then decreases sharply down to low temperature where the ESR spectra vanish totally for both directions indicating a transition into antiferromagnetic/ superconducting ground state. We attribute these results to the vibrations of the terminal ethylene groups which work as a dominant relaxation mechanism to the linewidth. The g-value along both directions in all compounds is temperature independent in the whole temperature range with a smooth anomaly at low temperatures.

The spin susceptibility at room temperature for all samples is found to be $(4 – 8) \times 10^{-4}$ emu/mole. The temperature dependence of the spin susceptibility for x = 0%, 20% and 40% Br samples is found nearly temperature independent in the temperature range 300 K – 40 K as expected for the Pauli susceptibility of a metals. Below 40 K down to 22 K, the spin susceptibility decreases rapidly. In the

superconducting samples, i.e. $x \geq 70\%$, the spin susceptibility at high temperature (T > 100 K) is similar to those with low Br ones. Below 100 K the susceptibility is observed to decrease with decreasing temperature with a sharp drop at 50 K. The energy gap obtained from the fitting of the spin susceptibility at low temperature is found comparable to the superconducting gap expected for these organic conductors within the BCS theory. The superconducting transition is confirmed by the observation the shielding signal for the superconducting samples.
Our dc, SQUID and ESR results enabled as to map the critical temperatures of the metal-to-insulator, antiferromagnetic and superconducting transitions into the phase diagram for different Br dopings. The temperature/Br concentration phase diagram showed that the κ-(BEDT-TTF)$_2$Cu[N(CN)$_2$]Br$_x$Cl$_{1-x}$ is served as a model of a bandwidth controlled Mott insulator.

6.2 Future Work

While our multi-frequency ESR measurements on (TMTTF)$_2$AsF$_6$ and (TMTTF)$_2$SbF$_6$ strongly point forward the anisotropic Zeeman interaction as a relaxation mechanism in the charge ordered state, the absence of the splitting of the ESR signal corresponding to this interaction is still an open question. Therefore, performing high frequency ESR measurements (higher than 95 GHz) would be very important to verify the proposed mechanism. Furthermore, observing two signals at high frequency will give more information about the anisotropy of the g-tensors related to the two inequivalent magnetic sites. Pulse ESR measurements on comparable compounds like (TMTTF)$_2$PF$_6$ would be useful to resolve any contributions to the relaxation mechanism in the charge ordered state. Finally, performing high frequencies ESR experiments on κ-(BEDT-TTF)$_2$Cu[N(CN)$_2$]-Br$_x$Cl$_{1-x}$ in the temperature range 80 – 300 K to estimate the frequency of the vibrations of the terminal ethylene groups and to clarify the frequency dependence of the relaxation mechanism would be very interesting.

Appendix *A*

ESR Studies of κ-(BEDT-TTF)$_2$[Hg(SCN)$_2$Cl]

In addition to the magnetic investigations of (TMTTF)$_2X$ and κ-(BEDT-TTF)$_2$-Cu[N(CN)$_2$]Br$_x$Cl$_{1-x}$, another 2-D organic conductor from the κ-(BEDT-TTF)$_2X$ salts with the anion X = [Hg(SCN)$_2$Cl] is studied by X-band ESR. In this appendix the crystal structure and the physical properties of the studied compound are introduced shortly in section A.1. The ESR results with a brief discussion are presented in section A.2.

A.1 Crystal Structure and Physical Properties

The crystal structure of the investigated compound has a packing pattern of κ-type (See Figure A.1). The cationic sheets of BEDT-TTF molecules alternate with anionic ones of [Hg(SCN)$_2$Cl] along *a*-axis. The interplanar distances between the BEDT-TTF molecules in the dimers are equal to 3.59 and 3.53 Å, respectively. The BEDT-TTF radical-cations are mutually shifted on the length of central C=C bond, and the dimers are connected by shortened S…S contacts in the range of 3.40 – 3.53 Å. In the conduction plane (*b*-*c* plane), the BEDT-TTF molecules form "corrugated bands" stretching along the *c*-axis in such a manner, that one band contains only "A" radical-cations (A has six shortened S…S distances), while another band consists of only "B" radical-cations (B has eight shortened S…S distances) [180]. The crystallographic parameters of κ-(BEDT-TTF)$_2$[Hg(SCN)$_2$Cl] are listed in Table A.1.

	κ-(BEDT-TTF)$_2$[Hg(SCN)$_2$Cl]
a (Å)	36.69
b (Å)	8.302
c (Å)	11.732
β (^{o})	90.02
V_{cell} (Å^3)	3573.2

Table A.1: The unit cell dimensions of κ-(BEDT-TTF)$_2$[Hg(SCN)$_2$Cl] at room temperature [180].

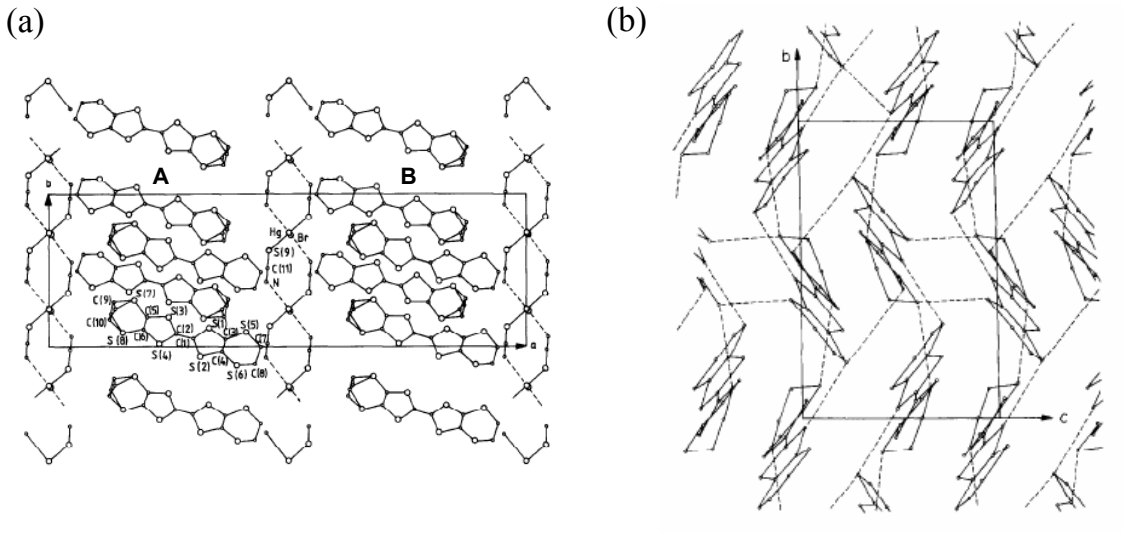

Figure A.1: Projection of the crystal structure of κ-(BEDT-TTF)$_2$[Hg(SCN)$_2$Cl] on the *a-b* plane (a), and *b-c* plane (b) [180,138].

Most of the reported studies on the κ-(BEDT-TTF)$_2$[Hg(SCN)$_2$Cl and the related compounds κ-(BEDT-TTF)$_2$[Hg(SCN)$_2$*X*] (*X* = Cl$_2$, Br, I) were limited to characterization measurements [180,181,182,183,184]. Figure A.2 shows the temperature dependence of the conductivity of κ-(BEDT-TTF)$_2$[Hg(SCN)$_2$Cl]. At high temperatures (T > 100 K), the conductivity has a metallic behavior. It increases four times with the temperature decrease down to T_{max} = 50 K, following a metal-insulator phase transition when the temperature decreases below 50 K [180].
The reported ESR study on κ-(BEDT-TTF)$_2$[Hg(SCN)$_2$Cl] [184] showed that the linewidth at room temperature is around 60 Oe which is within the range typical for BEDT-TTF based κ-type salts.

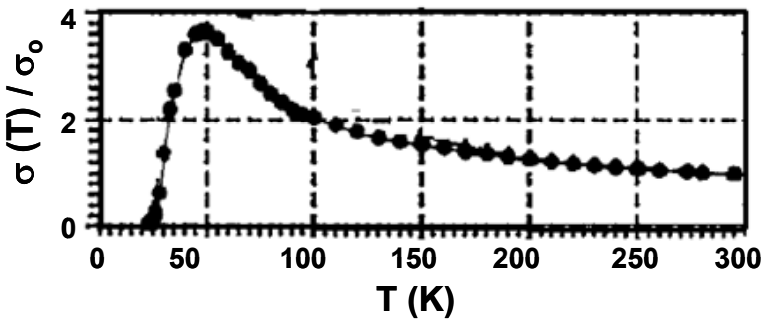

Figure A.2: Temperature dependence of conductivity of κ-(BEDT-TTF)$_2$[Hg(SCN)$_2$Cl]. σ_o is the conductivity at room temperature [180].

A.2 Electron Spin Resonance Results

The ESR spectra of the single crystal from κ-(BEDT-TTF)$_2$[Hg(SCN)$_2$Cl] are recorded when the static magnetic field H_o is applied parallel to the conduction plane (*b*-*c* plane) and perpendicular to it. At room temperature a single Dysonian line is observed when H_o is applied parallel to the conduction plane while a single Lorentzian line is observed when H_o is applied perpendicular to it. Figure A.3 shows the angular dependence of the g-value and the linewidth when H_o is applied parallel to *b*-*c* plane. The dashed lines are the square fits of the measured data using equations 5.4 and 5.5. The *g*-value and the linewidth show a distinct anisotropy with a different qualitative angular pattern. The *g*-value has a maximum along *b*-axis with a value of 2.0058 and minimum along *c*-axis with a value of 2.0034, while the maximum of the linewidth along *c*-axis with a value of 64 Oe and the minimum along *b*-axis with a value of 57 Oe.

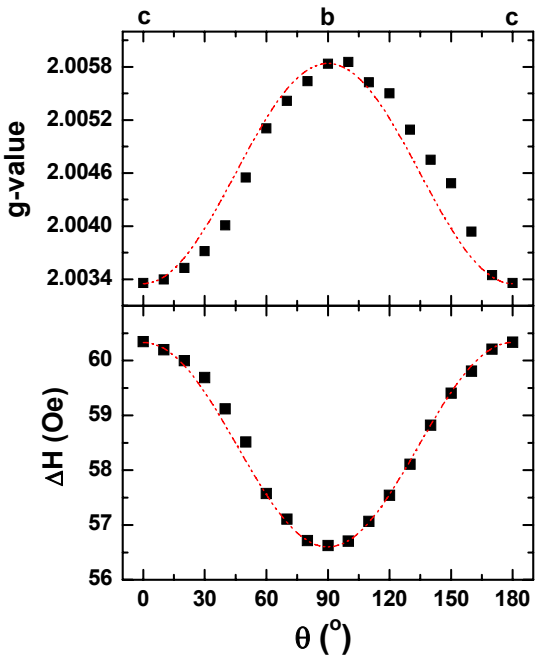

Figure A.3: Angular dependence of the linewidth and the *g*-value at room temperature of κ-(BEDT-TTF)$_2$[Hg(SCN)$_2$Cl] when the static magnetic field (H_o) is applied parallel to the *b*-*c* plane. The least square fittings of the linewidth and the *g*-value are shown by the dashed lines.

The angular dependence of the *g*-value is similar to that one observed in the alloyed series κ-(BEDT-TTF)$_2$Cu[N(CN)$_2$]Br$_x$Cl$_{1-x}$. As this dependence is similar also to that observed in many κ-(BEDT-TTF)-based systems, the anisotropy of the *g*-value has the same origin which was discussed in section 5.3.2.

Temperature dependent measurements of the ESR spectra were performed when the static magnetic field H_o is applied parallel (H_o // *b*-axis) and perpendicular ($H_o \perp$ *b*-axis) to the conduction plane. When H_o is applied parallel to the conduction plane (H_o // *b*-axis), at high temperatures (T > 50 K), a single asymmetric Dysonian line is observed. The Dysonian line is gradually converted to Lorentzian line with decreasing temperature below about 50 K and becomes more symmetric by decreasing the temperature as shown in Figure A.4.

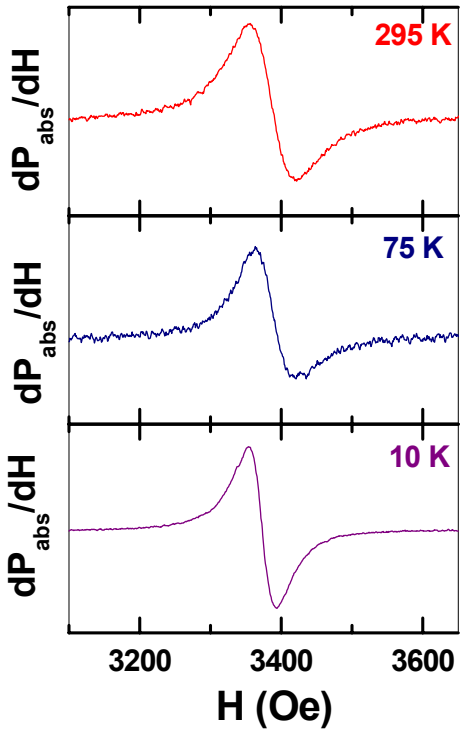

Figure A.4: The ESR spectra of κ-(BEDT-TTF)$_2$[Hg(SCN)$_2$Cl] at different temperatures when the static magnetic field (H_o) is applied parallel to the *b*-axis.

The temperature dependence of the microwave conductivity (MW) at 9.5 GHz evaluated from the ESR Dysonian lineshape analysis (see section 3.1.3.1) is shown in Figure A.5. The behaviour of MW conductivity is qualitatively identical to the dc conductivity (see Figure A.2), it increases with decreasing temperature down to T_{max} = 50 K, then a sharp decrease towards lower temperatures indicating metal-to-insulator phase transition.

The temperature dependence of the linewidth and the *g*-value when H_o is parallel and perpendicular to *b*-axis are shown in Figure A.6. Along *b*-axis, the linewidth increases with decreasing temperature, reaches a broad maximum at about 150 K, and then decreases sharply with decreasing temperature down to 28 K. At around 27 K a drastic change is observed, the linewidth increased sharply to value five times

higher than the value at 28 K then decreased with decreasing temperature down to 4.2 K. When $H_o \perp b$-axis, the linewidth decreases very slowly with decreasing temperature down to 150 K, and below 150 K it has the same behavior as in case of H_o // b-axis.

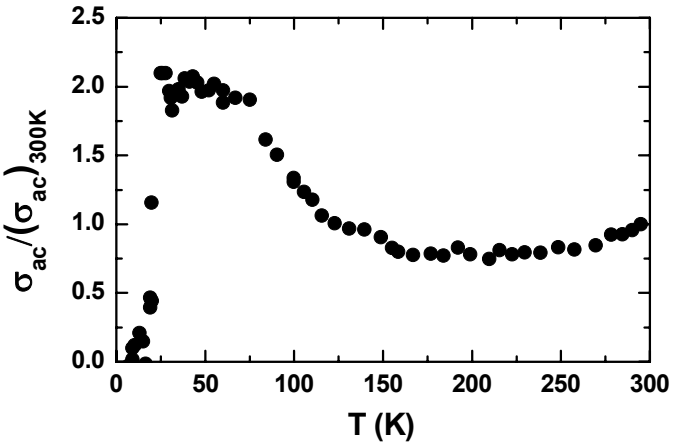

Figure A.5: The normalized temperature dependence of the microwave (MW) conductivity $\sigma_{ac}/(\sigma_{ac})_{300K}$ at 9.5 GHz as evaluated from the ESR Dysonian line of κ-(BEDT-TTF)$_2$[Hg(SCN)$_2$Cl].

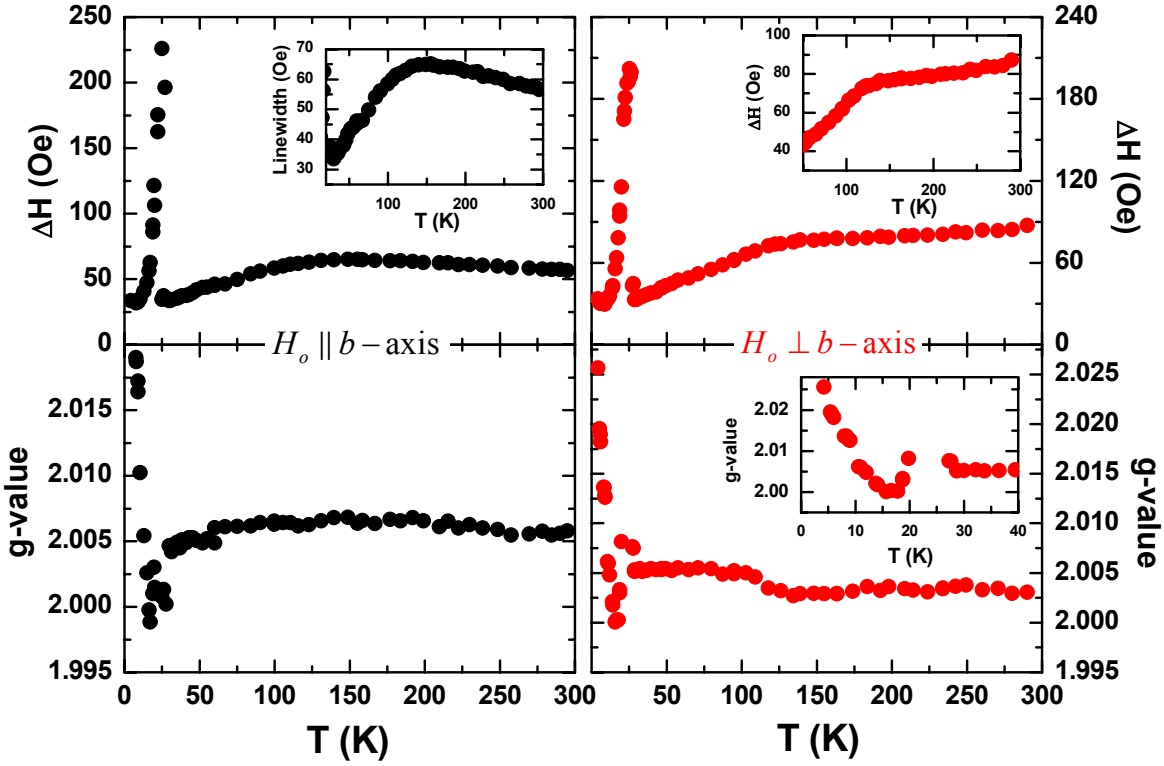

Figure A.6: Temperature dependence of the linewidth and the *g*-value of κ-(BEDT-TTF)$_2$[Hg(SCN)$_2$Cl] when the static magnetic field (H_o) is applied parallel (in-plane) and perpendicular (out-of-plane) to the *b*-axis.

The *g*-value along both directions is approximately temperature independent from the room temperature down to 28 K. At around 27 K a step-like decrease is observed then a sharp increasing with decreases temperature down to 4.2 K.

The temperature dependence of the linewidth at high temperature is similar to that one observed in κ-(BEDT-TTF)$_2$Cu[N(CN)$_2$]Br$_x$Cl$_{1-x}$, but the maximum of the linewidth shifted to higher temperature. X-ray studies on κ-(BEDT-TTF)$_2$-[Hg(SCN)$_2$Br] showed that a two-positional disorder exists in the ethylene groups of deuterated salt while such disorder appears only in a one of the ethylene groups in hydrogenated salt [138,181]. This means that in κ-(BEDT-TTF)$_2$[Hg(SCN)$_2$Cl] the broadening mechanism of the linewidth can be attributed to the ordering-disordering of the terminal ethylene groups (as in κ-(BEDT-TTF)$_2$Cu[N(CN)$_2$]Br$_x$Cl$_{1-x}$) and the shift in the maximum of the linewidth to higher temperature can be due to the high coupling between the anions and the cation sheets which induces freezing of the terminal ethylene groups at higher temperature. However, the slow decrease of the linewidth with decreasing temperature when $H_o \perp b$-axis can be due to the weak effect of this ordering along this direction, where the sharp decrease of the linewidth at the same temperature observed for H_o // *b*-axis (150 K) supports this argument.
The sharp increase of the linewidth at 27 K which is accompanied with increasing the *g*-value with decreasing temperature is a strong indication that a magnetic phase transition occurs. Similar behaviour was observed in (EDT-TTF-CONMe$_2$)$_2$AsF$_6$ [134], (TMTTF)$_2$SbF$_6$ (this work, [2]) and (TMTTF)$_2$Br [12], close to the transition into the antiferromagnetic (AFM) ground state. In order to clarify the phase transition in κ-(BEDT-TTF)$_2$[Hg(SCN)$_2$Cl] angular dependence measurements of the *g*-value at 4.2 K in both planes (H_o // *b*-*c* plane and $H_o \perp$ *b*-*c* plane) were performed as shown in Figure A.7. When H_o // *b*-*c* plane the *g*-value at 4.2 K has the same angular dependence as at room temperature, but the resonance field shifts to higher values along *c*-axis (decrease the *g*-value) and to lower value along *b*-axis (increase the *g*-value). In the other case, a slight shift in the *g*-values from the principle axes is observed when $H_o \perp$ *b*-*c* plane. These observations are characteristics of the antiferromagnetic resonance in an antiferromagnet with low spin-flop field $H_{SF} << H_o$.

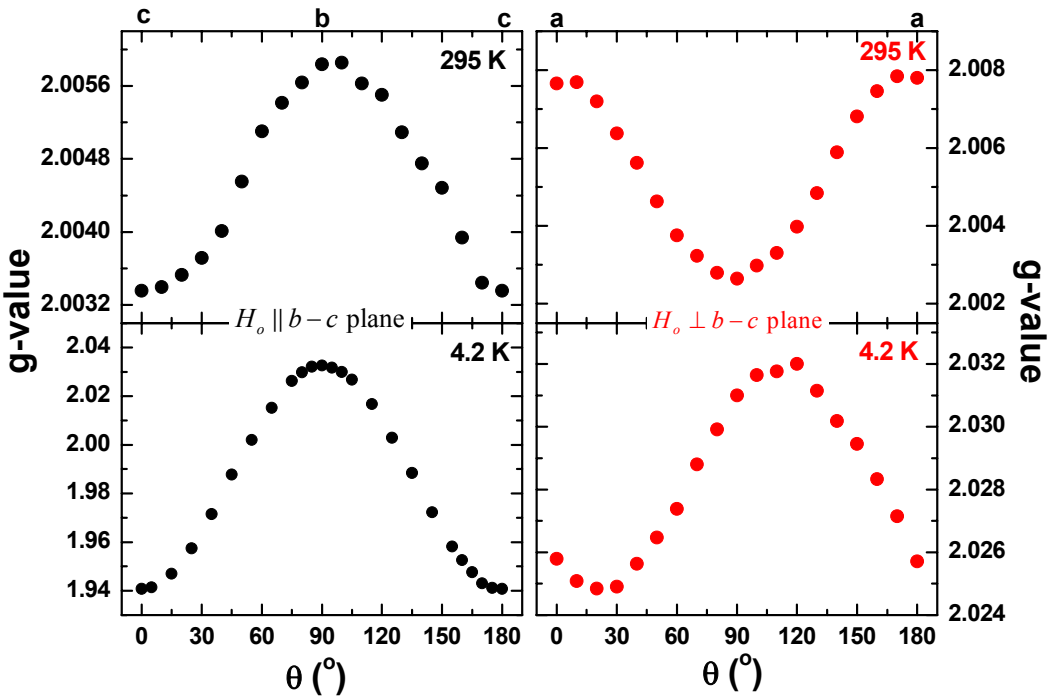

Figure A.7: Angular dependence of the *g*-value at 295 K 4.2 K of κ-(BEDT-TTF)$_2$[Hg(SCN)$_2$Cl] when the static magnetic field (H_o) is applied parallel and perpendicular to the conduction plane (*b*-*c* plane) .

The temperature dependence of the spin susceptibility is shown in Figure A.8. The spin susceptibility shows an activated behaviour in the temperature range 300 K – 28 K, where below 28 K the susceptibility increases sharply with decreasing temperature down to 4.2 K. This behaviour was observed in the deuterated κ-(BEDT-TTF)$_2$[Hg(SCN)$_2$Br] [181]. Since the spin susceptibility shows an activated behaviour in the temperature range 300 K – 28 K, $\ln(T \times (\chi_s / (\chi_s)_{RT})$ versus $1/T$ is plotted in Figure A.9. The plot shows a change in the slope at around T = 70 K, which is close from the metal-insulator phase transition temperature (T = 50 K). This behaviour is fitted using equation 5.9. From the fitting curve shown in Figure A.9 the energy gap in the high temperature region (T > 70 K) is found equal to 63 K and in the temperature region 27 < T < 70 K is equal to 395 K. This increase of the energy gap below 70 K seems to be correlated with the phase transition into the insulating ground state.

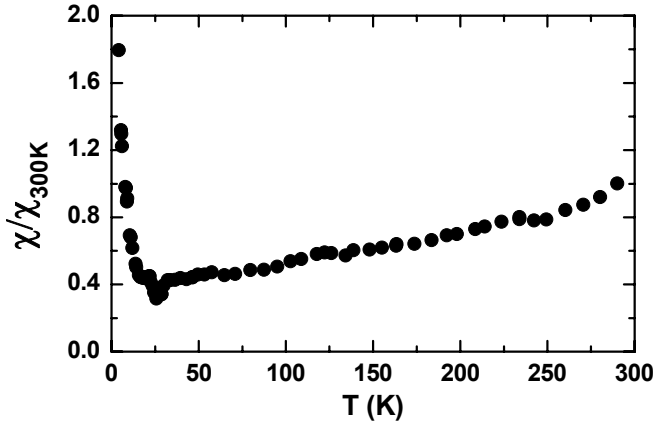

Figure A.8: Temperature dependence of the spin susceptibility normalized to the room temperature value [$\chi_s/(\chi_s)_{300K}$] of κ-(BEDT-TTF)$_2$[Hg(SCN)$_2$Cl].

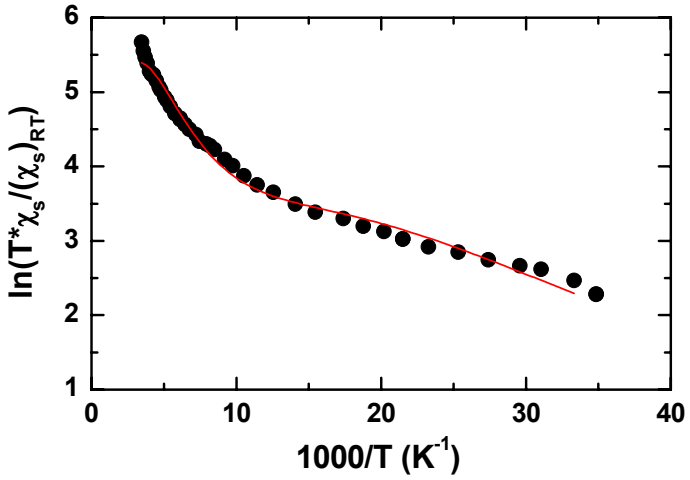

Figure A.9: Plot of $\ln(T\times(\chi_s/(\chi_s)_{RT})$ versus $1/T$ of κ-(BEDT-TTF)$_2$[Hg(SCN)$_2$Cl]. The black lines are the fitting lines using equation 5.9.

References

[1] D. S. Show, F. Zamborszky, B. Alavi, D. J. Tantillo, A. Baur, C. A. Merlic and S. E. Brown, Phys. Rev. Lett. **85**, 1698 (2000).

[2] B. Salameh, Ph. D. Thesis, Universität Stuttgart (2005).

[3] T. Nakamura, J. Phys. Soc. Jpn. **72**, 213 (2003).

[4] M. Dumm, B. Salameh, M. Abaker, L. K. Montgomery and M. Dressel, Phys. IV France 57, 57 (2004).

[5] F. Ya. Nad, P. Monceau, C. Carcel and J. M. Fabre, Synth. Met. **133**, 265 (2003).

[6] F. Ya. Nad, P. Monceau, C. Carcel and J. M. Fabre, J. Phys.: Condens. Matter **13**, L717 (2001).

[7] N. Toyota, M. Lang and J. Müller, *Low-Dimensional Molecular Metals*, (2007), (Springer-Verlag).

[8] P. Limelette, P. Wzietek, S. Florens, A. Georges, T. A. Costi, C. Pasquier, D. Jérome, C. Mézière and P. Bateil, Phys. Rev. Lett. **91**, 16401 (2003).

[9] M. de Souza, A. Brühl, Ch. Strack, B. Wolf, D. Schweitzer and M. Lang, Phys. Rev. Lett, **99**, 073003 (2007).

[10] J. Müller, M. Lang, F. Steglich, J. A. Schlueter, A. M. Kini and T. Sasaki, Phys. Rev. B **65**, 144521 (2002).

[11] V. Kataev, G. Winkel, N. Knauf, A. Gruetz, D. Khomskii, D. Wohlleben, W. Crump, J. Hahn and K. F. Tebbe, Physica B **179**, 24 (1992).

[12] M. Dumm, Ph. D. Thesis, Universität Augsburg (1999).

[13] J. C. Bonner and M. E. Fisher, Phys. Rev. **135**, 640 (1964).

[14] S. Eggert, I. Affleck, M. Takahashi, Phys. Rev. Lett. **73**, 332 (1994).

[15] B. Pilawa, J. Phys: Condens. Matter **9**, 3779 (1997).

[16] C. Yasuda, S. Todo, K. Hukushima, F. Alet, M. Keller, M. Keller, M. Troyer and H. Takayama, Phys. Rev. Lett. **94**, 217201 (2005).

[17] C. Bourbonnais, in *Interacting Electrons in Reduced Dimensions*, D. Baeriswyl and D. K. Campbell (eds), NATO ASI Ser. B, Physics **213** (Plenum Press, New York 1989), P. 227.

[18] N. F. Mott, J. Non-Cryst. Solids **1**, 1 (1968).

[19] M. Dumm, D. Faltermeier, N. Drichko, M. Dressel, C. Meziere, P. Batail, J. Merino and R. McKenzie. In preparation.

[20] A. C. Jacko, B. J. Powell and J. O. Ejaerestad, arXiv:0805.4275v2 [cond-mat.str-el].

[21] K. Frikach, M. Poirier, M. Castonguay and K. D. Truong, Phys. Rev. B. **61**, R6491 (2000).

[22] P. Delhaes, C. Coulon, J. Amiell, S. Flandrois, E. Toreilles, J. M. Fabre and L. Giral, Mol. Crys. Liq. Crys. **50**, 43 (1979).

[23] K. Bechgaard, C. S. Jacobsen, K. Mortensen, H. J. Pedersen and N. Thorup, Solid State Commun. **33**, 1119 (1980).

[24] J. P. Pouget, in *Low-Dimensional Conductors and Superconductors*, ed. By D. Jérome and L. G. Caron, NATO ASI Ser. B, Physics **155**, (Plenum Press, New York 1987).

[25] T. Ishiguro, K. Yamaji and G. Saito, Organic Superconductors, (Springer-Verlag, Berlin 1998).

[26] K. Petukhov, Ph. D. Thesis, Universität Stuttgart (2003).

[27] S. S. P. Parkin, J. J. Mayerle and E. M. Engler, J. Phys. (France) Coll. **44**, C3-1105 (1983).

[28] B. Liautard, S. Peytavin, G. Brun and M. Maurin, J. Phys. (France) Coll. **44**, C3-951 (1983).

[29] J. P. Pouget and S. Ravy, J. Phys. I France **6**, 1501 (1996).

[30] Y. Nogami, T. Ito, K. Yamamoto, N. Irie, S. Horita, T. Kambe, N. Nagao, K. Oshima, N. Ikeda and T. Nakamura, J. Phys. IV France **131**, 39 (2005); An oral presentation in Electronic Crystals Workshop (Corsica-France) 2005.

[31] Y. Nogami and T. Nakamura, J. Phys. IV France **12**, 145 (2002).

[32] L. Balicas, K. Behnia, W. Kang, E. Canadell, P. Auban-Senzier, D. Jérome, M. Ribault and J. M. Fabre, J. Phys. I France **4**, 1539 (1994).

[33] R. Laversanne, C. Coulon, B. Gallois, J. P. Pouget and R. Moret, J. Phys. Lett. **45**, L393 (1984).

[34] M. Dressel, P. Hesse, S. Kirchner, G. Untereiner, M. Dumm, J. Hemberger and L. K. Montgomery, Synth. Met. **120**, 719 (2001).

[35] B. Korin-Hamzić, E. Tafra, M. Basletić, G. Untereiner and M. Dressel, Phys. Rev. B **67**, 014513 (2003).

[36] D. Jérome and J. Schulz, Adv. Phys. **51**, 293 (2002).

[37] K. Bechgaard, K. Carneiro, M. Olsen, F. Rasmussen and C. S. Jacobsen, Phys. Rev. Lett. **13**, 852 (1981).

[38] R. L. Greene and E. M. Engler, Phys. Rev. Lett. **45**, 1587 (1980).

[39] M. Dumm, A. Loidl, B. W. Fravel, K. P. Strkey, L. K. Montgomery and M. Dressel, Phys. Rev. B **61**, 511 (2000).

[40] K. Penc and F. Mila, Phys. Rev. B **50**, 11431 (1994); K. Penc and F. Mila, J. Phys. IV (France) **3**, C2-155 (1993).

[41] B. Köhler, *Diploma Thesis*, Universität Stuttgart (2007).

[42] S. Nishimoto, M. Takahshi and Y. Ohta, J. Phys. Soc. Jpn. **69**, 1594 (2000).

[43] F. Nad and P. Monceau, J. Phys. Soc. Jpn. **75**, 51005 (2006).

[44] C. Coulon, P. Delhaes, S. Flandrois, R. Lagnier, E. Bonjour and J. M. Fabre, J. Phys. (France) **43**, 1059 (1982).

[45] S. Flandrois, C. Coulon, P. Delhaes, D. Chasseau, C. Hauw, J. Gaultier, J. M. Fabre and L. Giral, Mol. Cryst. Liq. Cryst **79**, 307 (1982).

[46] P. Delhaes, C. Coulon, J. Amiell, S. Flandrois, E. Toreilles, J. M. Fabre and L. Giral, Mol. Cryst. Liq. Cryst. **50**, 43 (1979).

[47] C. Coulon, J. C. Scott and R. Laversanne, Phys. Rev. B **33**, 6235 (1986).

[48] C. Coulon, S. S. P. Parkin and R. Laversanne, Phys. Rev. B. **31**, 3583 (1985).

[49] W. Yu, F. Zhang, F. Zamborszky, B. Alavi, A. Baur, C. A. Merlic and S. E. Brown, Phys. Rev. B **70**, 121101 (2004).

[50] T. Nakamura, K. Furukawa and T. Hara, J. Phys. Soc. Jpn. **75**, 13707 (2006).

[51] W. Yu, F. Zamborszky, B. Alavi, A. Baur, C. A. Merlic and S. E. Brown, J. Phys. IV France 114, 35 (2004).

[52] P. Monceau, F. Ya. Nad and S. Brazovskii, Phys. Rev. Lett. **86**, 4080 (2001).

[53] S. Fujiyama and T. Nakamura, J. Phys. Soc. Jpn. **75**, 14705 (2006).

[54] F. Nad, P. Monceau, T. Nakamura and K. Furukawa, J. Phys.: Condens. Matter **17**, L399 (2005).

[55] O. Klein, S. Donovan, M. Dressel and G. Grüner, Int. J. Infrared and Millimeter Waves **14**, 2489 (1993).

[56] M. de Souza, P. Foury-Leylekian, A. Moradpour, J.-P. Pouget and M. Lang, arXiv:0807.0735v1 [cond-mat.str-el].

[57] P. Wzietek, F. Creuzet, C. Bourbonnais, D. Jérome, K. Bechgaard and P. Patail, J. Phys. I (France) **1**, 171 (1993).

[58] B. Gallois, J. Gaultier, C. Hauw, D. Chasseau, A. Meresse, A. Filhol and K. Bechgaard, Mol. Cryst. Liq. Cryst. **119**, 225 (1985); B. Gallois, J. Gaultier, F. Bechtel, A. Filhol, L. Ducasse and Abderrabba, Synth. Met. **19**, 321 (1987).

[59] C. Bourbonnais, J. Phys. I (France) **3**, 143 (1993).

[60] W. A. Little, Phys. Rev. **134**, A1416 (1964).

[61] M. Mizuno, A. F. Garito and M. P. Cava, J. Chem. Soc. Chem. Comm. **18**, (1978).

[62] T. Mori, H. Mori and S. Tanaka, Bull. Chem. Soc. Jpn. **72**, 179 (1999).

[63] D. Faltermeier, J. Barz, M. Dumm, N. Drichko, M. Dressel, C. Meziere and P. Batail, Phys. Rev. B 76, 165113 (2007).

[64] H. Seo, C. Hotta and H. Fukuyama, Chem. Rev. **104**, 5005 (2004).

[65] D. Jérome, in Organic Conductors, ed. by J.-P. Farges (Marcel Dekker, New York, 1994).

[66] R. H. McKenzie, Science **31**, 820 (1997).

[67] J. Wosnitza, Studies of High Temperature Superconductors 34, 97 (2000).

[68] Y. V. Sushko and K. Andres, Phys. Rev. B **47**, 330 (1993).

[69] Ch. Strack, C. Akinci, V. Pashchenko, B. Wolf, E. Uhrig, W. Assmus, M. Lang, J. Schreuer, L. Wiehl, J. A. Schlueter, J. Wosnitza, D. Schweitzer, J. Müller and J. Wykhoff, Phys. Rev. B **72**, 54511 (2005).

[70] T. Nakamura, T. Nobutoki, T. Takahashi, G. Saito, H. Mori and T. Mori, J. Phys. Soc. Jpn. **63**, 4110 (1994); T. Nakamura, T. Noubutoki, M. Miyamoto, Y. Tsubokura, R. Tsuchiya, T. Takahashi, K. Canola and G. Saito, J. Superconductivity **7**, 671 (1994).

[71] P. Bele, H. Brunner, D. Schweitzer and H. J. Keller, Synth. Met. **89**, 231 (1997).

[72] M. A. Tanatar, T. Ishiguro, T. Kondo and G. Saito, Phys. Rev. B **61**, 3278 (2000).

[73] H. Ito, T. Ishiguro, M. Kubota and G. Saito, J. Phys. Soc. Jpn. **65**, 2987 (1996).

[74] Yu. V. Sushko, K. Andres, N. D. Kusch and E. B. Yagubskii, Solid State Comm. 87, 589 (1993).

[75] V. A. Bondarenko, R. A. Petrosov, M. A. Tanatar, V. S. Yefanov and N. D. Kushch, Physica C **235**, 2467 (1994).

[76] V. J. Emery and S. A. Kivelson, Phys. Rev. Lett. **74**, 3253 (1995).

[77] M. Dressel, G. Grüner, K. D. Garlson, H. H. Wang and J. M. Williams, Synth. Met. **70**, 927 (1995).

[78] K. Miyagawa, A. Kawamoto, Y. Nakazawa and K. Kanoda, Phys. Rev. Lett. **75**, 1174 (1995).

[79] U. Welp, S. Fleshler, W. K. Kwok, G. W. Crabtree, K. D. Carlson, H. H. wang, U. Geiser, J. M. Williams and V. M. Hitsman, Phys. Rev. Lett. **69**, 840 (1992).

[80] M. Kubota, G. Saito, H. Ito, T. Ishiguro and N. Kojima, Mol. Cryst. Liq. Cryst. **284**, 367 (1996).

[81] H. Ito and T. Ishiguro, Phys. Rev. B **61**, 3243 (2000).

[82] A. Kawamoto, K. Miyagawa and K. Kanoda, Phys. Rev. B **55**, 14140 (1997).

[83] S. Wanka, D. Beckmann, J. Wosnitza, E. Balthes, D. Schweitzer, W. Strunz and H. J. Keller, Phys. Rev. B **53**, 9301 (1996).

[84] U. Geiser, A. M. Kini, H. H. Wang, M. A. Beno and J. M. Williams, Acta Cryst. C **47**, 190 (1991).

[85] L. G. Caron, in Organic Conductors, ed. by J.-P. Farges (Marcel Dekker, New York, 1994).

[86] J. M. Ziman, *Principles of the theory of solids*, 2nd edition (1972). Cambridge University Press.

[87] N. Mott, Proc. Roy. Soc. Lond. **382**, 1 (1982).

[88] N. F. Mott, Proc. Phys. Soc. Lond. **62**, 416 (1949).

[89] N. F. Mott, Rev. Mod. Phys. **40**, 677 (1968).

[90] V. J. Emery, in Highly Conducting One-Dimensional Solids, ed. by J. T. Devreese, R. P. Evrard and V. E. van Doren (Plenum Press, New York, 1979).

[91] H. Kino and H. Fukuyama, J. Phys. Soc. Jpn. **64**, 2726 (1995).

[92] M. Pope and C. E. Swenberg, *Electronic Processes in Organic Crystals and Polymers*, 1999, Oxford University Press, Inc.

[93] L. Landau, Sov. Phys. JETP **3**, 920 (1957).

[94] J. Singleton, *Band Theory and Electronic Properties of Solids*, 2001, Oxford University Press Inc.

[95] J. Bardeen, L. N. Cooper and J. R. Schrieffer, Phys. Rev. **106**, 162 (1957)

[96] J. Bardeen, L. N. Cooper and J. R. Schrieffer, Phys. Rev. **108**, 1175 (1957)

[97] C. Kittel, *Introduction to Solid State Physics*, 8th ed., 2005, John Wiley and Sons, Inc.

[98] S. Blundell, *Magnetism in Condensed Matter*, 2001, Oxford University Press Inc.

[99] W. E. Estes, D. P. Gavel, W. E. Hatfield and D. J. Hodgson, Inorg. Chem. **17**, 1415 (1978).

[100] M. S. Makivic and H. Q. Ding, Phys. Rev. B **43**, 3562 (1991).

[101] J. Wang, Phys. Rev. B **44**, 2396 (1991).

[102] N. D. Mermin and H. Wagner, Phys. Rev. Lett. **17**, 1133 (1996).

[103] H. Seo and H. Fukuyama, J. Phys. Soc. Jpn. **66**, 1249 (1997).

[104] J. P. Pouget, R. Moret, R. Comes and K. Bechgaard, J. Phys. Lett. France **42**, 543 (1981).

[105] R. Moret, J. P. Pouget, R. Comes and K. Bechgaard, Phys. Rev. Lett. **49**, 1008 (1982).

[106] G. Subias, T. Abbaz, J. M. Fabre and J. Fraxedas, Phys. Rev. B **76**, 085103 (2007).

[107] C. P. Poole, *Electron Spin Resonance*, 2nd edition, Dover Puplications, INC. Mineola, New York.

[108] C. P. Slichter, *Principles of Magnetic resonance*, 2nd edition (Springer-Verlag).

[109] M. Heinrich, H. A. Krug von Nidda, A. Krimmel, A. Loidl, R. M. Eremina, A. D. Ineev, B. I. Kochelaev, A. V. Prokofiev and W. Assmus, Phys. Rev. B **67**, 224418 (2003).

[110] R. K. Kukkadapu and J. E. Amonette, Spectrometer: EPR/ESR, Continuous wave. EMSL capabilities. http://www.emsl.pnl.gov/instruments.

[111] J. Dyson, Phys. Rev. **98**, 349 (1955).

[112] G. Feher and F. Kip, Phys. Rev. **98**, 337 (1955).

[113] A. C. Chapman, P. Rhodes and E. F. Seymour, Proc. Phys. Soc. **LXX (4-B)**, 354 (1957).

[114] H. Hau Wang, M. L. Vanzile, J. A. Schlueter, U. Geiser, A. M. Kini, P. P. Sche, H. J. Koo, M. H. Whangbo, P. G. Nixon, R. W. Winter and G. L. Gard, J. Phys. Chem. B **103**, 5493 (1999).

[115] F. Bloch, Phys. Rev. **70**, 460 (1946).

[116] A. Carrington and A. D. McLachlan, *Introduction to Magnetic Resonance: With application to Chemistry and Chemical Physics*, 2nd edition, Harper and Row, New York.

[117] R. T. Schumacher and C. P. Slichter, Phys. Rev. **101**, 58 (1956).

[118] R. Kuba and K. Tomita, J. Phys. Soc. Jpn. **9**, 888 (1954).

[119] G. F. Kokoszka, *Low-Dimensional Cooperative Phenomena*, ed. by H. J. Keller, (1975), Plenum Press, New York.

[120] K. Itoh and M. Kinoshita, *Molecular Magnetism: New Magnetic Materials*, 2000, Gordon and Breach Science Publishers, Tokyo-Japan.

[121] D. Gatteschi, R. Sessoli and J. Villain, *Molecular Nanomagnets*, 2006, Oxford University Press.

[122] T. Moriya, Phys. Rev. 120, 91 (1960).

[123] R. J. Elliott, Phys. Rev. **96**, 266 (1954).

[124] M. Weger, J. Phys. (France) Coll. **6**, C6-1456 (1978).

[125] F. J. Adrian, Phys. Rev. B **26**, 2682 (1982).

[126] F. J. Adrian, Phys. Rev. B **33**, 1537 (1986).

[127] N. W. Ashcroft and N. D. Mermin, *Solid State Physics*, (1976) Thomson Learing , Inc, USA.

[128] R. L. Fagaly, Rev. Sci. Inst. **77**, 101101 (2006).

[129] P. Atkins and J. De Paula, Atkins' Physical Chemistry, 7th edition, OXFORD UNIVERSITY PRESS.

[130] A. Janossy "Private communications".

[131] C. Coulon and R. Clerac, Chem. Rev. **104**, 5655 (2004).

[132] Eugen Merzbacher, *Quantum Mechanics*, 1970, John Wiley and Sons, Inc.

[133] K. Heuzé, M. Fourmigué, Patric Batail, C. Coulon, R. Clérac, E. Canadell, P. Auban-Senzier, S. Ravy and D. Jérome, Adv. Mater. **15**, 1251 (2003).

[134] Balint Nafradi "Private communications".

[135] J. Riera and D. Poilblanc, Phys. Rev. B **63**, 241102 (2001).

[136] D. Halliday and R. Resnick, *Physics*, 1992, by John Wiley and Sons, Inc., New York.

[137] C. E. More, Atomic Energy Levels (US. GPO, Washinton, D. C., 1971), Vol. I and II.

[138] E. I. Yudanova, S. K. Hoffmann, A. Graja, S. V. Konovalikhin, O. A. Dyachenko, R. B. Lubovskii and R. N. Lyubovskaya, Synth. Met. **73**, 227 (1995).

[139] H. A. Krug von Nidda "Private communications".

[140] A. Abragam and B. Bleany, *Electron Paramagnetic Resonance of Transition Ions*, 1986, Oxford University Press-United Kingdom.

[141] A. Zorko, D. Arcon, K. Biljakovic, C. Carcel, J. M. Fabre and J. Dolinsek, Phys. Rev. B **64**, 172404 (2001).

[142] S. Tomić, J. Cooper, W. Kang, D. Jérome and K. Maki, J. Phys. I (France) **1**, 1603 (1991).

[143] S. Lefebvre, P. Wzietek, S. Brown, C. Bourbonnais, D. Jérome, C. Mézière, M. Fourmigué and P. Batail, Phys. Rev. Lett. **25**, 5420 (2000).

[144] The measurements are performed by B. Salameh at 1. Physikalisches Institut -Universität Stuttgart.

[145] H. Sato, T. Sasaki and N. Toyota, Physica C **185**, 2679 (1991).

[146] M. Oshima, H. Mori, G. Saito and K. Oshima, in *The physics and chemistry of organic superconductors*, ed. By G. Saito and S. Kagoshima (Springer, Berlin, Heidelberg 1990).

[147] A. Kobayashi, T. Udagawa, H. Tomita, T. Naito and H. Kobayashi, Chem. Lett. 2179 (1993).

[148] N. L. Wang, B. P. Clayman, H. Mori and S. Tanaka, J. Phys.: Condens. Matter **12**, 2867 (2000).

[149] S. Gärtner, E. Gogu, I. Heinen, H. J. Keller, T. Klutz and D. Schweitzer, Solid State Comm. **65**, 1531 (1988).

[150] N. Toyota, T. Sasaki, H. Sato and Y. Watanabe, Physica C **178**, 339 (1991).

[151] I. D. Parker, R. H. Friend, M. Kurmoo, P. Day, C. Lenoir and P. Batail, J. P hys.: Condens. Matter **1**, 4479 (1989).

[152] M. Kund, H. Müller, W. Biberacher and K. Andres, Physica B **191**, 274 (1993).

[153] M. A. Tanatar, T. Ishiguro, T. Kondo and G. Saito, Phys. Rev. B **59**, 3849 (1999).

[154] D. Schweitzer "Private communications".

[155] L. K. Montgomery, R. M. Vestal, K. P. Starkey, B. W. Fravel, M. J. Samide, D. G. Peters, C. H. Mielke and J. D. Thompson, Synth. Met. **103**, 1878 (1999).

[156] X. Su, F. Zuo, J. A. Schlueter, M. Kelly and J. M. Williams, Phys. Rev. B **57**, 14056 (1998).

[157] R. Rosenbaum, Phys Rev. B **44**, 3599 (1991).

[158] S. Nakatsuji, V. Dobrosavljevic, D. Tanaskovic, M. Minakata, H. Fukazawa and Y. Maeno, Phys. Rev. Lett. **93**, 146401 (2004).

[159] M. Imada, A. Fujiimori and Y. Tokura, Rev. Mod. Phys. **70**, 1039 (1998).

[160] G. R. Stewart, Rev. Mod. Phys. **56**, 755 (1984).

[161] K. Kadowaki and S. B. Woods, Solid State Comm. **58**, 507 (1986).

[162] K. Miyaki, T. Matsuura and C. M. Varma, Solid State Comm. **71**, 1149 (1989).

[163] Y. Maeno, K. Yoshida, H. Hashimoto, S. Nishizaki, S. I. Ikeda, M. Nohara, T. Fujita, A. P. Mackenzie, N. E. Hussey, J. G. Bednorz and F. Lichtenberg, J. Phys. Soc. Jpn. **66**, 1405 (1997).

[164] M. J. Rice, Phys. Rev. Lett. **20**, 1439 (1968).

[165] J. Merino, M. Dumm, N. Drichko, M. Dressel and R. H. McKenzie, Phys. Rev. Lett. **100**, 086404 (2008).

[166] B. Andraka, C. S. Jee, J. S. Kim and G. R. Stewart, Solid State Comm. **79**, 57 (1991).

[167] J. Merino and R. H. Mckenzie, Phys. Rev. B **61**, 7996 (2000).

[168] B. Salameh "Private communications".

[169] M. Dressel, O. Klein and G. Grüner, Phys. Rev. B **50**, 13603 (1994).

[170] P. Bele, H. Brunner, I. Heinen and D. Schweitzer, Appl. Magn. Reson. **17**, 481 (1999).

[171] E. I Yudanova, S.K. Hoffmann, A. Graia and R. N. Lyubovskaya, Synth. Met. 66, **43** (1994).

[172] A. N. Bloch, in Lecture Notes in Physics, ed. By W. Beiglböck, Vol. 65 (Springer, Berlin 1977).

[173] U. Geiser, A. J. Schultz, H. H. Wang, D. M. Watkins, D. L. Strupka and J. M. Williams, Physica C **174**, 475 (1991).

[174] E. Yusuf, B. J. Powell and R. H. Mckenzie, Phys. Rev. B **75**, 214515 (2007).

[175] P. M. Richard, in K. A. Müller and A. Rigamoti, Proc. Int. School of Physics "Enrico Fermi" Course LIX, Local Properties at Phase Transitions, Varenna, Italy, 1993, North-Holland, Amesterdam, 1976.

[176] J. P. Pouget, Mol. Cryst. Liq. Cryst. **230**, 101 (1993).

[177] K. Kanoda, J. Phys. Soc. Jpn. 75, 051007 (2006).

[178] N. Elster, R. R. P. Singh and A. P. Young, J. Appl. Phys. **75**, 5943 (1994).

[179] N. Barisic "Private communications".

[180] M. Z. Aldoshina, R. N. Lyubovskaya, S. V. Konovalikhin, O. A. Dyachenko, M. K. Makova and R. B. Lyubovskii, Mol. Cryst. Liq. Cryst. **230**, 185 (1993).

[181] E. I. Yudanova, R. N. Lyubovskaya, S. K. Hoffmann and A. Graja, Synth. Met. **70**, 971 (1995).

[182] E. I. Yudanova, L. M. Makarova, S. V. Konovalikhin, O. A. Dyachenko, R. B. Lyubovskii and R. N. Lyubovskaya, Synth. Met. **79**, 201 (1996).

[183] R. B. Lyubovskii and R. N. Lyubovskaya and O. A. Dyachenko, J. Phys. I (France) **6**, 1609 (1996).

[184] E. I. Yudanova, R. N. Lyubovskaya, R. B. Lyubovskii, S. V. Konovalikhin and O. A. Dyachenko, Synth. Met. **86**, 2195 (1997).

Curriculum Vitae

February 15, 1978	Born in Kuwait, Jordanian
1985-1991	Elementary school study -Kuwait
1991-1997	Secondary school study -Jordan
July1997	General Secondary Education Certificate Examination - Jordan
1997-2001	Student of physics at University of Jordan- Jordan
February 2001	Bachelor degree in Physics
2001-2003	Graduate student of physics at the University of Jordan- Jordan
September 2003	Master of Science, thesis: "The Electrical Behavior of Laminated Conductive Polymer Composite at Low Temperatures", Advisor: Prof. A. Zihlif.
2003-2005	Teacher (Ministry of Education - Jordan)
Since February 2005	A member of the graduate college "Modern methods of magnetic resonance in materials science" of the Faculties of Physics and Chemistry, Universität Stuttgart
Since February 2005	PhD student at the 1. Physikalisches Institut, Universität Stuttgart

List of Publications

B. P. Gorshunov, A.S. Prokhorov, S. Kaiser, D. Faltermeier, S. Yasin, M. Dumm, N. Drichko, E. S. Zhukova, I. E. Spektor, S. Vongtragool, M. B. S. Hesselberth, J. Aarts, G. J. Nieuwenhuys and M. Dressel.
”Charge Localization due to RKKY Interaction in the Spin Glass AuFe”.
Europhys. Lett. ***76****, 938 (2006).*

A.S. Prokhorov, V. B. Anzin, D. A. Vitukhnovskii, E. S. Zhukova, I. E. Spektor, B. P. Gorshunov, S. Vongtragool, M. B. S. Hesselberth, J. Aarts, G. J. Nieuwenhuys, M. Dumm, D. Faltermeier, S. Kaiser, S. Yasin, M. Dressel and N. Drichko.
” Terahertz spectroscopy of AuFe spin glasses”.
JETP ***103****, 887 (2006)*.

S. Yasin, A. M. Zihlif, G. Ragosta.
“The electrical behaviour of laminated conductive polymer composite at low temperatures”.
Journal Materials Science: Materials in Electronic ***16****, 63 (2005).*

T. M. Tawalbeh, S. Saq’an, S. Yasin, A. M. Zihlif, G. Ragosta.
“Low temperature electrical conductivity of low-density polyethylene/carbon black composites”.
Journal Materials Science: Materials in Electronic, ***16****, 351 (2005).*

M. Glied, S. Yasin, S. Kaiser, N. Drichko, M. Dressel and J. A. Schlueter.
”DC and high-frequency conductivity of the organic metals β´´-(BEDT-TTFF)$_2$SF$_5$*R*SO$_3$ (*R* = CH_2CF_2 and CHF)”.
Submitted to European Physical Journal B.

Acknowledgements

Firstly, I would like to thank my Supervisor Prof. Martin Dressel for giving me this opportunity to perform this project in his group, and also for all his encouragement and support in achieving the completion of this project.

I am deeply indebted to my advisor Dr. Michael Dumm whose assistance, long discussions, stimulating suggestions, brilliant ideas and encouragement helped me in all the time of research for writing of this thesis. I am also greatly appreciating his patience, friendship and kindness during my work with him.

I would like to thank Prof. Dieter Schweitzer for his agreement to be a second supervisor for my thesis and for his grateful ideas for this project.

I express my thanks to Dr. Belal Salameh for all the assistance during the first steps in my project, and also for his continuous encouragement.

Special thanks to Gabriele Untereiner for growing the single crystals of the TMTTF salts, and also for preparing the dc contacts of BEDT-TTF salts and solving several of experimental problems. Indeed, I can not estimate her contribution to this work.

I am very grateful to Prof. G. Denninger and Dr. H. J. Kümmerer from the 2. Physikalisches Institut for their collaboration and assistance in performing the W-band ESR measurements.

Furthermore, I thank very much Dr. H. A. Krug von Nidda from the Lehrstuhl institute für Experimentalphysik V of the Universität Augsburg for his collobration in performing the Q-band ESR measurements in his lab, and for the useful discussion with him.

I would like to thank all of my colleagues at Prof. Dressel's group, in particular, Eva Rose, Fadi El-Hallak, Stephan Kaiser, Christoph Schlegel, Neven Barisic and Joris van Slageren for their friendship and assistance.

I would like to thank the Graduate College of the Magnetic Resonance, Universität Stuttgart for their educational and financial support during this project.

I am very grateful to the technical support and the help of the low-temperature workshop headed by Jürgen Maurer and of the glass workshop.

Finally, I am very gratitude to my parents and my family whose love and caring make me possible to complete the doctorate works.